UNIVERSITY OF PADOVA

DEPARTMENT OF CHEMICAL SCIENCE

MOLECULAR SCIENCE

Light-induced electronic dynamics of molecules close to plasmonic nanostructures: a quantum chemistry approach

Supervisor: Prof. Stefano Corni

Ph.D. Student: Giulia Dall'Osto

Academic Year 2022/2023

Contents

PART II   101

Chapter 4   101

Chapter 5   155

Chapter 6   175

Conclusion   200

List of pubblications

List of publications related to this thesis:

1. Dall'Osto, G., Gil, G., Pipolo, S., Corni, S., *Real-time dynamics of plasmonic resonances in nanoparticles described by a boundary elements method with generic dielectric function* J. Chem. Phys. 153, 184114 (2020);

2. Romanelli, M., Dall'Osto, G., Corni S., *Role of metal-nanostructure features on tip-enhanced photoluminescence of single molecules* J. Chem. Phys. 155, 214304 (2021);

3. Dall'Osto, G., Corni, S., *Time Resolved Raman Scattering of Molecules: A Quantum Mechanics Approach with Stochastic Schrödinger Equation* J. Chem. Phys. A 126, 43, 8088–8100 (2022);

4. Dall'Osto, G., Vaccarelli, O., Guido, C. A., Corni, S., *Role of ions in solvated Amino acids Raman spectra*, in preparation

5. Dall'Osto, G., Marsili, M., Vanzan, M., Toffoli D., Stener M., Corni, S., Coccia, E.,*Photoinduced hole injection explains the reaction selectivity in CO_2 hydrogenation on Rh nanocube*, in preparation

List of other publications:

1. Dall'Osto, G., Coccia, E., Guido, C. A., Corni, S., *Investigating ultrafast two-pulse experiments on single DNQDI fluorophores: a stochastic quantum approach*, Phys. Chem. Chem. Phys., 22, 16734, (2020).

2. Shiraogawa, T., Dall'Osto, G., Cammi, R., Ehara, M., Corni, S., *Inverse design of molecule–metal nanoparticle systems interacting with light for desired photophysical properties* Phys. Chem. Chem. Phys. 24, 22768 (2022);

3. Rosa, M., Dall'Osto, G., Cammi, R., Corni, S., *Quantum Optimal Control Theory for a Molecule Interacting with a Plasmonic Nanoparticle*, submitted

4. Coane, C., Romanelli, M., Dall'Osto, G., Di Felice, R., Corni, S., *Unraveling the Mechanism of Tip-Enhanced Molecular Energy Transfer*, submitted

Introduction

The interaction between light and matter has fascinated many generations throughout history, but it is only in recent decades that the advent of new technologies has made it possible to manipulate electromagnetic radiation at the nanoscale. The interest in nano-optics stems from the fact that the energy range of typical light quanta perfectly matches electronic and vibrational transitions, making them suitable for the study of molecules.[1, 2] Particularly useful in this regime are nanosystems such as metal nanoparticles or nanosurfaces that exhibit special properties when interacting with light: collective oscillations of conduction electrons are activated. Such electron oscillations, namely surface plasmons, are particularly relevant as they can amplify the incident electric field nearby the nanoparticle.

Nano-optics applied to plasmonic systems has given such promising results that researchers have made great efforts to improve their manipulation. Nowadays, plasmon resonances can be fine-tuned to achieve precise plasmon frequencies by adjusting the properties of nanosystems such as composition, size and shape.[3, 4]

Strong control over plasmon resonances makes plasmonic nanosystems suitable to be coupled with molecules to tune and enhance their optical response to incident radiation.[5, 6] Nowadays, so-called molecular plasmonics has a variety of applications, from telecommunication technology, which uses emitting molecules as electromagnetic antennas, to biology, where it is used to realise plasmonic biosensors[7, 8] or for molecular imaging to improve the understanding of biological processes.[9, 10] From a chemical point of view, molecular plasmonics is an interdisciplinary topic that interests inorganic chemistry from the synthesis side, organic chemistry that

3

exploits the binding properties of metal nanoparticles to ligands, and quantum chemistry that focuses on the study of nano-optical phenomena.[11] In addition, surface plasmons have been exploited for photochemistry[12, 13, 14] and catalysis.[15, 16]

Among the many applications that have been developed since then, plasmonic nanosystems have been used in the field of molecular detection to enhance the Raman scattering of molecules (as in surface enhanced Raman scattering, SERS),[17, 18] the infrared spectra (in surface enhanced infrared spectroscopy, SEIRA),[19, 20, 21] or the fluorescence (in plasmon enhanced fluorescence, PEF).[22]

This thesis aims to find a suitable way to describe some of these applications from a theoretical viewpoint and to apply the developed models to some test cases or chemical problems of relevant scientific interest. It is well known that theoretical modelling of phenomena in the field of molecular plasmonics is not an easy task, as many characters that play an important role in the processes are combined. A good model must at least take into account the presence of a molecule, a nanosystem and an electromagnetic radiation interacting with each other. A first non-trivial complication to consider is the difference in dimension, shape and physical properties between nanosystems and molecules, which usually requires different models and a different level of accuracy for their description. Fortunately, using different theoretical models for molecules and nanosystems is an acceptable way to simulate many of the processes mentioned, as the focus is on the investigation of the molecular response so the nanosystem can be tackled with less accuracy. The usual way to study the interaction between molecules and nanosystems is therefore through multiscale approaches, which combine a more accurate quantum chemical description of the molecules with a low-level description of the nanosystems (which are usually much larger than molecules and consist of atoms, whose quantum-level description requires a large computational effort).

The other fundamental element of the process is light. Incident radiation is essential to excite surface plasmons. It must therefore interact with the nanosystem and at the same time with the molecule. As response to the interaction with the

incident light, the nanosystem releases a reflected field. The two electric fields acting on the molecule (the incident and the reflected) induce a charge oscillation, which in turn polarizes the metal nanosystem and generates a new electric field, that modifies again the molecular response. This picture clearly shows that the three main components cannot be considered as separate systems, but that a connection is needed to include all mutual interactions.[23]

Various methodologies have been examined to simulate processes in the field of molecular plasmonics. Some of them have been developed in quasi-static approximation, which is valid for incident radiation frequencies much larger than the system dimension. If this condition is not met, the full electrodynamics problem must be solved. Common models for spherical nanoparticles are based on Mie theory[24], while nanosystems with other shapes are treated by discretising the volume as in the Discrete Dipole Approximation (DDA)[25, 26] or the surface as in the Boundary Element Methods (BEM).[27, 28] The previous models are developed in the frequency domain, while other strategies such as the Finite-Difference Time-Domain (FDTD)[29, 30] method solve Maxwell's equations for the electrostatic problem in the time domain. The advantage of time-domain approaches lies in the nature of light: the electromagnetic radiation involved in the problem changes in time and instantaneously affects the molecule and the response of the nanosystem, so frequency-domain models can only provide a limited amount of information.

In this thesis I have mainly considered time-domain models, which can give an immediate picture of the process taking place. In all the calculations reported here, the molecule has been treated at the quantum level, using mainly Density Functional Theory (DFT) methods, while the nanoparticle has been treated as a continuum body using the Polarizable Continuum Model-Nanoparticle (PCM-NP). The fundamentals of these theories are described in the following chapter, while new implementations developed during the Ph.D. activity can be found along the thesis.

Outline

The next chapter summarizes the basis of different computational procedures employed along the thesis, not implemented by me. They are subdivided in DFT, vibronic model and PCM. After that, this thesis is divided into two main blocks: the first part deals with calculations on electronic excited states and the second part with the simulation of Raman scattering processes. In both parts, there are methods I developed during the Ph.D., not mentioned in the chapter *Methods*, as well as some applications of these methods.

The first part of the thesis begins with a development chapter that lays the foundation for time-dependent calculations of molecular dynamics in the presence of metal nanoparticles. The first chapter is based on the article "Real-time dynamics of plasmonic resonances in nanoparticles described by a boundary element method with generic dielectric function" by G. Dall'Osto, G. Gil, S. Pipolo and S. Corni and explains in detail the TD-BEM (time-dependent BEM). This model is useful to propagate polarization charges on the metal nanoparticle surface when the metal is described by the experimental dielectric function. The novelty of the proposed method lies in the possibility to combine the experimental dielectric function of metals, which is more realistic than the modelled one such as Drude, with a time-dependent approach. Before this implementation, one had to decide whether to use an experimental dielectric function but perform the calculation in the frequency domain, or to use a time-dependent approach but with a modeled dielectric function. Chapter 1 contains the derivation of the model and its validation by comparing results that can also be calculated with another method. In addition, in the Results section, the TD-BEM model is applied to a LiCN molecule in the vicinity of a gold nanocube as an example to highlight the additional information provided by TD-BEM compared to a previously developed TD model.

The second chapter is based on the article "Role of metal-nanostructure features on tip-enhanced photoluminescence of single molecules" by M. Romanelli, G.

Dall'Osto and S. Corni. The aim of this paper is to calculate the photoluminescence of a molecule already studied experimentally by simulating the same experimental setup. It also examines how the properties of the tip influence the results. A methodological section describes all the new implementations required to calculate the photoluminescence (PL) of molecules starting from a BEM-PCM solver in the frequency domain. In particular, I have focused on the implementation of the equations needed to perform the PL calculations, but I have also presented a new way to solve the BEM-PCM equations when simulating nanoparticles with a particularly complex shape, a routine that is also useful for other types of calculations.

Chapter 3 is based on the manuscript in preparation "Photoinduced hole injection explains the reaction selectivity in CO_2 hydrogenation on Rh nanocube" by G. Dall'Osto, M. Marsili, M. Vanzan, D. Toffoli, M. Stener, S. Corni and E. Coccia. This chapter reports an application of TD-BEM, developed in Chapter 1, to the calculation of the electron dynamics of a rhodium cluster bound to a CHO residue near a larger rhodium nanoparticle. This simulation is motivated by an attempt to explain how the presence of a rhodium NP, irradiated by an incident radiation, is crucial for the catalysis of CO_2 hydrogenation leading to the preferential formation of methane instead of carbon monoxide. Previous DFT calculations have suggested a light-favoured electron injection mechanism from the metal to the activated residue CHO formed during the reaction. The correct way to simulate a charge transfer is to consider part of the metal NP and the CHO at the quantum level. Even though not all the NP can be described at atomistic level, its effect was taken into account by including most of it at the continuum level. In addition, a time-dependent approach was considered to understand the actual effects of the incident radiation on the process.

The second part of the thesis focuses on Raman calculations performed with different strategies and on different target molecules. Chapter 4 is based on the manuscript in preparation "Role of ions in solvated amino acids Raman spectra" by G. Dall'Osto, O. Vaccarelli, C. A. Guido and S. Corni. The focus of this first chapter

on Raman scattering is on the target molecules rather than on the methods. Indeed, a standard strategy has been applied, making use of the Placzek approximation, and the calculations have been carried out in the presence of water treated as a continuum. On the other hand, the molecules considered are N-methylacetamide, which is studied as prototypes of peptide bonds, and four amino acids. They were chosen to provide a complete list of the behaviour they show in Raman experiments in the presence of some specific cations. This type of calculation is very useful to facilitate the interpretation of some new experiments aimed at identifying individual amino acids of a peptide chain by Raman spectroscopy. These experiments are carried out in solution and in the presence of some cations that favour peptide flow along a metal nanopore under the action of an external electric field. The calculations presented in Chapter 4 do not aim to simulate the whole process, but to give an impression of the possible differences between the Raman spectra in the presence or absence of some ions, using existing methods.

Chapter 5 shifts the focus from the target to the methodology used to calculate the Raman spectra. It is based on the article "Time Resolved Raman Scattering of Molecules: A Quantum Mechanics Approach with Stochastic Schrödinger Equation" by G. Dall'Osto and S. Corni. The aim is to propose a strategy for calculating the Raman spectra of molecules in the time domain that imparts time dependence to the Raman cross section. The strategy has been developed on the basis of the pillar Lee and Heller's theory for time-dependent Raman scattering, developed in 1979.[31] Although some time-dependent strategies for calculating Raman scattering have been proposed in the past, none of them allows to obtain information about the ongoing process that takes place during the interaction with an incident radiation and the subsequent collection of scattering photons that represent the evolution of the Raman signal. A methodology section in Chapter 5 explains in details the developed theory and the results for the porphyrin molecule as a test case of non-trivial target molecule are presented. The focus is on the effect of the duration of the incident electric field, the spectral changes that occur when working in the

resonance or non-resonance region, and the effect of including vibrational relaxation in the model.

Chapter 6 comprises the final part of my Ph.D. activity, which aims to combine the TD-BEM strategy developed at the beginning of the path with the time-dependent model developed to calculate the Raman scattering of molecules to calculate the plasmon enhanced time-dependent Raman scattering. The chapter is reported as a manuscript, which is currently in preparation. It contains an introduction, a methodological section and some preliminary results related to calculations performed on a porphyrin molecule near a gold nanoellipsoid. The method described in Chapter 5 is also partially applicable in this case, although some modifications have to be made to take into account the effects of the plasmonic nanoparticle both during the interaction with the incident photons that excite the system and on the scattering process responsible for the accumulation of the Raman signal.

My Ph.D. activity is reported here in the form of published articles and manuscripts in preparation. The main aim was to develop new strategies in the field of molecular plasmonics in order to develop tools for the simulation of some specific phenomena (such as TEPL, charge transfer and Raman scattering). All the proposed methods can be applied to physical systems or experiments of interest in order to simulate existing experimental results or to predict the results for specific experimental setups, and to give hints for establishing useful experimental protocols based on the calculated results.

Methods

Density Functional Theory

Treating a molecule at the quantum mechanical level is not a trivial task, as it requires solving the Schrödinger equation for a system with many particles. One of the most commonly used strategies is density functional theory (DFT), which combines good accuracy of results with affordable computational costs. It is based on shifting the objective of the calculation from the electronic wave function to the electron density, which is particularly advantageous since a problem with *3N* variables (with N electrons) is reduced to a problem with 3 variables by integrating the squared wave function over *N-1* electron coordinates.

DFT is based on two theorems of Hohenberg and Kohn.[32] The first states that the ground state electron density of a multi-particle system experiencing an external potential is uniquely determined by its electron density and hence by the ground state wave function and all other properties of the system.

According to the second theorem, the global minimum of the ground state energy is determined by the variational principle, i.e. the ground state electron density is the one that minimizes the energy functional $E[\rho]$. A practical implementation of DFT methods has been proposed by Kohn and Sham (KS)[33] who suggested introducing orbitals that are used to calculate exactly the kinetic energy of the non-interacting electrons, while the other part of the kinetic energy goes into the so-called exchange-correlation term. An explicit functional for the ground state energy can be written on the basis of the KS orbitals as the sum of the kinetic energy K_e, the

electron-electron interaction V_{ee} and the electron-nuclei interaction V_{eN} functionals

$$E_0[\rho] = K_e[\rho] + V_{ee}[\rho] + V_{eN}[\rho]. \tag{1}$$

The electron-nuclei attraction is computed exactly as the integral of the electron density multiplied by nuclear external potential $V_{eN}[\rho] = \int \rho(\mathbf{r})\nu_{ext}(\mathbf{r})\mathbf{dr}$ while the exact functional of the kinetic energy and electron repulsion are unknown. An approximate electron density can be derived from the KS wave function by integration over the coordinates of *N-1* electrons

$$\rho(\mathbf{r}) = N \int |\Phi_{KS}(\mathbf{r_1}, \mathbf{r_2}, \mathbf{r_3}, ..., \mathbf{r_N})|^2 d\mathbf{r_2} d\mathbf{r_3}...d\mathbf{r_N} = \sum_i^N |\phi_i(\mathbf{r})|^2 \tag{2}$$

where Φ_{KS} is written as a single Slater determinant with $\phi_i(\mathbf{r})$ single-electron orbitals. An approximate form for the functional of kinetic energy (K_S) and electron interaction energy (J) are obtained on the basis of the electron density computed from the KS wave function and a general DFT energy functional can be written as

$$E_0[\rho] = K_S[\rho] + J[\rho] + V_{eN}[\rho] + E_{xc}[\rho]. \tag{3}$$

The last term of the equation is the exchange-correlation functional which is equal to the difference between exact and approximate functionals for kinetic energy and electronic repulsion

$$E_{xc}[\rho] = (K_e[\rho] - K_S[\rho]) + (V_{ee}[\rho] - J[\rho]). \tag{4}$$

It includes the electron exchange energy, that in the exact theory is part of electron repulsion, the electron correlation energy related to kinetic energy and the electron correlation potential due to electron repulsion. Starting from the energy functional, a KS single-electron equation can be written for each mono-electronic

orbitals $\phi_i(\mathbf{r})$

$$(-\frac{1}{2}\bigtriangledown^2 + \nu_{eff}(\mathbf{r}))\phi_i(\mathbf{r}) = \epsilon_i\phi_i(\mathbf{r}) \tag{5}$$

The effective potential ν_{eff} is obtained minimizing the energy in equation 3 as follows

$$\nu_{eff}(\mathbf{r}) = \frac{\delta J[\rho]}{\delta\rho} + \frac{\delta E_{xc}[\rho]}{\delta\rho} + \nu_{ext}(\mathbf{r}). \tag{6}$$

Solving the N Kohn-Sham equations gives the N orbitals $\phi_i(\mathbf{r})$, which allows a new electron density and effective potential to be formed. The method is applied recursively to self-consistency.

Although DFT is in principle an exact theory, the exchange-correlation term is included by approximations. Different strategies have been developed to compute the XC functional, starting from the local density approximation (LDA) based on the computation of the XC functional as an expression of the local value of the electron density. The LDA approach has been improved by including a correction based on the density gradient as in the generalized gradient approximation (GGA) or the Laplacian of the electron density as in the meta-GGA. Among all the XC functionals developed so far, B3LYP is a hybrid functional (which mixes the Hartee-Fock exchange energy with the DFT exchange energy) that has been widely used thanks to its good performance and high accuracy in predicting results. Along this thesis, most of the DFT calculations were performed using the B3LYP XC functional.

Vibronic model

When the molecular response to be calculated is in the electronic transition region, as in fluorescence calculations, an electronic wave function is usually informative enough to provide the needed results. In contrast, for processes involving vibrational transitions, as in Raman spectroscopy[34, 35] a more sophisticated wave function is needed to adequately account for all transitions involved in the process. In many

cases, the Born-Oppenheimer approximation (BO) can be used to consider a vibronic wave function where the electronic and vibrational parts are decoupled. This approximation holds if the vertical excitation region of the lowest excited state is far enough away from the avoided crossings, where it would break down.[36, 37] Under this assumption, the system wave function can be written as a direct product between the vibrational and electronic wave functions, which is equivalent to writing each vibronic state as $|J\rangle = |\phi_{el}\rangle|\chi_\nu^{el}\rangle$ where $|\phi_{el}\rangle$ denotes the electronic part and $|\chi_\nu^{el}\rangle$ represents the vibrational wave function related to the normal mode ν on the electronic state el. The vibronic state energies are calculated within the harmonic oscillator model, neglecting the anharmonicity effect, so that each vibronic state level is calculated as the sum between the electronic energy and the vibrational energy as $E_\nu = (\nu + \frac{1}{2})\omega$, where ω is the normal mode frequency (atomic units are used here). The transition dipole moment expanded on the vibronic states in BO approximation is

$$\vec{\mu}_{if} = \langle\chi_i^g|\langle\phi_g|\vec{\hat{\mu}}|\phi_e\rangle|\chi_f^e\rangle = \langle\chi_i^g|\vec{\mu}_{ge}|\chi_f^e\rangle \tag{7}$$

where the term $\vec{\mu}_{ge}$ includes the electronic transition dipole moment between the ground state and an excited state (assuming that $|\phi_g\rangle$ and $|\phi_e\rangle$ are the ground state and the excited electronic state, respectively). The electronic transition dipole moment can be written as a Taylor expansion on the normal mode coordinates Q_k around the electronic transition dipole moment in the equilibrium geometry

$$\vec{\mu}_{ge} = (\vec{\mu}_{ge})_0 + \sum_k \left(\frac{\partial\vec{\mu}_{ge}}{\partial Q_k}\right)_0 Q_k + o(Q^2) \tag{8}$$

In this way, the effect of the vibronic structure on the electronic coordinates is partially recovered, although only approximately, since the expansion is usually truncated at the first order derivative. Substituting the equation 8 into the equation 7 yields a new expression for the transition dipole moments between two vibronic

states

$$\vec{\mu_{if}} = \langle\chi_i^g|\chi_f^e\rangle(\vec{\mu}_{ge})_0 + \sum_k \langle\chi_i^g|Q_k|\chi_f^e\rangle\left(\frac{\partial\vec{\mu}_{ge}}{\partial Q_k}\right)_0 \qquad (9)$$

with electronic transition dipole moment at the nuclei equilibrium position in the first term on the r.h.s. multiplied by the Franck-Condon (FC) integral and a second term, the Herzberg-Teller (HT) contribution, accounting for the dependence of the electronic transition dipole moment on the nuclei vibration along the normal mode coordinates.[38, 39] Santoro et Al.[40, 41] proposed a practical method for calculating the Franck-Condon and Herzberg-Teller contributions based on the Sharp and Rosenstock approach.[42] This method, implemented in the FCclasses3 code[43], is based on the explicit calculation of the 0-0 Franck-Condon integral (e.g., between the lower level of the ground and excited electronic states), followed by an iterative calculation of all other required FC and HT terms, starting from the results of the DFT vibrational calculations (gradient and Hessian of the electronic states of interest must be provided).

This strategy is used when an explicit vibronic wave function is required for the calculation. In this thesis, it is employed to prepare the wave function for time-dependent Raman scattering calculations, as described in Chapters 5 and 6.

Polarizable continuum model

In most cases, the nanosystem is too extended to be treated at quantum level of theory and for this reason it is usually considered as a continuum body. The polarizable continuum model (PCM)[44] was originally used for modelling solvents and gave reliable results on the solvation effect. In PCM, a quantum system is hosted in a cavity whose surface is characterized by the apparent surface charges representing the polarization of the medium produced by the charge distribution of the solute.[45] More recently, PCM has been applied to metal nanoparticles, assuming that the apparent surface charges lay on the NP surface rather than on the surface
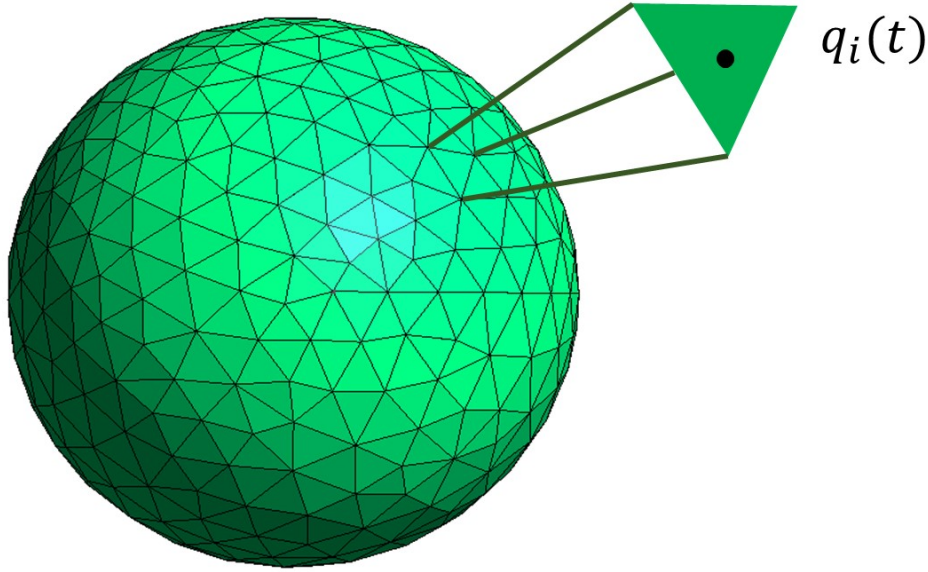
Figure 1: Representation of a discretized nanosphere, highlighting the polarization charge on one tessera of its surface.

of a fictitious cavity.[46, 47] The metal, considered as a continuous body, is characterized by its electrical response. The electrostatic interaction between the molecule and the NP is described as the polarization of the molecule induced by the NP and the mutual polarization of the NP induced by the molecule. The interaction between the molecule and NP is then described by the potential V generated on the NP surface by the polarization charges, and this term enters the Hamiltonian, as

$$\hat{H}(t) = \hat{H}_{mol}(t) + \mathbf{q}(t) \cdot \hat{V} \qquad (10)$$

where $\hat{H}_{mol}$ is the Hamiltonian related to the molecule decoupled with the NP. The total Hamiltonian is thus composed of the molecular Hamiltonian plus the interaction between the charges generated on the NP surface by the molecular potential. In equation 10, the surface charges are expressed in time domain and are usually calculated as the inverse Fourier transform (FT) of the surface charges in the frequency domain, which are the solution of the PCM equation, as will be explained later. Along this thesis, the polarization charges on the NP surface are computed within

the framework of the integral equation formalism (IEF)[48] which allows the surface charges to be defined on the basis of the potential.[49] A useful numerical method for solving the PCM equation is the boundary element method (BEM), which is based on discretizing the NP surface into small tesserae, each of which is associated with a polarization charge, as represented in figure 1 for the case of a nanosphere. To derive the BEM equation from the continuous equation for the apparent surface charges, the partial differential equations that control the solution in a domain are replaced by an equation that only controls the solution at the boundary. In this framework, the discretized surface charges in the frequency domain are as follows

$$\mathbf{q}(\omega) = -\mathbf{S}^{-1} \left(2\pi \frac{\epsilon(\omega) + 1}{\epsilon(\omega) - 1} \mathbf{I} + \mathbf{DA} \right)^{-1} \left(2\pi \mathbf{I} + \mathbf{DA} \right) \mathbf{V} \tag{11}$$

where the matrices $\mathbf{S}$ and $\mathbf{D}$ are representative of the Calderon projectors, whose elements are given as $D_{ij} = \frac{(\vec{r}_i - \vec{r}_j) \cdot \vec{n}_j}{|\vec{r}_i - \vec{r}_j|^3}$, $S_{ij} = \frac{1}{|\vec{r}_i - \vec{r}_j|}$, where the vector $\vec{r}_i$ points towards the centre of the tesserae position and the vector $\vec{n}_j$ points perpendicular to the tesserae surface with unitary modulus. $\mathbf{A}$ is a diagonal matrix with tesserae area and $\epsilon(\omega)$ is the frequency dependent dielectric function of the metal.

BEM has been used in the frequency domain to treat many phenomena such as SERS,[50] PEF[51] or to investigate excitation energy transfer[52] of molecules near plasmonic nanoparticles. However, solving the problem in the time domain can provide more insight into the interaction between the molecule and NP. The BEM equation of polarization charges can be shifted in the time domain by the inverse FT of equation 11. This step is quite straightforward when the dielectric function can be written explicitly as a function of frequency, in particular using the Drude-Lorentz or Debye models. This has already been discussed in Ref. [47], but the full explanation is not reported here as it is not used in this thesis. The strategy I used to move the problem from the frequency domain to the time domain is explained in Chapter 1 and was part of my Ph.D. activity.

PART I

Chapter 1

This chapter represents the beginning of my Ph.D. project, which had the aim to pave the way for the next steps. It reports the formalism developed to perform time-dependent simulations of molecules in the vicinity of plasmonic nanoparticles.[53] An earlier work[47] has already addressed the problem in a BEM-PCM framework with the constraint of describing the metallic nature of nanoparticles by analytical equations such as Drude-Lorentz or Debye[54, 55] which limits the applicability of the method to metals with *simple* dielectric functions, i.e., exhibiting only a single plasmonic peak. On the other hand, the experimental frequency-dependent dielectric function could already be used for frequency-domain calculations, which can be useful in various context[56, 57] e.g., to predict absorption or emission spectra[58] but this is not useful when studying the interaction with an incident radiation. Moreover, a time-dependent picture can reveal many aspects that are hidden in a frequency-domain calculation. An extension of the theory was necessary to describe metals such as gold or rhodium, whose dielectric functions do not have simple shapes.

I have endeavored to improve the strategy already developed to incorporate a better description of the dielectric function of metals in a time-dependent picture. The proposed method is based on the inverse Fourier transform of the time-dependent BEM-PCM [59] equation for the polarization charges located on the nanoparticle surface when the part related to the dielectric function is appropriately fitted with a frequency-dependent function that represents the same contribution as when the experimental dielectric function is used.

This chapter is reported as a paper published by *The Journal of Chemical Physics.* After an introduction, the detailed description of the developed method and some calculations to validate the model are presented. In particular, I have reported the comparison of the absorption spectrum of a gold NP calculated using the experimental dielectric function in a frequency domain calculation and the fitted function in a time domain calculation. A comparison was also made with theoretical results to validate the model, and the absorption spectra of nanoparticles with different shapes are also reported, showing the applicability of the method. Finally, the response of a molecule near a gold nanocube was studied when using the analytical Drude-Lorentz equation for the dielectric function or the experimental equation to highlight the importance of a good description of the metal.

The method was developed by me in collaboration with Dr. Gabriel Gil, then I took care of the implementation of the new propagation algorithm for the polarization charges within the TDPlas code developed in the group of Prof. Corni.[60] I also performed the fitting of the dielectric function of different metals and the calculations whose results are given below. The manuscript was drafted by me and I took care of including and harmonizing the suggestions received by all the other authors.

Real-time dynamics of plasmonic resonances in nanoparticles described by a boundary element method with generic dielectric function

View Online   Export Citation   CrossMark

Giulia Dall'Osto,[1] [ID] Gabriel Gil,[1,2,a)] [ID] Silvio Pipolo,[3] [ID] and Stefano Corni[1,4,b)] [ID]

AFFILIATIONS

[1] Department of Chemical Sciences, University of Padova, via Marzolo 1, Padova, Italy
[2] Instituto de Cibernética, Matemática y Física, Calle E esq 15 Vedado, 10400 La Habana, Cuba
[3] Université de Lille, CNRS, Centrale Lille, ENSCL, Université d'Artois UMR 8181 Unité de Catalyse et Chimie du Solide, F-59000 Lille, France
[4] CNR Institute of Nanoscience, via Campi 213/A, Modena, Italy

Note: This paper is part of the JCP Special Topic on Spectroscopy and Microscopy of Plasmonic Systems.
[a)] gabriel@icimaf.cu
[b)] Author to whom correspondence should be addressed: stefano.corni@unipd.it

ABSTRACT

Investigating nanoplasmonics in an explicit time-dependent perspective is a natural choice when light pulses are used and may also reveal aspects that are hidden in a frequency-based picture. In the past, we proposed a method time domain-boundary element method (TD-BEM) to simulate the time dependent polarization of nanoparticles based on a boundary element method that is particularly suitable to interface with a quantum atomistic description of nearby molecules. So far, however, metal dielectric functions in TD-BEM have been modeled through analytic expressions, such as those of Debye and Drude–Lorentz, which cannot account for multiple electronic resonances. Our approach allows us to include in the TD-BEM framework also the description of metals with complicate dielectric function profiles in the frequency domain. Particularly, among all metals, gold is a challenging case due to the presence of many transition frequencies. We applied our methods to different metals (gold, silver, and the less commonly investigated rhodium) and different shaped nanoparticles (spheres, ellipsoids, and cubes), the approach has been tested comparing TD-BEM and frequency domain BEM absorption spectra, and it has been used to investigate the time-dependent field acting locally close to nanoparticle vertices.

Published under license by AIP Publishing. https://doi.org/10.1063/5.0022329

I. INTRODUCTION

Plasmon resonances of metal nanoparticles (NPs) allow us to focus the electromagnetic radiation within the nanoscale,[1,2] giving rise to the so-called optical nanoantenna effect.[3] The localized field enhancement they provide gives rise to new phenomena, such as surface enhanced Raman scattering, surface enhanced infrared absorption, and metal enhanced fluorescence.[1,4,5] Furthermore, when coupled to ultrafast lasers, plasmonic NPs might be key to

disclosing, probing, and manipulating a host of other photochemical phenomena at a single-molecule level, such as excited state dynamics, high-harmonic generation, and photosynthetic energy-transfer pathways.[6–8]

From a theoretical viewpoint, localized surface plasmons and the associated electric field enhancement are in many circumstances (i.e., when quantum[9] and non-local effects[10] are not relevant) well described by classical electromagnetic modeling. The plasmonic material is described as a continuous medium

characterized by an empirical frequency dependent dielectric function, and Maxwell equations are solved in the presence of the external electromagnetic field. In practice, several approaches are available to numerically solve Maxwell equations in the presence of dielectrics.[11] Among them, the Boundary Element Method (BEM)[12] has been successfully applied to investigate localized surface plasmons, first in the quasi-static (i.e., long wavelength) limit[13] and then for the full Maxwell equations,[14–16] providing accurate results for non-trivial geometries.[17] The basic idea is to translate the differential Maxwell equations into integral equations defined on the boundaries of the nanostructure, where the proper boundary conditions of the fields/the potentials are imposed. The integral equations, which may be written in terms of fictitious surface current densities and charges,[12] are then solved by proper discretization of the boundary into a mesh (boundary elements) leading to standard linear algebra problems.

BEM is usually formulated in the frequency domain (we call this Freq BEM, heretofore), i.e., monochromatic source EM fields have to be used. However, the time dimension is nowadays central in molecular plasmonics[18] from the application of nanostructures together with laser pulses to achieve few-molecule sensitivity in femtochemistry measurements[19] to the exploration of chemical reactions in the strong coupling regime.[20] If results in the time domain are needed, a possible strategy (possible because of the linear character of macroscopic Maxwell equations) is to calculate the response for a large enough range of frequencies with a dense enough frequency grid, perform all the Freq BEM calculations, and then derive the time-dependent physical quantities through a Fourier transform (FT). This is a viable but somewhat involved approach, which becomes unpractical when the dynamics of the localized surface plasmons is coupled with other dynamics, such as the electronic dynamics of a nearby molecule.[21] Beside switching to a wholly different numerical approach, such as Finite Difference Time Domain (FDTD),[11] an alternative way of getting to the time dependent description is reformulating BEM in terms of equations of motion (EOMs) governing the evolution of the relevant BEM quantities (we will call this TD-BEM). Quasi-static TD-BEM admits the real-time numerical propagation of polarization charges, one time step at a time.[21]

So far, the computational strategy tackling TD-BEM has been accessible only for NP materials described by analytical frequency dependent dielectric functions using either the Debye or the Drude–Lorentz (DL) form.[21,22] Stemming from a free-electron treatment of the metal conduction, the DL model is adequate, but it does not fully conform with the dielectric properties of realistic metallic NP media.[23] The main drawback of the DL model is that it includes a single electronic transition, while real metal involves free-electron behaviors as well as (in general) multiple interband transitions.

The main goal with this contribution is to lay down an extension of TD-BEM to study plasmonic NPs featuring any general and physically sound dielectric function. Our proposal relies only on the knowledge of discrete values of the frequency-dependent, complex dielectric function $\epsilon(\omega)$, e.g., coming from measurements or *ab initio* calculations. The core idea is to fit an auxiliary function $f(\omega)$ (whose form is derived here) to a series of DL terms that respect key properties of a dielectric function, in turn inherited by $f(\omega)$. Similar fits to a DL expansion have been proposed before in the context of

FDTD approaches.[23,24] In particular, Ref. 23 shows that a DL expansion with four terms accurately describes the dielectric function of challenging noble metals, such as gold.

The aforementioned DL series is convenient to derive TD-BEM from Freq BEM equations. The result of such a derivation is a set of EOM (second-order differential equations representing a set of forced, damped, and coupled harmonic oscillators) for BEM polarization charges, each associated with a different DL term in the expansion.

Based on such a description, we can accurately calculate the real-time dynamics of the electromagnetic field acting locally in a region of space nearby the plasmonic NP, once a laser pulse arbitrarily shaped in time impinges on the nanoparticle. Exploiting the relatively small number of elements coming from BEM compared to spatial formulation such as FDTD, this approach also opens up the way to effectively simulate the evolution of a molecular wavefunction described by quantum chemistry time dependent methods mutually coupled with a NP described by a generic dielectric function. To illustrate the numerical approach, we carry out real-time simulations on prototypical NPs made of different materials (gold, silver, and rhodium) and shaped in different geometries (sphere, ellipsoid, cube, and rod).

The outline of this article is as follows: In Sec. II, we formulate TD-BEM starting from traditional Freq BEM in the quasi-static limit. Section III reports on our results and is subdivided into Subsections III A–III G. Section III B focuses on the assessment of TD vs Freq BEM for a prototypical case of a gold nanosphere. Section III C is devoted to a comparison of TD-BEM against analytical results available for the absorption spectrum of specific NP geometries, such as a sphere and an ellipsoid. In Sec. III D, we perform further TD-BEM tests in the case of silver and rhodium NPs with less symmetric shapes, such as a cube and a rod. Section III E shows the computational time scaling of TD and Freq BEM with respect to the number of tesserae in the NP surface discretization. In Sec. III F, we analyze the local time-dependent electric field near the NP (particularly close to a gold nanocube corner). In Sec. III G, we perform dynamics of an LiCN molecule close to a gold nanocube interacting with an incident electric field. Finally, conclusions are given in Sec. IV.

II. METHODS

We treat the metal NP as a polarizable continuum body within the quasi-static approximation, i.e., neglecting retardation effects. In this framework, the NP is described through PCM-NP,[25] an extension of the Polarizable Continuum Model (PCM)[26] in the Integral Equation Formalism (IEF).[27] As it is customary with PCM, the problem is reformulated in terms of BEM for its numerical implementation: the NP surface is discretized in small portions or tesserae, each of which is associated with an apparent charge located in its geometrical center. The apparent surface charges enclose all the relevant electromagnetic information related to the interaction of the NP with an external potential due to an incident electric field or the presence of a charge distribution (e.g., a molecule) nearby. The frequency dependent IEF-PCM equation of polarization charges associated with the tesserae is written as

$$\mathbf{q}(\omega) = \mathbf{Q}(\omega)\mathbf{V}(\omega), \tag{1}$$

where

$$\mathbf{Q}(\omega) = -\mathbf{S}^{-1}\left(2\pi\frac{\epsilon(\omega)+1}{\epsilon(\omega)-1}\mathbf{I} + \mathbf{DA}\right)^{-1}(2\pi\mathbf{I} + \mathbf{DA}). \tag{2}$$

$\mathbf{D}$ and $\mathbf{S}$ are matrices representative of the Calderon's projectors whose out-of-diagonal matrix elements are given as $D_{ij} = \frac{(\vec{s}_i - \vec{s}_j)\cdot\vec{n}_j}{|\vec{s}_i - \vec{s}_j|^3}$ and $S_{ij} = \frac{1}{|\vec{s}_i - \vec{s}_j|}$ and diagonal elements are $D_{ii} = -(2\pi + \sum_{k\neq i} D_{ik}A_k)\frac{1}{A_i}$ and $S_{ii} = 1.0694\sqrt{\frac{4\pi}{A_i}}$,[26] $\mathbf{A}$ is a diagonal matrix with elements equal to the area of the tesserae, $\epsilon(\omega)$ is the dielectric function of the metal, and $\mathbf{V}(\omega)$ is the external frequency-dependent electrostatic potential associated, in this case, to an incident electromagnetic radiation in the long-wavelength limit. Here, we focus on the case of an incoming light exciting the NP, but actually our TD-BEM treatment is general enough to tackle other situations, for instance, where the external potential is generated by a molecule close to the NP.

Equation (1) is rearranged to isolate the contribution that depends on the dielectric function, i.e.,

$$\mathbf{q}(\omega) = \frac{1}{2\pi}f(\omega)\mathbf{F}(\omega), \tag{3}$$

with

$$f(\omega) = \frac{\epsilon(\omega)-1}{\epsilon(\omega)+1} \tag{4}$$

and

$$\mathbf{F}(\omega) = -[\mathbf{AD}^*\mathbf{q}(\omega) + \mathbf{S}^{-1}(2\pi\mathbf{I} + \mathbf{DA})\mathbf{V}(\omega)]. \tag{5}$$

$f(\omega)$ is a function collecting all dependencies on $\epsilon(\omega)$, whereas $\mathbf{F}(\omega)$ builds up from the scalar potential of the impinging radiation field and a self-consistent dependence on polarization charges.

This equation is conceptually different from the standard formulation of IEF-PCM in Eq. (1). While the physical meaning of Eq. (1) is clear ($\mathbf{q}$ are the charges induced by the external electrostatic potential collected in $\mathbf{V}$), Eq. (3) requires a specific discussion. The physical dimension of the term $\mathbf{F}(\omega)$ in Eq. (3) is that of an area times an electric field, as shown by its first term and the definition of $\mathbf{D}$. Letting aside the area (which could be moved on the lhs obtaining surface charge density instead of charges), $\mathbf{F}(\omega)$ can be interpreted as the normal component of the total electric field acting in a given portion (tessera) of the surface. The factor $f(\omega)$ expresses the response of the dielectric medium to this total electric field, driving the local surface charge oscillation. In fact, the expression for $f(\omega)$ appears in other dielectric responses of a planar surface to an external perturbation, such as in the image potential for an external charge or dipole, and the zero of the denominator would correspond to the surface plasmon resonance of a planar surface. In Eq. (3), the total electric field depends on two contribution: the field produced by the charge distribution on the NP surface itself [first term of Eq. (5)] and the external field [second term of Eq. (5)]. The mutual dependence of the polarization charges is representative of the macroscopic polarization, and it encodes the effect of the shape on the frequency of the nanoparticle resonances. In this perspective, Eq. (3) indicates that the resonances of the nanoparticle as a whole can be interpreted as arising from the hybridization of the resonances of the single planar tesserae [all happening at the same frequency determined by the factor $f(\omega)$], with a small correction embodied in the diagonal element of the matrix D, due to the tesserae curvature coupled by the mutual electromagnetic interactions and excitable by an external field.

Shifting to the time domain, Eq. (3) reads

$$\mathbf{q}(t) = \frac{1}{2\pi}\int_{-\infty}^{+\infty} dt' f(t-t')\mathbf{F}(t'), \tag{6}$$

where $f(\tau)$ ($\tau = t - t'$) and $\mathbf{F}(t')$ are the FT of $f(\omega)$ and $\mathbf{F}(\omega)$, respectively. The polarization charges in time domain depends on the whole history of the system through the integral as in Eq. (6). This equation is the starting point of our derivation in a similar spirit of what was done starting from Eq. (1) for molecules in solution described by a Debye dielectric function[22] and close to a NP, described by a DL expression.[21]

Compared to such previous studies, we anticipate that the rearrangement leading to Eq. (3) from Eq. (1) has two important advantages, which will be illustrated in the rest of the work. They both derive from the possibility of writing the charges as a scalar function of the dielectric function [$f(\omega)$] times a vectorial term independent from the dielectric function. The first advantage is that the EOMs that we shall derive from Eq. (1) do not require a preliminary matrix diagonalization, at odds with Refs. 21 and 22. The second advantage lies particularly on the shape of $f(\omega)$ drawn from the dielectric function of choice. Previously,[21] the dielectric function of metals has been modeled by a DL expression. This approximation produces acceptable results in some cases but does not allow properly describe metals with interband transitions. Among different metals, the description of gold plasmonic behavior is quite a numerical challenge due to the very complicated $\epsilon(\omega)$ profile, resulting from many transition frequencies. The strategy recently employed in the framework of FDTD to overcome this limitation is based on a formulation of the dielectric function as a sum of DL terms.[23,24] However, we cannot apply directly the latter scheme, since the FT of $f(\omega)$, when substituting the so formulated expression for $\epsilon(\omega)$, is not useful to derive EOMs for the charges.

Our TD-BEM approach overcomes such a difficulty by setting up a frequency-dependent model directly for $f(\omega)$ that (a) works for any dielectric function, (b) accounts for a collection of plasmonic frequencies, and (c) leads to a straightforward formulation in the time domain through EOMs. We fit $f(\omega)$ [built from an $\epsilon(\omega)$ known by points] to a sum over N DL-like terms, i.e.,

$$f(\omega) = \frac{\epsilon(\omega)-1}{\epsilon(\omega)+1} \simeq \sum_{p=1}^{N}\frac{A_p}{\omega_p^2 - \omega^2 - i\gamma_p\omega}. \tag{7}$$

This choice is motivated by the fact that $f(\omega)$ and $\epsilon(\omega)$ share a similar behavior. Especially, both of them have poles lying on the lower half of the complex frequency plane, although $f(\omega)$ poles are $\epsilon(\omega) + 1$ roots. Furthermore, when $\epsilon(\omega)$ is written by a single DL term, we obtain again a DL expression for $f(\omega)$. As stated above, the term $f(\omega)$ represents the resonance frequencies of an infinite plane surface in the quasi-static limit. The shape chosen for the function $f(\omega)$ allows

us to include a number of resonances that, combined, generate the overall plasmonic resonance of the system. The number of poles of the function $f(\omega)$ determines the number of DL terms needed to obtain a reasonable accordance between its analytical expression and its numerical profile depending on the experimental dielectric function. Each DL term has two symmetric poles corresponding to the complex numbers,

$$\overline{\overline{\omega_p}} = -i\frac{\gamma_p}{2} \pm \sqrt{\omega_p^2 - \frac{\gamma_p^2}{4}} = -i\frac{\gamma_p}{2} \pm \overline{\omega_p}. \qquad (8)$$

Practically, we perform the regression in two steps. First, the imaginary part of $f(\omega)$ is fitted to $N - 1$ DL terms, and then, an extra DL term with real poles ($\gamma_p = 0$) is added to fit the real part of $f(\omega)$. This last function accounts for a vertical translation of the real part of $f(\omega)$, i.e., it takes care of the high frequency behavior of the dielectric function that, in the UV/visible spectral region, gives rise to an approximately constant real part of $\epsilon(\omega)$.

Introducing the fitted function $f(\omega)$ in Eq. (3), the polarization charges can be decomposed as a sum of pole-dependent charges $\mathbf{q}_p(\omega)$, i.e.,

$$\mathbf{q}(\omega) = \sum_p^N \mathbf{q}_p(\omega), \qquad (9)$$

where

$$\mathbf{q}_p(\omega) = \frac{1}{2\pi} \frac{A_p}{\omega_p^2 - \omega^2 - i\gamma_p\omega} \mathbf{F}(\omega). \qquad (10)$$

Note that each pole-dependent charge is affected by the rest of the charges through a recursive dependence on the total charge $\mathbf{q}(\omega)$.

A simple way to obtain the EOM is provided by direct FT of the pole-dependent charges in Eq. (10) written in a compact form, i.e.,

$$\left(\omega_p^2 - \omega^2 - i\gamma_p\omega\right)\mathbf{q}_p(\omega) = \frac{A_p}{2\pi}\mathbf{F}(\omega). \qquad (11)$$

Recalling, in particular, that

$$\ddot{\mathbf{q}}_p(t) = -\frac{1}{2\pi} \int_{-\infty}^{+\infty} d\omega e^{-i\omega t} \omega^2 \mathbf{q}_p(\omega), \qquad (12)$$

$$\dot{\mathbf{q}}_p(t) = -i\frac{1}{2\pi} \int_{-\infty}^{+\infty} d\omega e^{-i\omega t} \omega \mathbf{q}_p(\omega), \qquad (13)$$

we got a second order differential equation, i.e.,

$$\ddot{\mathbf{q}}_p(t) = -\omega_p^2 \mathbf{q}_p(t) - \gamma_p \dot{\mathbf{q}}_p(t) + \frac{A_p}{2\pi}\mathbf{F}(t), \qquad (14)$$

where

$$\mathbf{F}(t) = -\mathbf{AD}^*\mathbf{q}(t) - \mathbf{S}^{-1}(2\pi\mathbf{I} + \mathbf{DA})\mathbf{V}(t). \qquad (15)$$

All the geometrical features of the NP are included in $\mathbf{F}(t)$. Equation (14) resembles the one for a set of coupled forced and damped

harmonic oscillators (each characterized by a displacement $q_{p,i}$, where i is the tessera index), where $\sqrt{\omega_p^2 + \frac{A_p}{2\pi}A_{ii}D_{ii}^*}$ is the intrinsic resonance frequency of the $q_{p,i}$ oscillator, which is then coupled to all the other $q_{p',j}$ oscillators via the $A_{ii}D_{ij}^*q_{p',j}$ terms. The set of EOM (14) (with $p = 1, \ldots, N$) extends the analogous result in Ref. 21 (derived for a dielectric function with a single DL term) to the case of several resonance frequencies. At the same time, it is a general method able to describe different metal NPs, once we know $\epsilon(\omega)$.

Practically, we integrate Eq. (14) by means of the velocity-Verlet algorithm.[28] In particular, we get

$$\mathbf{q}_p(t + dt) = \mathbf{q}_p(t) + \dot{\mathbf{q}}_p(t)dt + \left[-\omega_p^2\mathbf{q}_p(t) - \gamma_p\dot{\mathbf{q}}_p(t) + \frac{A_p}{2\pi}\mathbf{F}(t)\right]\frac{dt^2}{2} \qquad (16)$$

and

$$\begin{aligned}\dot{\mathbf{q}}_p(t + dt) = {}&\dot{\mathbf{q}}_p(t) + \left[-\omega_p^2\mathbf{q}_p(t) - \omega_p^2\mathbf{q}_p(t + dt)\right.\\ &+ \frac{A_p}{2\pi}\left(\mathbf{F}(t) + \mathbf{F}(t + dt)\right)\left]\frac{dt}{2} - \gamma_p\dot{\mathbf{q}}_p(t)dt\right.\\ &+ \left[\gamma_p^2\dot{\mathbf{q}}_p(t) + \gamma_p\omega_p^2\mathbf{q}_p(t) - \gamma_p\frac{A_p}{2\pi}\mathbf{F}(t)\right]\frac{dt^2}{2}. \quad (17)\end{aligned}$$

The EOM of pole-dependent charges $\mathbf{q}_p(\omega)$ due to the last purely real term in $f(\omega)$ expansion would be even simpler since the imaginary part of the pole is missing. In the analyzed cases, this pole generates, in time domain, a non-decaying, faster, and less ample oscillations in comparison with other contributions to the total polarization charge. The presence of this term is crucial for the choice of the time step, which needs to be very small to correctly describe its fast oscillation. However, the equation in frequency domain can be simplified as

$$\mathbf{q}_p(\omega) = \frac{1}{2\pi}\frac{A_p}{\omega_p^2 - \omega^2}\mathbf{F}(\omega) \simeq \frac{1}{2\pi}\frac{A_p}{\omega_p^2}\mathbf{F}(\omega) \qquad (18)$$

within the limit of $\omega_p^2 \gg \omega^2$, which is verified in the spectral range where common dielectric functions are experimentally available. Therefore, the EOM for the last pole reads

$$\mathbf{q}_p(t) = \frac{1}{2\pi}\frac{A_p}{\omega_p^2}\mathbf{F}(t). \qquad (19)$$

A first order finite-difference approximation to Eq. (19) reads

$$\mathbf{q}_p(t + dt) = \mathbf{q}_p(t) + \frac{1}{2\pi}\frac{A_p}{\omega_p^2}\left(\mathbf{F}(t + dt) - \mathbf{F}(t)\right). \qquad (20)$$

Otherwise, the term $\mathbf{q}_p(t)$ can be made explicit from the sum over pole-dependent charges in $\mathbf{F}(t)$ as

$$\begin{aligned}\mathbf{q}_p(t) = {}&\left(-1 - \frac{1}{2\pi}\frac{A_p}{\omega_p^2}\mathbf{AD}^*\right)^{-1}\frac{1}{2\pi}\frac{A_p}{\omega_p^2}\\ &\times\left[\mathbf{AD}^*\sum_k^{N-1}\mathbf{q}_k(t) + \mathbf{S}^{-1}(2\pi\mathbf{I} + \mathbf{DA})\mathbf{V}(t)\right]. \quad (21)\end{aligned}$$

Equations (20) and (21) give the same results in the $dt \to 0$ limit, and both of them have been implemented; however, the latter requires a matrix inversion that increases the computational cost of the calculation, so we use the first method [Eq. (20)] as default. It has to be noticed that the velocity-Verlet algorithm is a second-order accurate integrator, while the propagator in Eq. (20) has a first order accuracy. Thus, Eq. (20) can lead to less precise results when the contribution of this last term becomes large in $\mathbf{q}(t)$. Equation (21), on the other hand, comes about from solving exactly for $\mathbf{q}_p$ in Eq. (19) [even though Eq. (19) itself is an accurate approximation of Eq. (14)].

Another strategy to obtain the equation of the polarization charges dependent on the last pole consists in taking the second derivative of Eq. (19),

$$\ddot{\mathbf{q}}_p(t) = \frac{1}{2\pi} \frac{A_p}{\omega_p^2} \ddot{\mathbf{F}}(t). \tag{22}$$

The equation of motion for the last pole is obtained through velocity-Verlet propagator, a second-order accurate algorithm,

$$\begin{aligned}
\mathbf{q}_p(t+dt) &= \mathbf{q}_p(t) + dt\dot{\mathbf{q}}_p(t) + \frac{A_p}{2\omega_{0p}^2\pi} \ddot{\mathbf{F}}(t) \frac{dt^2}{2}, \\
\dot{\mathbf{q}}_p(t+dt) &= \dot{\mathbf{q}}_p(t) + \frac{A_p}{2\omega_{0p}^2\pi} \left(\ddot{\mathbf{F}}(t+dt) + \ddot{\mathbf{F}}(t) \right) \frac{dt}{2},
\end{aligned} \tag{23}$$

where

$$\ddot{\mathbf{F}}(t) = \frac{1}{dt^2} \left[3\mathbf{F}(t-dt) - 8\mathbf{F}(t-2dt) + 7\mathbf{F}(t-3dt) - 2\mathbf{F}(t-4dt) \right]. \tag{24}$$

Equation (23) is computationally more demanding with respect to Eqs. (20) and (21) because we need to store a larger number of data for each cycle since $\ddot{\mathbf{F}}(t)$ at the second order accuracy depends on $\mathbf{F}(t)$ at 4 different time steps. On the other hand, this algorithm is second order accurate (same accuracy of the velocity-Verlet algorithm employed for propagation of the other pole-dependent charges), and for this reason, it has been employed when previous approaches need very short time steps to give accurate enough results.

III. RESULTS AND DISCUSSION

This section reports on real-time simulations of the NP polarization charges induced by an incident electromagnetic field. In order to assess our TD-BEM approach, the results from time-dependent propagation of polarization charges are compared with those stemming from direct BEM calculation in the frequency domain (i.e., Freq BEM), as in Ref. 21. The quantity we check when testing TD-BEM accuracy and performance is the NP isotropic polarizability $\alpha(\omega)$, which is linked to the absorption cross section through the linear equation[29]

$$\kappa_\alpha = \frac{4\pi\omega}{n(\omega)c} Im\{\alpha(\omega)\}, \tag{25}$$

where $n(\omega)$ is the refractive index of the medium surrounding the NP, here assumed to be vacuum. The isotropic polarizability is computed as

$$\alpha(\omega) = \frac{1}{3} \sum_{i=1}^{3} \frac{d_i(\omega)}{E_i(\omega)}, \tag{26}$$

$$\alpha(\omega) = \frac{1}{3} \sum_{i=1}^{3} \frac{1}{E_i(\omega)} \int_{-\infty}^{\infty} dt\, d_i(t) e^{i\omega t}, \tag{27}$$

in the case of Freq and TD-BEM, respectively. $E_i(\omega)$, $d_i(\omega)$, and $d_i(t)$ are the ith Cartesian components of the external electric field, the NP dipole moment in the frequency domain, and its FT to time domain, respectively.

A. Computational details

Within all of our TD simulations, the dynamics is 32 fs long, and the incident electric field features a Gaussian dependence in time and a linear polarization along the x-axis. We assign different time steps depending on the modeled situation. In most cases and unless stated otherwise, such an electric field is written as

$$\vec{E}(t) = \vec{E}_0 e^{-\frac{t^2}{2\sigma^2}}, \tag{28}$$

where the intensity $I = \frac{1}{2}\epsilon_0 c |E_0|^2 = 10^6$ W/cm^2. This electric field shape is close to a delta pulse, relative to the propagation time scale, and thus, it can excite a broad band at optical wavelengths.

All the calculations have been performed on an Intel Xeon 24 Core with 256 GB of RAM and 2×300 GB HD SAS (10 krpm). Both TD-BEM and Freq BEM fortran 90 codes have been compiled with the ifort compiler and optimized with the compilation FLAGS: -O3 -ftz -align all -heap-arrays 1024. We employed the software gmsh to produce 2D meshes of the NPs surfaces that generates triangular and quadrangular finite elements. Charge propagation has been performed through TDPlas, a homemade code.

The fitting of the function $f(\omega)$ obtained by the experimental dielectric function of the metals considered here (gold,[30] silver,[31] and rhodium[32]) to a sum of DL-like terms plus the high-frequency, purely real DL term discussed previously has been performed by a homemade Matlab script. In the first place, we have to fix the number of DL terms in the fitting function. There is a clear trade-off between optimal fit quality and computational time. Increasing the number of parameters, which in our scheme means to increase the number of DL terms in Eq. (7), can accomplish systematically better regressions, but it also implies considering more (coupled) EOM to integrate [see Eqs. (14), (16), and (17)], slowing down the real-time simulations. As good compromises between these two aspects, we chose six (five plus the high frequency real term) terms for all the three metals considered here. Data and plots with different numbers of DL terms in the expansion of $f(\omega)$ for gold, silver, and rhodium are reported in the supplementary material.

In Sec. III G, we report the dynamics of an LiCN molecule close to a gold nanocube performed with the homemade code WaveT.[21,33] The molecule is described in terms of 10 electronic excited states (energies have been reported in Table S11 of the supplementary material) and relative transition dipole moments calculated at CIS level of theory. All the information related to the

molecule and the potential on the NP tesserae due to the presence of the molecule have been computed with a locally modified version of Gamess.[34,35]

B. Comparison with frequency domain calculations results

In order to assess our time propagation scheme to tackle a NP described by a general dielectric function, here, we compare the results of TD-BEM with a Freq BEM benchmark. The frequency dependent polarization charge on each tessera is calculated through Eq. (1).

Before analyzing the accuracy of TD-BEM, we test approximation 7 by contrasting Freq BEM results with the fitted and the experimental dielectric function. Such a test allows us to determine whether the fitted function is good enough for practical use.

In Fig. 1(a), we report the fitting of the function $f(\omega)$ obtained by the experimental dielectric function of gold[30] to a sum of five DL-like terms plus the high-frequency, purely real DL term discussed previously. We chose the smaller possible number of DL terms that lead to the best fitting of the function $f(\omega)$. Fitting parameters are reported in Table I. Since $f(\omega)$ is effectively acting as a response function connecting the total electric field acting on a tessera and the induced charge density, the fitting parameters could be identified as
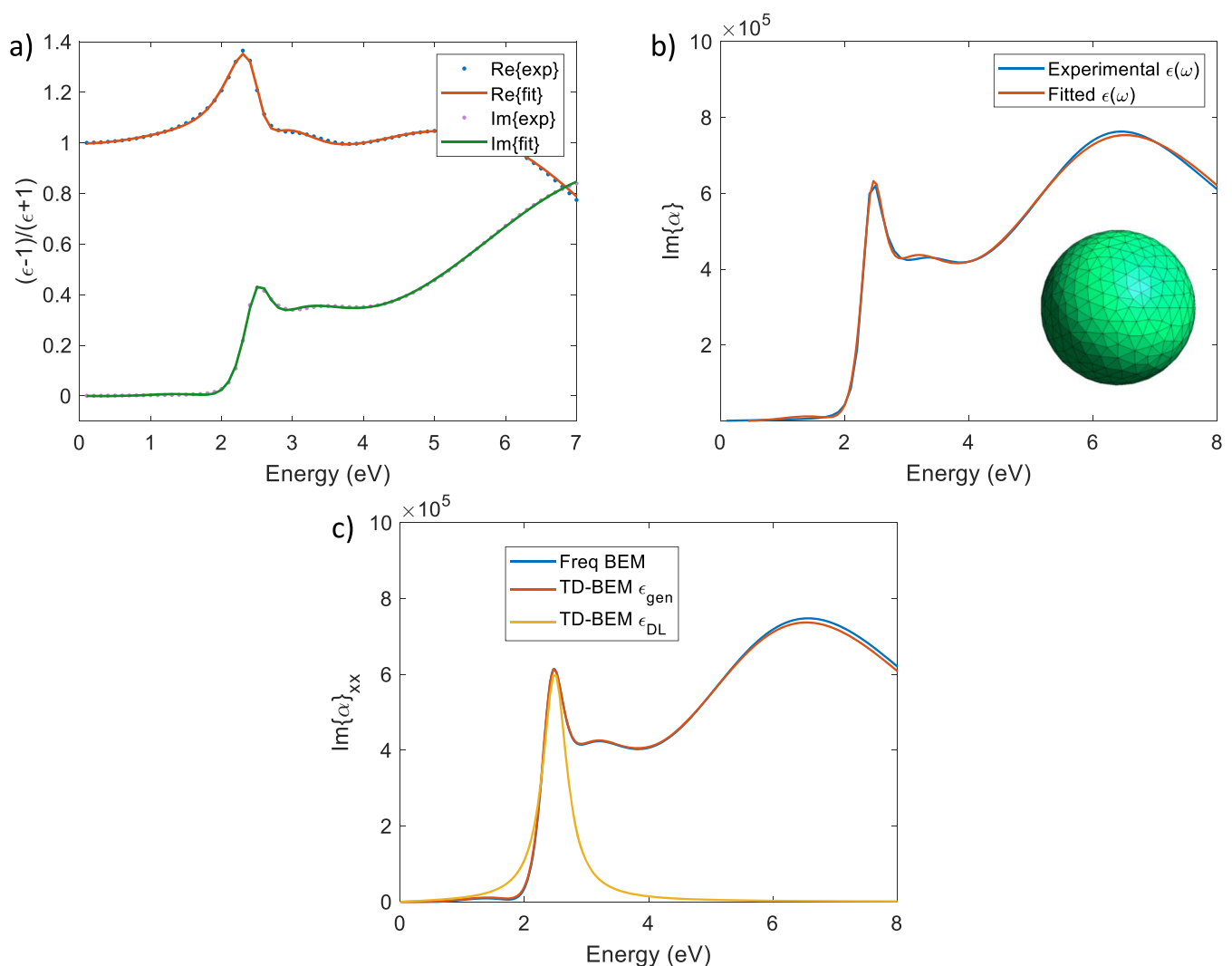

FIG. 1. (a) Fitting of the Au function $f(\omega)$ with a sum of six DL-like equations, (b) comparison between the imaginary part of polarizability of the Au nanosphere calculated with TD-BEM and Freq BEM with the experimental dielectric function in order to verify the reliability of the fitted equation $f(\omega)$ with respect to the experimental dielectric function, (c) comparison between the imaginary part of polarizability of the Au nanosphere calculated with Freq BEM and TD-BEM employing dielectric function from fitted parameters and with TD-BEM employing one Drude–Lorentz equation as the dielectric function with the resonance frequency closer to the peak at 2.3 eV.

TABLE I. Parameters of $f(\omega)$ when substituting the gold dielectric function, fitted by six DL-like terms.

p	ω_p (eV)	γ_p (eV)	A_p (eV^2)
1	2.43	0.882	−5.19
2	2.49	0.287	0.675
3	2.60	1.17	7.90
4	2.64	4.53	−15.4
5	7.49	3.76	63.0
6	42.4	0	643

the frequency, damping, and strength of a series of excitations of the single tessera. However, the parameters A_p obtained from the fitting assume both positive and negative values: in principle, this result is nonphysical since A_p should be squared terms of matrix elements[36] (or a generalized plasma frequency in a classical perspective)[37] and therefore positive. Nevertheless, the fitting of the function $f(\omega)$ for gold using only the positive value of A_p leads to inaccurate results even if more terms are included in the fitting (data not shown). The latter findings are in line with a discussion in the literature on the model required to best fit the metal dielectric functions when interband transitions are present,[38] which includes the possibility of using complex (thus potentially real negative) A_p and poles of higher order. Fitting of the gold dielectric functions with the model proposed in Ref. 38 indeed provided A_p with negative real parts.[39] In particular, we note that the values with the lowest values of ω_p come in pair (i.e., ω_p = 2.43 eV, 2.49 eV and ω_p = 2.60 eV, 2.64 eV) that effectively provide asymmetric line shapes in the range of frequency around the ω_p.

We perform real-time simulations on a prototypical NP, a gold nanosphere with 5 nm radius, subject to the electric field in Eq. (28). Here, the time step is 2.42 a.s. (0.1 a.u.), and the field duration is set as σ = 0.0242 fs. We use a sphere surface discretization with 352 boundary elements (tesserae).

Figure 1(b) shows the imaginary part of the polarizability resulting from Freq BEM calculation with the experimental dielectric function and from TD-BEM calculation with the fitted dielectric function. As expected, the fitting results match very well those obtained from the experimental dielectric function particularly for the position and the height of the plasmon peak at 2.5 eV. Minor discrepancies can be seen for the interband peak around 3 eV. If needed, systematic improvement of the fitting is possible by increasing the number of DL terms.

In Fig. 1(c), we report the imaginary part of the polarizability calculated by Freq and TD-BEM, both featuring the fitted dielectric function and the polarizability obtained by TD-BEM with the dielectric function modeled by the Drude–Lorentz equation whose parameters are chosen in order to represent the peak due to the transition frequency at 2.3 eV. The parameters employed to model the Drude–Lorentz dielectric function are ω_p = 2.32 eV, γ_p = 0.464 eV, and A = 2.61 eV^2. As apparent in the latter plot, methods TD-BEM (with the general dielectric function) and Freq BEM are in good agreement. The two profiles are quite superposed, but for a slight displacement between 6 eV and 8 eV, that depends on the choice of the

propagation time step. The numerical effect of the time step is discussed in the supplementary material. On the other hand, the results obtained with a dielectric function modeled through a Drude–Lorentz equation are very partial since it can take into account only one resonance frequency. In sight of these results, the time-propagation algorithm employed can be considered validated with respect to the same BEM formalism in the frequency domain.

C. Ellipsoidal and spherical NP: Comparison with analytical results

An analytical solution of the Poisson equation is available for simple homogeneous shapes such as spheres and ellipsoids.[40] The polarizability of a spherical NP is

$$\alpha(\omega) = 3\, V \epsilon_s \frac{\epsilon(\omega) - \epsilon_s}{\epsilon(\omega) + 2\epsilon_s}, \tag{29}$$

where V is the volume of the sphere, $\epsilon(\omega)$ is the dielectric function of the metal, and ϵ_s is the dielectric constant of the surrounding medium. Analogously, the equation for the polarization along the dimension j of an ellipsoidal NP is calculated as

$$\alpha_j(\omega) = V\epsilon_s \frac{\epsilon(\omega) - \epsilon_s}{\epsilon_s + L_j(\epsilon(\omega) - \epsilon_s)},$$
$$L_j = \frac{R_1 R_2 R_3}{2} \int_0^\infty \frac{ds}{(s + R_j^2)\sqrt{(s + R_1^2)^2 + (s + R_2^2)^2 + (s + R_3^2)^2}}, \tag{30}$$

where R_1, R_2, and R_3 are the semiaxes lengths of the ellipsoid.

Figure 2 reports the comparison between Eqs. (29) and (30) and TD-BEM results obtained for a gold nanosphere with radius r = 5 nm [panel (a)] and a gold nanoellipsoid with semi-axes R_1 = 10 nm and $R_2 = R_3$ = 5 nm [panel (b)]. In both cases, the modeled NP is placed in vacuum (ϵ_s = 1) and it is excited by a Gaussian electric field with σ = 0.0242 fs [see Eq. (28)]. We compute the polarizability along the direction of the electric field, which, in the case of the ellipsoidal NP, coincides with its major axis.

Here, we consider two different resolutions of tessellation in order to study the effect of the number of tesserae on the final results. The spherical NP surface is divided in 390 and 1250 tesserae, while for the ellipsoidal one, 336 and 1110 tesserae have been used. The results confirm the agreement between the analytical solutions of the Poisson problem and the TD-BEM results. In addition, a better correspondence is found when a larger number of tesserae is employed, as expected, due to the effective volume of the discretized sphere (practically a polyhedron) that increase with the number of tesserae and tends to the volume of the sphere. The relative variation between the profile of the imaginary part of polarizability with different tessellation resolutions is larger for the spherical NP. As a consequence of the larger curvature of ellipsoidal NP, a larger resolution is needed to obtain the same calculation accuracy with respect to spherical NP.

D. Different metals and different NP shapes

Next, we perform other simulations varying the NP geometries and materials. Specifically, we consider cubes and rods shapes
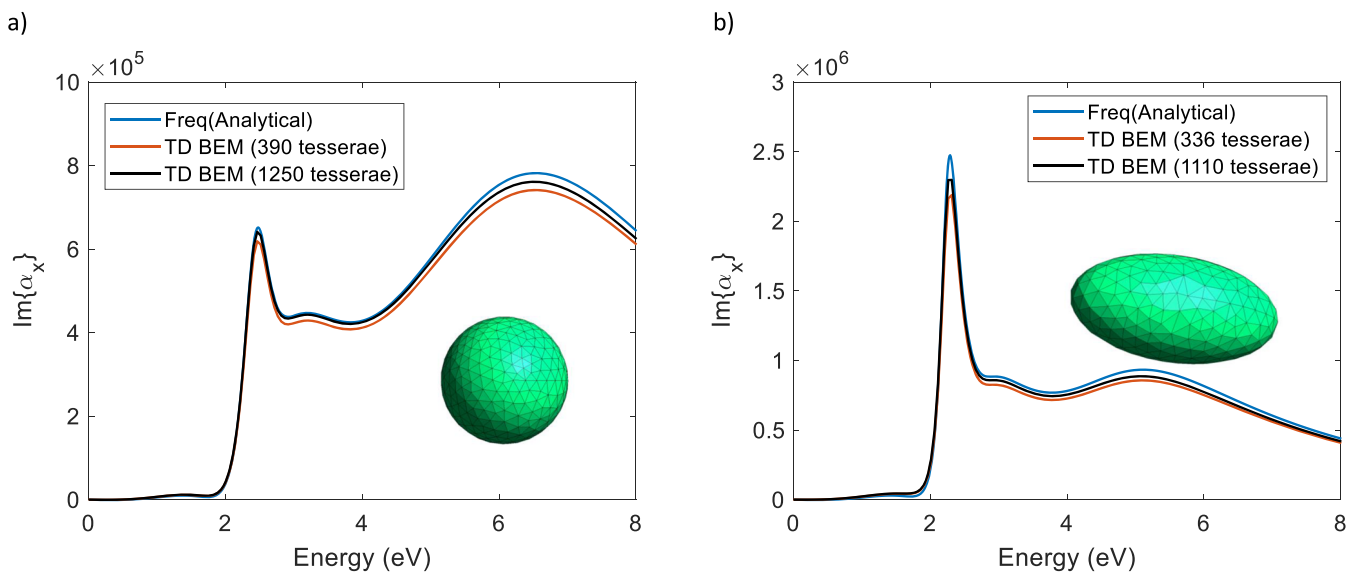
a)

b)

FIG. 2. Comparison between analytical calculation performed with Eqs. (29) and (30) and TD-BEM results obtained for (a) Au nanosphere and (b) Au nanoellipsoid polarized along the x axis. The TD-BEM calculations have been performed by varying the number of tesserae.

together with Ag and Rh metals in all combinations. Silver and rhodium dielectric functions were obtained from Refs. 31 and 32, respectively. Again, we fit $f(\omega)$ with a DL expansion with six terms, one of which misses the imaginary part. Figure 3 shows the plot of the fitted function $f(\omega)$ of silver and rhodium, while the fitted parameters have been reported in Tables S6 and S10 of the supplementary material, respectively. We use the data reported in Ref. 32 for the dielectric function of rhodium: these data are collected from two different measurements that lead to the discrepancy

around 6 eV because a single experimental measurement of the dielectric function was not available in the region 0 eV–8 eV.

In every TD-BEM propagation, the NP is interacting with an electric field polarized along the larger dimension of the rod and normal to the cube face in each case. Here, the bandwidth is $\sigma = 0.0242$ fs [see Eq. (28)] and the time step is $dt = 2.42$ a.s.

We model the *nanocube* as a geometric cube with smooth edges and vertices and the *nanorod* as a cylinder with same radius hemispheres covering both flat faces. In particular, the nanocube has a
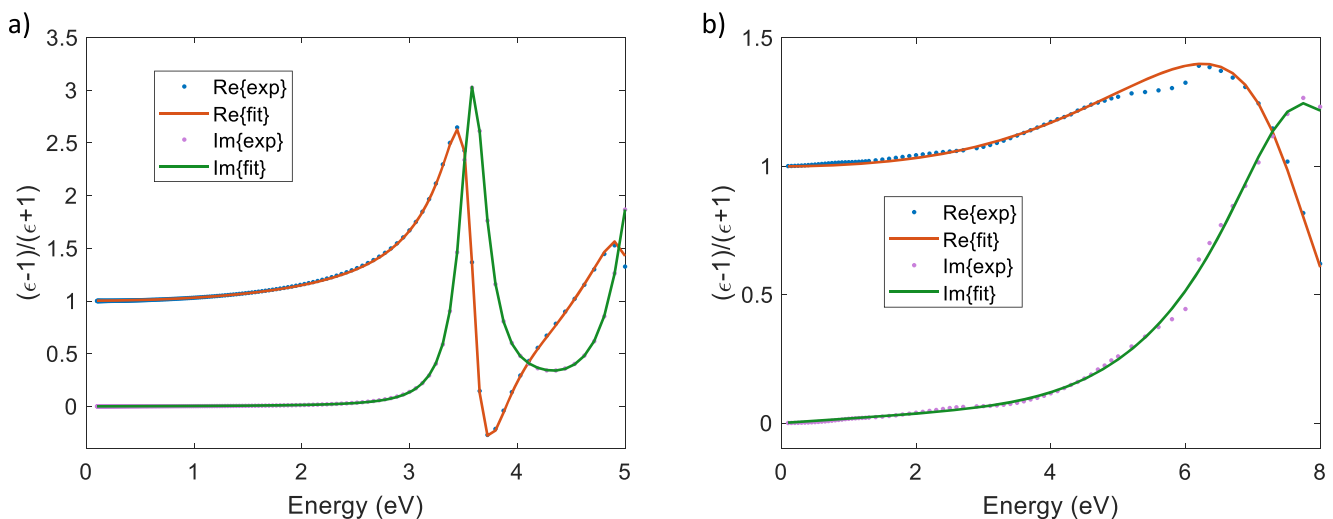
a)

b)

FIG. 3. (a) Fitting of the Ag function $f(\omega)$ with a sum of six DL-like equations. (b) Fitting of the Rh function $f(\omega)$ with a sum of six DL-like equations.

side length of 10 nm and a curvature radius at the edges of 1 nm, whereas the nanorod is 10 nm long and has cylinder radius of 1.5 nm. In both cases, the surface is tasseled with 636 tesserae. In Fig. 4, we plot the polarizabilities of silver and rhodium nanocubes and nanorods.

In all the reported cases, the last pole-dependent charges are propagated through Eq. (23) instead of Eq. (20), employed in previous sections for gold NPs, in order to obtain results in full agreement with the Freq BEM simulated spectra. The latter algorithm [Eq. (20)] is first order accurate, and thus, it is more sensitive on time step variation. Particularly when simulating silver and rhodium NPs, a smaller time step (0.242 a.s.) is needed to obtain good results. The polarizability of the silver nanocube and nanorod shows very narrow peaks (therefore sensitive to the long-time behavior of the

charge oscillations) that are not fully reproducible, in terms of intensity, with a first-order accurate algorithm and the same time step employed with a second-order accurate approach. On the other hand, the necessity of a more accurate algorithm for simulating rhodium NPs is related to the parameters of the function $f(\omega)$ obtained from the fitting to the experimental values of $f(\omega)$ for rhodium. The real term of Eq. (7) has a weight, A_p larger than in gold or silver fitting, such that it influences the spectra at optical frequencies in a stronger way.

Silver and rhodium, compared to gold, have almost twice as large a ratio A_p/ω_p^2 for the high frequency real term, which is the factor multiplying the external perturbation in Eq. (19). The associated $\mathbf{q}_p$ set of charges is therefore more relevant for silver and rhodium, and a better description of such a term (i.e., second order vs first
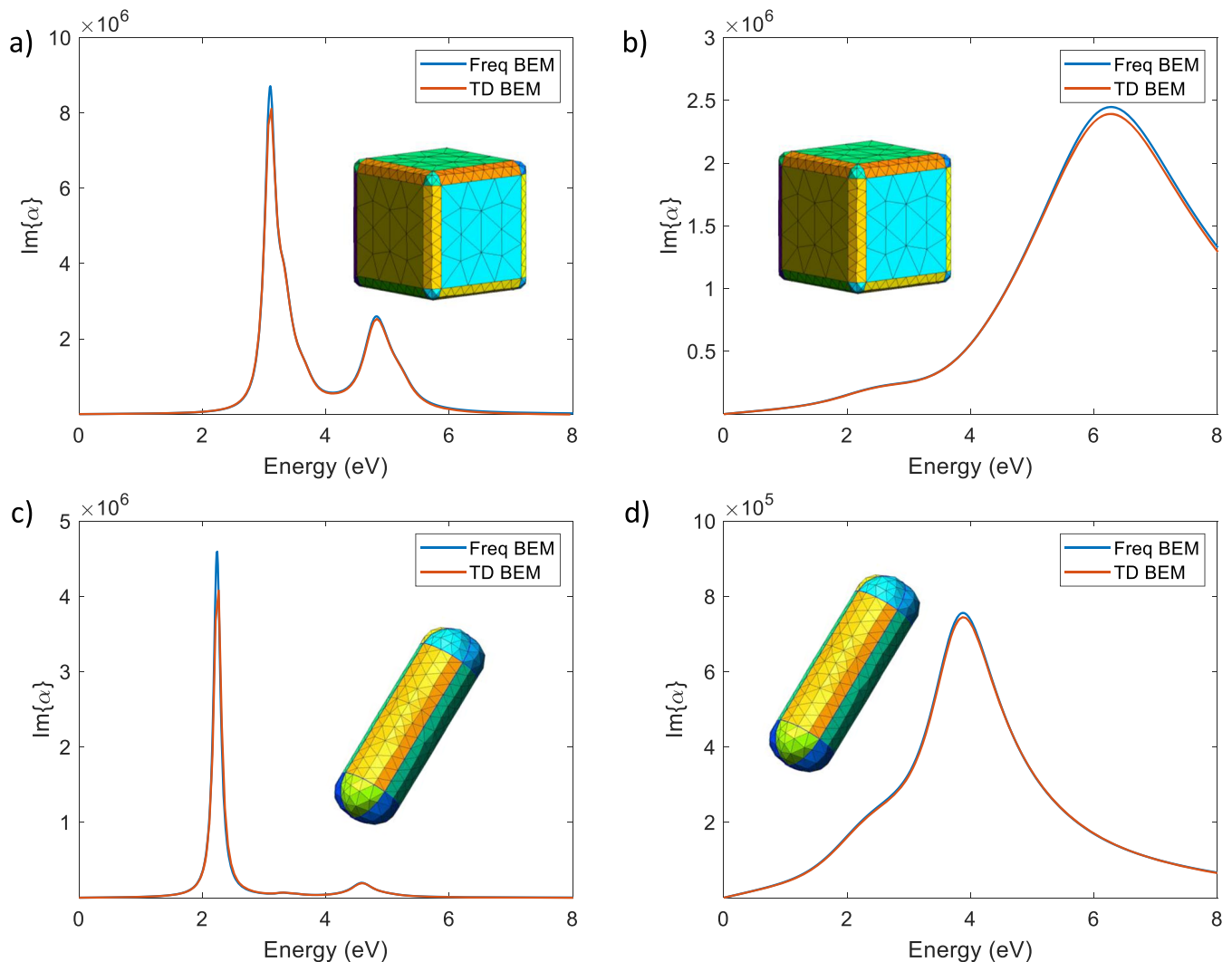

FIG. 4. Imaginary part of the polarizability of (a) Ag nanocube, (b) Rh nanocube, (c) Ag nanorod, and (d) Rh nanorod calculated in frequency and time domain, within BEM formalism.

order) is therefore needed. Through Eq. (23), a second-order accurate algorithm, the propagation is performed with a longer time step of 2.42 a.s. and consequently with a shorter calculation time.

The results of time dependent calculations have been compared with the results of the frequency formulation of BEM where the dielectric function is obtained from the fitted parameters (which anyway match well the spectra obtained by the experimental dielectric functions). Freq and TD-BEM simulated spectra are fully compatible. The minor discrepancies seen for the plasmonic peak of silver is mostly due to the discretization of the spectrum in the frequency domain than due to real differences between the two approaches.

E. Computational scaling of frequency and time domain calculations

Our main interest in TD-BEM is in the extra information on the nanoplasmonic system it straightforwardly provides, in terms of the time evolution of the local field and the real-time representation of the surface charge density. Yet, it should also have a better scaling of the computational time with the number of tesserae compared to the same calculation performed in the frequency domain. Indeed, the algorithm employed for the charge propagation in time domain scales approximately as the square of the number of tesserae, since the most computationally demanding calculation is a vector-matrix product [see Eqs. (16) and (17)]. On the other hand, BEM in the frequency domain also includes matrix inversions (or matrix diagonalization, depending on the implementation) and matrix–matrix products that lead to an overall computational time scaling (formally) as the third power of the number of tesserae. Therefore, for a large enough number of tesserae, TD-BEM should be more computationally inexpensive than Freq BEM.

In Fig. 5, we show the different computational time scaling of TD and Freq BEM runs for different tessellation resolutions from 390 up to 2266 tesserae. Each point in the graph corresponds to a full polarizability spectrum calculation of a gold nanosphere with radius $r = 5$ nm, taken as a representative case. The spectral region we want to explore is fixed between 0 eV and 10 eV, with an energy resolution of 0.01 eV. TD-BEM simulations are performed with a $dt = 2.42$ as time step and are 32 fs long, meaning 1.3×10^4 propagation steps. Actually, such a time step would allow a much larger spectral region to be explored, which would require more calculations in the frequency domain compared to what we performed. Yet, such ample spectral regions are usually not of interest (also would require additional fitting of the dielectric function), so we do not push the comparison to what is technically possible with TD-BEM and stay rather with what is useful for calculations of the absorption spectra.

The double logarithmic plot shows that both TD-BEM and Freq BEM computational times stay on straight lines (i.e., they have polynomial scaling as expected). The slope of the straight line (i.e., the exponent of the scaling fitting the computational time) in TD-BEM calculations is close to 2, while the data collected from frequency domain calculation lie on a line with a slope around 2.7 (instead of 3). These numerical results substantially confirm the theoretical expectations. In practice, employing a relatively small number of tesserae, the algorithm developed in the frequency domain is more convenient than that in the time domain in terms of
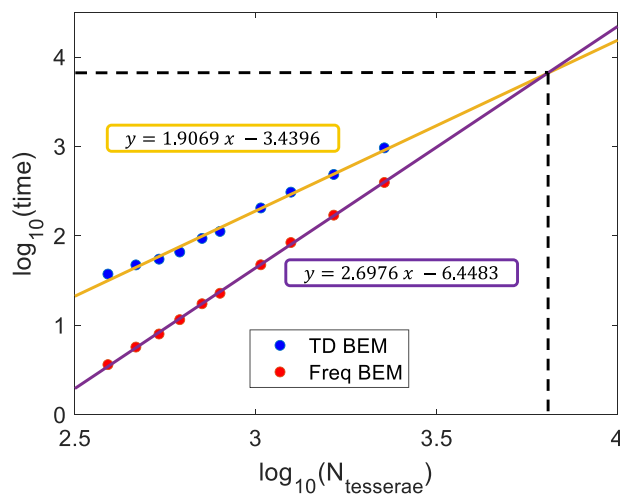

FIG. 5. Time calculation as a function of the number of tesserae employed for the NP surface tessellation in a double decimal logarithmic scale for calculation in time and frequency domains. The dashed lines indicate where TD-BEM becomes more convenient than Freq BEM for the calculation of absorption spectra in our implementations. Computational time is in seconds.

computational cost. When the number of tesserae increases, the situation is the other way around, being the time domain algorithm the most efficient. Notice that the overturn takes place near 3800 tesserae. Considering small aggregates of only 2 NPs and the most accurate tessellation resolution we have employed thus far, TD-BEM calculations will be already more convenient than Freq BEM. The time scaling of Freq BEM and TD-BEM approaches clearly depends on their code implementation. Particularly, the Freq BEM
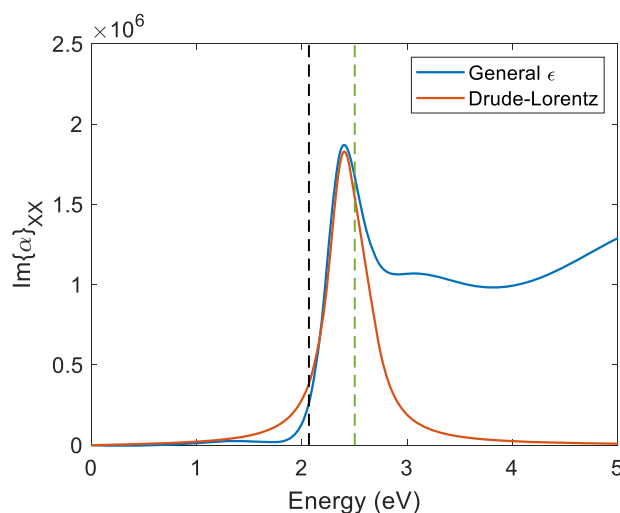

FIG. 6. Absorption spectrum of gold nanocube described through the general dielectric function (TD-BEM) and Drude–Lorentz model—the dashed lines represent the pulse frequencies employed in the dynamics of Fig. 7.

code has been optimized through a diagonal formulation of IEF-PCM equation in which the calculation is performed through an initial slow step [the diagonalization of the $\mathbf{Q}(\omega)$ matrix in Eq. (1) that formally scales as $N_{tesserae}^3$] followed by faster steps (vector-matrix products). There are different possible implementations of the same approach that will lead to different overall computational performances. Here, our purpose is to check that the computational scaling of the present implementation of Freq BEM and TD-BEM as a function of the number of tesserae conforms to the theoretical expectations.

F. Local electric field nearby the NP

As stated in the Introduction, the main goal of the present approach is to provide a viable strategy to accurately investigate time-dependent fields in the proximity of the metal nanoparticles. Here, we perform simulations on a gold nanocube (geometrically identical to those of Sec. III D) interacting with a laser pulse described as a sinusoidal electric field modulated by a Gaussian envelope. We are interested in illustrating the relation between the pole complex frequency and properties of the local field induced by the incidence of an *external* electric field, which is tuned to include a plasmonic resonance frequency within its spectral shape. The applied field evolves in time as

$$\vec{E}(t) = E_0 e^{\left(-\frac{(t-t_0)^2}{2\sigma^2}\right)} \sin(\omega_{exc}t), \tag{31}$$

where $\sigma = 1.2$ fs, and its central frequency ω_{exc} is close to the dipolar plasmonic frequency (i.e., $\omega_p = 2.3$ eV, as obtained through
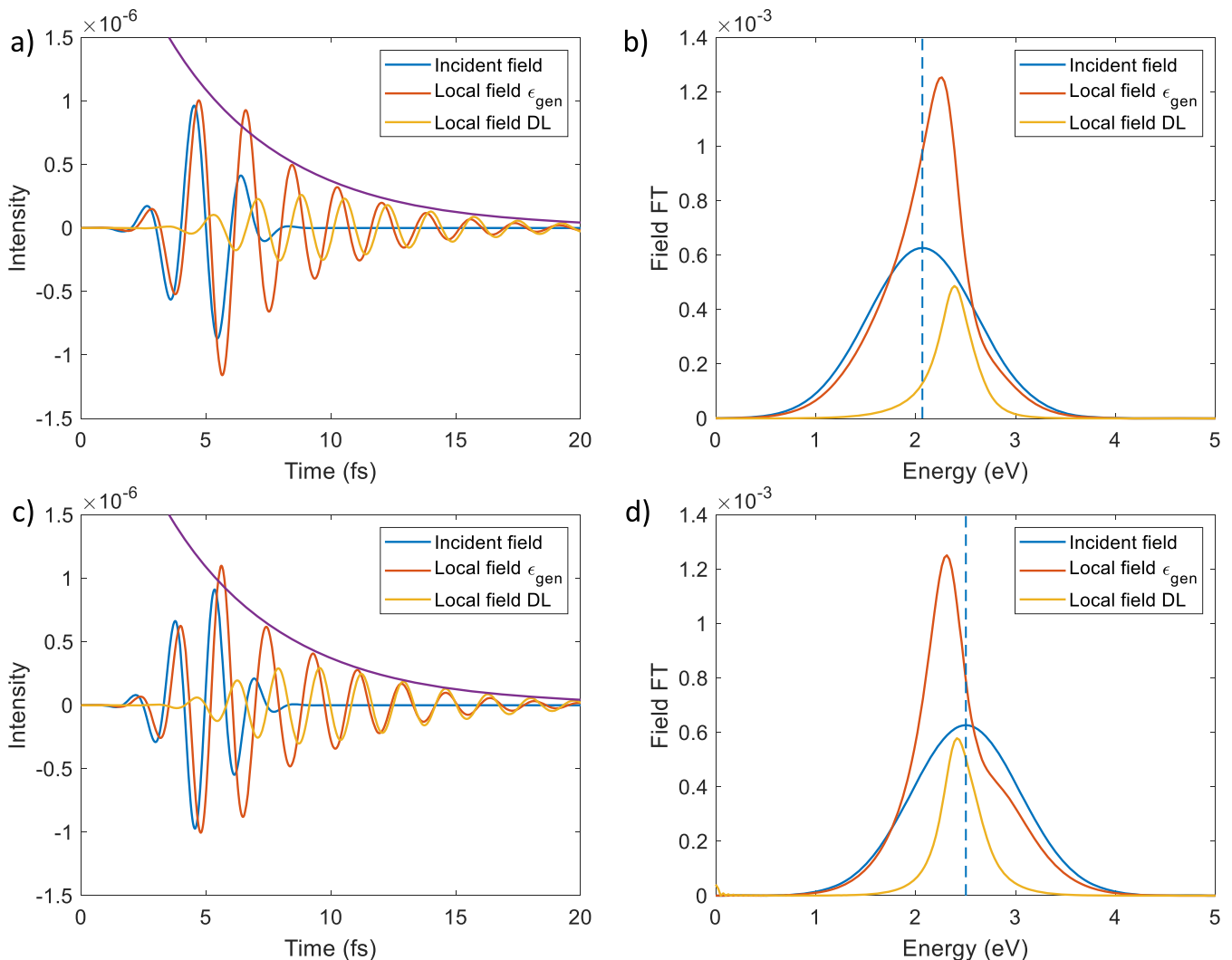

FIG. 7. Time propagation of the incident field and local field induced on a gold nanocube at distance 3 Å when (a) ω_{exc} = 2.07 eV and (c) ω_{exc} = 2.50 eV. (b) FT of the incident electric field and local field in panels (a). (d) FT of the incident electric field and local field in panel (c). The dashed lines in panels (b) and (d) represent the pulse frequencies.

simulation of the absorption spectrum). We calculate the local field at the distance of 3 Å from one of the NP corners employing the TD-BEM approach with the general dielectric function and the Drude–Lorentz dielectric function. In dye-functionalized NP setups, 3 Å is a realistic distance for NP localized surface plasmons to be effective at inducing molecular polarization. The absorption spectra of the gold nanocube obtained employing the TD-BEM approach with the general dielectric function and the Drude–Lorentz dielectric function are shown in Fig. 6.

The local fields calculated with the general and Drude–Lorentz dielectric function and the incident electric fields are shown in Fig. 7 with their respective FT, when the system is excited with a frequency lower [ω_{exc} = 2.07 eV, panels (a) and (b)] and higher [ω_{exc} = 2.50 eV,

panels (c) and (d)] than the dipolar plasmonic frequency at 2.3 eV. In both cases, with the general dielectric function, the local field propagates in time with a little delay with respect to the incident field and oscillates with a frequency close to the plasmonic frequency. The local field generated when the dielectric function is modeled as the Drude–Lorentz equation is less intense than the local field generated when the propagation is performed with the general dielectric function. In fact, the DL absorption band is much narrower than the absorption region for the empirical dielectric function, and thus, less of the incident field (that spans a range of frequencies) is absorbed and translated in a local field.

Notice that the local fields decay in time with a rate equal to γ_p. We evidence such an exponential decay with a purple line in
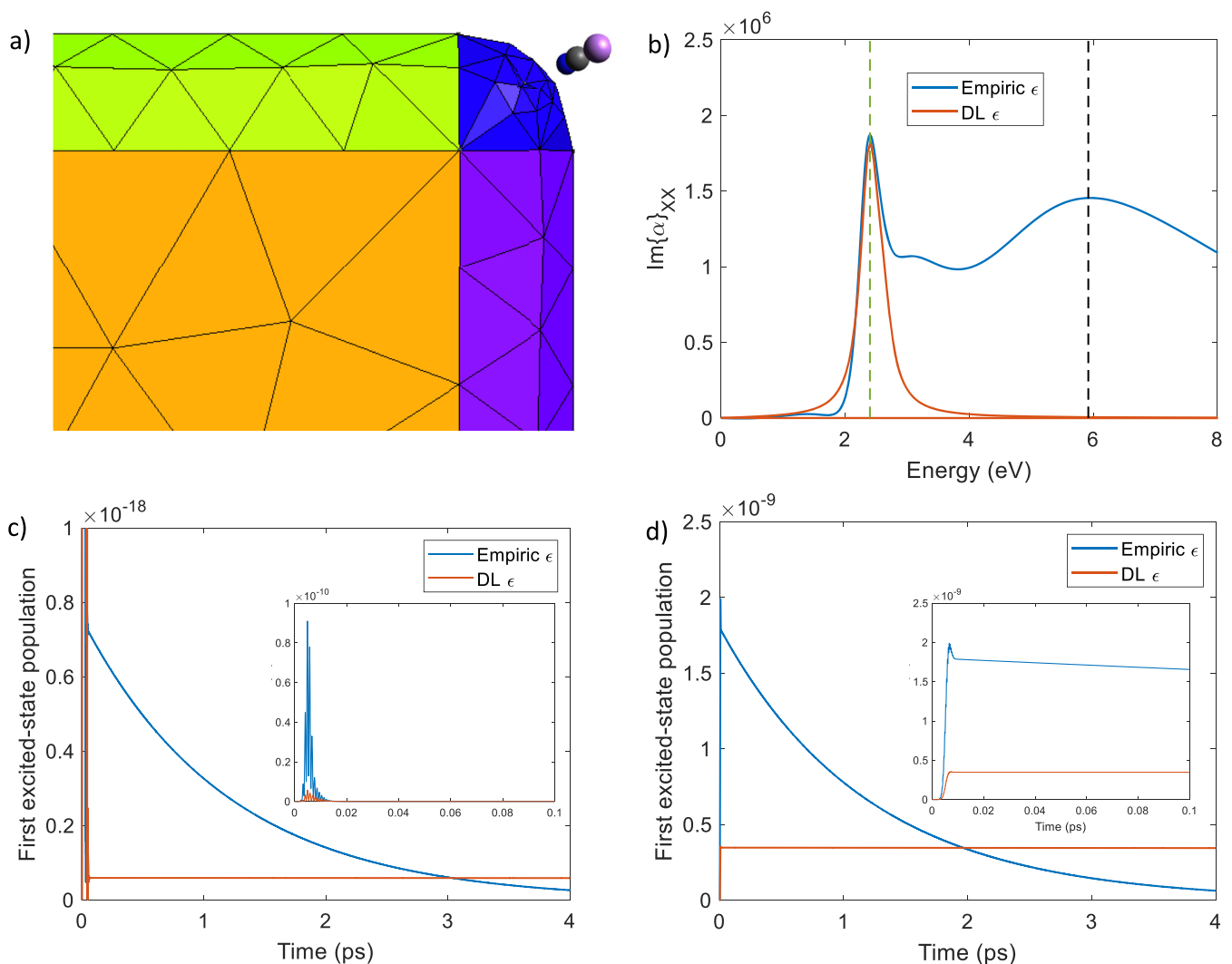

FIG. 8. (a) Representation of the gold nanocube corner tessellation and LiCN molecule and (b) absorption spectrum of the gold nanocube when using its empirical dielectric function and Drude–Lorentz dielectric function. Time evolution of the first excited state population of the LiCN molecule at a distance of 5 Å from the corner of a gold nanocube describing the NP through its empirical dielectric function and the Drude–Lorentz dielectric function when interacting with a Gaussian enveloped sinusoidal electric field with pulse frequency 2.40 eV (c) and 5.92 eV (d). The insets are magnifications of the first few tens of fs of the evolution.

Figs. 7(a) and 7(c). Remarkably, the field's main frequency shifts from ω_{exc} to ω_p as a consequence of the polarization induced on the NP surface. Moreover, the FT of the local fields shows an inhomogeneous broadening corresponding to the frequencies of the excitation band when the general dielectric function is employed, while with the Drude–Lorentz dielectric function, only one frequency can be excited and the local field cannot be influenced by the presence of interband transitions. When the central excitation energy is larger than the plasmonic frequency [panels (c) and (d) of Fig. 7], a larger portion of the polarizability spectrum is superposed to the electric field FT due to a more pronounced shoulder at 2.7 eV. These results point to the connection between the real part of the complex pole frequency and the leading frequency of the local electric field, as well as the connection between the imaginary part of such pole frequency and the decay rate in the time-dependent profile. As anticipated earlier, such a connection might be extremely useful to control the excitation of specific states of a molecule close to the NP.

G. Excitation of a molecule close to a nanocube

In this section, we report an example of real-time propagation of the electronic wave-function of a molecule subject to an external electromagnetic field and close to a gold nanocube. In particular, we model the NP dielectric function via Drude–Lorentz equation and via the empirical frequency dependent dielectric function to show how such different descriptions affect the results of the dynamics. To this aim, we consider an LiCN molecule at a distance of 5 Å from one corner of a gold nanocube, with its principal axis placed along the direction of the nanocube diagonal, as in panel (a) of Fig. 8. The nanoparticle surface has been discretized in 764 tesserae with different areas, refining the region close to the molecule.

The system interacts with a Gaussian enveloped sinusoidal electric field with σ = 1.21 fs and centered at t_0 = 4.84 fs [see Eq. (31)]. We perform the dynamics of the system using two different pulse frequencies: 2.40 eV (corresponding to the lowest plasmonic frequency) and 5.92 eV (corresponding to the highest plasmonic frequency). Panel (b) of Fig. 8 shows the absorption spectra of the gold nanocube described with the Drude–Lorentz dielectric function and the empirical dielectric function, and the excitation frequencies are reported as dashed lines. As in the previous cases [panel (c) of Fig. 1], the Drude–Lorentz dielectric function can only partially describe the absorption spectrum of gold nanoparticles; indeed, only one excitation frequency (in this case at 2.40 eV) contributes to the NP spectrum.

Panels (c) and (d) of Fig. 8 show the dynamics of the first excited state population of LiCN (neglecting spontaneous emission) when the pulse frequency is 2.40 eV and 5.92 eV, respectively. The 2.40 eV pulse frequency [green line in panel (b) of Fig. 8] allows us to excite the plasmonic peak, but the LiCN first excited state is only transiently populated at the beginning of the dynamics [inset of panel (c)] because it is out of resonance (excitation energy is 6.34 eV). The final population after the pulse is therefore very small, both for the TD-BEM with the empirical dielectric function and with the Drude–Lorentz one. Yet, such populations are very different one from the other. In fact, the nanoparticle dielectric response at higher energies is (slightly) excited only using TD-BEM with the

empirical dielectric function and not in the Drude–Lorentz case. The presence of the interaction with the NP in the empirical dielectric function case is exhibited also by the decay of the excited state population, which depends on the possibility to transfer energy from the molecule to the NP.

The population of LiCN first excited state is higher when the frequency pulse is closer to the excitation energy of the molecule [panel (d) of Fig. 8], as expected. Nevertheless, when the dielectric function of the NP is modeled as the Drude–Lorentz equation, a smaller population is excited than when the empirical dielectric function is used. In the Drude–Lorentz case, the molecule is almost completely excited by the incident field because the local field generated by surface plasmons is not resonant with LiCN excitation energy. On the other hand, in the TD-BEM case, the local field generated close to the NP surface, due to the interaction with the incident field, contributes to the excitation of the molecule. Moreover, in the latter case, the population decays in time because of the energy transfer from the molecule to the NP, as in panel (c).

In summary, the different models of the NP dielectric function differ for both the initial population of an excited state and the subsequent evolution of the population as a function of time, showing clearly the importance of using the realistic empirical dielectric function rather than the model Drude Lorentz one.

IV. CONCLUSION

In this work, we developed a novel Time-Dependent Boundary Element Method (TD-BEM) suitable to study the real-time dynamics of plasmonic NPs of arbitrary geometrical shape and material. The strong point of our approach lies in the consideration of a general frequency dependence for the NP dielectric function, possibly coming from measurements or numerical calculations, keeping the favorable small number of finite elements typical of BEM approaches. In practice, we successfully fit an auxiliary function depending on the frequency-dependent complex dielectric function—known by points—to an expansion in Drude–Lorentz (DL) terms. Such a DL expansion is convenient to obtain our TD-BEM from a FT of the more customary BEM formulation in the frequency domain (Freq BEM) without further approximations. At the core of our approach, there are equations of motion (EOMs) governing the evolution of polarization charges induced at the surface of the NP by an external electric field. There is one EOM per each DL term in the aforementioned expansion. Such EOMs are second-order differential equations resembling those of a damped and forced harmonic oscillators, and they couple the evolution of both (a) distant point-like polarization charges and (b) polarization charges contributions associated with different DL terms.

As anticipated, the main goal of TD-BEM is to provide insight into plasmonic resonances evolving in real time, particularly in view of coupling with a microscopic time-dependent description of a molecule or anyway an external charge distribution. In this article, we establish that TD-BEM shows little departure from Freq BEM results for any of the NPs we have studied, independently of their geometry and underlying material. Moreover, we show that our TD-BEM implementation is numerically robust by comparing with analytical benchmark results for spheres and ellipsoids. Remarkably,

arriving to such a good agreement requires a careful selection of (i) the tessellation resolution and (ii) the time step in the propagation algorithm for the polarization charges. Furthermore, we discuss some properties of the plasmonic near field that allow tuning the spectral shape of light pulses in the proximity of a NP. Generally speaking, BEM approaches have been shown to be particularly suitable to be interfaced with first/principle descriptions of molecules, independently from the underlying basis sets (e.g., localized[26] or grid based[41]). Therefore, the present approach opens the way to a realistic, flexible, and computationally effective time-dependent description of the electronic dynamics of molecules close to metal nanoparticles (including a solvent medium), able to describe many aspects of molecular nanoplasmonics.

SUPPLEMENTARY MATERIAL

See the supplementary material for plot and data for fitting of the gold $f(\omega)$ function with four and five DL terms (Fig. S1 and Tables S1 and S2), plot for fitting of the silver $f(\omega)$ function with three, four, and five DL terms (Fig. S2), and data for fitting of the silver $f(\omega)$ function with three, four, five, and six DL terms (Tables S3–S6), plot for fitting of the rhodium $f(\omega)$ function with three, four, and five DL terms (Fig. S3), data for fitting of the silver $f(\omega)$ function with three, four, five, and six DL terms (Tables S7–S10), analysis of the role of the time step in the EOM numerical propagation of TD-BEM (Fig. S14), and CIS energies of LiCN reported in Table S11.

ACKNOWLEDGMENTS

DATA AVAILABILITY

The data that support the findings of this study are available within the article and its supplementary material.

REFERENCES

[1] S.-Y. Ding, J. Yi, J.-F. Li, B. Ren, D.-Y. Wu, R. Panneerselvam, and Z.-Q. Tian, Nat. Rev. Mater. **1**, 1 (2016).

[2] R. P. Van Duyne, Science **306**, 985 (2004).

[3] V. Giannini, A. I. Fernández-Domínguez, S. C. Heck, and S. A. Maier, Chem. Rev. **111**, 3888 (2011).

[4] L. S. Nair and C. T. Laurencin, J. Biomed. Nanotechnol. **3**, 301 (2007).

[5] F. Le, D. W. Brandl, Y. A. Urzhumov, H. Wang, J. Kundu, N. J. Halas, J. Aizpurua, and P. Nordlander, ACS Nano **2**, 707–718 (2008).

[6] S. Kim, J. Jin, Y.-J. Kim, I.-Y. Park, Y. Kim, and S.-W. Kim, Nature **453**, 757–760 (2008).

[7] O. Andreussi, A. Biancardi, S. Corni, and B. Mennucci, Nano Lett. **13**, 4475–4484 (2013).

[8] J. Lee, J. Song, D. Lee, and Y. Pang, Sci. Rep. **9**, 3551 (2019).

[9] W. Zhu, R. Esteban, A. G. Borisov, J. J. Baumberg, P. Nordlander, H. J. Lezec, J. Aizpurua, and K. B. Crozier, Nat. Commun. **7**, 11495 (2016).

[10] C. Ciracì, R. T. Hill, J. J. Mock, Y. Urzhumov, a. I. Fernández-Domínguez, S. a. Maier, J. B. Pendry, a. Chilkoti, and D. R. Smith, Science **337**, 1072 (2012).

[11] U. U. Hohenester, *Nano and Quantum Optics: An Introduction to Basic Principles and Theory* (Springer, 2020), p. 665.

[12] J. L. Volakis and K. Sertel, *Integral Equation Methods for Electromagnetics* (SciTech Publishing, 2012), pp. 1–392.

[13] R. Fuchs, Phys. Rev. B **11**, 1732 (1975).

[14] F. García de Abajo and A. Howie, Phys. Rev. B **65**, 115418 (2002).

[15] U. Hohenester and A. Trügler, Comput. Phys. Commun. **183**, 370 (2012); arXiv:1109.5783.

[16] M. T. H. Reid and S. G. Johnson, IEEE Trans. Antennas Propag. **63**, 3588 (2015); arXiv:1307.2966.

[17] J. Marcheselli, D. Chateau, F. Lerouge, P. Baldeck, C. Andraud, S. Parola, S. Baroni, S. Corni, M. Garavelli, and I. Rivalta, J. Chem. Theory Comput. **16**, 3807 (2020).

[18] X.-W. Chen, A. Mohammadi, A. H. B. Ghasemi, and M. Agio, Mol. Phys. **111**, 3003 (2013).

[19] E. Wientjes, J. Renger, A. G. Curto, R. Cogdell, and N. F. van Hulst, Nat. Commun. **5**, 4236 (2014).

[20] J. Fregoni, G. Granucci, E. Coccia, M. Persico, and S. Corni, Nat. Commun. **9**, 1 (2018).

[21] S. Pipolo and S. Corni, J. Phys. Chem. C **120**, 28774 (2016).

[22] S. Corni, S. Pipolo, and R. Cammi, J. Phys. Chem. A **119**, 5405 (2015).

[23] F. Hao and P. Nordlander, Chem. Phys. Lett. **446**, 115 (2007).

[24] H. S. Sehmi, W. Langbein, and E. A. Muljarov, Phys. Rev. B **95**, 115444 (2017).

[25] B. Mennucci and S. Corni, Nat. Rev. Chem. **3**, 315 (2019).

[26] J. Tomasi, B. Mennucci, and R. Cammi, Chem. Rev. **105**, 2999 (2005).

[27] E. Cancès, B. Mennucci, and J. Tomasi, J. Chem. Phys. **107**, 3032 (1997).

[28] E. Vanden-Eijnden and G. Ciccotti, Chem. Phys. Lett. **429**, 310 (2006).

[29] S. Mukamel, *Principles of Nonlinear Optical Spectroscopy* (Oxford University Press, 1995).

[30] P. B. Johnson and R. W. Christy, Phys. Rev. B **6**, 4370 (1972).

[31] A. D. Rakić, A. B. Djurišić, J. M. Elazar, and M. L. Majewski, Appl. Opt. **37**, 5271 (1998).

[32] E. Palik, *Handbook of Optical Constants of Solids* (Academic Press, Cambridge, MA, USA, 1998).

[33] E. Coccia and S. Corni, J. Chem. Phys. **151**, 044703 (2019).

[34] C. Dykstra, G. Frenking, K. Kim, and G. Scuseria, *Theory and Applications of Computational Chemistry: The First Forty Years* (Elsevier, 2011).

[35] M. W. Schmidt, K. K. Baldridge, J. A. Boatz, S. T. Elbert, M. S. Gordon, J. H. Jensen, S. Koseki, N. Matsunaga, K. A. Nguyen, S. Su et al., J. Comput. Chem. **14**, 1347 (1993).

[36] G. Grosso and G. Pastori Parravicini, *Solid State Physics* (Academic Press, 2000), p. 727.

[37] L. Novotny and B. Hecht, *Principles of Nano-Optics* (Cambridge University Press, Cambridge, UK, 2006).

[38] P. G. Etchegoin, E. C. Le Ru, and M. Meyer, J. Chem. Phys. **125**, 164705 (2006).

[39] M. G. Blaber, A.-I. Henry, J. M. Bingham, G. C. Schatz, and R. P. Van Duyne, J. Phys. Chem. C **116**, 393 (2012).

[40] V. Myroshnychenko, J. Rodríguez-Fernández, I. Pastoriza-Santos, A. M. Funston, C. Novo, P. Mulvaney, L. M. Liz-Marzán, and F. J. García de Abajo, Chem. Soc. Rev. **37**, 1792 (2008).

[41] G. Gil, S. Pipolo, A. Delgado, C. A. Rozzi, and S. Corni, J. Chem. Theory Comput. **15**, 2306 (2019).

Real-time dynamics of plasmonic resonances in nanoparticles described by a boundary elements method with generic dielectric function

Giulia Dall'Osto,[a] Gabriel Gil,[ab] Silvio Pipolo,[c] and Stefano Corni[ad‡]

[a] Department of Chemical Sciences, University of Padova, via Marzolo 1, Padova, Italy

[b] Instituto de Cibernetica, Matematica y Fisica, Calle E esq 15 Vedado 10400, La Habana, Cuba

[c] Université de Lille, CNRS, Centrale Lille, ENSCL, Université d'Artois UMR 8181
Unité de Catalyse et Chimie du Solide F-59000, Lille, France

[d] CNR Institute of Nanoscience, via Campi 213/A, Modena, Italy

We report the fitting of the function $f(\omega)$ when substituting the experimental dielectric function of Gold [1], Silver [2] and Rhodium [3] employing different numbers of Drude-Lorentz like terms in equation 3 in the main text.

Fitting of $f(\omega)$ of Au

Figure S1 reports the fitting of gold [1] function $f(\omega)$ with three DL terms plus the high frequency term (panel a) and with four DL terms plus the high frequency term (panel b). The fitting paramenters are reported in Table S1 (four DL terms) and in Table S2 (five DL terms). The fitting in panel (a) are substantially not good enough to represent the function as the large difference between the fitting and the experimental data show. The fitting in panel (b) is closer to the experimental data but for slight variance around 3 eV. We added one more DL term (figure 1a of main text) in order to better describe this region because it is very close to the plasmonic peak.
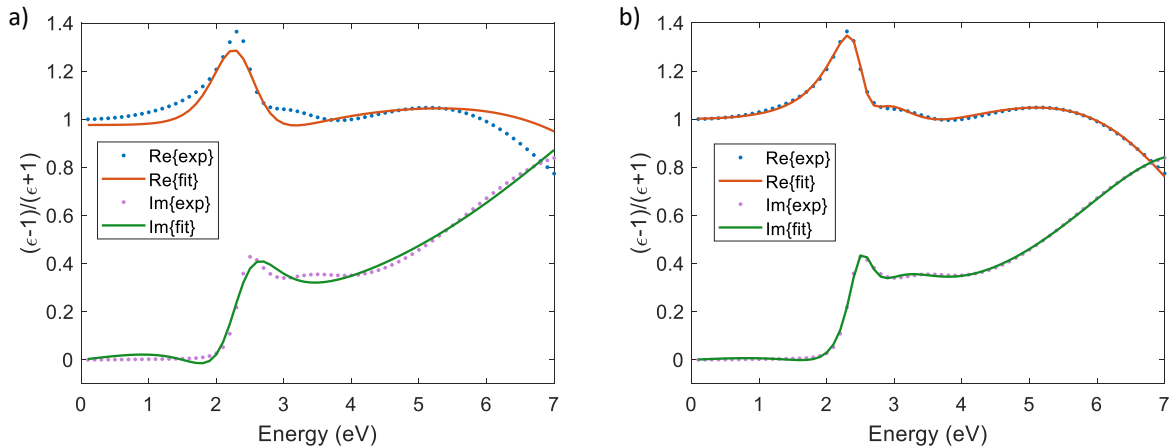

Figure S1: Fitting of Au function $f(\omega)$ with a sum of four (a) DL like terms and five (b) DL like terms.

Table S1: Parameters of $f(\omega)$ when substituting the gold dielectric function, fitted by four Drude-Lorentz like terms.

p	ω_p (eV)	γ_p (eV)	A_p (eV^2)
1	2.32	0.664	-110
2	2.33	0.663	110
3	9.17	3.67	84.9
4	73.0	0.00	694

Table S2: Parameters of $f(\omega)$ when substituting the gold dielectric function, fitted by five Drude-Lorentz like terms.

p	ω_p (eV)	γ_p (eV)	A_p (eV^2)
1	2.51	0.257	0.527
2	2.72	0.974	-40.6
3	2.74	0.970	40.7
4	7.31	2.52	32.3
5	18.1	0.00	145

Fitting of $f(\omega)$ of Ag

Figure S2 reports the fitting of silver[2] function $f(\omega)$ with two DL terms plus the high frequency term (panel a), with three DL terms plus the high frequency term (panel b) and with four DL terms plus the high frequency term (panel c). The fitting paramenters are reported in Table S3 (three DL terms), in Table S4 (four DL terms), in Table S5 (five DL terms) and in Table S6 (six DL terms). The fitting in panel (a) and in panel (b) diverge from the experimental data in many region. Adding one more DL term in the expansion leads to a better result but in the region around 5 eV persist a discrepancy and for this reason we employed the parameters results of fitting obtained with six terms overall to describe the function $f(\omega)$ for silver NPs (Figure .

Table S3: Parameters of $f(\omega)$ when substituting the silver dielectric function, fitted by three Drude-Lorentz like terms.

p	ω_p (eV)	γ_p (eV)	A_p (eV^2)
1	3.60	0.144	3.12
2	5.17	0.237	6.78
3	129	0.00	8429

Table S4: Parameters of $f(\omega)$ when substituting the silver dielectric function, fitted by four Drude-Lorentz like terms.

p	ω_p (eV)	γ_p (eV)	A_p (eV^2)
1	3.27	0.491	-0.485
2	3.59	0.156	3.40
3	5.30	0.185	13.0
4	122	0.00	3985

Table S5: Parameters of $f(\omega)$ when substituting the silver dielectric function, fitted by five Drude-Lorentz like terms.

p	ω_p (eV)	γ_p (eV)	A_p (eV^2)
1	3.59	0.146	3.13
2	3.65	0.632	-2.01
3	3.78	0.491	1.86
4	5.16	0.233	6.42
5	128	0.00	8766

Table S6: Parameters of $f(\omega)$ when substituting the silver dielectric function, fitted by six Drude-Lorentz like terms.

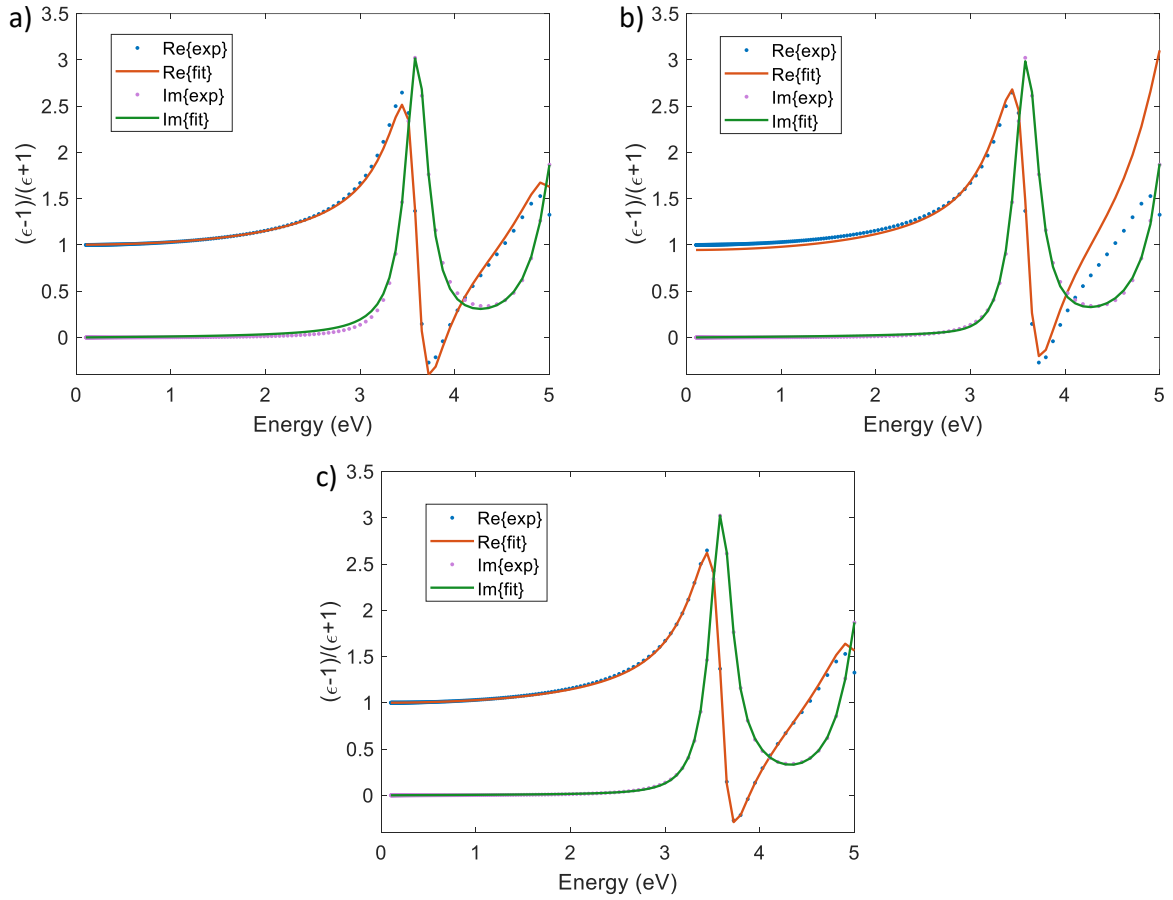| p	ω_p (eV)	γ_p (eV)	A_p (eV^2)
1	3.59	0.141	2.90
2	3.71	0.205	0.452
3	3.82	0.767	-1.77
4	4.02	0.559	1.36
5	5.13	0.231	5.86
6	30.5	0.000	518

Figure S2: Fitting of Ag function $f(\omega)$ with a sum of three DL like terms (a), four DL like terms (b) and five DL like terms (c).

3

Fitting of $f(\omega)$ of Rh

Figure S3 reports the fitting of rhodium function $f(\omega)$ with two DL terms plus the high frequency term (panel a), with three DL terms plus the high frequency term (panel b) and with four DL terms plus the high frequency term (panel c). A single experimental measurement of dielectric function was not available in the region 0-8 eV and thus we employed the data reported in [3] made up by two different measurement that lead to the discrepancy around 6 eV. The fitting paramenters are reported in Table S7 (three DL terms), Table S8 (four DL terms), in Table S9 (five DL terms) and in Table S10 (six DL terms). The fitting in panel (a) is quite different from the experimental data while fitting with four or more terms are closer to the experimental profile. The fitting with four terms (panel b) is not good enough in the region between 3 and 5 eV while the fitting with five terms (panel c) shows an artificial peak due to the discrepancy between the two set of data around 6 eV. We employed the parameters obtained from the fitting with six terms (reported in the main text) because the profile is closer to the experimental values without being too influenced by the discrepancy of the set of data at 6 eV.
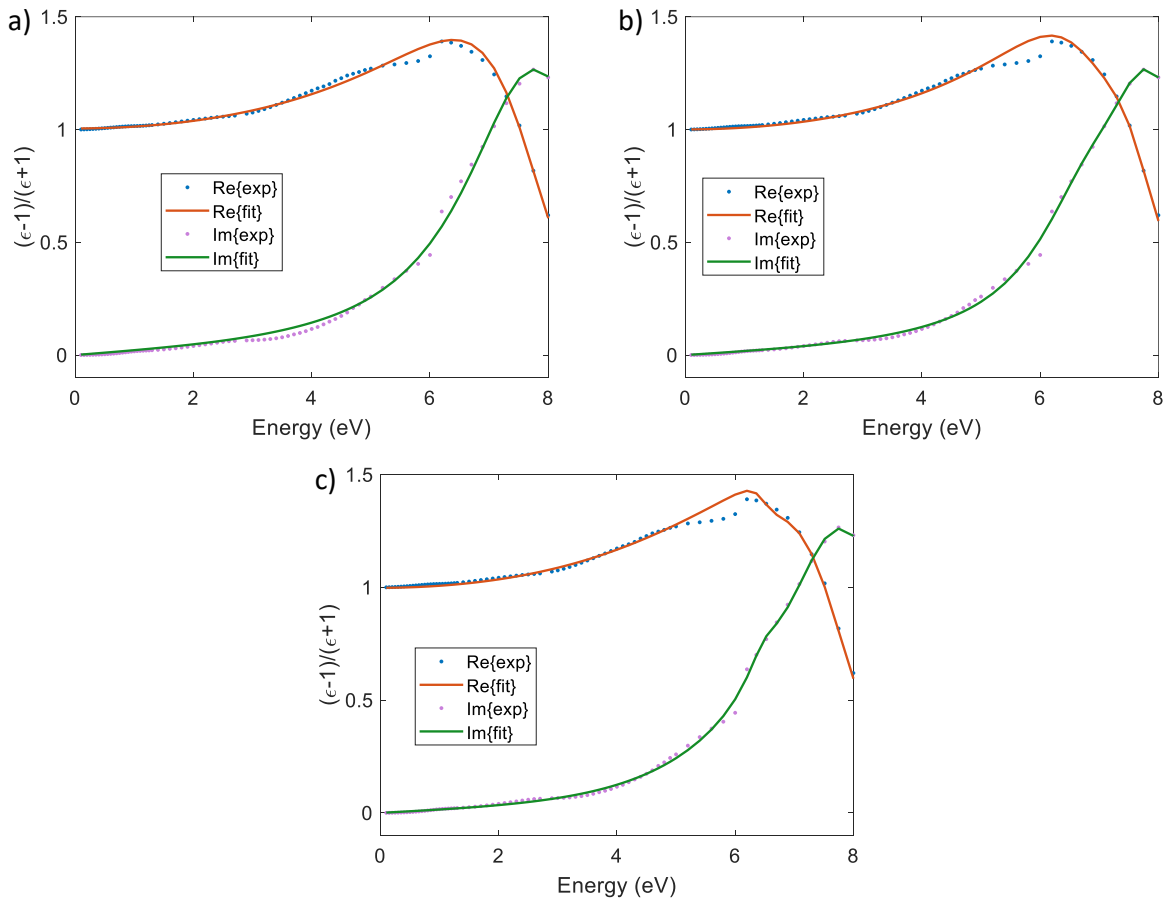

Figure S3: Fitting of Rh function $f(\omega)$ with a sum of three DL like terms (a), four DL like terms (b) and five DL like terms (c).

Table S7: Parameters of $f(\omega)$ when substituting the rhodium dielectric function, fitted by three Drude-Lorentz like terms.

p	ω_p (eV)	γ_p (eV)	A_p (eV^2)
1	7.80	1.49	14.8
2	7.80	1.49	14.8
3	17.5	0.00	164

Table S8: Parameters of $f(\omega)$ when substituting the rhodium dielectric function, fitted by four Drude-Lorentz like terms.

p	ω_p (eV)	γ_p (eV)	A_p (eV^2)
1	6.72	1.09	4.70
2	7.88	1.13	18.2
3	9.96	1.49	7.68
4	20.7	0.000	230

Table S9: Parameters of $f(\omega)$ when substituting the rhodium dielectric function, fitted by five Drude-Lorentz like terms.

p	ω_p (eV)	γ_p (eV)	A_p (eV^2)
1	5.05	4.09	-8.82
2	6.50	0.360	0.553
3	7.75	1.14	16.5
4	7.97	4.50	0.553
5	22.3	0.00	251

Table S10: Parameters of $f(\omega)$ when substituting the rhodium dielectric function, fitted by six Drude-Lorentz like terms.

p	ω_p (eV)	γ_p (eV)	A_p (eV^2)
1	2.44	3.09	4.23
2	2.59	1.58	2.86
3	2.66	2.13	-7.18
4	7.00	1.86	-20.9
5	7.51	1.81	53.6
6	134	0	1.01×10^4

Role of the propagation time step

The choice of the propagation time step greatly influences the simulation outcomes. The best time step value, in terms of TD and Freq BEM agreement, depends on the poles frequencies ω_p, and in general, should be suitable to describe the faster charge oscillation (i.e., characterized by the highest ω_p). However, the time step cannot be unequivocally determined on the basis of the largest frequency value because of the mutual dependence of the polarization charges. To determine the optimal time step (i.e., the largest possible such that TD BEM reproduces all the qualitative features of Freq BEM results), we performed a batch of TD BEM tests varying the time step. We choose a broader gaussian profile for the time-dependent electric field by setting $\sigma = 0.121$ fs, in order to have a good resolution of the field propagation even with larger time steps. In figure S4, we show the results for the imaginary part of the polarizability for five TD BEM simulations with different time steps. Spectral bands between 5 eV and 9 eV and below 2 eV are the most affected by the variation of time step. In particular, the peak around 6 eV becomes broader and more intense when the time step is increased. The results with $dt = 0.242$, 1.21 and 2.42 as are superposed and the accuracy is so high to reveal the weak peak at 1.8 eV. When higher time steps are employed the accuracy of the results progressively decrease. For this reason, we select $dt = 2.42$ as (0.1 au) for the rest of the calculations involving gold NPs.
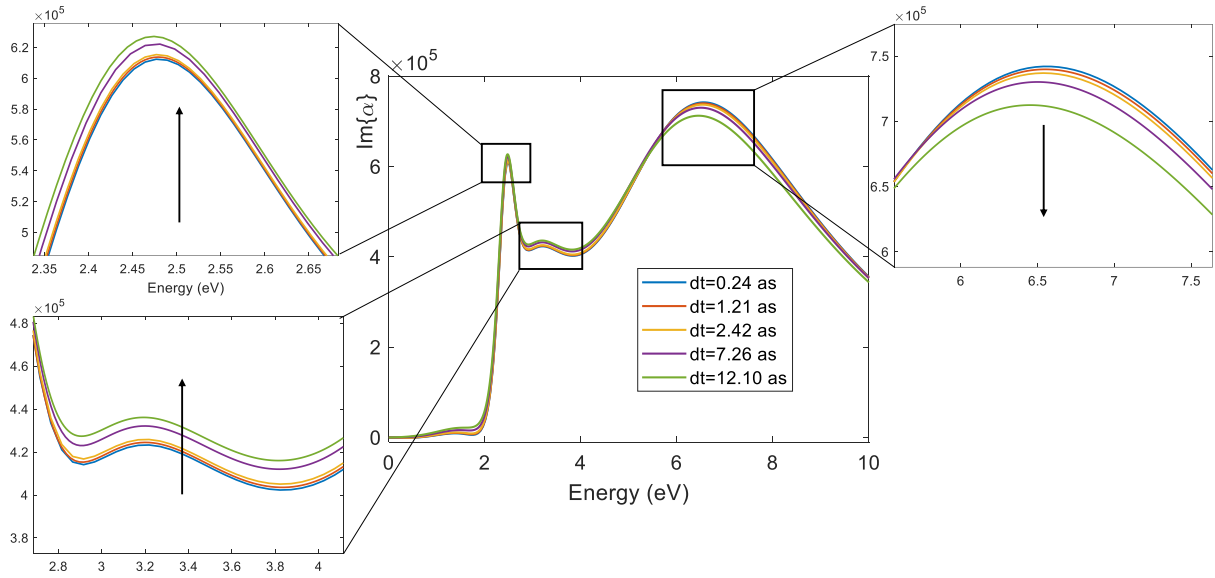
Figure S4: Imaginary part of the polarizability of a gold nanosphere with radius 5 nm obtained through time dependent calculation with different time steps of propagation, the black arrows highlight how the spectrum changes in different areas increasing the time step.

Table S11: CIS energies of LiCN calculated with GAMESS.

State	Energy (eV)
1	6.3409
2	7.5859
3	7.5860
4	8.2405
5	8.2406
6	9.0270
7	9.1694
8	9.1694
9	9.6432
10	10.5005

References

[1] P. B. Johnson and R. W. Christy, *Phys. Rev. B*, 1972, **6**, 4370–4379.

[2] A. D. Rakić, A. B. Djurišić, J. M. Elazar and M. L. Majewski, *Appl. Opt.*, 1998, **37**, 5271–5283.

[3] E. Palik, *Handbook of Optical Constants of Solids*, Academic Press: Cambridge, MA, USA, 1998.

Chapter 2

One of the applications I have focused on in the field of molecular plasmonics is tip-enhanced photoluminescence of molecules.[61, 62] In collaboration with Marco Romanelli (UniPD), we simulated the photoluminescence of zinc phthalocyanine sandwiched between a silver nanotip and a silver substrate. The setup was chosen to reproduce recent experimental results[22] showing the image of a single molecule thanks to the submolecular resolution achieved.[63, 64] This chapter is reproduced as a published paper on *The Journal of Chemical Physics* and consists of a theoretical part, which contains the basis of the theory used in the calculation and a section on the calculated results. The methodology section contains the main equations of BEM-PCM [65] with the improvements of the model needed to cope with the complexity of the system (two nanoparticles with non-trivial shapes) and the equations used to calculate the photoluminescence intensity. In the results, we explored the role of the experimental setup, such as the shape of the tip and the distance between the tip and the molecule, which are useful for the interpretation of the experimental outcomes. Finally, the calculated TEPL intensity is compared with the experimental intensity. To reproduce the experimental results, a time-dependent treatment was not required, so we used a frequency-domain version of the BEM-PCM equation. The innovation in the theory was implemented in the existing TDPlas code[60] developed in the group of Prof. Corni.

My role in the project was mainly dedicated to the implementation of a new diagonalization procedure required to deal with complex nanostructures as those used in this experiment and the equations used to calculate the photoluminescence

quantities. Moreover, some precautions must be deployed when the calculation is performed with more than one nanostructure to avoid misalignment of vectors normal to tesserae on the NP surface. To this end, I have developed a strategy to properly manage multiple nanoparticles, even with different geometries. My contribution to the writing of the manuscript is related to the method part while figures have been handled by Marco Romanelli, the effort for writing the other paragraphs have been equally divided between all the authors.

Role of metal-nanostructure features on tip-enhanced photoluminescence of single molecules

View Online   Export Citation   CrossMark

Marco Romanelli,[1] [ID] Giulia Dall'Osto,[1] [ID] and Stefano Corni[1,2,a)] [ID]

AFFILIATIONS

[1] Department of Chemical Sciences, University of Padova, via Marzolo 1, Padova, Italy
[2] CNR Institute of Nanoscience, via Campi 213/A, Modena, Italy

Note: This paper is part of the JCP Special Topic on Chemical Imaging.
[a)]Author to whom correspondence should be addressed: stefano.corni@unipd.it

ABSTRACT

Tip-enhanced photoluminescence (TEPL) experiments have recently reached the ability to investigate single molecules exploiting resolution at the submolecular level. Localized surface plasmon resonances of metallic nanostructures have the capability of enhancing an impinging electromagnetic radiation in the proximity of their surface, with evident consequences both on absorption and emission of molecules placed in the same region. We propose a theoretical analysis of these phenomena in order to interpret TEPL experiments on single molecules, including a quantum mechanical description of the target molecule equilibrated with the presence of two nanostructures representative of the nanocavity usually employed in STMs. The approach has been applied to the zinc phthalocyanine molecule, previously considered in recent TEPL experiments [Yang *et al.*, Nat. Photonics **14**, 693–699 (2020)]. This work has the aim of providing a comprehensive theoretical understanding of the experimental results, particularly focusing on the investigation of the tip features that majorly influence the excitation and fluorescence processes of the molecule, such as the geometry, the dielectric function, and the tip–molecule distance.

Published under an exclusive license by AIP Publishing. https://doi.org/10.1063/5.0066758

I. INTRODUCTION

Localized surface plasmon resonances (LSPRs) of metallic nanostructures can lead to strong field enhancements where the impinging electromagnetic radiation is focused at the nanoscale, thus allowing one to get around Abbe's diffraction limit of classical optics.[1–3] Among many different peculiar consequences, focusing light at the nanoscale has proved to be extremely useful for single-molecule imaging,[4–6] where by cleverly harnessing subtle plasmon–molecule interactions, it was possible to detect and visualize single molecules in real life experiments,[7–10] even achieving submolecular resolution.[11,12] Various kinds of "tip-enhanced" spectroscopies take advantage of the local field enhancement related to the excitation of plasmons associated with the metallic tip of scanning probe microscopes, giving rise to highly resolved, both in space and time, experimental techniques, such as tip-enhanced Raman spectroscopy (TERS).[13–21] Recently, it has been shown that sub-nanometer single-molecule resolution is also attainable in

photoluminescence imaging, where the metallic atomistic tip of a STM has been used to confine the electromagnetic field down to the nanoscale,[22,23] eventually leading to an enhanced fluorescence emission of a single molecular compound that has been used to record photoluminescence images with submolecular spatial resolution [tip-enhanced photoluminescence (TEPL)].[24–27]

The interpretation of the outcomes of such experiments is not trivial, and thus, a theoretical approach is helpful in elucidating the complex dynamics that is taking place. Hereafter, we theoretically investigate the influence of a metallic STM-like nanostructure on the photoluminescence properties of a single zinc phthalocyanine molecule that has been used for single-molecule TEPL imaging in recent experiments,[24] eventually pointing out some features of the system[28] that affect the PL images significantly.

Different approaches[29] have been explored so far to study plasmonic nanostructures as the classical dielectric description through Mie theory,[30,31] the discrete dipole approximation,[32] the boundary element method (BEM),[33–37] and the finite difference time domain

method.[38] These latter two approaches have also been coupled to an atomistic quantum mechanical description of nearby molecules to model their plasmon-affected optical properties without giving up molecular chemical details.[35,39–44]

Other proposed models are based on a classical but atomistic description of the metallic nano-object, while the molecule is still described through quantum-mechanics.[45,46] The coupling between molecular emitters and plasmonic cavities has been recently investigated by Neuman *et al.*[42] adopting the canonical quantization of plasmons and density functional theory (DFT) treatment of the molecule, and very recently, the coupling between quantized plasmons and molecules has been considered at the coupled cluster level.[47] Moreover, the full quantum mechanical description of the overall system has been reported,[48] allowing one to directly study the whole hybrid system on the same footing. This approach allows us to take into account challenging effects, such as "strong-coupling," with the limit of considering rather small nanostructures (i.e., composed of few hundred atoms), but it becomes unfeasible when larger nanostructures are considered as those employed in STMs.

Here, we employ a semiclassical description of the overall system through the Polarizable Continuum Model–NanoParticle, PCM-NP (an extension of the PCM implicit solvation model),[49] where the metallic nanostructure is described as an homogeneous body of complex shape characterized by its own frequency-dependent dielectric function, whereas the molecule is treated at an atomistic quantum mechanical level.[35,50,51] This approach allows us to have submolecular information, overcoming the limitation of using point-dipole models for the molecule, while keeping a description of the nanostructures that takes into account the main plasmonic effects. In our model, the electromagnetic problem is solved at an affordable computational cost through the BEM, which requires discretizing in small portions only the nanostructure surface (as opposed to its volume). A similar approach has been satisfactorily used to interpret the experimental data in Ref. 24. Here, this approach has been employed to analyze the role of some critical features of both the tip and the substrate, which affect the photoluminescence process of a molecule in their proximity. In particular, we focus our investigation on the geometry of the metal nano-tip, the empirical dielectric function employed to describe the metal response and the tip–molecule distance. Moreover, we specifically analyze an issue that was not investigated before: The presence of the tip can polarize the ground and excited electronic states of the molecule and thus can indirectly change excited state properties as well. To clearly identify the origin of the dependence of the results on the investigated parameters, we do not only calculate photoluminescence intensity maps as a function of tip position, but we also analyze absorption spectra, the local enhancement of the incident fields, and the non-radiative decay rates induced by the presence of the metallic tip and substrate.

This work is organized as follows: Sec. II summarizes the theoretical approach employed to describe the system and to calculate the photoluminescence intensity of the molecule (the original theory can be found in Refs. 35, 50, 52, and 53, and an overall account is given in Ref. 54), followed by Sec. III that reports the computational details of our calculations; all the analysis and results are reported in Sec. IV, and the conclusions are drawn in Sec. V.

II. METHODS

A. The PCM NP model

The NP is considered as a continuum body in the quasi-static limit, i.e., retardation effects are not included, described within the PCM framework in the integral equation formalism. The PCM problem is numerically solved with the BEM approach: The NP surface is discretized in small portions called tesserae, each of which is associated with a polarization charge located in its geometrical center. The polarization charges describe the interaction between the NP and the external potential that could be generated by the presence of an incident electric field or by the transition potential of a molecule close to its surface.[35] The polarization charges are expressed as a function of potential $\mathbf{V}(\omega)$, a vector containing the transition potential numerically evaluated at each tessera position, and the response matrix $\mathbf{Q}(\omega)$,

$$\mathbf{q}(\omega) = \mathbf{Q}(\omega)\mathbf{V}(\omega), \qquad (1)$$

where

$$\mathbf{Q}(\omega) = -\mathbf{S}^{-1}\left(2\pi\frac{\epsilon(\omega)+1}{\epsilon(\omega)-1}\mathbf{I} + \mathbf{DA}\right)^{-1}(2\pi\mathbf{I} + \mathbf{DA}). \qquad (2)$$

The BEM matrices $\mathbf{S}$ and $\mathbf{D}$ are representative of Calderon's projectors,[49] and $\mathbf{A}$ is a diagonal matrix with elements equal to the tessera areas. In the present work, the external potential $\mathbf{V}(\omega)$ is generated either by an incident electric field when the field enhancement is calculated nearby the NP or by the transition potential of a molecule when molecular photoluminescence calculations are performed in the presence of the NP.

Previously,[55] the inversion in Eq. (2) has been solved through the transformation of $\mathbf{DA}$, exploiting the integral relation $\mathbf{DAS} = \mathbf{SAD}^\dagger$,

$$\mathbf{Q}(\omega) = -\mathbf{S}^{-1/2}\left(2\pi\frac{\epsilon(\omega)+1}{\epsilon(\omega)-1}\mathbf{I} + \mathbf{S}^{-1/2}\mathbf{DAS}^{1/2}\right)^{-1}$$
$$\cdot\left(2\pi\mathbf{I} + \mathbf{S}^{-1/2}\mathbf{DAS}^{1/2}\right)\mathbf{S}^{-1/2}. \qquad (3)$$

In this procedure, the matrix $\mathbf{S}$ is diagonalized in order to calculate $\mathbf{S}^{1/2}$ and $\mathbf{S}^{-1/2}$, but occasionally, we have experienced numerical problems (non-positive eigenvalues) for complex meshes. A different approach is here explored to obtain a diagonal version of Eq. (2). This is done through the diagonalization of the term $\mathbf{DA} = \mathbf{U}\mathbf{\Lambda}\mathbf{U}^{-1}$ leading to

$$\mathbf{Q}(\omega) = -\mathbf{S}^{-1}\mathbf{U}\left(2\pi\frac{\epsilon(\omega)+1}{\epsilon(\omega)-1}\mathbf{I} + \mathbf{\Lambda}\right)^{-1}(2\pi\mathbf{I} + \mathbf{\Lambda})\mathbf{U}^{-1}, \qquad (4)$$

$$\mathbf{Q}(\omega) = -\mathbf{S}^{-1}\mathbf{U}\mathbf{K}(\omega)\mathbf{U}^{-1}, \qquad (5)$$

where $\mathbf{K}(\omega)$ encloses the diagonal elements. The matrix $\mathbf{DA}$ is a real non-symmetric matrix; therefore, it is not Hermitian and its diagonalization does not lead to a unitary eigenvector matrix $\mathbf{U}$ as assured with Eq. (3). This alternative diagonalization procedure should be more robust than the previous one [through Eq. (3)] in all those situations (e.g., complex meshes) where some eigenvalues of $\mathbf{S}$ might be negative, thus hindering the calculation of $\mathbf{S}^{1/2}$. Real

eigenvalues and eigenvectors are expected as a result of the equivalence of Eq. (2) with Eq. (3); however, we observe that it is not always fulfilled due to numerical reason. If complex eigenvectors (and thus also eigenvalues) are obtained, they are always complex conjugated pairs.

The nanoparticle is a neutral body, and thus, the total charge on its surface should be equal to zero. From a numerical point of view, this is not trivial and some corrections have to be applied in order to assure this condition. Two possible strategies have been exploited to do so. In first place, the elements of matrices $\mathbf{U}^{-1}$ and $\mathbf{S}^{-1}\mathbf{U}$ have been scaled in order to assure that the sum over each eigenvector coefficient is equal to zero,

$$\left(U^{-1}\right)'_{ij} = \left(U^{-1}\right)_{ij} - \frac{\sum_k \left(U^{-1}\right)_{ik}}{N_{tess}} \qquad (6)$$

and

$$\left(S^{-1}U\right)'_{ij} = \left(S^{-1}U\right)_{ij} - \frac{\sum_k \left(S^{-1}U\right)_{kj}}{N_{tess}}, \qquad (7)$$

where the sum runs over the tesserae on the NP surface and N_{tess} is the number of tesserae. This step has the aim to ensure *a priori* that the sum over the polarization charges is zero. The second strategy is *a posteriori* normalization: After the calculation of the polarization charges, they are averaged in order to obtain a null total charge on the NP surface, as

$$\mathbf{q}'(\omega) = \mathbf{q}(\omega) - \frac{\sum_i q_i(\omega)}{N_{tess}}, \qquad (8)$$

where the sum runs over the tesserae on the NP surface. When disjointed nanostructures are considered in the same calculation, as in the present case, the sum of the surface charges has to be zero for each part of the system (in this case separately for the tip and the substrate) in order to avoid fictitious charge transfer effects that would affect the results of calculation. For the shapes considered here, we have numerically verified that the second approach, with the *a posteriori* normalization, is more effective than the first one (see Figs. S1 and S2 of the supplementary material): With the first approach, eigenvector coefficients related to different NPs are separately normalized, but they mix in the subsequent step when using Eq. (5) and the null sum over polarization charges on separate NPs is no more assured.

B. Photoluminescence calculations

The photoinduced molecular fluorescence is influenced by the presence of the metal nanostructure in different ways.[56–64] First, the absorption of the incident radiation is increased by means of a strong field enhancement due to the presence of the nearby metallic nano-object[65] that we describe in terms of induced dipole on the nanostructure by the molecular transition potentials [see Eqs. (10) and (11)]. Then, after vibrational relaxation upon light excitation, the molecule decay to the ground state through radiative and nonradiative processes is in both cases affected by the presence of nanostructures. Specifically, in this work, the molecule under study, zinc phthalocyanine, has two degenerate emitting states; therefore, both of them can be excited by the incident radiation and then decay, leading to fluorescence emission.

The tip-enhanced photoluminescence intensity has been computed by using the following equation, making the use of the Einstein coefficients (in a.u.) to calculate the modified absorption and emission rates:[54]

$$\frac{I}{I_0} = \frac{\eta_1^{enh} \cdot A_1^{enh} + \eta_2^{enh} \cdot A_2^{enh}}{\eta_1^0 \cdot A_1^0 + \eta_2^0 \cdot A_2^0}, \qquad (9)$$

where η is the quantum efficiency discussed later, A is the absorption coefficient, the indices 1 and 2 indicate the two lowest isoenergetic excited states S_1 and S_2, respectively, of the molecule responsible for the emission, and I_0 is the intensity of photoluminescence *in vacuo*. Moreover, the enhanced absorption A_1^{enh} (the same for state 2) in the presence of the NP is expressed as[53]

$$A_1^{enh} = \frac{2\pi |\overrightarrow{\mu}^{met}_{abs,1} + \overrightarrow{\mu}^{ind}_{abs,1}|^2}{3c}, \qquad (10)$$

where $\overrightarrow{\mu}^{met}_{abs,1}$ is the molecular transition dipole in the presence of nanostructure, which is computed from the QM transition density of the ground to S1 transition, which is in turn evaluated from the TDDFT equation. The latter includes the interacting terms with the metallic object (more details can be found in Fig. S7 of the supplementary material and Refs. 50 and 66). $\overrightarrow{\mu}^{ind}_{abs,1}$ is instead the dipole induced in the metallic nano-object by the molecular transition density, which is evaluated as

$$\overrightarrow{\mu}^{ind}_{abs,1} = \sum_i q^{ind}_{i,abs,1} \overrightarrow{s_i}, \qquad (11)$$

where $q^{ind}_{i,abs,1}$ is the polarization charge induced by the molecular transition density located in the i-th tessera and $\overrightarrow{s_i}$ is the center of such tessera. The quantum efficiency η_1^{enh} is instead given by[50,54]

$$\eta_1^{enh} = \frac{\Gamma_1^{rad}}{\Gamma_1^{rad} + \Gamma_1^{nr,met} + \Gamma^{nr,0}}, \qquad (12)$$

where Γ_1^{rad} is the radiative decay rate evaluated as[50,54]

$$\Gamma_1^{rad} = \frac{4\omega_1^3 |\overrightarrow{\mu}^{met}_{emi,1} + \overrightarrow{\mu}^{ind}_{emi,1}|^2}{3c^3}, \qquad (13)$$

while $\Gamma^{nr,0}$ is the intrinsic non-radiative decay rate of the molecule and $\Gamma_1^{nr,met}$ is the non-radiative decay rate due to the presence of the metal (which does not include non-local contributions from the metal response[67]). The latter has been evaluated through the imaginary component of the self-interaction between the surface charges and the molecular transition potentials, i.e.,[52]

$$\Gamma_1^{nr,met} = -2 \cdot \text{Im}\left\{\sum_i q_i V_i\right\}, \qquad (14)$$

where V_i is the molecular transition potential evaluated at the position of the i-th tessera.

It is worth pointing out that even though Eqs. (10) and (13) involve analogous quantities ($\overrightarrow{\mu}^{ind}_{abs,1}$, $\overrightarrow{\mu}^{met}_{abs,1}$, $\overrightarrow{\mu}^{ind}_{emi,1}$, and $\overrightarrow{\mu}^{met}_{emi,1}$), they are calculated at different frequencies (that of the absorption and that of the emission, respectively) and for different transition densities [that at the ground state geometry for Eq. (10) and that at the excited state geometry for Eq. (13)].

The real component of the self-interaction is instead associated with the medium-induced Lamb shift $\Delta\omega$, that is, the transition energy of the excited states is affected by the interaction with the polarization charges induced by the molecular transition potentials,[66]

$$\Delta\omega = \text{Re}\left\{\sum_i q_i V_i\right\}. \quad (15)$$

The gas-phase radiative quantum efficiency η^0 for the two states in Eq. (9) is related to the intrinsic non-radiative decay of the molecule through

$$\eta_1^0 = \frac{\Gamma_1^{rad,0}}{\Gamma_1^{rad,0} + \Gamma^{nr,0}}, \quad (16)$$

where $\Gamma_1^{rad,0}$ is the vacuum radiative decay rate for the excited state 1 that can be evaluated through Eq. (13) using the gas-phase molecular transition dipole and removing the term due to the metal response. Starting from Eq. (16), $\Gamma^{nr,0}$ can be computed if experimental values of η_1^0 are available. Since experimental data are only available in solution, η_1^0 has been set to 0.2, as reported by previous measurements in DMSO.[68] This assumption, even if approximated because we are using solvent-based molecular quantum efficiency for gas-phase calculations, is a reasonable choice, as shown in Sec. IV. Indeed, the photoluminescence emission in the presence of the metal is strongly enhanced compared to the vacuum values, even assuming unitary gas-phase quantum efficiency [that would result by neglecting $\Gamma^{nr,0}$ in Eq. (16)]; thus, the choice of this parameter (setting it either to 1 or to 0.2) does not strongly affect the order of magnitude of the TEPL ratio (see Figs. 9 and S3 for a comparison between two different values of η^0). Therefore, the contribution of the intrinsic non-radiative decay rate in Eq. (12) has been neglected, which is a sensible approximation keeping in mind that the main contribution to the overall non-radiative decay rate in the presence of the nanostructure is due to the metal–molecule interaction $\Gamma_1^{nr,met}$.

III. COMPUTATIONAL DETAILS

The NP structure (Fig. 1) is similar to that reported in a recent study.[24] The tip was modeled as a truncated cone with a height of 200 nm and a radius of 50 nm, featuring an additional atomistic protrusion (Fig. 1, red inset) that we defined as a smaller truncated cone at the tip apex with a base radius of 0.6 nm and a radius of the spherical cap of 0.5 nm. The cylindrical substrate has an height of 100 nm and a radius of 100 nm, where we left out the NaCl dielectric spacer used in the experiments[24] [we also tested the explicit inclusion of part of the NaCl layer (see Fig. S9 of the supplementary material)]. The structures of the tip and substrate are close to each other in order to generate a picocavity, shown in the inset, where to place the molecule. All results were obtained by setting the tip–molecule distance to 0.4 nm and the molecule–substrate separation to 1.4 nm unless specified differently. The molecule, if present, is placed in the point with coordinates (0,0,0), lying on the xy plane (parallel to the substrate surface), and the tip-axis direction is oriented along the z axis. More in detail, the substrate and tip meshes have been computed separately by using the Gmsh code[69] and then has been joined. The overall structure is characterized by 3818 tesserae more refined close to the atomistic protrusion and has been described using the
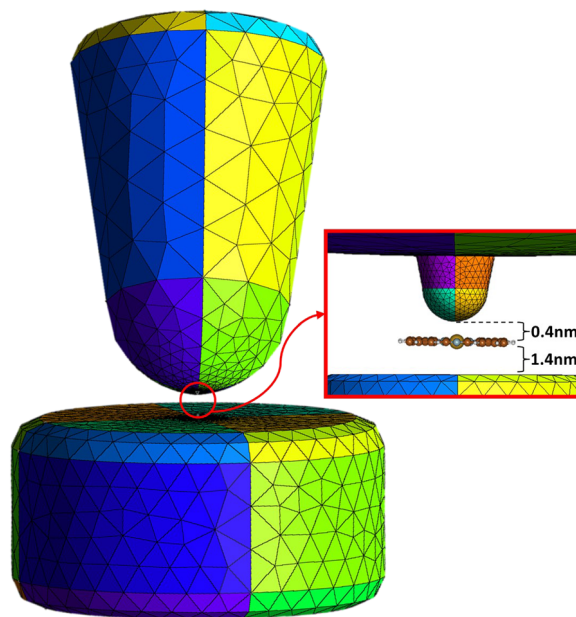

FIG. 1. Reference mesh structure used for the simulations computed by the Gmsh code.[69] In the red inset, a close-up of the atomistic protrusion at the tip apex responsible for the strong field enhancement predicted by the simulations is shown. The tip–molecule distance is always set to 0.4 nm, and the protrusion base radius is 0.6 nm unless specified differently.

Brendel–Bormann[70] fitting model of the silver dielectric function[71] unless otherwise stated.

The molecule, zinc phthalocyanine, has been considered at the atomistic level, and DFT calculations with the software Gaussian[72] have been performed for the gas-phase. No explicit Ag atoms were considered in the QM part, so charge transfer states are not included. More in detail, the ground state geometry of the molecule has been optimized at the B3LYP/6-31G(d) level of theory and excited state transition dipole moments in the gas-phase have been computed through time-dependent DFT calculations. The optimization of the first excited state has been done at the B3LYP/6-31G(d) level of theory; the comparison of ground and excited state optimized geometries is reported in the supplementary material (Fig. S5). After the calculation of the vibrational normal modes in the ground and first excited state, the vibrationally resolved emission spectrum has been computed through the code FCclasses.[73] The spectrum has been reported in the supplementary material (Fig. S6) comparing it with the experimental one[24] obtained in a vacuum for a molecule close to the nanostructures and in DMSO.[74] The spectrum shows signatures of the vibrational structure, represented by the Q(0,1) band (transition between the lowest level of the first excited state to excited vibrational states of the ground state). In the calculation of the PL intensity, we focused on the Q(0,0) band only; the ground state optimized geometry was considered for evaluating the absorption rates, whereas emission-related quantities were computed from the excited state optimized structure. We also note that throughout this work, photoluminescence data are calculated by exciting the lowest excited states from which emission occurs. Starting from the

ground state geometry optimized in a vacuum, we performed DFT calculations of the molecule in the presence of the nanostructures (both the tip and substrate together) at the B3LYP/6-31G(d,p) level of theory with a locally modified version of GAMESS[75,76] in order to compute the excited state energies, transition dipole moments, and molecular potential on NP tesserae. The potential on the nanostructure surface computed with GAMESS is equilibrated with the molecule charge distribution, i.e., a self-consistent procedure assures that the molecule ground state is in equilibrium with the surrounding nanostructures, and this effect is exploited in Sec. IV E. The basis set of the molecule wave function employed in the calculation of photoluminescence intensity includes, in addition to the ground state, ten excited states computed as frozen states that is they are influenced by the nanostructure polarization equilibrated with the ground state of the molecule. Another set of input data (energies, transition dipole moments, and potential) has been computed to also include the equilibration of the excited states with the surrounding nanostructures. To this point, the CIS calculation of the molecule close to the nanostructures has also been performed in order to compute the transition dipole moments between electronic excited states, needed to perform SCF equilibration of excited states with the nanostructures and go beyond the approximation of frozen excited states. Considering the first five excited states, we performed the self-consistent equilibration of the molecular ground and excited states in the presence of the nanostructures to compute energies, transition dipole moments, and the transition potentials on the tesserae. These results have been employed in Sec. IV E where the effect of the presence or absence of excited state equilibration with the nanostructures is investigated. In order to obtain the results reported in Sec. IV, we performed GAMESS calculations moving the molecule with respect to the tip and substrate center along the x and y axis through a grid with step 2.5 Å to finally obtain results on 36 different molecule positions. The z coordinate of the molecule has not been varied.
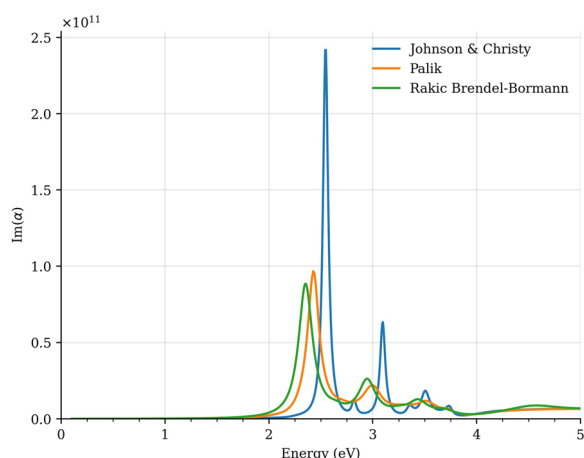
The polarization charges located on each tessera have been computed with the homemade code TDPlas[55] in both cases with or without the presence of the molecule. In the first case, an incident radiation along the z axis has been considered to compute the potential on the polarization charges, while in photoluminescence calculations (e.g., in the presence of the molecule), the transition potential from the GAMESS TDDFT calculations due to the first two degenerate excited states has been employed in order to calculate the photoluminescence intensity due to the excitation of these degenerate low-lying states.

In photoluminescence calculation, the absorption frequency has been set to 532 nm (as in the experiment[24]), which is close to the maximum absorption of the silver nanostructures, as shown in Sec. IV by Fig. 2, while the emission frequency is set to 653 nm that corresponds to the experimental one.[24]

IV. RESULTS AND DISCUSSION

In this section, we report the results obtained with the methods explained in Sec. II. First, the results concerning the isolated nanostructure are reported as a benchmark test regarding the choice of the dielectric function, where we consider some choices between those that are mostly employed in the literature for modeling silver: Palik,[71] Johnson and Christy,[77] and the Brendel–Bormann fitting of Palik data.[70] In Sec. IV B, we report a study related to the effect of the nanostructure geometry, in particular the protrusion of the tip, on the local field enhancement. In Sec. IV C, the effect of the absorption frequency of the incident radiation is investigated, considering the calculation of the local field performed with the same nanostructure. Then, a study related to the effect of the distance between the tip and substrate on the intensity of the field enhancement is reported. Finally, in Sec. IV E, our results on the tip-enhanced photoluminescence of a single zinc phthalocyanine molecule are displayed. They include the calculation of the enhanced absorption rate, the enhanced radiative decay, the spectral shift, and the non-radiative decay rate induced by the molecule–metal interaction, as well as a comparison of the photoluminescence intensity computed when the self-consistent equilibration of the molecular states with the nanostructures is or is not considered.

A. Comparison of different dielectric functions

We computed the imaginary part of the polarizability, proportional to the absorption cross section, of the silver nanostructure reported in Fig. 1 for different dielectric functions documented in the literature, by plotting the imaginary component of the polarizability associated with the induced dipole originated by an incoming electric field polarized along the tip-axis direction. As it is shown in Fig. 2, the energy of the brighter plasmonic resonance of interest (≈2.3–2.4 eV) is quite sensitive to the dielectric function that is considered to model the metallic response. In the tests performed, two experimental dielectric functions have been considered (Palik[71] and Johnson and Christy[77]), while the Rakić[70] dielectric function is the result of the fitting of Palik data through the Brendel–Bormann model; indeed, as expected, the two profiles are very close to each other. Comparing the two experimental sets of data (Palik[71] and Johnson and Christy[77]), the results show some differences not only in the intensity of the absorption but also on the energies of the

FIG. 2. Different absorption spectra of the same structure (Fig. 1 is the reference structure) calculated using three distinct dielectric functions: Johnson and Christy[77] (blue), Palik[71] (yellow), and Rakić-BB[70] (green).

peaks. Moreover, the damping of the excitation related with the broadening of the bands is different in the two cases; it is larger when the Palik or Rakic dielectric functions are employed than in the case of Johnson and Christy. In the following calculations, the Rakic dielectric function is employed, which is the less efficient due to a larger damping, as shown by Fig. 2.

B. Dependence of the local field on the tip geometrical parameters

The response of a NP interacting with an incident electric field directed along the z axis has been computed by solving the frequency-dependent BEM equations [Eq. (2)] for different
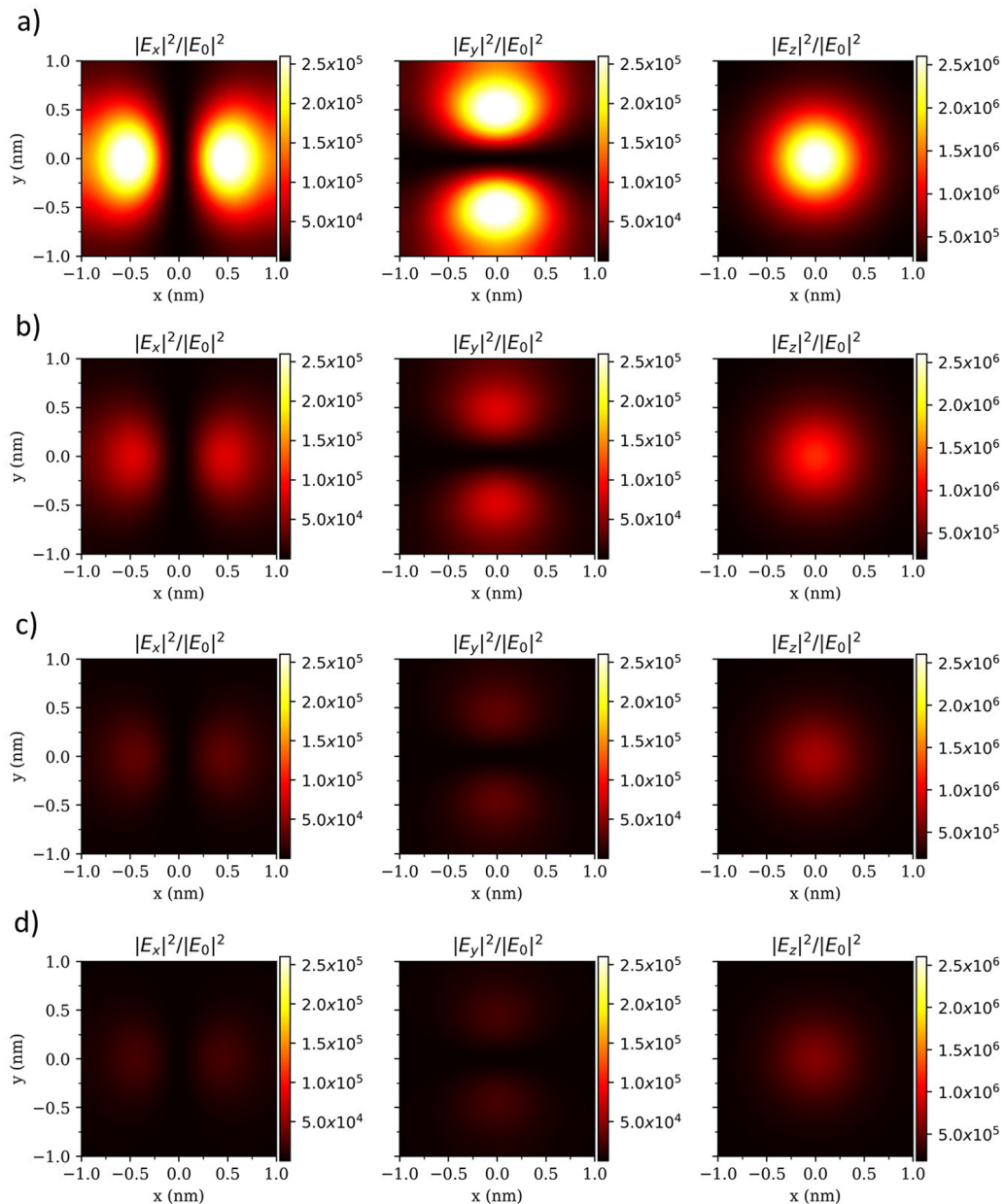
FIG. 3. Local field enhancement on a 1.0×1.0 nm^2 grid centered at $z = 0.0$ nm for different structures. From (a) to (d), the protrusion base radius (Fig. 1, red inset) increases [the radius is respectively: 0.5, 0.6, 0.8, 1.0 nm, as in Fig. 4(b)]. The local field enhancement is computed as the ratio $|E_i|^2/|E_0|^2$, where E_0 is the incoming electric field polarized along the tip-axis direction (z axis), whereas E_i assumes the values of E_x, E_y, E_z that are the components of the total local field obtained as the sum of the incident field $\vec{E}_0$ and the field generated by the charges on the nanostructure surface. The grid plane coincides with the molecular plane in the subsequent simulations (see Fig. 9).

structures obtained by changing the protrusion base radius (Fig. 1, red inset) in order to study the effect of structural modifications of the sharpest part of the tip. We found out that the local field on a 1.0 × 1.0 nm^2 grid oriented along the xy plane (z-coordinate = 0) has the maximum intensity in the same spatial points varying the NP structure: The field along the z axis has a spherical symmetry, while the x component of the field has the maximum intensity along the x axis and analogously the y component of the field has the maximum intensity along the y axis. On the other hand, the intensity of the field is strongly affected by the geometrical feature of the NP, as shown in Fig. 3. Indeed, the enhancement of the total local field upon excitation at 2.33 eV decreases as the protrusion base radius becomes larger, as can be inferred by Fig. 4 that shows the local field enhancement as a function of frequency for five different tip radii. This result is due to two main effects: an overall reduction of the intensity of the local field, particularly when structures with radius 0.6 and 0.7 nm are employed, and a gradual blue-shifting of the "local" resonance when the base radius increases. As Fig. 4 shows, if we considered the electric field at its maximum value for each structure, we would obtain color maps representing the field on a grid very close to each other, but the intermediate cases with radius protrusion equal to 0.6 and 0.7 nm would show a lower intensity of the enhanced field in correspondence with the maximum value.

C. Frequency dependence of the local field enhancement

As already suggested by Fig. 4, the intensity of the field enhancement strongly depends on the frequency. This is of particular interest when molecules close to the NP are considered: The closer the maximum frequency of the molecular absorption and the local field enhancement are, the more relevant the plasmonic effect on the molecule response will be. To better analyze this point, the local field enhancement has been computed on a 1.0 × 1.0 nm^2 grid oriented along the xy plane at different frequencies. In Fig. 5, we report the x and y components of the total field over the incoming electric field for different x [Fig. 5(a), top] and y [Fig. 5(a), bottom] displacements. As illustrated by the colored curves that correspond to different frequencies at which we evaluated the metallic response upon excitation, the maximum of the local field is reached at energies slightly higher than the "global" plasmonic resonance, which is at 2.33 eV (see Fig. 2, green curve).

Moreover, due to the symmetry of the structures involved in the calculation, the field intensity along the x direction (top panel) should be identical but for numerical accuracy to the field intensity along the y direction (bottom panel) for each frequency considered. Similar results can be observed in Fig. 6(a) that shows the field intensity along the x direction as a function of frequency, where the maximum of the total field for different grid points along the x direction is always achieved at energies above the "global" resonance. In addition, the frequency at which the x component of the total field reaches a maximum does not change moving on the grid along the x axis.

D. Field enhancement as a function of tip–molecule distance

Previous experiments and simulations[24] illustrated that TEPL measured for this kind of STM-like setup is distinctly affected by the tip–molecule distance. To investigate this point, we considered different distances between the tip and substrate moving the tip also along the x axis. Our results are reported in Fig. 7 where the x component of the local field intensity has been reported as a function of
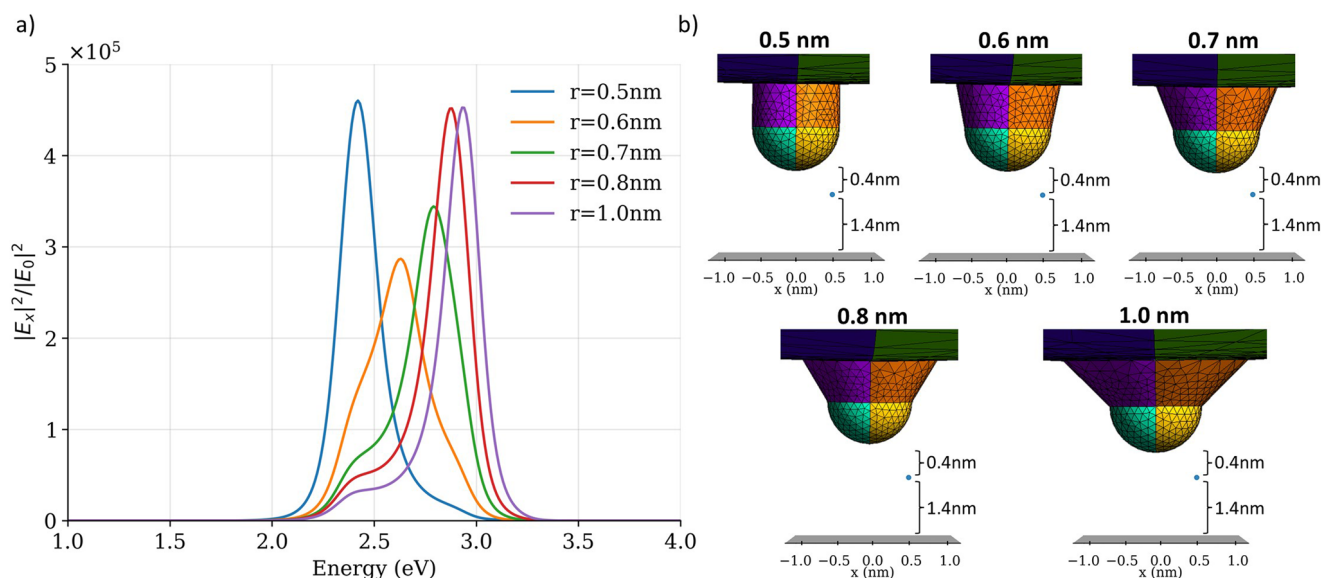

FIG. 4. (a) Local field enhancement as a function of frequency calculated on the grid point (x = 0.5 nm, y = 0.0 nm) for the five different structures reported in panel (b) (only the x component of the total field is shown). (b) Five different protrusion radii considered for the simulations in Fig. 3 and (a). The pale blue dot is the grid point where the field is computed, whereas the gray plane represents the substrate surface.
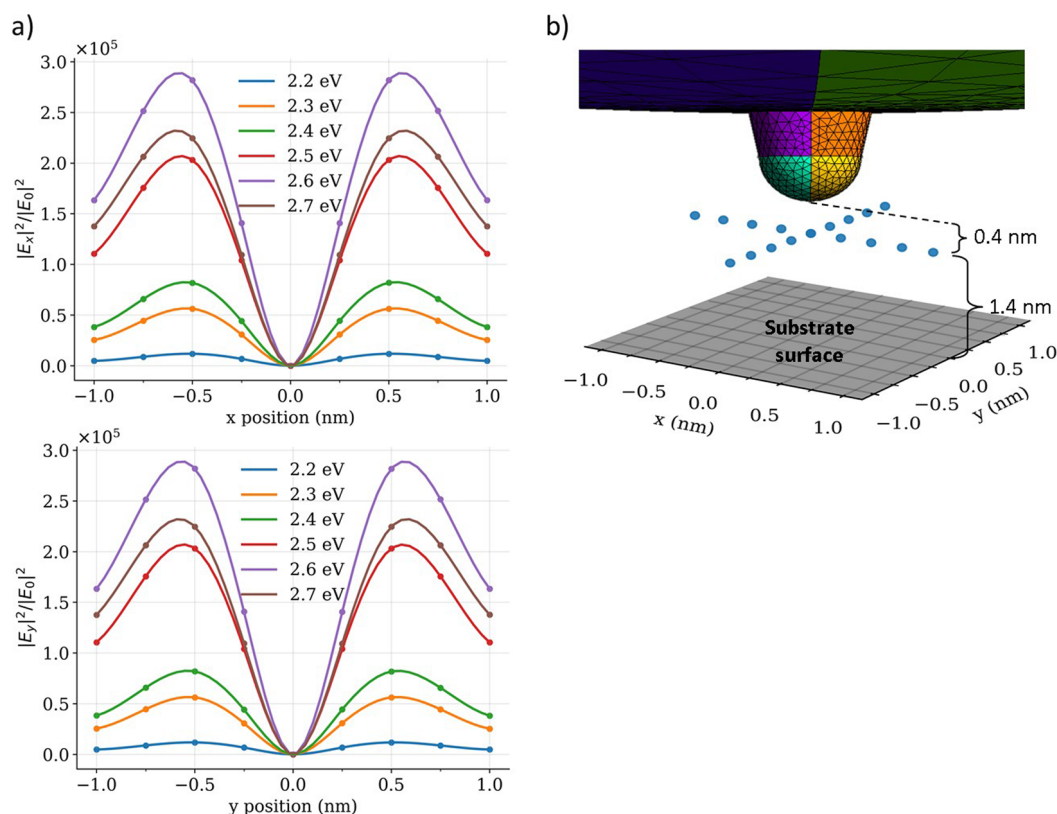
FIG. 5. (a) Square modulus of the x and y components of the total field over the incoming electric field along x (top) and y (bottom) displacements (the dots represent the calculated values, while the corresponding curves were obtained through cubic interpolation). The different colored lines correspond to the total field at different frequencies. The "global" plasmonic resonance of interest is predicted to be at 2.33 eV in the absorption spectrum (Fig. 2, highest green peak). (b) Schematic representation of the simulation setup used to obtain the results shown in panel (a), where the blue dots are representative of points where the electric field has been computed.

x position (with both y and z coordinates equal to 0 nm). The distances reported on the top of the figure are those between the tip and the center of the grid where the electric field is computed [with coordinates (0,0,0) nm] that would correspond to the molecule center. When the tip–molecule distance increases from 0.4 to 0.9 nm

[blue to red line, Fig. 7(a)], the x component of the total field, which is along with the y component, responsible for the coupling with the molecular transition dipoles, decreases in amplitude as expected. Moreover, the corresponding peak broadens, which means that the local field becomes less confined in the cavity.
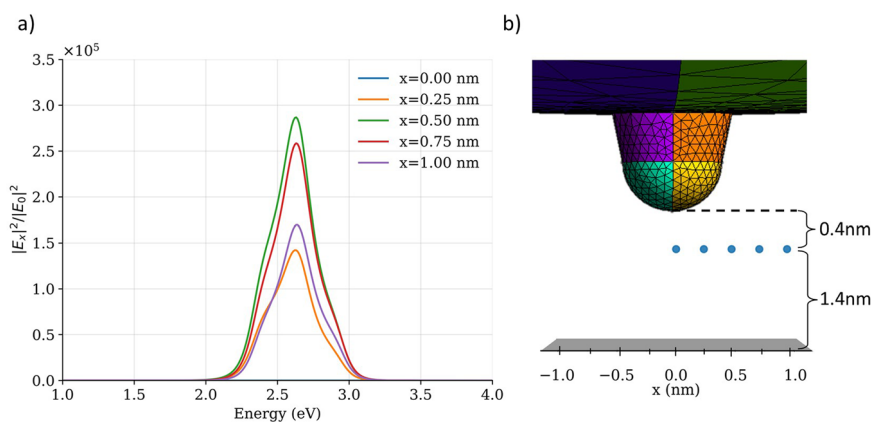
FIG. 6. (a) Local field enhancement as a function of frequency for different grid points along the x axis as shown in panel (b). The symmetrical results were obtained for the y component. The blue line has very low intensity, and it lies on the x axis. (b) Schematic representation of the simulation setup used to obtain the results shown in panel (a); the y coordinate is always set to 0.0 nm as in the top plot of Fig. 5(a).
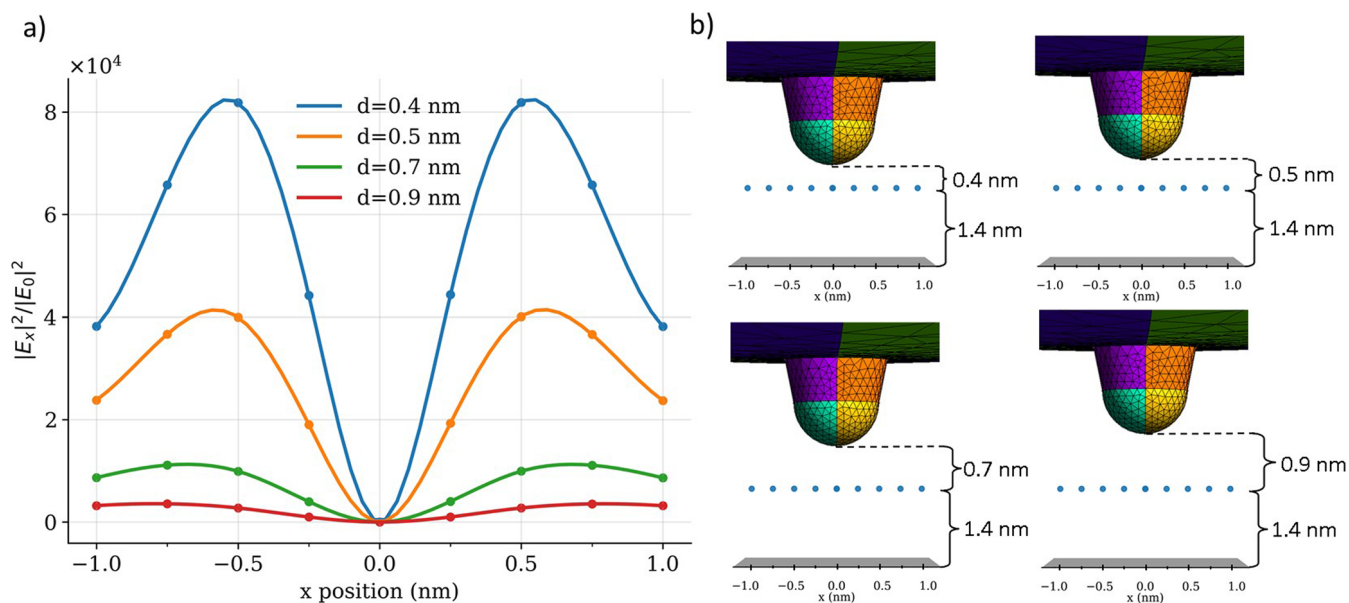
FIG. 7. (a) Square modulus of the x component of the total field over the incoming electric field along x for different tip–molecule distances (colored lines). The symmetrical results were obtained for the y component along the y-displacement (the dots represent the calculated values, while the corresponding curves were obtained through cubic interpolation). (b) Schematic representation of the simulation setup used to obtain the results shown in panel (a).

E. Coupling with the zinc phthalocyanine molecule

So far, we have focused our attention on the electromagnetic problem of the bare nanostructures without considering any molecular species. In order to simulate the electromagnetic effects due to the presence of the nanostructure on the photophysical properties of the zinc phthalocyanine molecule, we solved the frequency-dependent BEM equation [see Eq. (1)] where the perturbation term $\mathbf{V}(\omega)$ represents the transition potential associated with the molecular excited state of interest. The potential has been computed at the quantum mechanical level assuming the ground state electron density of the molecule polarized by the mutual interaction with the metallic nanoparticle. In particular, for this molecule, the first and second excited states are degenerate, so the contribution to photoluminescence (and also radiative and non-radiative decay rates) due to both excited states has been considered. We first present the simulated "photoluminescence quantities" that are necessary to compute the TEPL map, and then, we directly compare the results obtained with/without the self-consistent equilibration of the molecular states with the nanostructures.

1. Photoluminescence quantities

Using Eqs. (9)–(14), the corresponding radiative and non-radiative decay rates have been evaluated, allowing us to observe the effects of the metallic nanostructure on the excited state properties of the molecule, as shown in Fig. 8. It turned out that when the tip–molecule distance is set to 0.4 nm and the tip is above one of the molecular lobes (x = 0.5 nm and y = 0.5 nm), both stronger absorption [Fig. 8(a)] and a net reduction of the quantum yield [Fig. 8(b)] with respect to the vacuum value (0.2, as stated in Sec. II B) are observed. The enhancement in absorption means

more molecules in excited states, which more than compensate for the decreased quantum yield, overall resulting in a strong photoluminescence enhancement of the single molecule when the plasmon oscillation is efficiently able to couple with the molecular transition dipoles (see Fig. 9). It is worth noting that the images reported in Figs. 8 and 9 resemble the molecular structure, displaying stronger interactions at the position of the lobes. The possibility of retaining such "resolution" is made possible by the use of the transition potentials as the source of the perturbation instead of a point dipole, which encode the information related to the molecular shape. Moreover, we also noticed that the non-radiative decay rate due to the molecule–metal interaction [see Eq. (14)] is faster without the presence of the tip when the molecule is alone above the substrate, and taking this into account, the TEPL ratio (with respect to the tip-free setup) is predicted to be ≈10[8], in agreement with the experimental estimate of Yang et al.[24] The computed linewidths in Fig. 8(d) provide an interval of variation that is essentially the same as in the experiment[24] (around 2.5–3 meV). However, the experiment features an additional, apparently spatially independent, contribution of around 8 meV. This additional value is much in line with the vibronic broadening we estimate for the emission process, as shown in Fig. S6 (supplementary material), which is ≈9 meV (FWHM) and that we did not included in Fig. 8(d).

2. Molecule SCF equilibration with nanostructures

Additionally, we investigated the possible effects of the molecular electron density relaxation due to the presence of the nanostructure on the TEPL values. In order to do so, we computed self-consistently the equilibrated molecular electron density for both the ground state (which may affect the absorption rate) and the excited state (which may affect the emission rate), obtaining the results
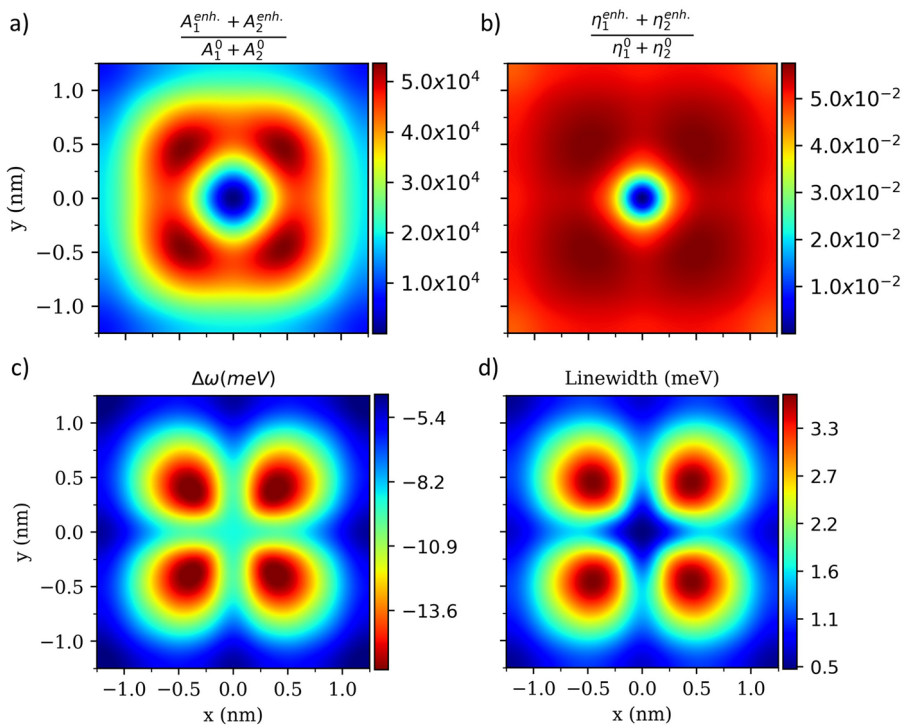
FIG. 8. 2D-maps on a 1.25×1.25 nm^2 grid of (a) the enhanced absorption rate, (b) quantum efficiency, (c) spectral shift, and (d) non-radiative decay rate due to the molecule–metal interaction [see Eqs. (10)–(15)]. The position of the molecular center is $x = y = 0.0$ nm. Panels (c) and (d) were obtained considering the contribution coming from each state weighted by the corresponding PL intensity on the same grid point.

shown in Fig. 9(b). By comparing the TEPL images in Figs. 9(a) and 9(b), it can be seen that at the position of the molecular lobes, where the tip–molecule interaction is stronger, only a negligible difference of $\approx 0.1 \times 10^3$ (over a value of $\approx 6 \times 10^3$) in the TEPL ratios is observed, and there is no significant change in the energy of the two isoenergetic excited states with respect to the center of the grid, where the tip–molecule interaction is much weaker. The outcomes clearly point out that the molecular electron density
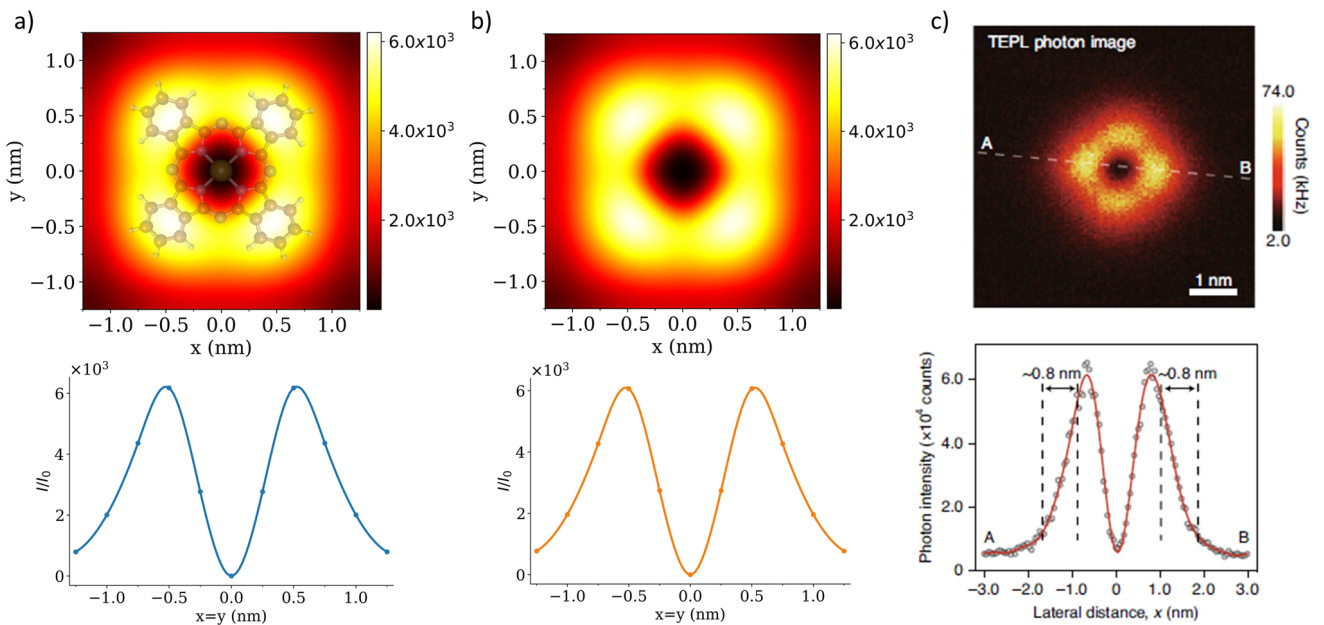
FIG. 9. (a) Tip-enhanced photoluminescence (TEPL) ratio simulated using Eq. (9) (Sec. II) on a 1.25×1.25 nm^2 grid (top) and along the main diagonal of the grid (bottom), without considering any electron density relaxation due to the nanostructure. I_0 is the computed vacuum emission obtained setting η^0 to the experimental value of 0.2 (see Sec. II B). (b) The same simulations obtained considering the self-consistent electron density relaxation for both ground and excited states. (c) Previously reported experimental results on the same system.[24]

equilibration with the nano-object does not strongly influence the computed photoluminescence intensity and thus, at least for this molecule in the applied conditions, can be disregarded. In light of these results, the approximation of ignoring the molecular electron density equilibration with the nanostructures[24] is justified.

V. CONCLUSIONS

Inspired by recent experimental work,[24] we investigated the photophysical properties of a single zinc phthalocyanine molecule underneath the atomistic protrusion of an STM-like silver nano-structure by means of a suitable PCM-NP description of the nanoparticle and full quantum mechanical treatment of the molecule. We found out that the geometrical features of the atomistic protrusion at the tip apex strongly influence the PL measurements, in particular varying the frequency of the plasmon enhanced local field maximum. This result suggests that the geometrical features of the nano-tip strongly influence the features of the picocavity and thus also the molecule–plasmon interaction strength. Therefore, in order to optimize the photoluminescence intensity, one needs to cleverly design the geometrical features of the nano-tip.

Moreover, concerning the theoretical side, we pointed out that the photoluminescence results are sensitive to the measurement uncertainty of the dielectric function, and for this reason, different experimental dielectric functions for the metal of interest have to be considered. Therefore, discrepancies between theoretical and experimental results on photoluminescence intensity can also depend on the choice of the dielectric function model. In addition, we illustrated that additional attention has to be paid to the adopted theoretical model because fictitious charge transfer excitation between different metallic nanoparticles within the same system might come up, as a result of numerical issues in the calculations. Additionally, we remark that the electronic polarization interaction with the tip is negligible. To conclude, taking into account each detail previously mentioned, theoretical simulations might be able to predict and support the state-of-the-art experiments, thus paving the way for studying plasmon–molecule interactions at the submolecular level, as well as to design new experiments.

SUPPLEMENTARY MATERIAL

See the supplementary material for additional details and numerical tests concerning charge conservation analysis, influence of the gas-phase radiative quantum efficiency η^0 on the TEPL results, basis set numerical test, ground and excited state optimized structures of zinc phthalocyanine, simulated vibrationally resolved emission spectrum of zinc phthalocyanine, detailed contribution of $\vec{\mu}^{met}$ and $\vec{\mu}^{ind}$ to Fig. 8(a), comparison between enhanced absorption rates and enhanced radiative decay rates, and influence of a single NaCl monolayer on the TEPL results.

ACKNOWLEDGMENTS

AUTHOR DECLARATIONS

Conflict of Interest

The authors have no conflicts to disclose.

DATA AVAILABILITY

The data that support the findings of this study are available within the article and its supplementary material.

REFERENCES

[1] V. Giannini, A. I. Fernández-Domínguez, S. C. Heck, and S. A. Maier, Chem. Rev. **111**, 3888 (2011).

[2] D. K. Gramotnev and S. I. Bozhevolnyi, Nat. Photonics **4**, 83 (2010).

[3] L. Xu, F. Li, Y. Liu, F. Yao, and S. Liu, Appl. Sci. **9**, 861 (2019).

[4] A. B. Taylor and P. Zijlstra, ACS Sens. **2**, 1103 (2017).

[5] A. B. Zrimsek, N. Chiang, M. Mattei, S. Zaleski, M. O. McAnally, C. T. Chapman, A.-I. Henry, G. C. Schatz, and R. P. Van Duyne, Chem. Rev. **117**, 7583 (2017).

[6] Z. Liu, S.-Y. Ding, Z.-B. Chen, X. Wang, J.-H. Tian, J. R. Anema, X.-S. Zhou, D.-Y. Wu, B.-W. Mao, X. Xu et al., Nat. Commun. **2**, 305 (2011).

[7] J. Lee, K. T. Crampton, N. Tallarida, and V. A. Apkarian, Nature **568**, 78 (2019).

[8] F. Benz, M. K. Schmidt, A. Dreismann, R. Chikkaraddy, Y. Zhang, A. Demetriadou, C. Carnegie, H. Ohadi, B. De Nijs, R. Esteban et al., Science **354**, 726 (2016).

[9] H. Imada, K. Miwa, M. Imai-Imada, S. Kawahara, K. Kimura, and Y. Kim, Phys. Rev. Lett. **119**, 013901 (2017).

[10] K. Kimura, K. Miwa, H. Imada, M. Imai-Imada, S. Kawahara, J. Takeya, M. Kawai, M. Galperin, and Y. Kim, Nature **570**, 210 (2019).

[11] F. Mohn, L. Gross, N. Moll, and G. Meyer, Nat. Nanotechnol. **7**, 227 (2012).

[12] C. Chen, P. Chu, C. A. Bobisch, D. L. Mills, and W. Ho, Phys. Rev. Lett. **105**, 217402 (2010).

[13] N. Jiang, D. Kurouski, E. A. Pozzi, N. Chiang, M. C. Hersam, and R. P. Van Duyne, Chem. Phys. Lett. **659**, 16 (2016).

[14] J. Langer, D. Jimenez de Aberasturi, J. Aizpurua, R. A. Alvarez-Puebla, B. Auguié, J. J. Baumberg, G. C. Bazan, S. E. J. Bell, A. Boisen, A. G. Brolo et al., ACS Nano **14**, 28 (2019).

[15] N. Chiang, N. Jiang, D. V. Chulhai, E. A. Pozzi, M. C. Hersam, L. Jensen, T. Seideman, and R. P. Van Duyne, Nano Lett. **15**, 4114 (2015).

[16] P. Liu, X. Chen, H. Ye, and L. Jensen, ACS Nano **13**, 9342 (2019).

[17] M. D. Sonntag, J. M. Klingsporn, A. B. Zrimsek, B. Sharma, L. K. Ruvuna, and R. P. Van Duyne, Chem. Soc. Rev. **43**, 1230 (2014).

[18] P. Liu, D. V. Chulhai, and L. Jensen, ACS Nano **11**, 5094 (2017).

[19] M. D. Sonntag, J. M. Klingsporn, L. K. Garibay, J. M. Roberts, J. A. Dieringer, T. Seideman, K. A. Scheidt, L. Jensen, G. C. Schatz, and R. P. Van Duyne, J. Phys. Chem. C **116**, 478 (2012).

[20] K. Fiederling, M. Abasifard, M. Richter, V. Deckert, S. Gräfe, and S. Kupfer, Nanoscale **12**, 6346 (2020).

[21] F. Latorre, S. Kupfer, T. Bocklitz, D. Kinzel, S. Trautmann, S. Gräfe, and V. Deckert, Nanoscale **8**, 10229 (2016).

[22] W. Zhu, R. Esteban, A. G. Borisov, J. J. Baumberg, P. Nordlander, H. J. Lezec, J. Aizpurua, and K. B. Crozier, Nat. Commun. **7**, 11495 (2016).

[23] M. Schnell, A. García-Etxarri, A. J. Huber, K. Crozier, J. Aizpurua, and R. Hillenbrand, Nat. Photonics **3**, 287 (2009).

[24]B. Yang, G. Chen, A. Ghafoor, Y. Zhang, Y. Zhang, Y. Zhang, Y. Luo, J. Yang, V. Sandoghdar, J. Aizpurua, Z. Dong, and J. G. Hou, Nat. Photonics **14**, 693–699 (2020).

[25]W. Su, N. Kumar, S. Mignuzzi, J. Crain, and D. Roy, Nanoscale **8**, 10564 (2016).

[26]T. Kumagai, Nat. Photonics **14**, 653 (2020).

[27]K.-Q. Lin, J. Yi, J.-H. Zhong, S. Hu, B.-J. Liu, J.-Y. Liu, C. Zong, Z.-C. Lei, X. Wang, J. Aizpurua *et al.*, Nat. Commun. **8**, 14891 (2017).

[28]K. L. Kelly, E. Coronado, L. L. Zhao, and G. C. Schatz, J. Phys. Chem. B **107**, 668–677 (2003).

[29]N. A. Mortensen, S. Raza, M. Wubs, T. Søndergaard, and S. I. Bozhevolnyi, Nat. Commun. **5**, 3809 (2014).

[30]G. Mie, Ann. Phys. **330**, 377 (1908).

[31]P. Gonçalves, T. Christensen, N. Rivera, A.-P. Jauho, N. A. Mortensen, and M. Soljačić, Nat. Commun. **11**, 366 (2020).

[32]W. H. Yang, G. C. Schatz, and R. P. Van Duyne, J. Chem. Phys. **103**, 869 (1995).

[33]R. Fuchs, Phys. Rev. B **11**, 1732 (1975).

[34]F. J. García de Abajo and J. Aizpurua, Phys. Rev. B **56**, 15873 (1997).

[35]S. Corni and J. Tomasi, J. Chem. Phys. **114**, 3739 (2001).

[36]F. J. García de Abajo and A. Howie, Phys. Rev. B **65**, 115418 (2002).

[37]U. Hohenester and A. Trügler, Comput. Phys. Commun. **183**, 370 (2012); arXiv:1109.5783.

[38]F. Hao and P. Nordlander, Chem. Phys. Lett. **446**, 115 (2007).

[39]K. Lopata and D. Neuhauser, J. Chem. Phys. **130**, 104707 (2009).

[40]H. Chen, J. M. McMahon, M. A. Ratner, and G. C. Schatz, J. Phys. Chem. C **114**, 14384 (2010).

[41]A. Sakko, T. P. Rossi, and R. M. Nieminen, J. Phys.: Condens. Matter **26**, 315013 (2014).

[42]T. Neuman, R. Esteban, D. Casanova, F. J. García-Vidal, and J. Aizpurua, Nano Lett. **18**, 2358 (2018).

[43]F. Aguilar-Galindo, S. Díaz-Tendero, and A. G. Borisov, J. Phys. Chem. C **123**, 4446 (2019).

[44]Y. Zhang, Z.-C. Dong, and J. Aizpurua, J. Phys. Chem. C **124**, 4674 (2020).

[45]S. M. Morton and L. Jensen, J. Chem. Phys. **133**, 074103 (2010).

[46]V. Arcisauskaite, J. Kongsted, T. Hansen, and K. V. Mikkelsen, Chem. Phys. Lett. **470**, 285 (2009).

[47]J. Fregoni, T. S. Haugland, S. Pipolo, T. Giovannini, H. Koch, and S. Corni, Nano Lett. **21**, 6664 (2021).

[48]T. P. Rossi, T. Shegai, P. Erhart, and T. J. Antosiewicz, Nat. Commun. **10**, 3336 (2019).

[49]J. Tomasi, B. Mennucci, and R. Cammi, Chem. Rev. **105**, 2999 (2005).

[50]O. Andreussi, S. Corni, B. Mennucci, and J. Tomasi, J. Chem. Phys. **121**, 10190 (2004).

[51]B. Mennucci and S. Corni, Nat. Rev. Chem. **3**, 315 (2019).

[52]S. Corni and J. Tomasi, J. Chem. Phys. **118**, 6481 (2003).

[53]M. Caricato, O. Andreussi, and S. Corni, J. Phys. Chem. B **110**, 16652 (2006).

[54]S. Vukovic, S. Corni, and B. Mennucci, J. Phys. Chem. C **113**, 121 (2009).

[55]S. Pipolo and S. Corni, J. Phys. Chem. C **120**, 28774 (2016).

[56]J. R. Lakowicz, C. D. Geddes, I. Gryczynski, J. Malicka, Z. Gryczynski, K. Aslan, J. Lukomska, E. Matveeva, J. Zhang, R. Badugu, and J. Huang, J. Fluoresc. **14**, 425 (2004).

[57]J. R. Lakowicz, Anal. Biochem. **337**, 171 (2005).

[58]J. R. Lakowicz, K. Ray, M. Chowdhury, H. Szmacinski, Y. Fu, J. Zhang, and K. Nowaczyk, Analyst **133**, 1308 (2008).

[59]T. V. Shubina, A. A. Toropov, V. N. Jmerik, D. I. Kuritsyn, L. V. Gavrilenko, Z. F. Krasil'nik, T. Araki, Y. Nanishi, B. Gil, A. O. Govorov, and S. V. Ivanov, Phys. Rev. B **82**, 073304 (2010).

[60]S. M. Morton, D. W. Silverstein, and L. Jensen, Chem. Rev. **111**, 3962 (2011).

[61]A. J. Haes, C. L. Haynes, A. D. McFarland, G. C. Schatz, R. P. Van Duyne, and S. Zou, MRS Bull. **30**, 368 (2005).

[62]P. Anger, P. Bharadwaj, and L. Novotny, Phys. Rev. Lett. **96**, 113002 (2006).

[63]B. L. Darby, B. Auguié, M. Meyer, A. E. Pantoja, and E. C. Le Ru, Nat. Photonics **10**, 40 (2016).

[64]M. Pelton, Nat. Photonics **9**, 427 (2015).

[65]F. Della Sala and S. D'Agostino, *Handbook of Molecular Plasmonics* (CRC Press, 2013).

[66]S. Corni and J. Tomasi, J. Chem. Phys. **117**, 7266 (2002).

[67]P. Johansson, H. Xu, and M. Käll, Phys. Rev. B **72**, 035427 (2005).

[68]A. Ogunsipe, D. Maree, and T. Nyokong, J. Mol. Struct. **650**, 131 (2003).

[69]C. Geuzaine and J.-F. Remacle, Int. J. Numer. Methods Eng. **79**, 1309 (2009).

[70]A. D. Rakić, A. B. Djurišić, J. M. Elazar, and M. L. Majewski, Appl. Opt. **37**, 5271 (1998).

[71]E. Palik, *Handbook of Optical Constants of Solids* (Academic Press, Cambridge, MA, 1998).

[72]M. J. Frisch, G. W. Trucks, H. B. Schlegel, G. E. Scuseria, M. A. Robb, J. R. Cheeseman, G. Scalmani, V. Barone, G. A. Petersson, H. Nakatsuji, X. Li, M. Caricato, A. V. Marenich, J. Bloino, B. G. Janesko, R. Gomperts, B. Mennucci, H. P. Hratchian, J. V. Ortiz, A. F. Izmaylov, J. L. Sonnenberg, D. Williams Young, F. Ding, F. Lipparini, F. Egidi, J. Goings, B. Peng, A. Petrone, T. Henderson, D. Ranasinghe, V. G. Zakrzewski, J. Gao, N. Rega, G. Zheng, W. Liang, M. Hada, M. Ehara, K. Toyota, R. Fukuda, J. Hasegawa, M. Ishida, T. Nakajima, Y. Honda, O. Kitao, H. Nakai, T. Vreven, K. Throssell, J. A. Montgomery, Jr., J. E. Peralta, F. Ogliaro, M. J. Bearpark, J. J. Heyd, E. N. Brothers, K. N. Kudin, V. N. Staroverov, T. A. Keith, R. Kobayashi, J. Normand, K. Raghavachari, A. P. Rendell, J. C. Burant, S. S. Iyengar, J. Tomasi, M. Cossi, J. M. Millam, M. Klene, C. Adamo, R. Cammi, J. W. Ochterski, R. L. Martin, K. Morokuma, O. Farkas, J. B. Foresman, and D. J. Fox, Gaussian 16, Revision B.01, Gaussian, Inc., Wallingford, CT, 2016.

[73]F. Santoro, R. Improta, A. Lami, J. Bloino, and V. Barone, J. Chem. Phys. **126**, 084509 (2007).

[74]J. Savolainen, D. van der Linden, N. Dijkhuizen, and J. L. Herek, J. Photochem. Photobiol., A **196**, 99 (2008).

[75]C. Dykstra, G. Frenking, K. Kim, and G. Scuseria, *Theory and Applications of Computational Chemistry: The First Forty Years* (Elsevier, 2011).

[76]M. W. Schmidt, K. K. Baldridge, J. A. Boatz, S. T. Elbert, M. S. Gordon, J. H. Jensen, S. Koseki, N. Matsunaga, K. A. Nguyen, S. Su *et al.*, J. Comput. Chem. **14**, 1347 (1993).

[77]P. B. Johnson and R. W. Christy, Phys. Rev. B **6**, 4370 (1972).

56

Role of metal-nanoparticle features on tip-enhanced photoluminescence of single molecules

Marco Romanelli[a], Giulia Dall'Osto[a] and Stefano Corni[ab‡]

[a] *Department of Chemical Sciences, University of Padova, via Marzolo 1, Padova, Italy*
[b] *CNR Institute of Nanoscience, via Campi 213/A, Modena, Italy*

Contents

- Charge conservation and numerical issues (Figures S1-S2).

- Influence of the gas-phase radiative quantum efficiency η^0 on the TEPL results (Figure S3).

- Basis set numerical test (Figure S4).

- Ground and Excited state optimized structures of Zinc-phthalocyanine (Figure S5).

- Simulated vibrationally resolved emission spectrum of Zinc-phthalocyanine (Figure S6).

- Detailed contribution of $\overrightarrow{\mu}^{met}$ and $\overrightarrow{\mu}^{ind}$ to the panel a) of Figure 8 main text (Figure S7).

- between enhanced absorption rates and enhanced radiative decay rates (Figure S8).

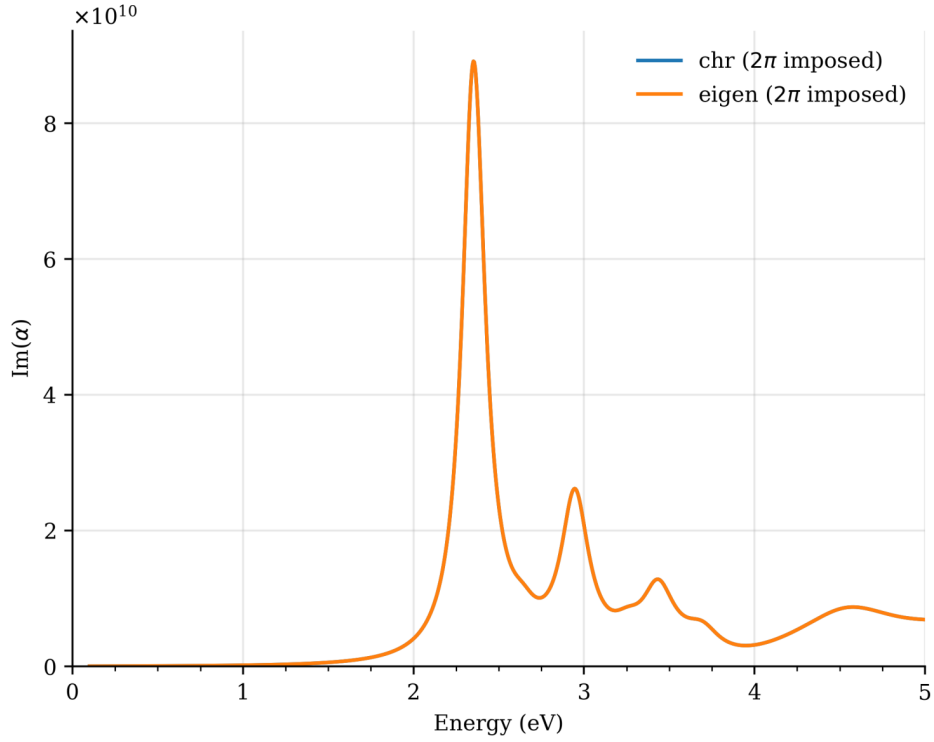- Influence of a single NaCl monolayer on the TEPL results (Figure S9).

1
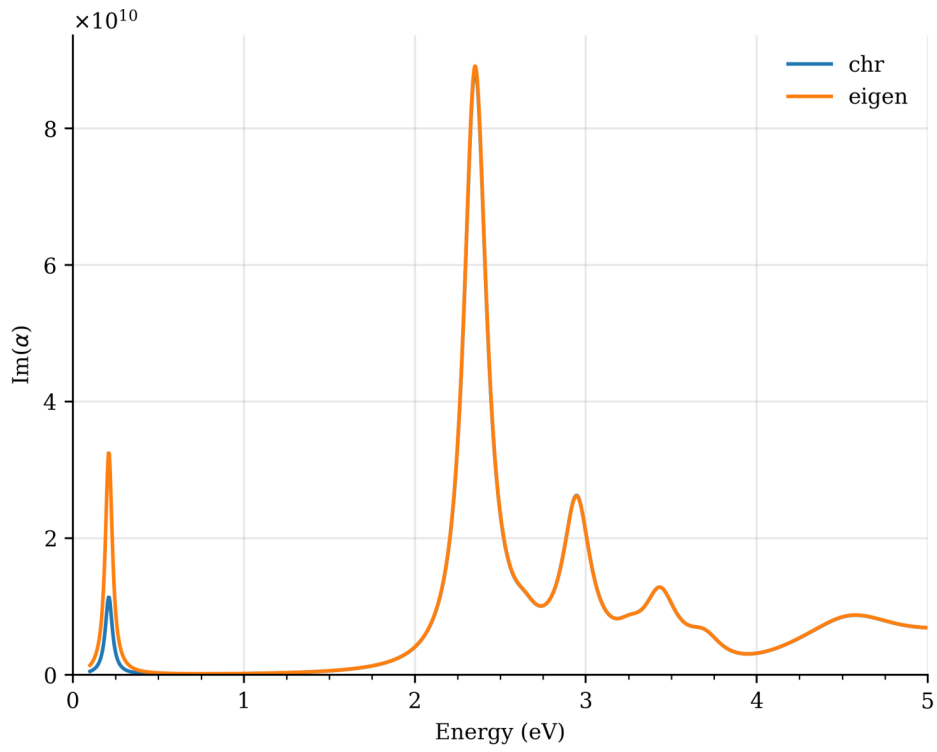
Figure S1: Absorption spectra of the nanostructure reported in Fig.1 (main text) computed by using the two different approaches mentioned in section II-A (main text) for ensuring 'charge conservation'. The a-posteriori normalization is the blue curve, whereas the normalization through the eigenvectors' coefficients is the orange one. The main difference between the two methods can be observed only at low energies (less than 1 eV), where the fictitious charge-transfer peak appears.

2

Figure S2: Absorption spectra of the nanostructure reported in FIG.1 (main text) computed by using the two different approaches mentioned in section II-A for ensuring 'charge conservation' and simultaneously forcing the two lowest eigenvalues of DA exactly to -2π (see equation 3, main text). The plasmon eigenmodes associated with these two eigenvalues are responsible for the charge-transfer peak that appears at low energies (FIG. S1). Indeed, if these two eigenvalues are exactly set to -2π their contribution to the induced charges should vanish (eq.3, main text). Although, in this figure, the fictitious peak is no longer evident in both methods,the total sum of the surface charges for the separate structures ,tip and substrate respectively, is closer to zero in the 'a posteriori' approach, which yields a more realistic scenario.
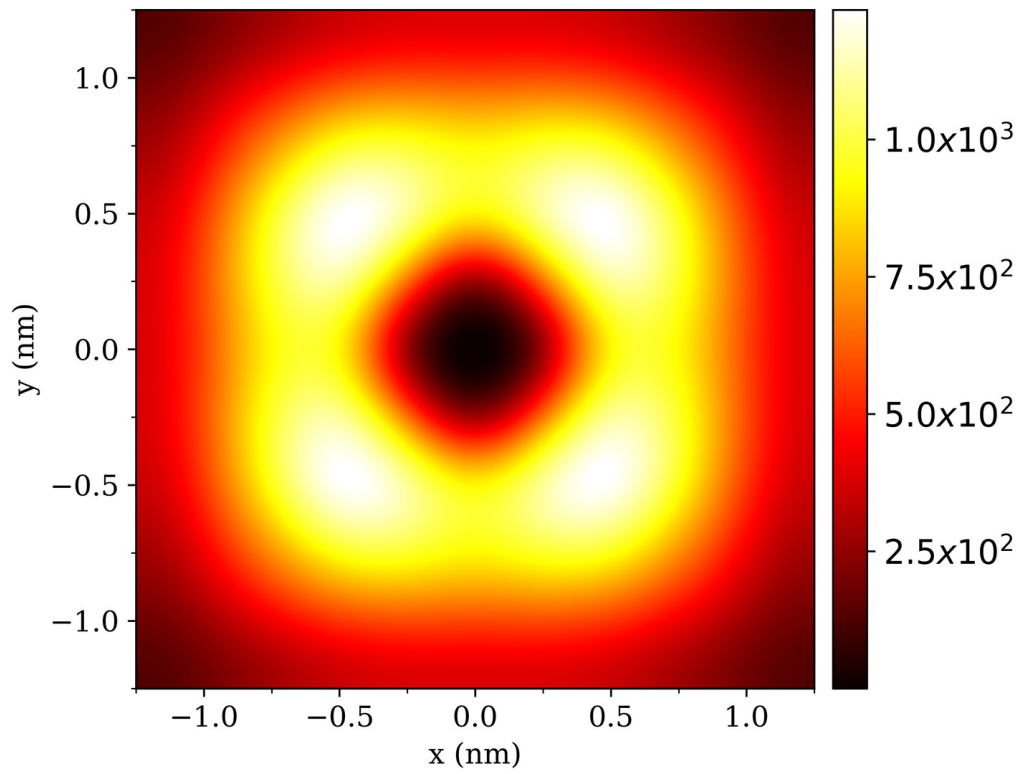
Figure S3: Tip-Enhanced Photo-luminescence (TEPL) ratio simulated using equation 5 (Section II-B, main text) on a 1.25 nm × 1.25 nm grid considering η^0 equals to 1 (i.e. unitary radiative quantum efficiency in vacuum).
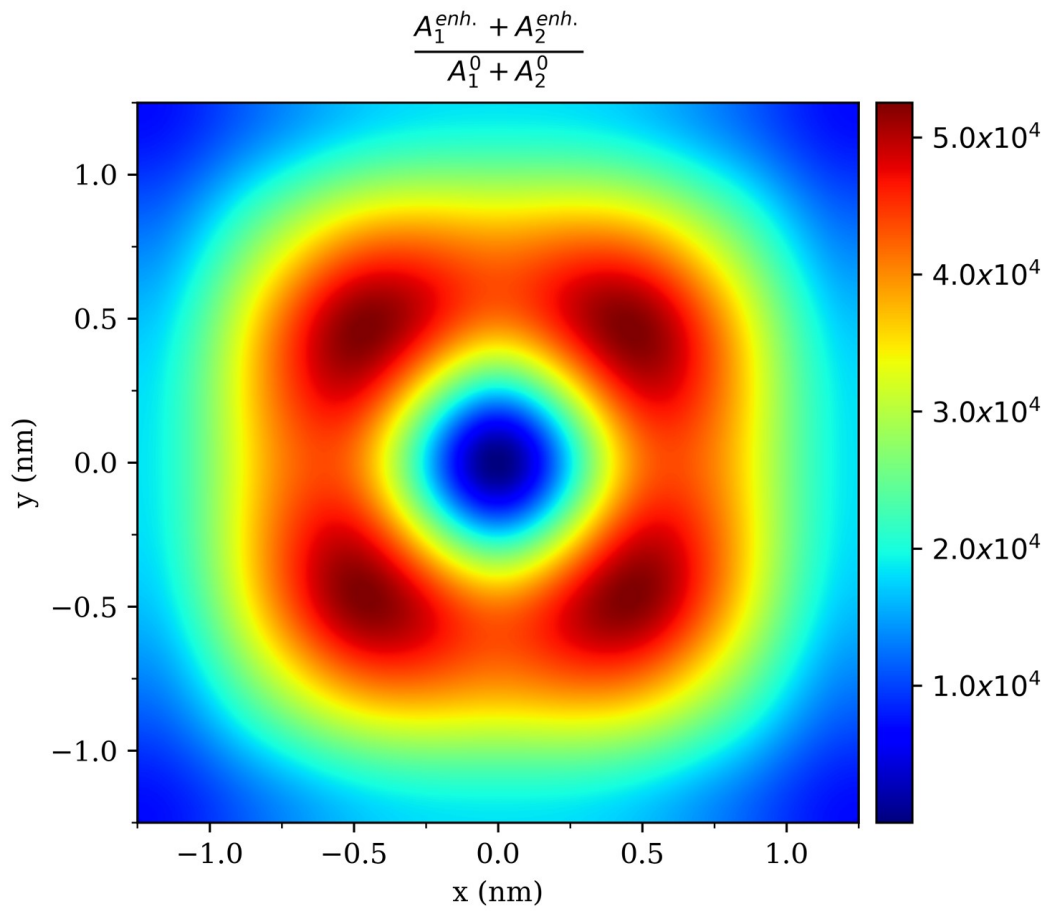
Figure S4: Enhanced absorption rate simulated using equation 10 (Section II-B, main text) on a 1.25 nm × 1.25 nm grid considering the TZP basis-set as implemented in GAMESS[1,2]. By comparing these data with Figure 8a) main text, it can be seen that the improvement of the basis set does not change the results.
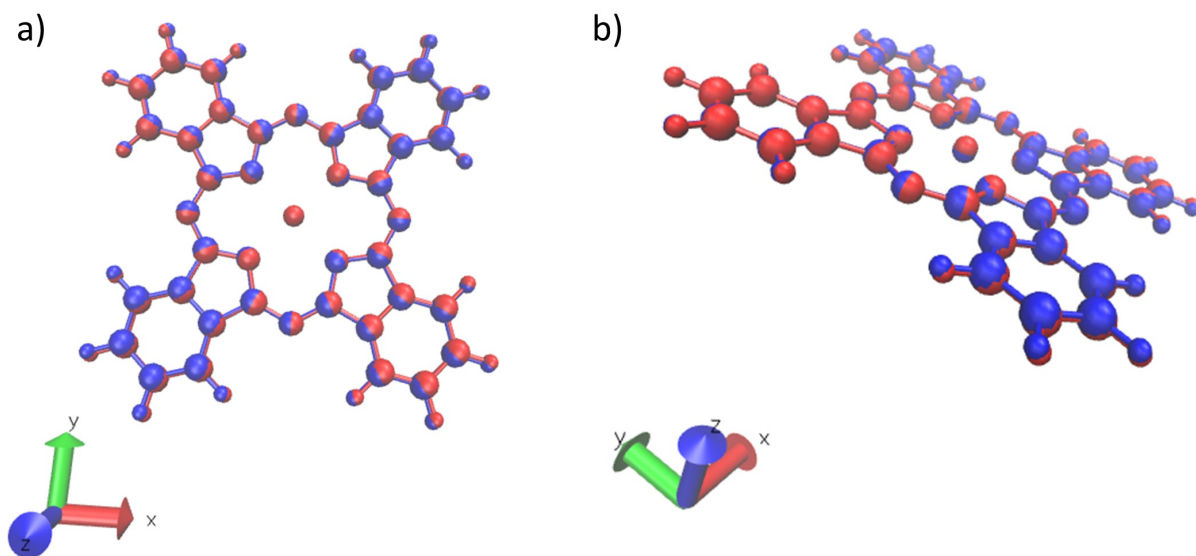
Figure S5: Superposition of ground and first excited state optimized geometries of Zinc-phthalocyanine, a) top view, b) side view.
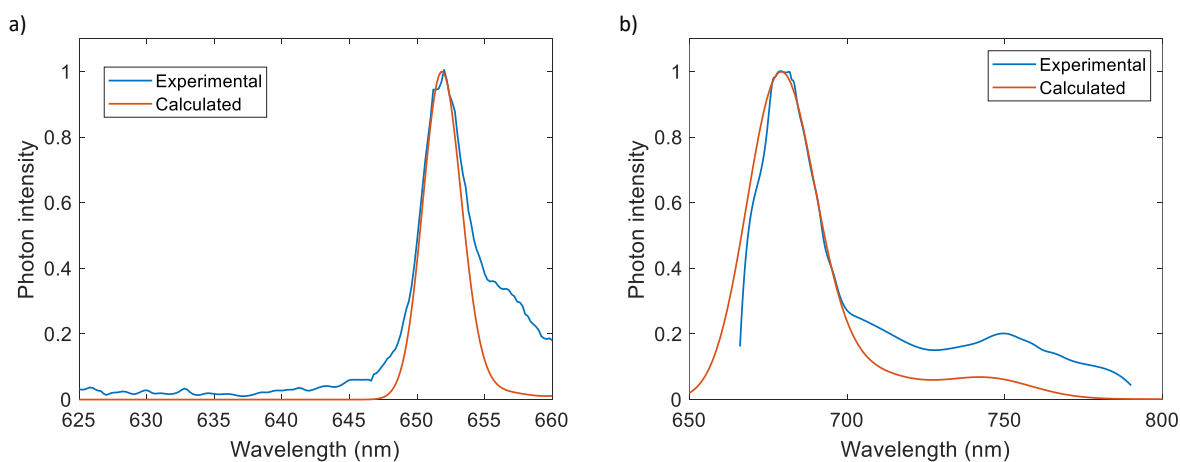
Figure S6: Comparison between computed vibrational resolved emission spectrum and experimental emission spectrum in vacuum when the molecule is close to the silver nanostructures where the computed one is red-shifted by 20.8 nm (panel a)[3] and in DMSO where the computed one is red-shifted by 49.6 nm (panel b).[4] It has to be noticed that the wavelength scale considered is shorter in panel (a) than in panel (b) and to compare the spectra, two different broadening have been considered to obtain the convoluted spectrum from emission transition calculations. In panel (a) the computed spectrum does not reproduce the shoulder detected experimentally at ≈ 657 nm, therefore it could be a result of the interaction between the molecule and the substrate rather than the effect of the presence of a vibronic structure, as mentioned in the experimental work.[3] On the other hand, the calculated spectrum is in good agreement with experimental spectrum in DMSO (panel b), although the shoulder at 700 nm is underestimated.
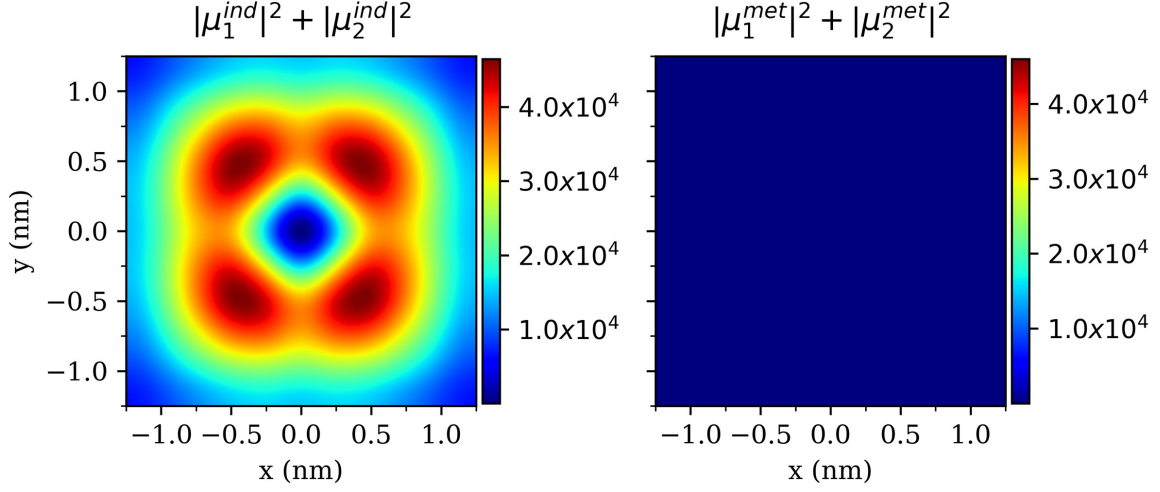
6

Figure S7: Detailed contribution of $\vec{\mu}^{ind}$ (left) and $\vec{\mu}^{met}$ (right) to the panel a) of Figure 8, main text. The contribution coming from the metallic response ($|\vec{\mu}^{ind}|^2$) is predominant, the molecular part($|\vec{\mu}^{met}|^2$) is ≈ 3 orders of magnitude lower. We also note that $\vec{\mu}^{met}$, which is the molecular transition dipole in the presence of the nanostructure, has been calculated by including in the typical TDDFT equations the following polarization term $K_{st,uv}^{pol}(\omega) = \sum_i q_\omega(s_i, [\psi_s^*\psi_t]) \cdot V(s_i, [\psi_u^*\psi_v])$, where $V(s_i, [\psi_u^*\psi_v])$ is the electrostatic potential evaluated at the i-th tessera due to the charge distribution $\psi_u^*\psi_v$ with ψ_u and ψ_v being molecular orbitals (more details can be found in[5,6]). The corresponding Casida response equations, that now account for the mutual molecule-metal polarization, have to be solved self-consistently as the matrix elements depend themselves on the eigenvalues that have to be found.
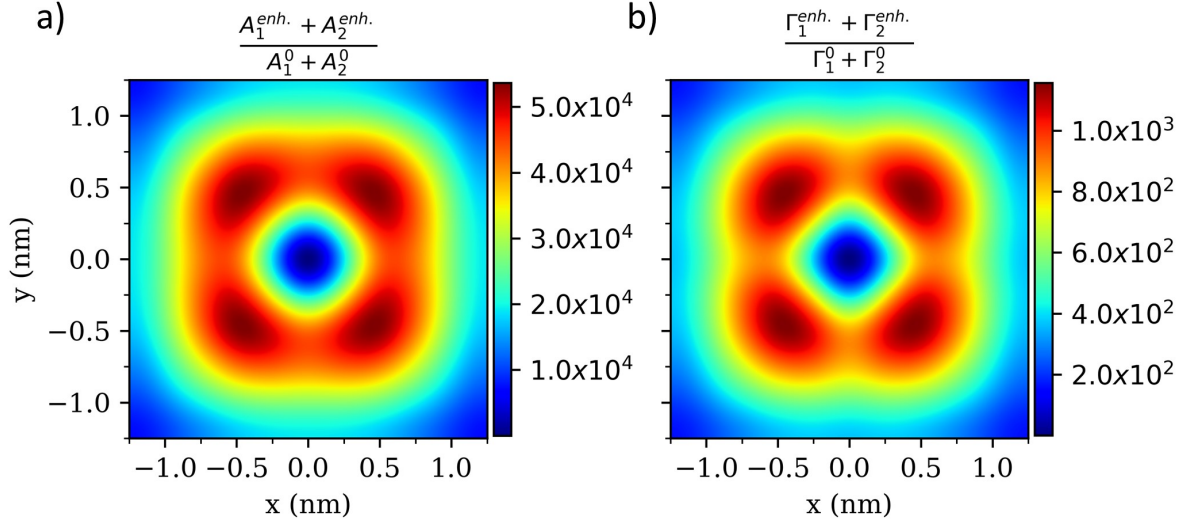

Figure S8: Comparison between enhanced absorption rate a) computed according to eq.10 (main text) and enhanced radiative decay rate b) computed according to eq.13 (main text). As stated in the main manuscript on page 7, even if the two quantities are analogous, they are calculated at different frequencies (that of the absorption and that of the emission, respectively) and for different transition densities (that at the ground state geometry a) and that at the excited state geometry b).
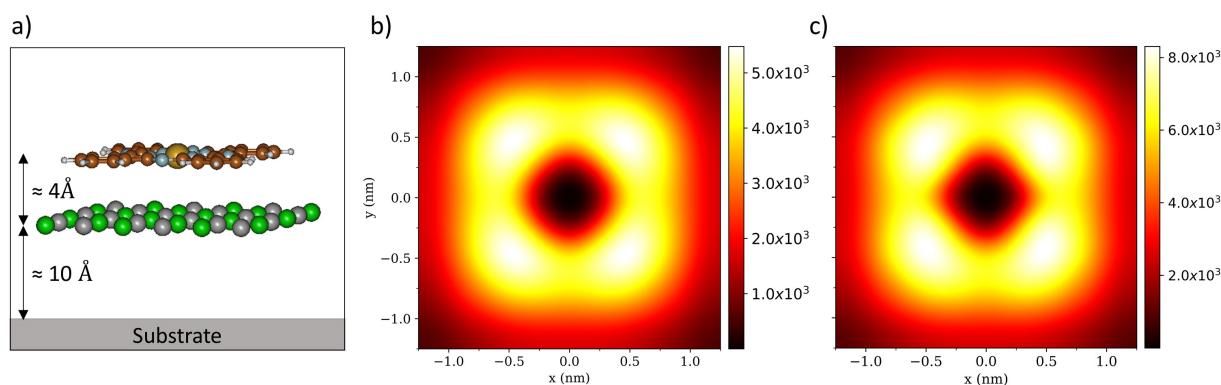
Figure S9: a) Scheme of the computational setup used to assess the influence of the NaCl layer on the simulated TEPL results. The single monolayer was directly included in the QM region fully treated at B3LYP/6-31g. The STM-like tip is not shown for simplicity, but it is always there, 0.4 nm above the molecular plane. The ground-state optimized geometry was considered both for the absorption and emission properties to save computational time, but as the excited-state minimum is very similar to the GS geometry (Figure S5), similar results are expected even considering the S_1 relaxed structure for the luminescence quantities. b) Simulated TEPL map with the presence of the NaCl single monolayer. c) Simulated TEPL map without the presence of the NaCl single monolayer. There is a fairly small quantitative difference in the TEPL intensity maxima between panels b) and c), but the overall result is qualitatively the same. In panel b) the intensity maximum is $\approx 5.5 \times 10^3$, whereas in panel c) it is $\approx 8.0 \times 10^3$.

References

[1] C. Dykstra, G. Frenking, K. Kim and G. Scuseria, *Theory and applications of computational chemistry: the first forty years*, Elsevier, 2011.

[2] M. W. Schmidt, K. K. Baldridge, J. A. Boatz, S. T. Elbert, M. S. Gordon, J. H. Jensen, S. Koseki, N. Matsunaga, K. A. Nguyen, S. Su *et al.*, *Journal of computational chemistry*, 1993, **14**, 1347–1363.

[3] B. Yang, G. Chen, A. Ghafoor, Y. Zhang, Y. Zhang, Y. Zhang, Y. Luo, J. Yang, V. Sandoghdar, J. Aizpurua, Z. Dong and J. G. Hou, *Nature Photonics*, 2020, **14**, 693–699.

[4] J. Savolainen, D. van der Linden, N. Dijkhuizena and J. L. Herek, *Journal of Photochemistry and Photobiology A: Chemistry*, 2008, **196**, 99–105.

[5] S. Corni and J. Tomasi, *The J. Chem. Phys.*, 2002, **117**, 7266.

[6] O. Andreussi, S. Corni, B. Mennucci and J. Tomasi, *J. Chem. Phys.*, 2004, **121**, 10190–10202.

Chapter 3

Plasmonic nanosystems are known to be very versatile, and their use in the field of photocatalysis has showed promising results. In this chapter, a challenging application of the TD-BEM developed in chapter 1 is presented, which deals with the study of charge injection onto a CHO residue adsorbed on a rhodium nanocube when it is irradiated, favouring a carbon hydrogenation reaction. The idea arose from experimental evidence of the overwhelming preference for the formation of methane rather than carbon monoxide when the rhodium-catalysed hydrogenation of carbon dioxide is carried out in the presence of light.[66] An initial attempt at an explanation was made on the basis of DFT calculations, which showed the presence of antibonding orbitals in CHO residues capable of accepting hot electrons injected by plasmon decay. However, a full explanation was lacking. In this chapter, I report the results of the work aimed at rationalizing the mechanism involved in the process, as a draft written in close collaboration with Prof. Margherita Marsili (now at UniBO), Prof. Emanuele Coccia (UniTS) and Dr. Mirko Vanzan (now at UniMI).

To study the phenomenon in depth, a time-dependent approach combining the interaction between the molecule, the nanoparticle and the incident radiation is required. The rhodium nanocube used in the experiment has a side length of 37 nm, so a full quantum description of the system was not feasible, even though at least a partial quantum mechanics treatment was required to study the charge injection mechanism. Therefore, a multiscale quantum mechanics/molecular mechanics approach (QM /MM) was adopted, in which most of the nanocube is described at the classical level, while a small part of it attached to the CHO residue is treated at the

quantum level. Some preliminary considerations have been made about the interface that arises in accordance with the cut on the NP vertex, where the quantum and classical parts of the same NP communicate with each other.

TD-BEM developed in Chapter 1 was used to calculate the coefficient dynamics of the quantum system (19 rhodium atoms bound to CHO) near the rhodium nanocube with a missing vertex. The dynamics was calculated when the system is irradiated with an incident light pulse whose properties are representative of the experimental light. Finally, the change in projected density of states (PDOS) and its integral (representative of charge injection) were evaluated using a post-processing Fortran90 code.[67]

The credits for the coding of the post-processing tool as well as for the draft preparation are equally shared by Prof. Margherita Marsili, Prof. Emanuele Coccia, Dr. Mirko Vanzan and me. Most calculations of coefficients dynamics and post-processing were done by me and I also did the description of the QM /MM interface as preliminary work following the supervision of Prof. Marsili.

Photoinduced hole injection explains the reaction selectivity in CO$_2$ hydrogenation on Rh nanocube

Giulia Dall'Osto,[†] Margherita Marsili,[*,‡] Mirko Vanzan,[†,¶] Daniele Toffoli,[§] Mauro Stener,[§] Stefano Corni,[†,‖] and Emanuele Coccia[*,§]

†*Department of Chemical Sciences, University of Padova, via Marzolo 1, Padova, Italy, 35100*

‡*Department of Physics and Astronomy "Augusto Righi", University of Bologna, Viale Berti Pichat 6/2, Bologna, Italy, 40127*

¶*Department of Physics, University of Milan, Via Giovanni Celoria 16, Milano, Italy, 20133*

§*Department of Chemical and Pharmaceutical Sciences, University of Trieste, Via Licio Giorgieri 1, Trieste, Italy, 34127*

‖*CNR Institute of Nanoscience, via Campi 213/A, Modena, Italy, 41100*

E-mail: margherita.marsili@unibo.it; ecoccia@units.it

Abstract

Plasmonic-driven photocatalysis may lead to reaction selectivity that cannot be achieved otherwise. A fundamental role is played by hot carriers, i.e. electrons and holes generated upon plasmonic decay within the metal nanostructure that interact with molecular species. In the case of carbon dioxide reduction, it was experimentally shown how in presence of a rhodium nanocube the photo-induced process selectively

produces methane against carbon monoxide as opposed to the thermal reaction pathway. Understanding the elusive microscopic mechanism behind such kind of results is a key step to rational design of hot carrier reactions. By means of a state of the art multiscale modeling approach going beyond density functional theory description, here we show that selectivity in this prototypical reaction is due to hole injection from the rhodium nanoparticle to the reaction intermediate CHO, that enhances the reactivity.

1   Introduction

Light is well-known to be an eclectic reagent, catalyst and possible product in chemical reactions.[1–4] Its interaction with nanostructures has further expanded the possibility of using light to manipulate chemical systems with extremely high precision and accuracy and, in turn, could affect many relevant technological fields such as sensing, catalysis, renewable energy, communication, and medicine.[5–9] Among all possible processes appearing at these scales, the activation of the Localised Surface Plasmon Resonances (LSPR) is one of the most peculiar and in the past decades its theoretical comprehension already gave notable outcomes.[10–12] A particularly interesting and technologically relevant feature arising from the activation of the LSPR resides in the use of the energy released by its decay, a process has been recently investigated unveiling a host of potential applications.[13–16] This phenomenon can be briefly described through the following stages. From the activation of LSPR, the collective oscillation of the electronic cloud starts to dephase because of its natural damping (i.e., Landau damping), resulting in the formation of electron-hole pairs excitations that store the energy originally absorbed by the plasmon. Such non-equilibrium state of excited electrons and holes rapidly thermalises, resulting in a configuration where the carriers (electrons or holes) can be described through a Fermi-Dirac distribution proper for a higher temperature compared to the actual lattice temperature, as if the electronic system was heated up.[17] This configuration remains until the electron-phonon scattering transfers all the extra electron energy to the lattice and gets further dissipated via thermalisation to

room temperature.[18–21]

Mechanisms for hot-carrier production were studied in detail both experimentally and theoretically over the past years and the community agrees on the steps just described.[22–24] However, there are still uncertainties regarding the way those carriers can be exploited, especially in the field of photocatalysis.[25–29] Indeed, once created, the hot carriers may interact with other species attached to the metallic nanoparticle, like a solid semiconductor or a molecule, and this can be exploited to activate chemical reactions. To date, several groups were able to harness hot carriers to perform different reactions, usually with higher selectivity and rates as compared with their thermal counterpart. It is worth mentioning that some of these catalysed reactions, such as nitrogen fixation and water splitting have a remarkable application potential, especially considering the problems posed by global warming and climate change and many people believe plasmon-driven photocatalysis could play a role towards a green and sustainable future.[30–35]

In this framework, considering the dramatic impact that carbon dioxide have on our environment, a lot of work is nowadays devoted to control reactions that allow efficient CO_2 conversion to methane or other short-chain hydrocarbons, as they could play a crucial role in a circular economy perspective.[36–41] In 2017 Zhang and co-workers demonstrated that in the presence of rhodium nanocubes (with a side length of 37 nm) and a hydrogen-rich environment, CO_2 is reduced to CH_4 and CO with a 60:40 ratio. However, in the presence of an external electromagnetic pulse matching the LSPR of the nanocubes, the selectivity toward CH_4 rises to values above 90%.[42,43] The effect was tentatively assigned to hot-electron injection in antibonding orbitals of a reaction intermediate (adsorbed CHO), based on ground-state density function theory (DFT) calculations for the fragment adsorbed on a model Rh (100) surface. However, the complexity of the system calls for a much more refined theoretical approach. Indeed, to adequately study such a complex photocatalytic phenomenon it is necessary to consider the presence of all the actors, namely the molecule, the nanoparticle and the external electromagnetic pulse.[44–46] All those elements have to

properly interact to account for the LSPR activation and decay and for the time-dependent dynamics of the hot carriers. Moreover, the electronic structure of the molecular moiety needs to be described accurately enough to consider the intrinsic quantum nature of the physical system. Indeed, even considering the sole interaction between the hot carriers and the molecular species, the plasmon enhancement of the reaction selectivity might be caused by different processes such as the charge transfer, the lowering of reaction barriers in excited state pathways, the near fields enhancement generating intramolecular transitions, the activation of specific molecular vibrations or simply the thermal effects as the local temperature in proximity of the nanoparticle might exceed the ambient one. [47–54] The size of the system (tens of nm) and the time scales involved (from fs to hundreds of ps) prohibit a full-quantum treatment of the entire system, and thus other computational approaches are needed. [19,55]

Recently our group has developed a multiscale methodology to deal with electronic dynamics of molecules close to metal nanoparticle, [56,57] encompassing post-DFT approaches such as GW+Bethe-Salpeter [58] whose accuracy for electronic excitations at interfaces is well-documented. [59,60] Here we apply such methodology to clarify the origin of the photoenhanced selectivity of CO_2 reduction by H_2. The results show that it is hole injection to speed up the reaction pathway leading to CH_4 production by making the CHO fragment's Oxygen more reactive, an apparently counter-intuitive results for a reduction reaction. We could also explore the microscopic mechanism of the injection, showing that direct photoinduced charge transfer is prevailing for the nanocube thanks to the electromagnetic enhancement effect associated to the metal NP electronic resonance.

2 Results

A multiscale approach has been applied to study the electron dynamics driven by an external pulse and assisted by plasmonic effects into the CHO adsorbed on a Rh nanocube, which

is the experimentally designed system.[42] In our simulations, the Rh nanoparticle (NP) is represented as a continuous dielectric nanocube of 37 nm edge, as in the experiment, characterized by the experimental dielectric function $\epsilon(\omega)$,[57] and edge curvature equal to Rh atomic radius. One of the vertexes of the nanocube is cut perpendicularly to the (111) direction. Above the cut, at the atomic interlayer distance, an atomistic Rh_{19} cluster is set, mimicking the vertex itself as shown in Fig. 1. Adsorbed to the cluster is a CHO fragment, being the CHO^* dissociation into CH^*+O^* the rate determining step in the thermally activated reaction.[61,62] The atomistic portion of the composite system has been described at quantum (QM) level, while a classical PCM has been used for the large remaining part of the NP. QM calculations are based on DFT, GW and Bethe-Salpeter equation. Details of the theoretical framework are given in Methods, while the strategy used to define the multiscale modelling is provided in the Supporting Information (SI).
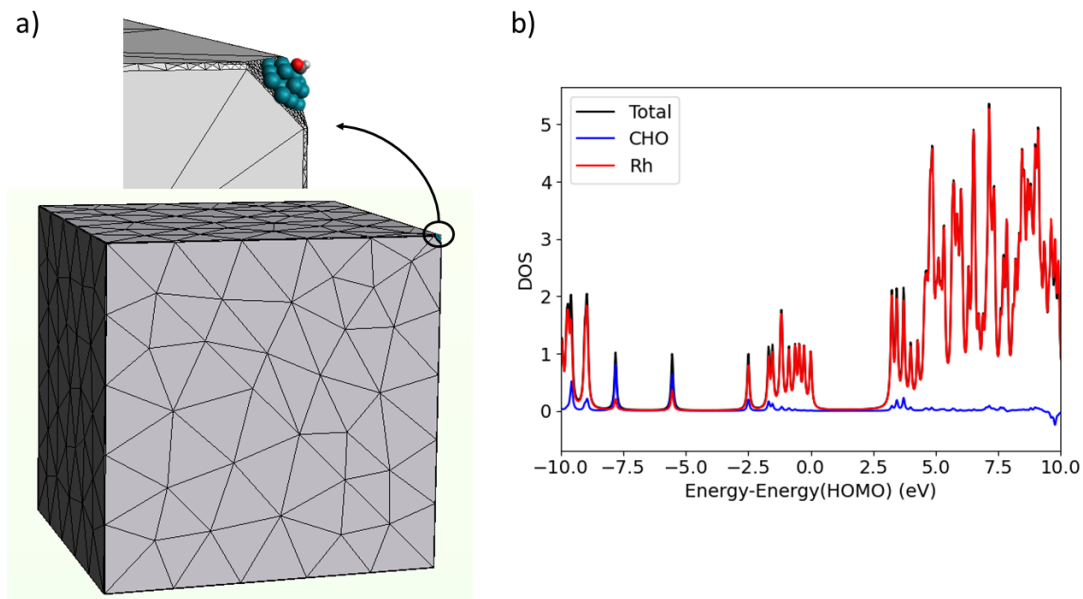

Figure 1: a) Multiscale modelling of system composed of Rh nanocube and CHO; b) ground-state DOS of QM portion, before the pulse is switched on.

The molecular orbitals (MOs) of the adsorbed CHO fragment are strongly mixed with those of the Rh atoms. The GW projected density of states of the Rh_{19}-CHO clusters, displayed in panel b) of Fig. 1, shows CO bonding MOs at low energies (around -8 eV and

-6 eV), and, interestingly, populated CO antibonding MOs below the Fermi level between -2.5 eV and -1.5 eV. Indeed, the C-O bond length for the adsorbed cluster is slightly larger in the case of the adsorbed CHO moiety than in vacuum.

All the following results have been obtained with clamped nuclei, focusing on the electronic degrees of freedom in the scale of tens of femtoseconds. Larger times would require the nuclear dynamics to be explicitly included in the simulations.
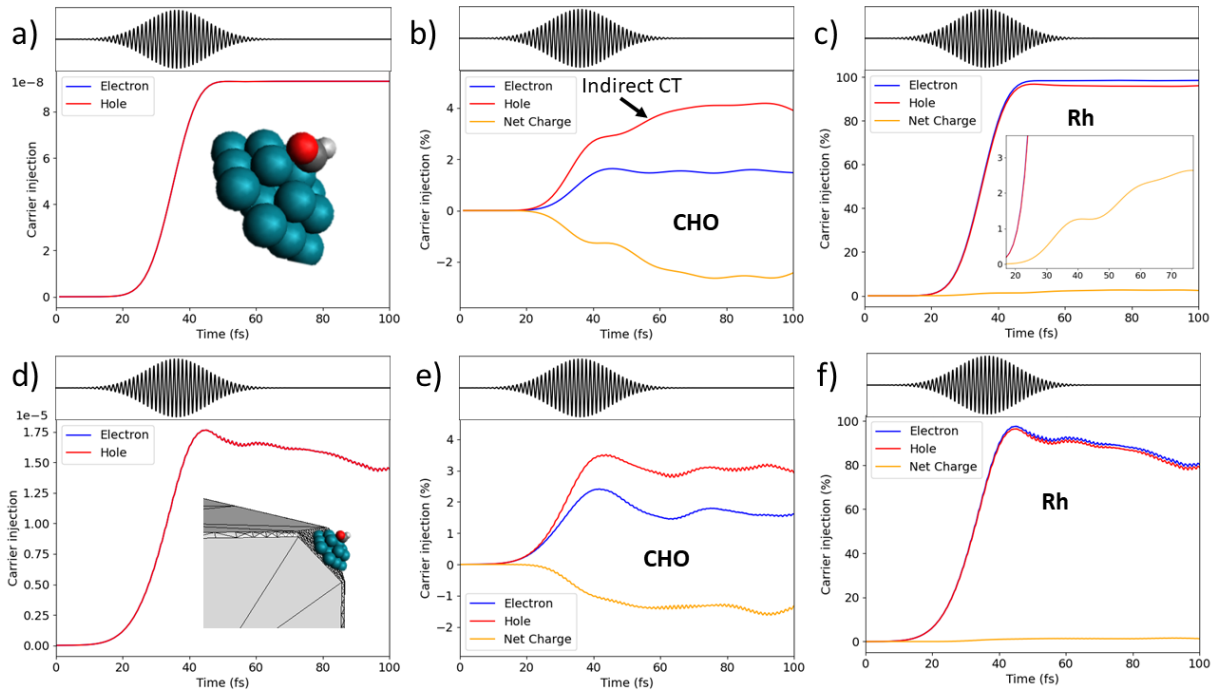

Figure 2: a) Time-evolution of the charge injection (electron and hole) into the QM portion of the system, without the classical portion of Rh nanocube. b) Time-evolution of the charge injection into CHO (%), without the classical portion of Rh nanocube. c) Time-evolution of the charge injection into Rh cluster (%), without the classical portion of Rh nanocube. d) Time-evolution of the charge injection into the QM portion of the system in presence of the classical portion of Rh nanocube; scales in panels a) and d) are different. e) Time-evolution of the charge injection into CHO (%), with the classical portion of Rh nanocube. f) Time-evolution of the charge injection into Rh (%), with the classical portion of Rh nanocube; the net charge as a function of time is magnified. Time evolution of the pulse is also shown for sake of clarity.

Dynamics without classical NP The TDSE has been propagated for the QM portion (Rh$_{19}$-CHO) in absence of the classical NP, when interacting with a Gaussian-enveloped pulse

with FWHM of 21 fs, centred at 3.4 eV (365 nm), pointing perpendicular to the rhodium cluster layers in linear regime. Panel a) of Fig. 2 reports the time evolution of electron and hole generation in the QM portion, in absence of the classical NP, when the pulse is switched on. The curves related to electron and hole are plotted with the same sign to show that they are exactly superimposed, as expected, since no other charge source/sink is modeled. Plotting the percentage of charge injection to CHO and Rh separately, shown respectively in panels b) and c) of Fig. 2, one observes a net hole (electron) injection into CHO (Rh cluster), evidenced by the yellow line representative of the net charge evolution (difference between electron and hole injection percentage at each time step). Looking at the Rh and CHO hole population within the first 40 fs of dynamics, the rising of the hole populations within the pulse duration suggests that a direct charge injection mechanism is in action. Moreover, between 50 fs and 60 fs an increase in the slope of the CHO hole population occurs, concurrently to a Rh hole population decrease. This may be linked to a subsequent indirect charge generation in which holes, originally excited in the Rh cluster, are transferred to the CHO fragment.

The absolute value of charge injection depends on the external field intensity (linearly in the present regime). Normalizing charge injection to the maximum total charge generated, we see that 3% of the generated holes are located on the CHO fragment for the isolated QM portion. The same percentage of electron injection are then generated on Rh residue, evidenced by the magnification of the net charge in panel c) of Fig. 2. This result is in line with previous calculations of incident photon conversion efficiencies, which achieve values between 2% and 5% at the plasmon resonance peak.[63]

Dynamics in presence of the classical NP We applied an equilibration procedure (see Ref. 58), in which the ground-state electronic density of the QM portion, i.e. Rh_{19}-CHO cluster, is relaxed in presence of the polarisable continuum describing the classical portion of the system. To reproduce the experimental conditions, the TDSE has been propagated in

73

presence of a Gaussian-enveloped pulse with FWHM of 21 fs, centred at 3.4 eV (365 nm), pointing perpendicular to the rhodium cluster layers in linear regime, consistently with the experiments. TDSE for the QM portion is coupled to the time evolution of apparent charges located on the surface of the classical NP,[57] see Methods.

Panel d) of Fig. 2 reports electron and hole injection as a function of time when the propagation is performed in presence of the classical NP. As in the other panels, the hole and electron injection are represented with the same sign to highlight that the total charge is conserved. Charge generation is around three orders of magnitude larger than in absence of the NP, an evidence of how Rh nanocube enhances an effect anyway present in the Rh_{19}-CHO cluster. However, at the same time, the presence of Rh nanocube modifies the charge generation time profile, providing a quicker charge separation. The electron and hole injection computed for the separate CHO and Rh fragments (panels e) and f) of Fig. 2) shows that only a direct charge transfer is observed in presence of the classical portion of Rh nanocube. From another point of view, the presence of the classical NP strongly enhances the direct charge transfer mechanism as consequence of the local field enhancement, that eventual other charge transfer mechanisms are negligible.

The percentage of the charge injection (computed normalizing charge injection to the maximum total charge generation) slightly decreases with respect to the results in absence of the classical NP, moving from ∼3% to ∼2% in presence of the additional portion of the nanoparticle, but of course the absolute number of injected holes at the same incident intensity is much higher in the present case. The absolute values obtained including the classical NP in the calculations, are very close to previous theoretical evaluation of injection rate for a gold slab which is around 10^{10} per second.[64,65]

In panels a)-e) of Figure 3 the dynamics of the charge generated specifically on the C, H and O atoms is shown, together with the results for the Rh atoms closest to C and O, labelled as Rh(C) and Rh(O) respectively. These results concern the full composite system, i.e. the coupled dynamics of the Rh_{19}-CHO cluster and classical nanocube. C and O atoms
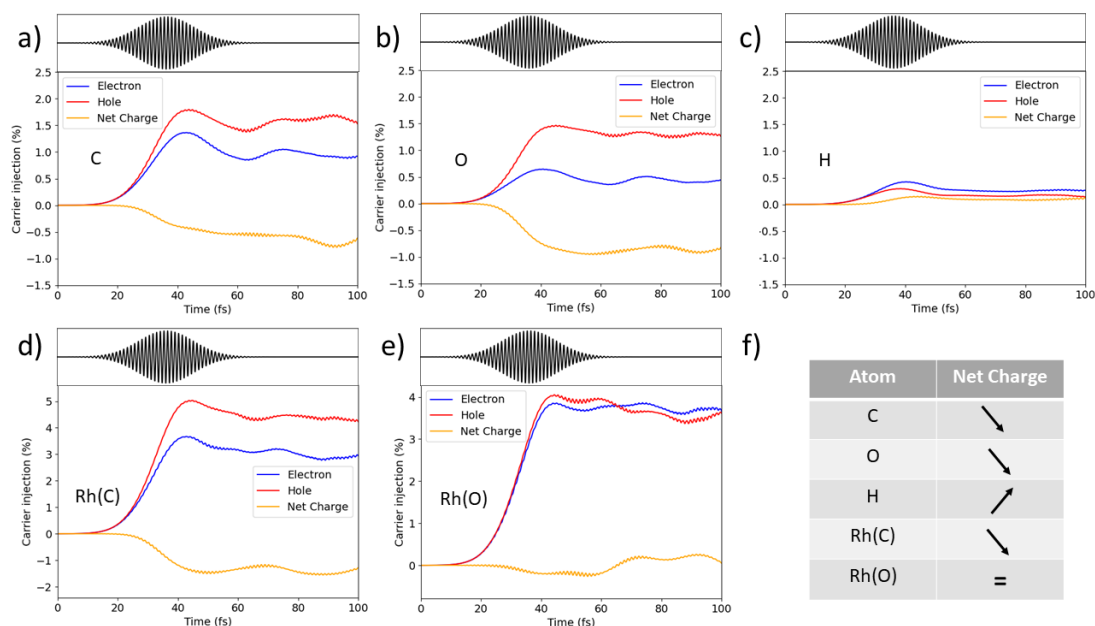
Figure 3: Electron, hole and net-charge injection for a) C, b) O, c) H, d) Rh closest to C, and e) Rh closest to O, from the electron dynamics performed with the classical portion of Rh nanocube. Panel f) summarises the change of electron charge.

are affected by a net hole injection (panels a) and b)), while H atom is characterised by a slight electron injection (panel c)). Rh(C) also becomes hole rich, while no appreciable charge change located on Rh(O) is found. All these features are sketchily summarised in panel f) of Figure 3.

One of the tools typically used to describe chemical reactivity of molecules is the Fukui function, defined as the ratio of charge localised on atom X, with X=C, O or H, and of total charge on the CHO fragment, at a given instant. The time evolution of the Fukui function is reported in Figure 4 for C, O and H atoms in the case of the coupled Rh_{19}-CHO and classical nanocube dynamics. Throughout the dynamics, oxygen species is made more electrophilic by the hole injection. An opposite behaviour is observed for hydrogen, which shows a negative Fukui function during the dynamics, increasing its nucleophilicity. In these conditions, oxygen has the tendency to acquire electrons, while hydrogen tends to release the electronic charge becoming more attracted to C atom, which is the closest electrophile. On the other hand, oxygen atom is not attracted by carbon atom, which is electron poor as
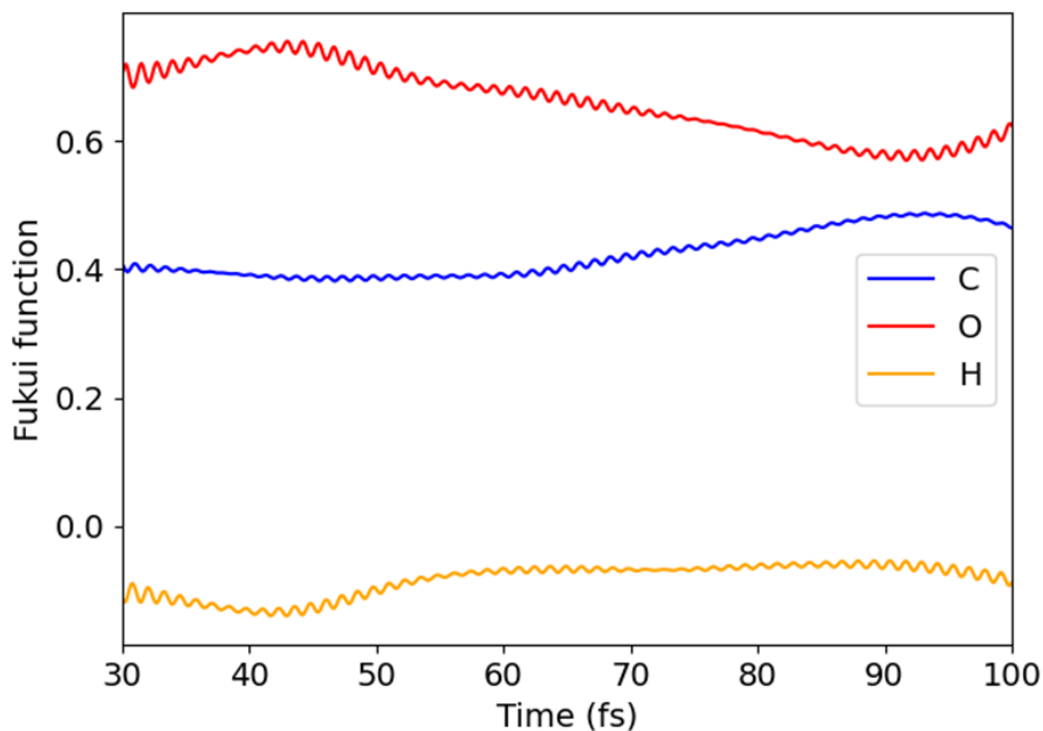
Figure 4: Time-resolved Fukui function for C, O and H atoms from the electron dynamics performed with the classical portion of Rh nanocube.

well.

3 Discussion

The goal of this work is to rationalise the reaction selectivity towards CH_4 in the case of a photocatalytic process, as observed experimentally.[66] In order to accomplish that, we focused on the understanding of two main aspects: i) the mechanism and nature of charge injection into CHO moiety, that is the reaction intermediate of the rate determining step:[62] dissociation of C-H or C-O bond in CHO leads to carbon monoxide or methane, respectively; ii) the fate of oxygen and hydrogen atoms along the plasmon-assisted photoinduced electron dynamics.

As discussed in Section 2, there is a net hole injection into the CHO fragment, that can

76

be identified as a direct photoinduced charge transfer from the Rh moiety to the molecule. This is by far the dominant mechanism in the presence of the entire nanoparticle, while for the Rh_{19}-CHO cluster alone a significant contribution of indirect hole transfer (moving from Rh to CHO after the pulse has passed) is visible in Fig. 2. Absolute values of electron and hole generation are in line with previous findings for hole/electron generation rate that are about 10^{10} s^{-1} for gold nanoparticles with similar dimension as the nanocube employed in our calculations and with similar intensity of incident laser pulse.[67,68]

Data collected in Figures 3 and 4 help us to answer the question about the fate of the final products of plasmon-assisted CO_2 hydrogenation. In fact, results show that the injected holes localize mostly on the Oxygen atom, making it more reactive. The C atom is also electron depleted, weakening their interaction and making the Oxygen prone to leave the fragment.

Hole injection instead of electron injection on CHO moiety may be considered a counter-intuitive mechanism to favour a reduction reaction on carbon atom. An analogous reaction, the Clemmensen reduction,[69,70] leads to carbonyl hydrogenation catalysed by amalgamated zinc in presence of concentrated hydrochloric acid. In this case, two possible mechanisms have been verified: the reaction goes on through direct protonation of the oxygen atom generating the carbanionic compound, or through oxygen adsorption on zinc surface via carbenoid mechanism. In both cases, the electrophilicity of the oxygen atom increases, favoured by the acidity of the solution, and the reaction is driven toward carbon-oxygen bond weakening. In the hydrogenation reaction of carbon dioxide catalysed by rhodium nanoparticles, the electrophilicity of the oxygen atom is favoured by hole injection, which makes it more reactive toward other species and inclined to break the bond with the carbon atom that bring the same charge.

Summarizing, shining light on the CHO fragment adsorbed on the Rh nanocubes generates an overall hole population on C and O atoms, which selects methane formation against carbon monoxide. The highest value of Fukui function for oxygen at all times, represents a further confirmation that O atom looks for electron excess along the Rh surface. Moreover,

OH species has a negligible probability to appear in reaction pathways.

4   Conclusion

We have proposed a strategy to investigate the mechanism of CO_2 reduction catalysed by rhodium in presence of light. A time-dependent approach based on a multiscale description of the system has revealed to be an efficient method to highlight the effect of light in the process, going beyond previous interpretation of the phenomenon based on standard DFT calculations. Charge injection dynamics of Rh_{19}-CHO system in proximity of a classically described rhodium nanocube has revealed holes injection from Rh atoms to CHO fragment, particularly oxygen and carbon atoms activated by the presence of a proper incident laser. Even though the calculations performed in absence of the rhodium NP revealed two possible hole injection mechanisms, a direct one promoted by the light and an indirect one where holes on Rh atoms move toward CHO, when the calculation is carried out in presence of the NP the direct mechanism prevails on the other. In any case, both results lead to the same possible mechanism: holes injection on oxygen atom makes it more electrophilic and reactive but not toward carbon atom which becomes more electrophilic due to hole injection as well, thus preferring to strengthen C-H bond, instead.

5   Methods

In order to provide an accurate and physically meaningful description of the electron dynamics occurring in the composite system with an external pulse, a time-resolved approach is mandatory. Our time-domain QM/continuum model describes the time evolution of the molecular density, via the appropriate formulation of the time-dependent (TD) Schrödinger equation (TDSE), coupled to a classical electromagnetic solver, based on the boundary element method (BEM),[71] for the NP polarization. The continuum part is modeled on the time-resolved extension of the polarisable continuum model, i.e. TD-PCM.[71] Dielectric func-

tion of NP is fitted from experimental data.[57]

A computationally convenient time-resolved version of BEM has been recently proposed,[56,72] where the set of apparent charges on the NP surface becomes time-dependent. This makes the time-resolved BEM a powerful tool for describing the time evolution of a quantum system interacting with a NP, giving rise to a model that can be dubbed TD-PCM-NP.[73] The method employed has been developed in the quasi-static limit.

Within the TD-PCM-NP, the time-dependent wave function of the QM portion, $|\Psi_S(t)\rangle$, is propagated using TDSE

$$i\frac{d}{dt}|\Psi_S(t)\rangle = \hat{H}_S(t)|\Psi_S(t)\rangle, \tag{1}$$

with

$$\hat{H}_S(t) = \hat{H}_0 - \vec{\hat{\mu}} \cdot \vec{E}_{ext}(t) + \hat{H}_{pol}, \tag{2}$$

where $\hat{H}_0$ is the field-free electronic Hamiltonian, $\vec{\hat{\mu}}$ is the system dipole, and $\hat{H}_{pol}$ is the polarization interaction term

$$\hat{H}_{pol}(t) = \mathbf{q}(t) \cdot \hat{\mathbf{V}}, \tag{3}$$

where $\hat{\mathbf{V}}$ is the generic electrostatic potential operator evaluated at the NP surface representative points. The electrostatic potential, which polarises the NP, originates from the external field $\vec{E}_{ext}(t)$ and from the molecular density. The time-dependent system wave function $|\Psi_S(t)\rangle$ is expanded using the eigenstate basis $\{|\lambda\rangle\}$ of an effective field-free Hamiltonian, $\hat{H}_{NP} = \hat{H}_0 + \mathbf{q}_{GS} \cdot \hat{\mathbf{V}}$:[56,58,74]

$$|\Psi_S(t)\rangle = \sum_\lambda C_\lambda(t)|\lambda\rangle, \tag{4}$$

with λ running over the electronic eigenstates, and $C_\lambda(t)$ are time-dependent coefficients evolving according to the Hamiltonian $\hat{H}_S(t)$. Charges $\mathbf{q}_{GS}$ are obtained by a self-consistent calculation for the QM ground-state in presence of the polarisable NP.

The set of $|\lambda\rangle$ states is composed of density-functional theory ground state and GW-BSE

derived excited states.[58] The GW-BSE derived active space allows us to overcome the limitations of the implementations that employ time-dependent configuration interaction singles and real-time density functional theory in terms of achievable accuracy without compromising on the accessible molecular sizes. Indeed, the GW-BSE approach is suited for an accurate description of electronic level alignments, charge transfer and optical excitations in both extended and low dimensional systems with excitation energies, transition dipoles in line with high level theoretical chemistry methods.[75–77]

To obtain the $|\lambda\rangle$ states, following Ref. 58, firstly, the GW-BSE effective two-particles Hamiltonian for the Rh_{19}-CHO cluster is diagonalised within the Tamm-Dancoff approximation. This provides a set of excitation energies, the eigenvalues E_λ and the corresponding eigenvectors A^λ_{cv} (here v and c identify occupied and empty states respectively). Typically, such eigenvalues and eigenstates would be used to build the optical excitation spectrum of the system,[59] in our case we use them to define the $|\lambda\rangle$ states:

$$|\lambda\rangle = \sum_{cv\sigma} A^\lambda_{cv\sigma} c^\dagger_{c\sigma} c_{v\sigma} |0\rangle \qquad (5)$$

so that, referring to Eq. 2:

$$\hat{H}_0 |\lambda\rangle \sim E_\lambda |\lambda\rangle \qquad (6)$$

with energy referred to the ground state Slater determinant $|\lambda\rangle = |0\rangle = |0\rangle$. The sum in Eq. 5 runs over valence (v) conduction (c) bands for a given spin state σ. This first set of $\{|\lambda\rangle\}$ states are obtained solving the GW-BSE equation in vacuum. Following the equilibration procedure, described in Ref. 58, that takes into account the mutual NP/Rh_{19}-CHO polarization in the absence of an external field, the coupled NP-quantum system dynamics is carried out.

The time-dependent $PDOS_K(t,\epsilon)$ for the fragment K is defined as the expectation value with respect to $|\psi(t)\rangle$ of the number operator $\hat{n}_i$ weighted by w^K_i Lowdin weights. In our case, the fragments are either two (CHO and the Rh cluster) or six (C, O, H, rhodium atom

closest to O, rhodium atom closest to C and all the other Rh atoms). We are interested in the $\Delta\text{PDOS}_K(\text{t},\epsilon) = \text{PDOS}_K(\text{t},\epsilon)$ - $\text{PDOS}_{ini}(\epsilon)$, which is explicitly given by[78]

$$
\begin{aligned}
\Delta\text{PDOS}_K(t,\epsilon) &= -\sum_i^{occ} w_i^K \text{Re}\left[\sum_{\lambda,\lambda'} C_\lambda^*(t)C_{\lambda'}(t)\sum_a^{vir} d_{i,\lambda}^a{}^* d_{i,\lambda'}^a\right] L_\eta(\epsilon - \epsilon_i) \qquad (7)\\
&+ \sum_a^{vir} w_a^K \text{Re}\left[\sum_{\lambda,\lambda'} C_\lambda^*(t)C_{\lambda'}(t)\sum_i^{occ} d_{i,\lambda}^a{}^* d_{i,\lambda'}^a\right] L_\eta(\epsilon - \epsilon_i).
\end{aligned}
$$

$d_{i,\lambda}^a$ ($d_{i,\lambda'}^a$) are the linear coefficients of the expansion for state λ (λ') in the atomic-orbital basis set and a Lorentzian function L centred on MO energies ϵ_i, with width, η is used to obtain a smooth profile.

Assuming that the wave function at the initial time is the ground state of the system, i.e. $\psi(t=0) = |0\rangle$ the initial $\text{PDOS}_{ini}(\epsilon)$ is defined as

$$
\text{PDOS}_{ini}(\epsilon) = \sum_i^{occ} w_i \langle 0|\hat{n}_i|0\rangle L_\eta(\epsilon - \epsilon_i) = 2\sum_i^{occ} w_i L_\eta(\epsilon - \epsilon_i). \qquad (8)
$$

Charge injection is defined as

$$
\text{electron injection} \qquad \frac{1}{2}\int_{-\infty}^{\infty}[\Delta\text{PDOS}(t,\epsilon) + |\Delta\text{PDOS}(t,\epsilon)|]\,d\epsilon \qquad (9)
$$

$$
\text{hole injection} \qquad \frac{1}{2}\int_{-\infty}^{\infty}[\Delta\text{PDOS}(t,\epsilon) - |\Delta\text{PDOS}(t,\epsilon)|]\,d\epsilon \qquad (10)
$$

When the ΔPDOS is applied to the SSE set of trajectories, averaged $\overline{C_\lambda^*(t)C_{\lambda'}(t)}$ arise in Eq. 8:

$$
\begin{aligned}
\Delta\text{PDOS}_K^{\text{SSE}}(t,\epsilon) &= -\sum_i^{occ} w_i^K \text{Re}\left[\sum_{\lambda,\lambda'} \overline{C_\lambda^*(t)C_{\lambda'}(t)}\sum_a^{vir} d_{i,\lambda}^a{}^* d_{i,\lambda'}^a\right] L_\eta(\epsilon - \epsilon_i) \qquad (11)\\
&+ \sum_a^{vir} w_a^K \text{Re}\left[\sum_{\lambda,\lambda'} \overline{C_\lambda^*(t)C_{\lambda'}(t)}\sum_i^{occ} d_{i,\lambda}^a{}^* d_{i,\lambda'}^a\right] L_\eta(\epsilon - \epsilon_i).
\end{aligned}
$$

SSE version of charge injection is defined by using $\Delta\mathrm{PDOS}_K^{\mathrm{SSE}}(t, \epsilon)$ in Equations 10.

Supplementary information

Supplementary material contains information on the modeling of the system and computational details.

Acknowledgments

Author information

These authors contributed equally: Margherita Marsili, Giulia Dall'Osto.

Declarations

Authors declare no conflict of interest.

References

(1) Dadashi-Silab, S.; Doran, S.; Yagci, Y. Photoinduced electron transfer reactions for macromolecular syntheses. *Chem. Rev.* **2016**, *116*, 10212–10275.

(2) Wenderich, K.; Mul, G. Methods, mechanism, and applications of photodeposition in photocatalysis: a review. *Chem. Rev.* **2016**, *116*, 14587–14619.

(3) Hou, W.; Cronin, S. B. A Review of Surface Plasmon Resonance-Enhanced Photocatalysis. *Adv. Funct. Mater.* **2013**, *23*, 1612.

(4) Melchionna, M.; Fornasiero, P. Updates on the Roadmap for Photocatalysis. *ACS Catal.* **2020**, *10*, 5493.

(5) Aslam, U.; Rao, V. G.; Chavez, S.; Linic, S. Catalytic conversion of solar to chemical energy on plasmonic metal nanostructures. *Nat. Catal.* **2018**, *1*, 656–665.

(6) Brongersma, M. L.; Halas, N. J.; Nordlander, P. Plasmon-induced hot carrier science and technology. *Nature Nanotechnol.* **2015**, *10*, 25–34.

(7) Longato, A.; Vanzan, M.; Colusso, E.; Corni, S.; Martucci, A. Enhancing Tungsten Oxide Gasochromism with Noble Metal Nanoparticles: The Importance of the Interface. *Small* **2023**, *19*, 2205522.

(8) Jiang, N.; Zhuo, X.; Wang, J. Active Plasmonics: Principles, Structures, and Applications. *Chem. Rev.* **2018**, *118*, 3054–3099.

(9) Koya, A. N. et al. Advances in ultrafast plasmonics. *Appl. Phys. Rev.* **2023**,

(10) Pilot, R.; Signorini, R.; Durante, C.; Orian, L.; Bhamidipati, M.; Fabris, L. A review on surface-enhanced Raman scattering. *Biosensors* **2019**, *9*.

(11) Yu, H.; Peng, Y.; Yang, Y.; Li, Z. Y. Plasmon-enhanced light–matter interactions and applications. *Npj Comput. Mater.* **2019**, *5*, 1–14.

(12) Li, J. F.; Li, C. Y.; Aroca, R. F. Plasmon-enhanced fluorescence spectroscopy. *Chem. Soc. Rev.* **2017**, *46*, 3962–3979.

(13) Halas, N. J. Spiers Memorial Lecture: Introductory lecture: Hot-electron science and microscopic processes in plasmonics and catalysis. *Faraday Discuss.* **2019**, *214*, 13–33.

(14) Gargiulo, J.; Berté, R.; Li, Y.; Maier, S. A.; Cortés, E. From Optical to Chemical Hot Spots in Plasmonics. *Acc. Chem. Res.* **2019**, *52*, 2525–2535.

(15) Besteiro, L. V.; Cortés, E.; Ishii, S.; Narang, P.; Oulton, R. F. Hot electron physics and applications. *J. Appl. Phys.* **2021**, *129*, 150401.

(16) Zhan, C.; Chen, X. J.; Yi, J.; Li, J. F.; Wu, D. Y.; Tian, Z. Q. From plasmon-enhanced molecular spectroscopy to plasmon-mediated chemical reactions. *Nat. Rev. Chem.* **2018**, *2*, 216–230.

(17) Brongersma, M. L.; Halas, N. J.; Nordlander, P. Plasmon-induced hot carrier science and technology. *Nat. Nanotech.* **2015**, *10*, 25.

(18) Christopher, P.; Moskovits, M. Hot Charge Carrier Transmission from Plasmonic Nanostructures. *Annu. Rev. Phys. Chem.* **2017**, *68*, 379–398.

(19) Narang, P.; Sundararaman, R.; Atwater, H. A. Plasmonic hot carrier dynamics in solid-state and chemical systems for energy conversion. *Nanophotonics* **2016**, *5*, 96–111.

(20) Manjavacas, A.; Liu, J. G.; Kulkarni, V.; Nordlander, P. Plasmon-induced hot carriers in metallic nanoparticles. *ACS Nano* **2014**, *8*, 7630–7638.

(21) Kazuma, E.; Kim, Y. Mechanistic Studies of Plasmon Chemistry on Metal Catalysts. *Angew. Chem. Int. Ed.* **2019**, *58*, 4800–4808.

(22) Lee, H.; Park, Y.; Song, K.; Park, J. Y. Surface Plasmon-Induced Hot Carriers: Generation, Detection, and Applications. *Acc. Chem. Res.* **2022**, *55*, 3727–3737.

(23) Newmeyer, E. R.; North, J. D.; Swearer, D. F. Hot carrier photochemistry on metal nanoparticles. *J. Appl. Phys.* **2022**, *132*, 230901.

(24) Zhan, C.; Yi, J.; Hu, S.; Zhang, X. G.; Wu, D. Y.; Tian, Z. Q. Plasmon-mediated chemical reactions. *Nat. Rev. Methods Primers* **2023**, *3*, 12.

(25) Zhang, Z.; Zhang, C.; Zheng, H.; Xu, H. Plasmon-Driven Catalysis on Molecules and Nanomaterials. *Acc. Chem. Res.* **2019**, *52*, 2506–2515.

(26) Chang, L.; Besteiro, L. V.; Sun, J.; Santiago, E. Y.; Gray, S. K.; Wang, Z.; Govorov, A. O. Electronic Structure of the Plasmons in Metal Nanocrystals: Fundamental Limitations for the Energy Efficiency of Hot Electron Generation. *ACS Energy Lett.* **2019**, *4*, 2552–2568.

(27) Ghosh, U.; Pal, A.; Pal, T. Plasmon Induced Near-Infrared Active Photocatalysts: A Review. *Adv. Mater. Interfaces* **2022**, *9*, 1–19.

(28) Jain, V.; Kashyap, R. K.; Pillai, P. P. Plasmonic Photocatalysis: Activating Chemical Bonds through Light and Plasmon. *Advanced Optical Materials* **2022**, *10*, 1–33.

(29) Schirato, A.; Maiuri, M.; Cerullo, G.; Della Valle, G. Ultrafast hot electron dynamics in plasmonic nanostructures: experiments, modelling, design. *Nanophotonics* **2023**, *12*, 1–28.

(30) Gellé, A.; Jin, T.; De La Garza, L.; Price, G. D.; Besteiro, L. V.; Moores, A. Applications of Plasmon-Enhanced Nanocatalysis to Organic Transformations. *Chem. Rev.* **2020**, *120*, 986–1041.

(31) Qian, K.; Sweeny, B. C.; Johnston-Peck, A. C.; Niu, W.; Graham, J. O.; Duchene, J. S.; Qiu, J.; Wang, Y. C.; Engelhard, M. H.; Su, D.; Stach, E. A.; Wei, W. D. Surface plasmon-driven water reduction: Gold nanoparticle size matters. *J. Am. Chem. Soc.* **2014**, *136*, 9842–9845.

(32) Yan, L.; Guan, M.; Meng, S. Plasmon-induced nonlinear response of silver atomic chains. *Nanoscale* **2018**, *10*, 8600–8605.

(33) Robatjazi, H.; Bao, J. L.; Zhang, M.; Zhou, L.; Christopher, P.; Carter, E. A.; Nordlander, P.; Halas, N. J. Plasmon-driven carbon-fluorine ($C(sp^3)$-F) bond activation with mechanistic insights into hot-carrier-mediated pathways. *Nature Catal.* **2020**, *3*, 564–573.

(34) Puértolas, B.; Comesaña-Hermo, M.; Besteiro, L. V.; Vázquez-González, M.; Correa-Duarte, M. A. Challenges and Opportunities for Renewable Ammonia Production via Plasmon-Assisted Photocatalysis. *Adv. Energy Mater.* **2022**, *12*, 2103909.

(35) Huang, J.; Zhao, X.; Huang, X.; Liang, W. Understanding the mechanism of plasmon-driven water splitting: Hot electron injection and a near field enhancement effect. *Phys. Chem. Chem. Phys.* **2021**, *23*, 25629–25636.

(36) Verma, R.; Belgamwar, R.; Polshettiwar, V. Plasmonic Photocatalysis for CO_2 Conversion to Chemicals and Fuels. *ACS Mater. Lett.* **2021**, *3*, 574–598.

(37) Jiang, X.; Huang, J.; Bi, Z.; Ni, W.; Gurzadyan, G.; Zhu, Y.; Zhang, Z. Plasmonic Active "Hot Spots"-Confined Photocatalytic CO_2 Reduction with High Selectivity for CH_4 Production. *Adv. Mater.* **2022**, 2109330.

(38) Hu, C.; Chen, X.; Low, J.; Yang, Y. W.; Li, H.; Wu, D.; Chen, S.; Jin, J.; Li, H.; Ju, H.; Wang, C. H.; Lu, Z.; Long, R.; Song, L.; Xiong, Y. Near-infrared-featured broadband CO2 reduction with water to hydrocarbons by surface plasmon. *Nature Communications* **2023**, *14*, 221.

(39) Ciocarlan, R.-G.; Blommaerts, N.; Lenaerts, S.; Cool, P.; Verbruggen, S. W. Recent Trends in Plasmon-Assisted Photocatalytic CO_2 Reduction. *ChemSusChem* **2023**, *16*, e202201647.

(40) Mittal, D.; Ahlawat, M.; Govind Rao, V. Recent Progress and Challenges in Plasmon-Mediated Reduction of CO_2 to Chemicals and Fuels. *Adv. Mater. Interfaces* **2022**, *9*, 1–24.

(41) Zhang, T.; Li, Z.; Shi, R.; Ma, Y.; Zhao, J. Photodriven CO_2 Hydrogenation into Diverse Products: Recent Progress and Perspective. *J. Phys. Chem. Lett.* **2022**, *13*, 5291–5303.

(42) Zhang, Y.; Meng, Q. S.; Zhang, L.; Luo, Y.; Yu, Y. J.; Yang, B.; Zhang, Y.; Esteban, R.; Aizpurua, J.; Luo, Y.; Yang, J. L.; Dong, Z. C.; Hou, J. G. Sub-nanometre control of the coherent interaction between a single molecule and a plasmonic nanocavity. *Nat. Commun.* **2017**, *8*, 15225.

(43) Li, X.; Everitt, H. O.; Liu, J. Confirming nonthermal plasmonic effects enhance CO_2 methanation on Rh/TiO_2 catalysts. *Nano Research* **2019**, *12*, 1906–1911.

(44) Pettine, J.; Meyer, S. M.; Medeghini, F.; Murphy, C. J.; Nesbitt, D. J. Controlling the Spatial and Momentum Distributions of Plasmonic Carriers: Volume vs Surface Effects. *ACS Nano* **2021**, *15*, 1566–1578.

(45) Rossi, T. P.; Erhart, P.; Kuisma, M. Hot-Carrier Generation in Plasmonic Nanoparticles: The Importance of Atomic Structure. *ACS Nano* **2020**, *14*, 9963–9971.

(46) Kim, S.; Lee, S.; Yoon, S. Effect of Nanoparticle Size on Plasmon-Driven Reaction Efficiency. *ACS Appl. Mater. Interfaces* **2022**, *14*, 4163–4169.

(47) Cortés, E.; Besteiro, L. V.; Alabastri, A.; Baldi, A.; Tagliabue, G.; Demetriadou, A.; Narang, P. Challenges in Plasmonic Catalysis. *ACS Nano* **2020**, *14*, 16202–16219.

(48) Martirez, J. M. P.; Carter, E. A. Prediction of a low-temperature N_2 dissociation catalyst exploiting near-IR-to-visible light nanoplasmonics. *Sci. Adv.* **2017**, *3*, eaao4710.

(49) Zhou, L.; Swearer, D. F.; Zhang, C.; Robatjazi, H.; Zhao, H.; Henderson, L.; Dong, L.; Christopher, P.; Carter, E. A.; Nordlander, P.; Halas, N. J. Quantifying hot carrier and thermal contributions in plasmonic photocatalysis. *Science* **2018**, *362*, 69–72.

(50) Linic, S.; Chavez, S.; Elias, R. Flow and extraction of energy and charge carriers in hybrid plasmonic nanostructures. *Nature Materials* **2021**, *15*.

(51) Sivan, Y.; Dubi, Y. Recent developments in plasmon-assisted photocatalysis - A personal Perspective. *Appl. Phys. Lett.* **2020**, *117*.

(52) Jain, P. K. Taking the Heat Off of Plasmonic Chemistry. *J. Phys. Chem. C* **2019**, *123*, 24347–24351.

(53) Vanzan, M.; Cesca, T.; Kalinic, B.; Maurizio, C.; Mattei, G.; Corni, S. Lanthanide Ions Sensitization by Small Noble Metal Nanoclusters. *ACS Photonics* **2021**, *8*, 1364–1376.

(54) Vanzan, M.; Gil, G.; Castaldo, D.; Nordlander, P.; Corni, S. Energy Transfer to Molecular Adsorbates by Transient Hot Electron Spillover. *Nano Letters* **2023**, *23*, 2719–2725.

(55) Martirez, J. M. P.; Bao, J. L.; Carter, E. A. First-Principles Insights into Plasmon-Induced Catalysis. *Annu. Rev. Phys. Chem.* **2021**, *72*, 1–21.

(56) Pipolo, S.; Corni, S. Real-Time Description of the Electronic Dynamics for a Molecule Close to a Plasmonic Nanoparticle. *J. Phys. Chem. C* **2016**, *120*, 28774–28781.

(57) Dall'Osto, G.; Gil, G.; Pipolo, S.; Corni, S. Real-time dynamics of plasmonic resonances in nanoparticles described by a boundary element method with generic dielectric function. *J. Chem. Phys.* **2020**, *153*, 184114.

(58) Marsili, M.; Corni, S. Electronic Dynamics of a Molecular System Coupled to a Plasmonic Nanoparticle Combining the Polarizable Continuum Model and Many-Body Perturbation Theory. *J. Phys. Chem. C* **2022**, *126*, 8768.

(59) Martin, R. M.; Reining, L.; Ceperley, D. M. *Interacting Electrons: Theory and Computational Approaches*; Cambridge University Press: Cambridge, 2016.

(60) Blase, X.; Duchemin, I.; Jacquemin, D. The Bethe–Salpeter equation in chemistry: relations with TD-DFT, applications and challenges. *Chem. Soc. Rev.* **2018**, *47*, 1022–1043.

(61) Avanesian, T.; Christopher, P. Adsorbate specificity in hot electron driven photochemistry on catalytic metal surfaces. *Journal of Physical Chemistry C* **2014**, *118*, 28017–28031.

(62) Vanzan, M.; Marsili, M.; Corni, S. Study of the Rate-Determining Step of Rh Catalyzed CO_2 Reduction: Insight on the Hydrogen Assisted Molecular Dissociation. *Catalysts* **2021**, *11*, 538.

(63) De Arquer, F. P. G.; Mihi, A.; Konstantatos, G. Molecular interfaces for plasmonic hot electron photovoltaics. *Nanoscale* **2015**, *7*, 2281–2288.

(64) Govorov, A. O.; Zhang, H.; Gun'Ko, Y. K. Theory of photoinjection of hot plasmonic carriers from metal nanostructures into semiconductors and surface molecules. *J. Phys. Chem. C* **2013**, *117*, 16616–16631.

(65) Govorov, A. O.; Zhang, H.; Demir, H. V.; Gun'ko, Y. K. Photogeneration of hot plasmonic electrons with metal nanocrystals: Quantum description and potential applications. *Nano Today* **2014**, *9*, 85–101.

(66) Zhang, X.; Li, X.; Zhang, D.; Su, N.; Yang, W.; Everitt, H. Product selectivity in plasmonic photocatalysis for carbon dioxide hydrogenation. *Nat. Commun.* **2017**, *8*, 14542.

(67) Kong, X. T.; Wang, Z.; Govorov, A. O. Plasmonic Nanostars with Hot Spots for Effi-

cient Generation of Hot Electrons under Solar Illumination. *Advanced Optical Materials* **2017**, *5*.

(68) Santiago, E. Y.; Besteiro, L. V.; Kong, X.-T.; Correa-Duarte, M. A.; Wang, Z.; Govorov, A. O. Efficiency of Hot-Electron Generation in Plasmonic Nanocrystals with Complex Shapes: Surface-Induced Scattering, Hot Spots, and Interband Transitions. *ACS Photonics* **2020**, *7*, 2807–2824.

(69) Brewster, J. H. Reductions at Metal Surfaces. II. A Mechanism for the Clemmensen Reduction1. *Journal of the American Chemical Society* **1954**, *76*, 6364–6368.

(70) Sánchez-Viesca, F.; Berros, M.; Gómez, R. A complete and sustained Clemmensen reduction mechanism. *Am. J. Chem* **2018**, *8*, 8–12.

(71) Mennucci, B.; Corni, S. Multiscale modelling of photoinduced processes in composite systems. *Nat. Rev. Chem.* **2019**, *3*, 315.

(72) Corni, S.; Pipolo, S.; Cammi, R. Equation of motion for the solvent polarization apparent charges in the polarizable continuum model: Application to real-time TDDFT. *J. Phys. Chem. A* **2014**, *119*, 5405–5416.

(73) Coccia, E.; Fregoni, J.; Guido, C. A.; Marsili, M.; Pipolo, S.; Corni, S. Hybrid theoretical models for molecular nanoplasmonics. *J. Chem. Phys.* **2020**, *153*.

(74) Coccia, E.; Corni, S. Role of coherence in the plasmonic control of molecular absorption. *J. Chem. Phys.* **2019**, *151*, 044703.

(75) Rangel, T.; Hamed, S. M.; Bruneval, F.; Neaton, J. B. Evaluating the GW Approximation with CCSD(T) for Charged Excitations Across the Oligoacenes. *J. Chem. Theory Comput.* **2016**, *12*, 2834–2842.

(76) Jacquemin, D.; Duchemin, I.; Blase, X. Benchmarking the Bethe–Salpeter Formalism on a Standard Organic Molecular Set. *J. Chem. Theory Comput.* **2015**, *11*, 3290–3304.

(77) Jacquemin, D.; Duchemin, I.; Blondel, A.; Blase, X. Assessment of the Accuracy of the Bethe–Salpeter (BSE/GW) Oscillator Strengths. *J. Chem. Theory Comput.* **2016**, *12*, 3969–3981.

(78) Grobas Illobre, P.; Marsili, M.; Corni, S.; Stener, M.; Toffoli, D.; Coccia, E. Time-Resolved Excited-State Analysis of Molecular Electron Dynamics by TDDFT and Bethe–Salpeter Equation Formalisms. *J. Chem. Theory Comput.* **2021**, *17*, 6314.

Supporting information for "Photoinduced hole injection explains the reaction selectivity in CO$_2$ hydrogenation on Rh nanocube"

Giulia Dall'Osto,[†] Margherita Marsili,[*,‡] Mirko Vanzan,[†,¶] Daniele Toffoli,[§] Mauro Stener,[§] Stefano Corni,[†,∥] and Emanuele Coccia[*,§]

†Department of Chemical Sciences, University of Padova, via Marzolo 1, Padova, Italy, 35100

‡Department of Physics and Astronomy "Augusto Righi", University of Bologna, Viale Berti Pichat 6/2, Bologna, Italy, 40127

¶Department of Physics, University of Milan, Via Giovanni Celoria 16, Milano, Italy, 20133

§Department of Chemical and Pharmaceutical Sciences, University of Trieste, Via Licio Giorgieri 1, Trieste, Italy, 34127

∥CNR Institute of Nanoscience, via Campi 213/A, Modena, Italy, 41100

E-mail: margherita.marsili@unibo.it; ecoccia@units.it

Effect of cutting a classical NP

As mentioned in the main text, performing quantum electrodynamics calculations on large nanoparticles is not feasible and for this reason we split the rhodium nanocube into an extended part described classically, and a small vertex treated at quantum level. We have carefully studied the system to ensure the goodness of our approach. Below we report some

results of our investigation: i) the comparison between the absorption spectra of a quantum cluster and classical clusters modeled in different ways but with similar dimension, ii) the comparison of the absorption spectra of the NP with either a classical or an atomistic cluster as vertex, iii) the comparison of the potential generated by the NP with either a classical or an atomistic cluster as vertex.

Taking on that calculations on a quantum nanocube with dimensions in the order of tens of nanometres are unfeasible, we decided to compare the response of a smaller cluster when it is treated either at quantum or classical level. The atomistic Rh_{19} cluster has been obtained by cutting a rhodium slab along the 111 direction, obtaining a two layers cluster. This structure is the same employed in the main text as the nanocube vertex bonded to the CHO residue. Its absorption spectrum has been computed at BSE level of theory using MolGW code on the basis of 400 electronic states below 5 eV. On the other hand, differently shaped clusters treated classically have been built following various strategies. One structure is built connecting the position of atoms in the Rh_{19} cluster multiplied by a factor useful to have a volume equal to the cluster volume estimated on the basis of the rhodium Van der Waals radius (figure 1a) or the Wigner-Seitz radius (figure 1d). Other structures have been obtained as continuation of the cut nanocube reported in the main text considering either a rounded (figure 1b) or a planar (figure 1c) vertex. In the framework of boundary elements methods (BEM),[1] the surface has been tasselled by different number of tessere (from 330 to 676) and metallic nature has been accounted by means of the Palik dielectric function of rhodium.[2] The absorption spectrum has been computed as the Fourier Transform of the dynamics of the surface charges on the cluster through the IEF-PCM equation in time domain[3,4] applying a Gaussian electric field oriented perpendicular to the cluster planar surface.

The absorption spectra (fig. 1e), reported in terms of the imaginary part of the polarizability, has the same trend both in terms of intensity and profile comparing the QM results and those of different atomistic clusters, meaning that the electrodynamics response
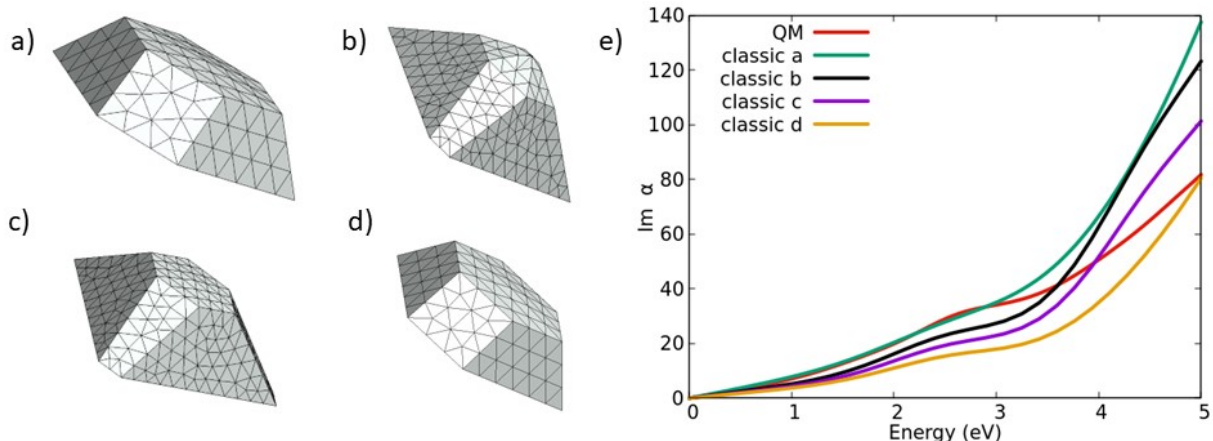
Figure 1: Structure of classical clusters built connecting the centre of the atoms position multiplied by the Van der Waals radius (a), built with a rounded vertex as continuation of the cut nanocube (b), built with a planar vertex as continuation of the cut nanocube(c), built connecting the centre of the atoms position multiplied by the Wigner-Seitz radius (d). e) Comparison between the absorption spectra of the quantum cluster (red line) and the absorption spectra computed at classical level for four different structures reported in panels (a-d).

is quite similar. In particular, in the frequency region interesting for the present work, around $2.5 - 3.5eV$ (where the pulse wavelength lies), there is a good agreement between the spectrum of the QM cluster and the classical one built on the basis of the Van der Waals radius (structure a). Moreover, the results point up that the absorption spectrum computed classically depends on the way the structure is built: structures a and d which have same shape but different dimension show similar spectra but with different intensity, as well as structures b and c have common features in the absorption spectra but slightly different intensities since structure b has a larger volume.

Moreover, we compared the absorption spectra of the cut nanocube close to the quantum cluster, the cut nanocube alone and the full NP (in which the nanocube and the vertex are a single body treated classically). As figure 2 shows, the absorption spectra of the three structures are perfectly superposed, since the structural differences are too small to be detected. This result points out that from the NP point of view, the dynamics in the three different situation are quite close.

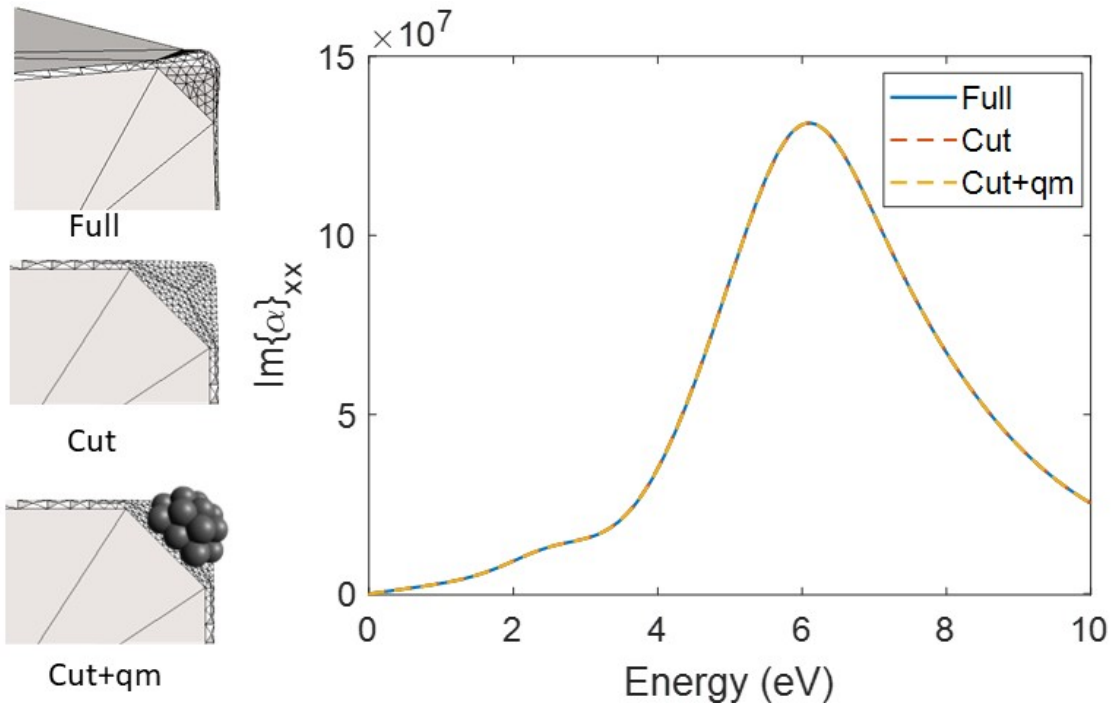Finally, in order to investigate how the cut close to the nanocube vertex impacts on the

Figure 2: Comparison between the absorption spectra of the nanocube close to the quantum cluster, the cut nanocube alone and the full NP. The three structures are reported on the left side of the figure.

NP response we computed the potential generated on a surface opposite to the atomistic vertex when close to the full NP (i.e. with the vertex "attached" to the cut surface) and in proximity to the cut nanocube close to a classic vertex (i.e. the vertex and the cut surface are spaced by the rhodium inter-layer distance). We report in table 1 the potential computed on the centre of the surface (at coordinates [0,0,0]) which is a point laying on the line perpendicular to the cut vertex and on one corner of the surface (at coordinates [6,3.5,6]). The results show a very good accordance in terms of potential and they are very close in particular in the lateral point of the surface (at coordinates [6,3.5,6]) while small discrepancies can be noticed on the potential computed in the central point that is more affected by the difference on the vertex in the two structures due to the vicinity. The overall effect of the two opposite surfaces generated when interfacing the cut NP with a classical vertex seems not to show a strong effect, at least in terms of generated potential and thus this structure can be safely employed for further calculation.

Table 1: Potential in atomic units generated on two points close to the NP vertex computed at two frequencies employed in the experiment[5] (2.7 eV and 3.4 eV) assuming the full NP (i.e. the vertex is attached to the cut NP) and the cut NP put close to the cut vertex.

Structure	V([0,0,0]) 2.7 eV	V([6,3.5,6]) 2.7 eV	V([0,0,0]) 3.4 eV	V([6,3.5,6]) 3.4 eV
	-1818.38	-1504.82	-1975.20	-1625.55
	-1715.43	-1555.20	-1769.81	-1664.25

Computational Details

- The atomistic structure of Rh_{19} cluster used to model the corner of the Rh nanocube has been carved from a Rh(111) slab, optimized at the Density Functional Theory (DFT) using a plane-waves basis set as implemented in Quantum Espresso, version 6.3.[6,7] In this calculation electron-electron interactions were described by the Perdew-Burke-Ernzerhof (PBE) exchange-correlation functional,[8] core-electrons were modelled with the Optimized Norm-Conserving Vanderbilt (ONCV) pseudopotential[9] and the energy cut-off for the basis set expansion was set to 1080 eV. Previous calculations[10] performed on bulk Rh found an equilibrium lattice constant of 3.833 Å and such a parameter were used to build a 4-layers slab exposing a 4x4 Rh (111) supercell. The geometry optimization of this system was made on a 8x8x1 k-point grid and included an extra 20 Å vacuum layer added along the direction orthogonal to the surface and for dipole corrections,[11] both accounted to prevent the formation of spurious electric fields in the system. Keeping the two bottom layers fixed at their ideal bulk positions, all the remaining atoms were relaxed according to the Broyden–Fletcher–Goldfarb–Shanno (BFGS) quasi-Newton algorithm[12] until the residual forces were lower than 10^{-4} eV/Å, with a convergence threshold on the ground state total energy of 10^{-9} eV. Once relaxed, Rh_{19} was extracted from the two outermost layers of the slab and then used as substrate

for the geometry optimization of CHO species. Such a calculation was performed at the DFT level, using PBE XC-functional and a double-zeta basis set by means of AMS package,[13] freezing the bottom layer of the cluster in order to maintain Rh(111) surface structure.

- DFT and GW-BSE calculations were performed as implemented in the MOLGW code,[14] employing def2-TZVP basis set[15] and the PBE0 functional.[16] Eigenvalue-self-consistent $G_n W_n$ calculations were carried out, with eigenenergies converging within 4 iterations. The contributions from core electrons were neglected in the calculation of the screened Coulomb interaction and of the single particle Green's function whereas all the empty orbitals allowed by the basis set were considered for both. 455 $|\lambda\rangle$ states were employed for the Rh_{19}-CHO cluster dynamics.

- Electron dynamics, with and without the classical NP, have been carried out with WaveT code.[17,18] We have employed a Gaussian envelope function for the time-dependent external field:

$$\vec{F}(t) = \vec{F}_{max} \exp\left(-\frac{(t - t_0)^2}{2\sigma^2}\right) \sin(\omega t), \tag{1}$$

where $\vec{F}_{max}$ is the field amplitude (the intensity I is equal to $\frac{1}{2}|\vec{F}_{max}|^2$), t_0 and σ are the centre and the amplitude of the Gaussian respectively, and ω is the pulse frequency. The pulse wavelength is 365 nm, with FWHM equal to 21 fs, within the weak field regime. The pulse has linear polarization perpendicular to the vertex of the nanocube. A second Euler algorithm[3] was used to propagate TDSE. We simulated 100 fs with a time step of 1.21 as, to obtain the dynamics of the surface charges and of the wave function coefficients.

- A homemade Fortran 90 code has been used to compute the ΔPDOS as in equation 7 of section Methods and its integral as in equations 9 and 10 in order to compute electron and hole injection. The amplitude of the Lorentzian function is 0.0272 eV and the energy grid used to compute ΔPDOS and its integration goes from -21.7 eV to

21.7 eV with a step of 0.0217 eV. The post-processing calculation has been performed considering either two fragments (CHO and all rhodium atoms) or six fragments (C, O, H, Rh closest to O, Rh closest to C and all the other Rh atoms).

References

(1) Volakis, J. L.; Sertel, K. *Integral Equation Methods for Electromagnetics*; 2012; pp 1–392.

(2) Palik, E.; Gosh, G. *Handbook of Optical Constants of Solids*; Academic Press: San Diego, USA, 1998.

(3) Pipolo, S.; Corni, S. Real-Time Description of the Electronic Dynamics for a Molecule Close to a Plasmonic Nanoparticle. *J. Phys. Chem. C* **2016**, *120*, 28774–28781.

(4) Dall'Osto, G.; Gil, G.; Pipolo, S.; Corni, S. Real-time dynamics of plasmonic resonances in nanoparticles described by a boundary element method with generic dielectric function. *J. Chem. Phys.* **2020**, *153*, 184114.

(5) Yang, B.; Chen, G.; Ghafoor, A.; Zhang, Y.; Zhang, Y.; Zhang, Y.; Luo, Y.; Yang, J.; Sandoghdar, V.; Aizpurua, J.; Dong, Z.; Hou, J. G. Sub-nanometre resolution in single-molecule photoluminescence imaging. *Nature Photonics* **2020**, *14*, 693–699.

(6) Giannozzi, P. et al. QUANTUM ESPRESSO: a modular and open-source software project for quantum simulations of materials. *Journal of Physics: Condensed Matter* **2009**, *21*, 395502.

(7) Giannozzi, P.; Andreussi, O.; Brumme, T.; Bunau, O.; Buongiorno, M.; Marsil, M.; Paulatto, L.; Rocca, D. Advanced capabilities for materials modelling with Quantum ESPRESSO. *Journal of Physics: Condensed Matter* **2017**, *29*, 465901.

(8) Perdew, J. P.; Burke, K.; Ernzerhof, M. Generalized gradient approximation made simple. *Physical Review Letters* **1996**, *77*, 3865–3868.

(9) Hamann, D. R. Optimized norm-conserving Vanderbilt pseudopotentials. *Physical Review B - Condensed Matter and Materials Physics* **2013**, *88*, 1–10.

(10) Vanzan, M.; Marsili, M.; Corni, S. Study of the Rate-Determining Step of Rh Catalyzed CO_2 Reduction: Insight on the Hydrogen Assisted Molecular Dissociation. *Catalysts* **2021**, *11*, 538.

(11) Bengtsson, L. Dipole correction for surface supercell calculations. *Phys. Rev. B* **1999**, *59*, 12301–12304.

(12) D. Head, J.; Zerner, M. C. A Broyden—Fletcher—Goldfarb—Shanno optimization procedure for molecular geometries. *Chemical Physics Letters* **1985**, *122*, 264–270.

(13) Rüger, R.; Franchini, M.; Trnka, T.; Yakovlev, A.; van Lenthe, E.; Philipsen, P.; van Vuren, T.; Klumpers, B.; Soini, T. AMS 2022.1, SCM, Theoretical Chemistry, Vrije Universiteit, Amsterdam, The Netherlands. 2022; `http://www.scm.com`.

(14) Bruneval, F.; Rangel, T.; Hamed, S. M.; Shao, M.; Yang, C.; Neaton, J. B. MOLGW 1: Many-body perturbation theory software for atoms, molecules, and clusters. *Comput. Phys. Commun.* **2016**, *208*, 149 – 161.

(15) Pritchard, B. P.; Altarawy, D.; Didier, B.; Gibson, T. D.; Windus, T. L. New Basis Set Exchange: An Open, Up-to-Date Resource for the Molecular Sciences Community. *J. Chem. Inf. Model.* **2019**, *59*, 4814–4820.

(16) Adamo, C.; Barone, V. Toward reliable density functional methods without adjustable parameters: The PBE0 model. *J. Chem. Phys.* **1999**, *110*, 6158–6170.

(17) Coccia, E.; Fregoni, J.; Guido, C. A.; Marsili, M.; Pipolo, S.; Corni, S. Hybrid theoretical models for molecular nanoplasmonics. *J. Chem. Phys.* **2020**, *153*.

PART II

Chapter 4

This chapter begins the second part of my Ph.D. thesis, which deals with the calculation of Raman spectra of molecules in different environments and with different approaches.[17] First, I considered an existing and validated strategy to calculate the Raman spectra of some particular amino acids in aqueous solution[68, 69] when they interact with certain cations. The choice of target molecules was motivated by the recent experimental purpose of sequencing a protein by high-resolution Raman spectroscopy, which is performed when a protein translates in a plasmonic nanopore.[70, 71] In this context, many features of the environment surrounding the proteins contribute to alter the response of the single amino acid within the chain, such as the solvent, the electric field generated by the nanopore, the electric field required for translocation, the frequency of the incident laser, the interaction with ions in the solution, and also the influence of the first neighbouring amino acids.[72] My focus was on studying the influence of ions on the Raman spectra of some amino acids with water as solvent and an incident monochromatic pulse with two common laser frequencies.

I have used a frequency-domain method based on the Placzek approximation[73] to calculate the Raman activity of individual amino acids in the vicinity of a cation, with the solvent accounted for by an implicit model in the framework of PCM. The equation for calculating Raman activity and the PCM equation for the implicit model were already implemented in the latest version of G16, [74] which I used for the calculations. The amino acids studied were selected on the basis of the distribution of electronic charge density on their side chain, giving preference to those that can

interact with positive charges in the vicinity, namely glutamate, tyrosine, serine, and cysteine. On the other hand, the variety of ions considered reflects the possibility to study the role of the cation dimension by testing different alkali ions (Li^+, Na^+, K^+), as well as the effect of transition metal cations (Cu^+, Ag^+, Au^+, Cu^{++}) that can modify certain normal mode frequencies or enhance Raman spectra in case of resonance conditions.

All the work was done in collaboration with Dr. Ornella Vaccarelli (UniLu), who assisted me in further calculations and analysis of the data. I took care of the preparation of images, tables and the first draft of the manuscript.

Role of ions in solvated Amino acids Raman spectra

Giulia Dall'Osto,[†] Ornella Vaccarelli,[‡] Ciro A. Guido,[¶] and Stefano Corni[*,†,§]

[†]Department of Chemical Sciences, University of Padova, via Marzolo 1, 35100, Padova, Italy

[‡]Department of Physics and Materials Science, Université du Luxembourg 162 A, avenue de la Faïencerie L-1511 Luxembourg

[¶]Department of Science and Technological Innovation, Università del Piemonte Orientale, Viale T. Michel 11, 15121 Alessandria, Italy

[§]CNR Institute of Nanoscience, via Campi 213/A, 41100, Modena, Italy

Abstract

Raman spectroscopy is a very informative technique that is routinely applied to proteins and peptides. It is no surprise therefore that Raman spectra of single amino acids are well-characterized. Yet, proteins and peptides are seldom present in absence of an ion in solution. The way ions can modify Raman spectra of amino acids (and in turns of peptides and proteins) have not been systematically characterized. In this paper, the ion effect on the Raman spectra of four significant amino acids (glutamate, tyrosine, cysteine, serine) and N-methylacetamide (prototype of the peptide bond) in aqueous solution has been studied at DFT level of theory. The investigation of band shifts and variations of peaks intensity has been carried out considering different cations commonly employed in experiments (Li^+, Na^+, K^+, Ag^+, Au^+, Cu^+, Cu^{++}). This study can serve as reference for the interpretation of Raman spectra of proteins and biological materials.

Introduction

Raman spectroscopy[1–4] is a well known tool useful to give insight on the molecular structure of molecules.[5,6] This spectroscopic technique focuses on the difference between the incident laser frequency and the scattered frequencies determined by the vibrational frequencies characteristic of the molecule. For this reason, Raman spectra of molecules are quite unequivocal, since they are the image of their vibrational structure.

In this work, we focus our attention on simulation of Raman spectra of amino acids in water solution.[7–9] Amino acids are the building blocks of proteins, one of the four macro molecules fundamental for life, and therefore they have been widely studied. Different approaches can be employed to characterize amino acids as single molecules in solution. However, the hardest challenge is to reveal the amino acidic sequence inside a protein chain exploiting both single-molecule spectroscopies[10–14] and high spatial resolution techniques.[15–17] To this point a sensitive technique, such as surface enhanced Raman scattering (SERS),[18–20] has already been employed in combination with plasmonic hot-spot where the electromagnetic field is highly localized and enhanced.[21–23] For the time being, this technique is limited to short peptides and more advanced technologies are developing based on the application of a static electromagnetic field able to orient the protein and an electrophoretic field that guides the protein movement.[24,25] In this framework, it is worth to mention that an opportune ionic composition can modify the properties of the fluid in which the protein is immersed and thus modifying also the molecule response. Indeed, the interaction between amino acids and ions in solution may affect the Raman signals[26] under several points of view. In the first place, the ion electronic states coupled with the vibrational modes of the molecule can modify the signal, either in terms of intensity or frequency position. Moreover, the electronic states of the ion may be closer to the amino acids electronic states fostering charge-transfer excitations which in some cases are close or match the Raman laser steering the process towards Resonance Raman scattering, instead of the non-resonance condition typical of all the natural amino acids in presence of laser fields in the optical range commonly employed.

Our work focuses on the investigation of the ion effects on the Raman spectra of four relevant amino acids in water solution through computational methodologies. All the target molecules are L-amino acids chosen for having a strong electron density on the lateral chain: glutamate ends with a carboxyl moiety, tyrosine lateral chain is an aromatic ring with a hydroxy termination, serine has an hydroxyl group, and cysteine has the same structure of cysteine but for the exchange of an oxygen atom with a sulfur atom at the end of its side chain. Moreover N-methylacetamide has been studied as prototype of the peptide bond in order to examine which is the ionic influence on the protein backbone.

We propose a quantum mechanical description of the amino acids including explicitly one ion for each simulation whereas the solvent has been included through an implicit model. To keep the same structure for all calculations, only one ion has been included in each simulation and it has been placed in proximity of the amino acids side chain as initial guess before the geometry optimization. On the other hand, in presence of N-methylacetamide the ions have been placed close to the oxygen of the amide, that is the most electronegative atom of the molecule. All the amino acids under study have been protected by an acetate at the N-terminus and a methyl-amine at the C-terminus to mimic the continuity of the protein chain beyond the peptide bond and to avoid effects due to the interaction between isolated amino acid charges generated on the carboxyl and amine terminations.

The Raman spectra of these amino acids have been computed highlighting how different ions affect the main Raman signals in the finger print region. This analysis is useful to assign Raman bands to the correct amino acids when peptide chains are immersed in an ionic solution. We have focused on the interaction of the amino acids with different meaningful cations: alkali metal ions (Li^+, Na^+, and K^+) to highlight the effect of the different radii of the alkali metal ions on the structure and vibrations of the amino acids-ion complex where the electrostatic interaction is predominant. Other cations that mostly have chemical interactions with the peptides have been taken into account to compare them with alkali metal ones. Among them we focus our attention on Ag^+, Au^+, Cu^+, and Cu^{++} which are

known to be relevant to enhance Raman signal as in the case of SERS.[27–29]

Hereafter, a section reports all the computational details of our calculations to ensure reproducibility, followed by our results and discussion on them. In the last section, final remarks have been reported.

Computational details

All the calculations have been performed at DFT level of theory with Gaussian16[30] employing B3LYP exchange-correlation functional and 6-31G** basis set for smaller atoms (C, H, O, N, S, Cu), 3-21G basis for Ag, and LanL2DZ for Au (with LanL2DZ pseudo-potential). The solvent has been included as a continuous embedded through the polarizable continuum model (PCM) framework.[31] We considered the amino acids solvated in water described by its dielectric constant at room temperature ($\epsilon = 78.3553$). The molecular cavity is built as the intersection of spheres, each of one is centred on one atom of the molecule with universal force field (UFF) radii. Fist, we performed a geometry optimization of all the amino acid-ion pairs by placing the cation close to the most electronegative atom of the amino acid lateral chain as initial guess. Afterwards, Raman calculations were carried out considering two laser frequencies, 530 nm and 785 nm, typical values used for Raman spectroscopy. For some pairs, in particular when a transition metal is involved, the calculation of electronic transitions has been performed at TDDFT level of theory using either B3LYP or CAM-B3LYP exchange correlation functional to check the possible role of charge transfer. In all the calculations performed, the excitation energies computed with the two different functionals are quite close. However with CAM-B3LYP the excitation energies predicted are a little larger than with B3LYP functional and in general further from the laser energy employed in Raman calculations. For this reason the excitation energies reported in the following section refer to calculations with B3LYP functional. We are aware that charge transfer excitations are usually better predicted by using CAM-B3LYP that B3LYP functional.[32] Calculations

have been performed on N-methylacetamide (as prototype of the peptide bond), glutamate, tyrosine, cysteine and serine while the cations considered in the calculations are Li^+, Na^+, K^+, Ag^+, Au^+, Cu^+, Cu^{++}. All the spectra reported below are a convolution of the stick spectra with width 10 cm^{-1}.
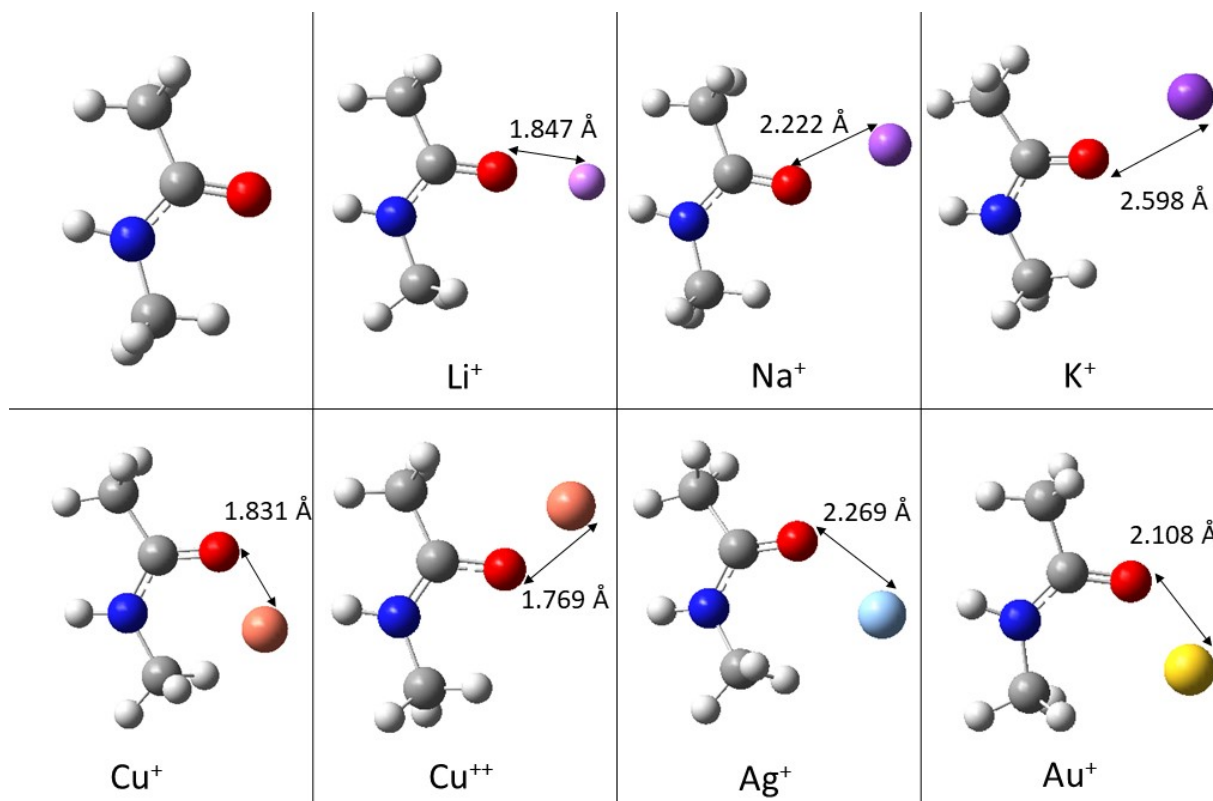

Figure 1: Optimized structures of N-methylacetamide in presence of different cations, the distance between the oxygen atom and the ion is reported.

Results and discussion

Here we present the main results of Raman calculations of different amino acid-cation pairs, focusing on the effects of the cations on the Raman bands of the amino acids in the fingerprint region. Raman calculations have been performed including the incident electric field, whose frequency is either 785 nm or 530 nm, to reproduce laser pulse usually employed in the experiments. In this section we focus on the results obtained at the longer wavelength,

because we find them to be the most interesting, particularly in the case of Raman resonance. The spectra calculated at a frequency of 530 nm can be found in the Supporting Materials. At the end of the results a summary of the main peaks and features of the Raman spectra calculated have been reported in table 1.

N-methylacetamide

The geometry of N-methylacetamide in presence of different cations has been optimized, as the structures reported in Fig. 1. As initial guess the cation has been placed close to the oxygen of the amide and it remained in that region after the optimization. As expected, the distance between the ion and the oxygen atom increases with the ion size, with Cu^{++} being the closest ion and K^+ the farthest, as reported in figure 1.
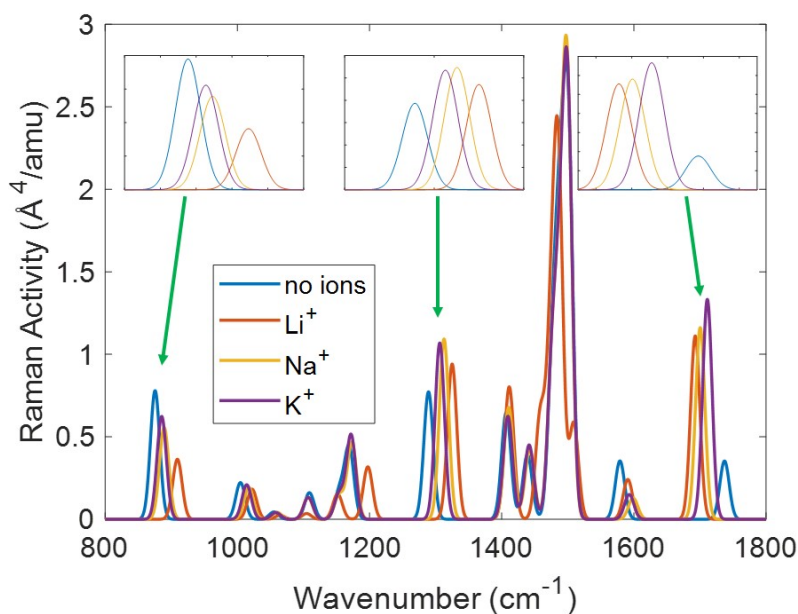
Figure 2: Raman spectra of N-methylacetamide in water without ions and in presence of Li^+, Na^+, K^+ in the fingerprint region, with incident laser frequency equal to 785 nm. The insets show a magnification of three regions.

Figure 2 compares the Raman spectra computed with incident laser frequency equal to 785 nm of N-methylacetamide in the presence of alkali metal ions to those obtained when ions are absent. The presence of different cations close to the molecule translates into a shift

of some Raman peaks. In particular, the peaks around 900 cm^{-1} and around 1300 cm^{-1} are blue-shifted in the presence of alkali metals. The effect is larger with lithium, as it is the closest ion, while it is less evident with larger metals, although the overall intensity of the signals is not strongly affected. On the contrary, the peak at 1700 cm^{-1} is enhanced when
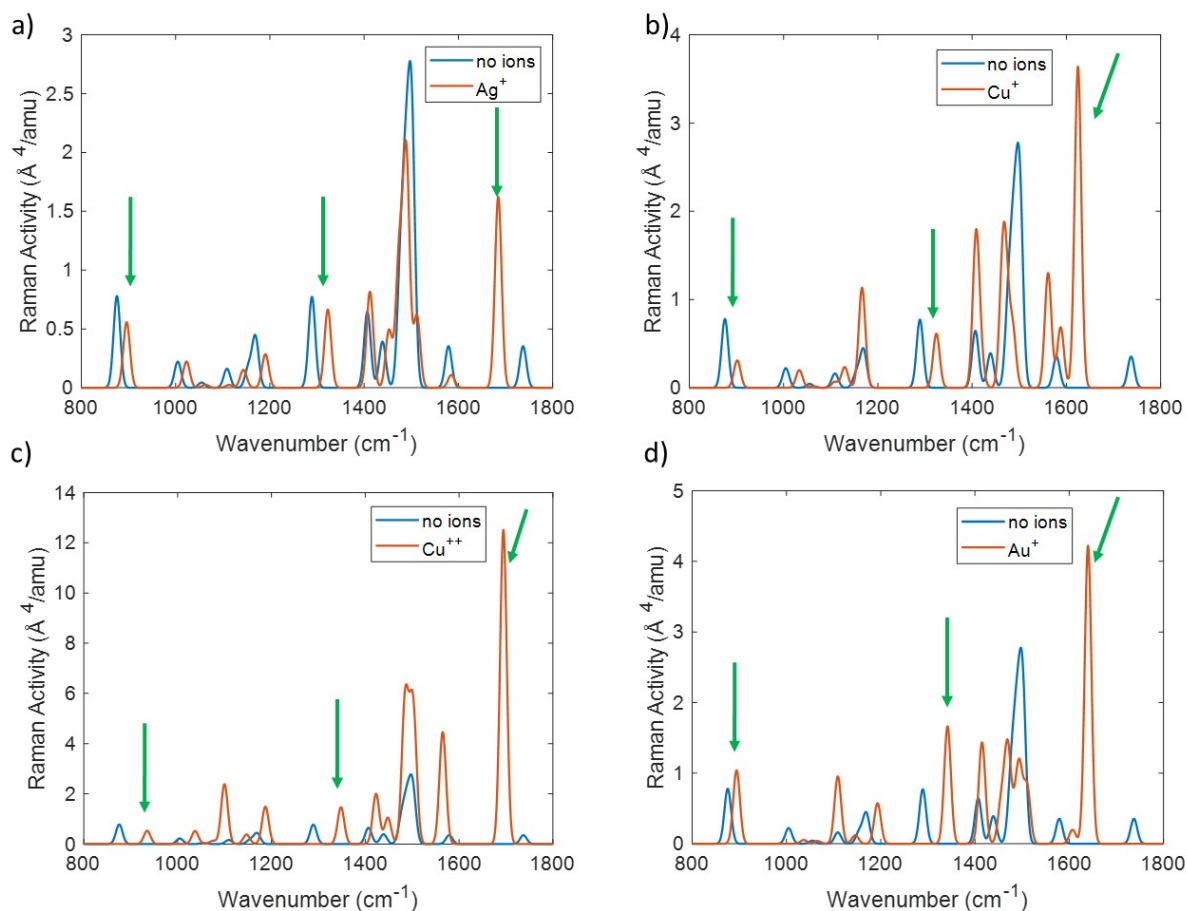

Figure 3: Raman spectra of N-methylacetamide in presence of Ag$^+$ (panel a), Cu$^+$ (panel b), Cu^{++} (panel c), Au$^+$ (panel d) in the fingerprint region, with incident laser frequency equal to 785 nm.

an alkali metal is placed close to N-methylacetamide and it is red-shifted, showing a larger effect with smaller cations as before. The peaks at 900 cm^{-1} and at 1300 cm^{-1} are primarily due to the CH$_3$ bending and, to a lesser extent, to the C=O bending. The main feature of the peak at 1700 cm^{-1}, on the other hand, is caused by the C=O stretching.

The same trend holds when N-methylacetamide is in the presence of Ag$^+$, Cu$^+$, Cu^{++},

Au$^+$, as reported in Fig. 3: the peaks at 900 cm^{-1} and at 1300 cm^{-1} are blue-shifted, while the peak at 1700 cm^{-1} is red-shifted. Nonetheless, the intensity of the peak at 1700 cm^{-1} and the energy shift is different with different metals: the energy shift is particularly larger in presence of Cu$^+$ and Au$^+$ while the intensity is mostly enhanced in the presence of Cu^{++}.

In this section, we have highlighted the prominent Raman peaks common to any peptide or protein backbone that change in terms of intensity and position when certain ions are present. In the following, the analysis is extended to bands associated with the later chains of specific amino acids.
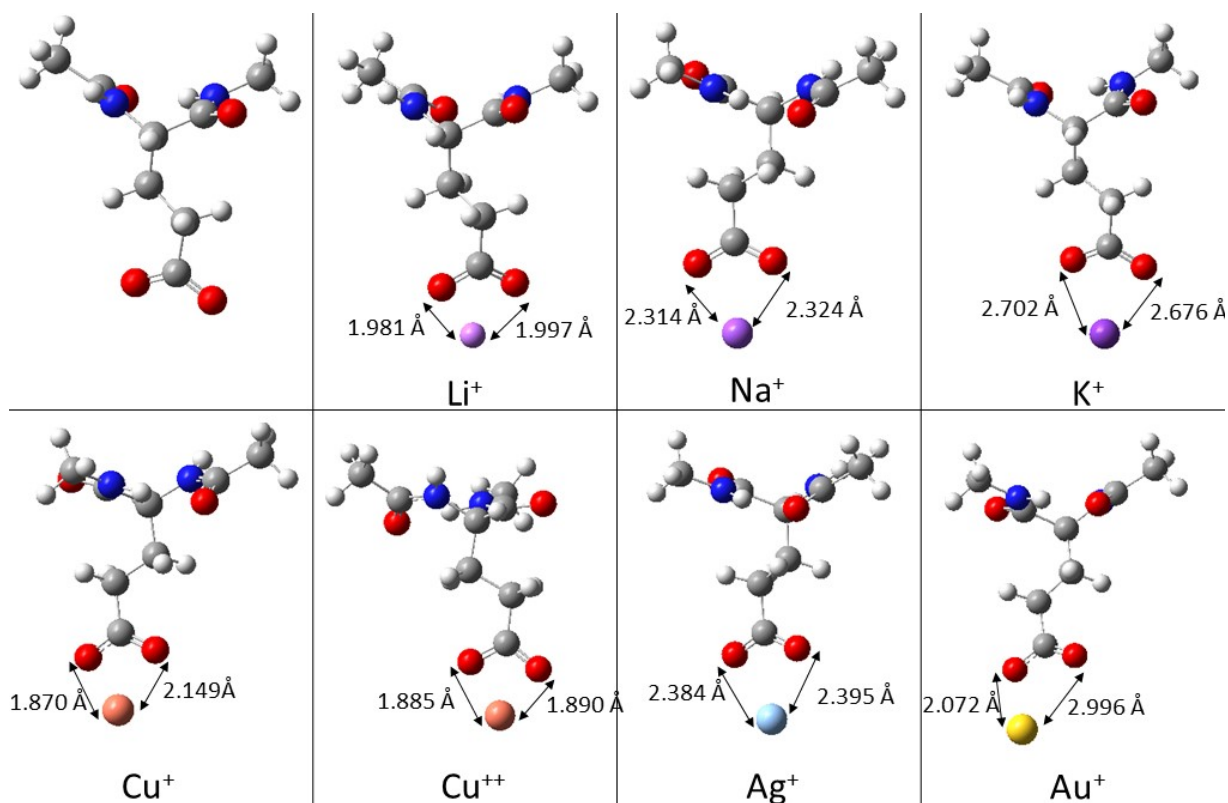
Figure 4: Optimized structures of glutamate in presence of different cations, the distance between the oxygen atoms and the ion is reported.

Glutamate

The geometry of glutamate has been optimized. The choice of considering the side chain deprotonated (i.e., glutamate as opposed to glutamic acid) is coherent with a neutral pH

112

condition. The optimized structures are reported in Fig. 4. All the calculations have been performed with water as solvent. In all the cases, the cation remains very close to the carboxyl group of the glutamate lateral chain. In particular, the distances between the oxygen atoms and the ions in all cases show that the ion is coordinated between the two oxygen atoms, except for gold, which is preferentially attached to one of the two oxygen atoms, where the distances are, in fact, 2.072 Å and 2.996 Å respectively, as reported in Fig. 4. The behaviour of Au^+ can be explained by its tendency to form linear complexes with two ligands,[33,34] instead of bonding to a bidentate ligand as a carboxyl group.

The Raman spectra of glutamate in presence of three alkali metal ions (Li^+, Na^+, K^+) is reported in Fig. 5 in comparison with the spectra without ions when the incident laser frequency is 785 nm. The spectra are extremely similar, except for the two regions where the asymmetric and symmetric stretching of the carboxyl group lay. Precisely, the peak at 900 cm^{-1}, corresponding to the symmetric stretching of the carboxyl group, is blue-shifted when glutamate is in presence of an alkali metal ion and the effect is more pronounced with smaller ions. On the other hand, the asymmetric stretching has very low intensity without the presence of ions and it is not visible due to the superposition with another peak at 1700 cm^{-1} corresponding to a stretching of the amide group. However, the peak related to the carboxyl asymmetric stretching become more evident when glutamate is in presence of alkali metals and it is also red-shifted, the smaller is the cation the larger is the shift (it shifts at 1605 cm^{-1} with Li^+, at 1621 cm^{-1} with Na^+, at 1643 cm^{-1} with K^+).

Hereafter, we focus on the glutamate Raman spectra in presence of Ag^+, Cu^+, Cu^{++}, Au^+. The glutamate in presence of Cu^+ and Cu^{++} presents an electronic transition very close to the frequency of the incident radiation. In particular, TDDFT calculations estimate an electronic transition at 771 nm with Cu^+ characterized by a large transition dipole moment, while with Cu^{++} glutamate shows a partially dark electronic transition at 775 nm. The presence of electronic transitions close to the incident laser frequency translates into an enhancement of the Raman spectra, due to the resonance between incident laser frequency
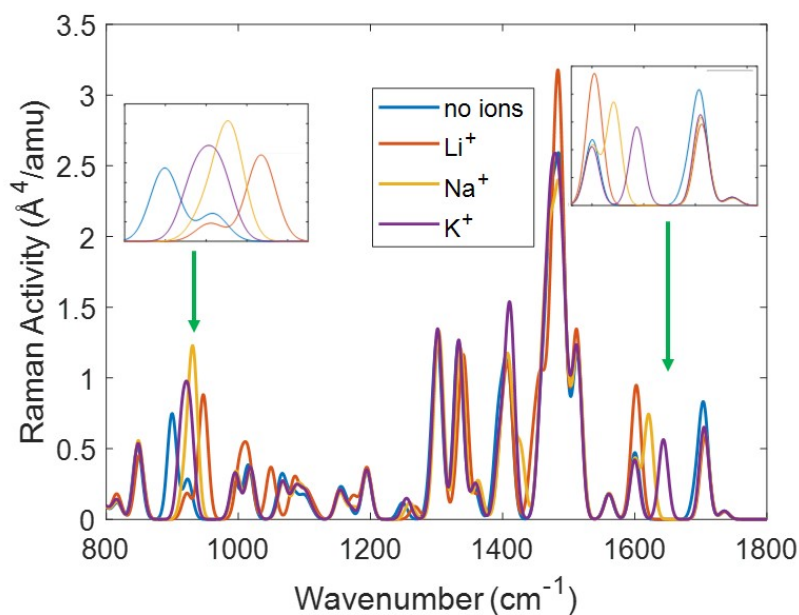
Figure 5: Raman spectra of glutamate close to Li^+, Na^+ or K^+ compared with the spectrum computed in absence of ions, with incident radiation frequency equal to 785 nm. The inset show a magnification of two regions of the spectra corresponding to the symmetric and asymmetric stretching of the carboxyl group.

and electronic transitions. On the other hand, the peaks position and the relative intensity is no more very reliable due to the Placzek approximation adopted in the Raman calculations performed here that is fully justified only for non-resonance Raman spectra and for this reason they are not reported here but can be found in figure S7 of SI. Yet, this finding is important as it shows that the presence of such ions can enhance the Raman spectrum of specific groups. This may be used for example to improve the sensitivity of the measurements, or to help disentangling spectral features coming from different amino acids.

The Raman spectra of Glutamate in presence of Ag^+ and Au^+ are reported in Fig. 6. In this case, the glutamate-ion complex has not electronic transitions matching the frequency of the incident radiation. By analysing the TDDFT results, it turns out that the enhancement seen with gold is the effect of low energy (but non-resonant) electronic transitions due to the presence of the metal that increases the electronic polarizability at the incident frequency and its derivatives with respect to the relevant normal modes.
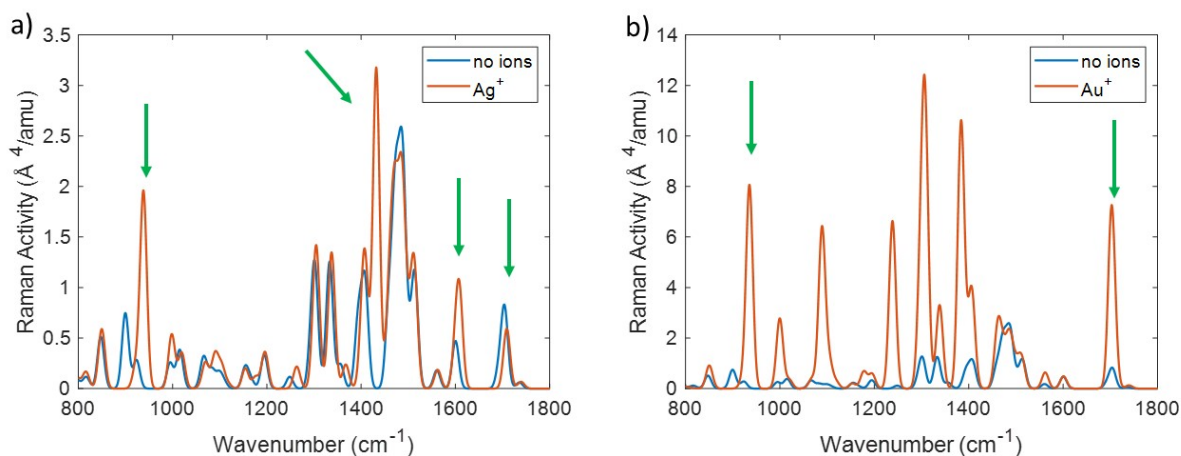
Figure 6: Raman spectra of glutamate in presence of Ag$^+$ (panel a) and Au$^+$ (panel b) in the fingerprint region, with incident laser frequency equal to 785 nm.

In presence of Ag$^+$, the symmetric and asymmetric stretching of the carboxyl group, respectively at 938 cm^{-1} and 1609 cm^{-1} are enhanced, a new peak emerges at 1432 cm^{-1}, that is a combination of the symmetric stretching of the carboxyl group and the C$-$C stretching which involves the carbon atom bonded to the oxygen atoms.

In presence of Au$^+$ the symmetric and asymmetric stretching of the carboxyl group, respectively at 935 cm^{-1} and 1702 cm^{-1}, are enhanced, while new peaks related to normal modes localized on the alkyl region of the glutamate lateral chain are enhanced at 1089 cm^{-1}, 1238 cm^{-1}, 1308 cm^{-1} and 1383 cm^{-1}.

Summarizing the results of this section, all the investigated ions can bind to the carboxyl group at the end of the chain (as shown by the geometry optimizations where the ions move toward the carboxyl group), and therefore the peaks in the Raman spectrum associated to normal modes more localized on the carboxyl group change in terms of position and intensity. Our results highlight the case of gold ions where also other peaks related to normal modes localized on the lateral chain of glutamate are enhanced as well as Raman spectra detected in presence of copper cations which are strongly enhanced due to resonance effect.

Tyrosine

The geometry of tyrosine has been optimized starting by an initial guess where a cation is placed close to the hydroxyl group. The resulting structures have been reported in Fig. 7. Among the metals considered, Li^+, Na^+, K^+, Ag^+ and Au^+ have settled close to the oxygen of the hydroxy at the end of the lateral chain, in the opposite position with respect to the hydrogen. Copper cations behave differently: Cu^{++} is positioned near the hydroxyl group but closer to the aromatic ring than the other cations mentioned above and Cu^+ is placed above the aromatic ring, equidistant from all the aromatic carbon atoms.
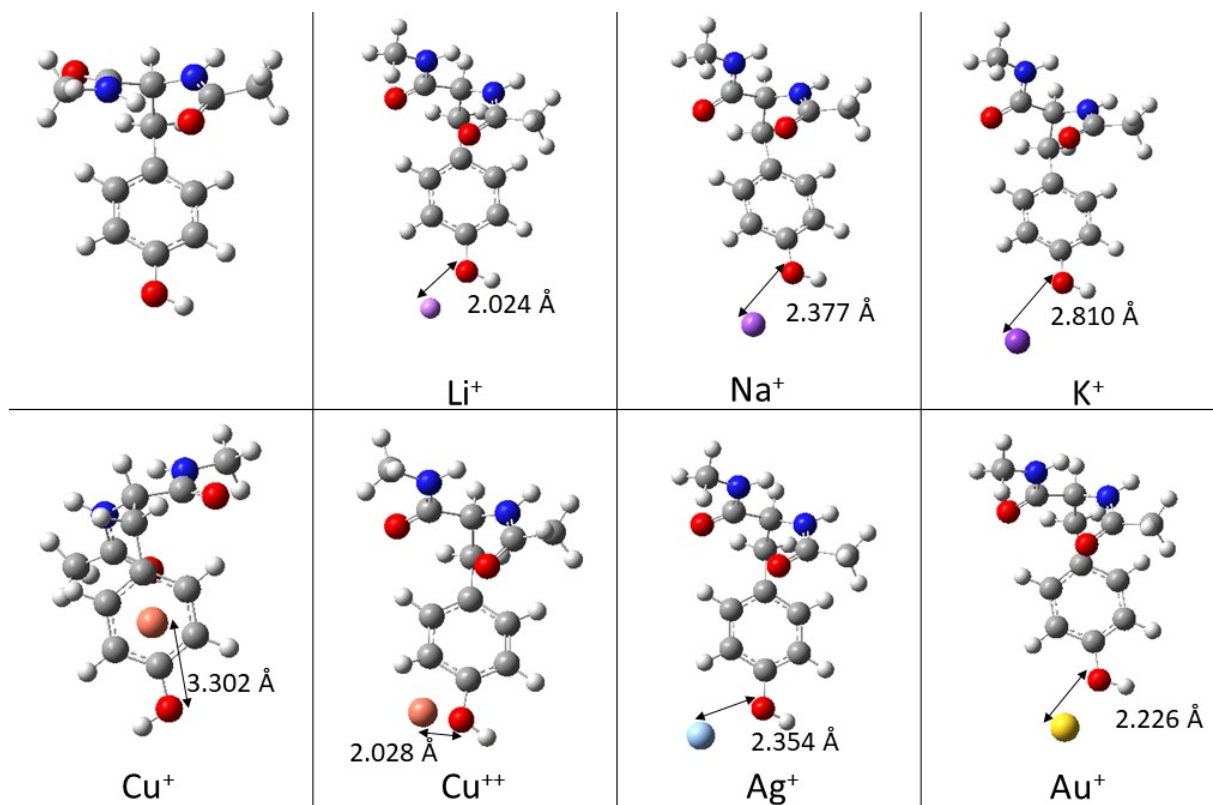
Figure 7: Optimized structure of tyrosine in presence of different cations, the distance between the oxygen atom and the ion is reported.

The Raman spectra in the fingerprint region have been reported in Fig. 8 in presence of different alkali metals (Li^+, Na^+, K^+). The presence of the cations does not strongly affect the position of the peaks. In particular, the peaks related to the motion of the carbon atoms in the aromatic ring (ring breathing at 839 cm^{-1} and stretching of the C−C bonds inside the

ring at 1664 cm^{-1}) remain in the same position and keep the same intensity. The peak at 1396 cm^{-1}, corresponding to the wagging of the $-CH_2$ belonging to the lateral chain, is quite superposed to the corresponding peak at 1399 cm^{-1} observed without ions. However, the peak at 1384 cm^{-1} observed in the spectrum of tyrosine without ions is a dark transition, not visible in presence of any alkali metals. This signal is related to a normal mode that involves the $-CH_2$ on the lateral chain, the α-carbon, the aromatic ring and also the hydroxyl group.
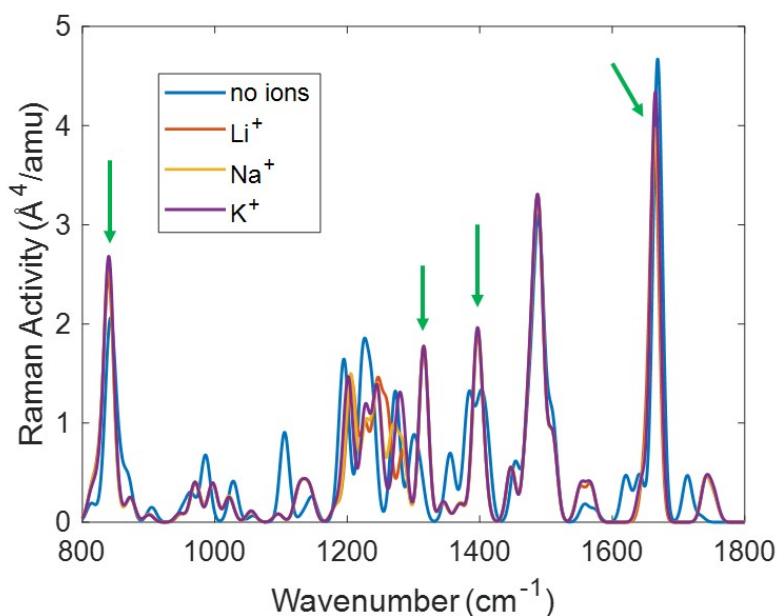
Figure 8: Raman spectra of tyrosine close to Li$^+$, Na$^+$ or K$^+$, with incident radiation frequency equal to 785 nm. The green arrows indicate specific peaks that are discussed in the main text.

Finally, the peak at 1315 cm^{-1} is more intense in presence of alkali metals, while without ions it is at 1310 cm^{-1} and has a very low intensity. This normal mode is related to a wagging of the $-CH_2$ of the lateral chain and to a bending of the N$-$H bond of the amides that is symmetric in the presence of the ion otherwise it is asymmetric. This variation seems dependent on the presence of the ion in proximity of the amino acid even though the cation is too far to affect directly this region of the molecule.

In the presence of Ag$^+$, the conformation of tyrosine and the position assumed by the ion is the same as in the presence of the alkali metals considered before. Moreover, the

Raman spectra in the fingerprint region is remarkably similar to those predicted when alkali metals are present. The spectrum, reported in Fig. 9 (a), shows the peak at 841 cm^{-1} related to the aromatic ring breathing and the peak at 1664 cm^{-1} corresponding to the C$-$C stretching inside the aromatic ring which are quite superposed to the same peaks in the spectrum of tyrosine without the presence of ions. On the same footing, also the peak at 1396 cm^{-1} is almost superposed with the corresponding one without the ion as well as the peak at 1384 cm^{-1} observed without the presence of the ion is missing. Finally, the peak at 1316 cm^{-1} is enhanced and also in this case this is due to the symmetric motion of the N$-$H bond in the amides while it is asymmetric without the cation.
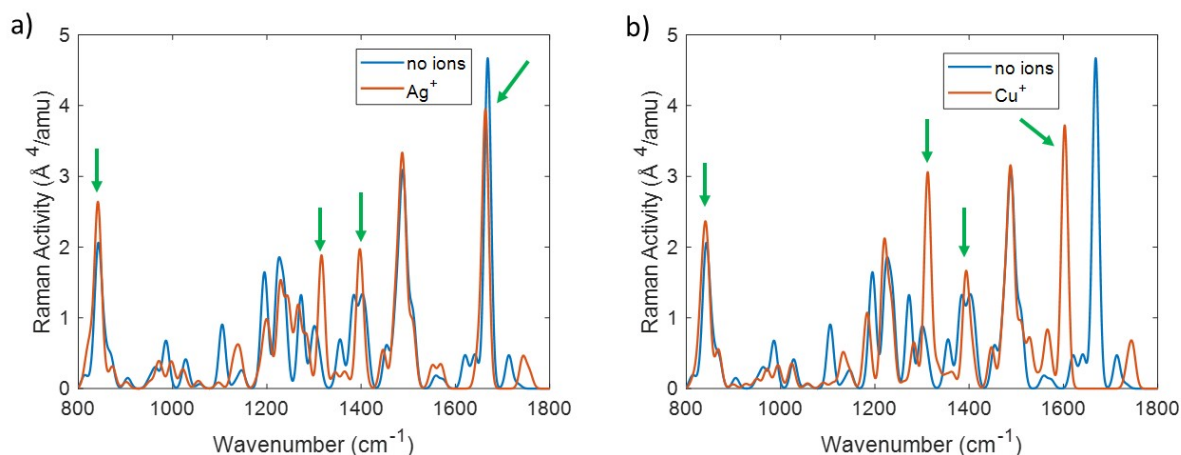
Figure 9: Raman spectra of tyrosine in the presence of Ag$^+$ (panel a) and Cu$^+$ (panel b) in the fingerprint region, with incident laser frequency equal to 785 nm.

When the Raman spectrum is computed in the presence of Cu$^+$ some differences can be noted, probably due to the different position that this cation assumes with respect to those previously mentioned. Indeed, the peak corresponding to the C$-$C stretching inside the aromatic ring is red-shifted at 1603 cm^{-1}, on the other hand the peak related to the ring breathing at lower energy is still at 842 cm^{-1} keeping the same intensity as in absence of ions. The $-$CH$_2$ wagging at 1393 cm^{-1} is still almost superposed with the one obtained without the ion, while the peak at 1384 cm^{-1} is still missing. Finally, the normal mode at frequency 1311 cm^{-1} is in this case strongly localized on the aromatic ring and on the

hydroxyl group and it is also enhanced.

The Raman spectra computed in the presence of Cu^{++} and Au^+ (reported in figure S12 of SI) are particularly enhanced due to the presence of an electronic transition close to the incident laser frequency. In particular, TDDFT calculations reveal an electronic excitation at 756 nm, when tyrosine is in the presence of Cu^{++}. For Au^+, an electronic transition is revealed by TDDFT calculations at 659 nm that, even if it is quite far from the laser frequency, affects the Raman spectrum because of the large transition dipole moment associated.

To sum up, there is a good correspondence on the Raman spectra in presence of different ions considered but for the enhancement of the peak around 1310 cm^{-1}. On the other hand, Cu^+ has the peculiar preference to stay closer to the aromatic ring that affects the Raman spectrum of tyrosine more than the other ions. Out of these considerations, two of the cations considered (Cu^{++} and Au^+) induce the presence of low energy electronic transitions which strongly affect the spectra, at least with the incident laser frequency employed, due to the resonance conditions.

Cysteine

The optimized cysteine structures, shown in Fig. 10, are computed with different cations placed in proximity of the thiol in the cysteine lateral chain as initial guess. The alkali ions moved close to the carboxyl group during the optimization so the expectation is that their presence can influence the same peaks of Raman spectrum mentioned for N-methylacetamide. On the other hand, the transition metal ions investigated bridged between the carboxyl and the thiol group. Although the gap between the distance from oxygen and sulfur reduces with silver and even more with gold, the ion is always closer to the oxygen atom than the sulfur atom.

The comparison of the spectra computed with an incident laser frequency of 785 nm in presence of the alkali metal ions and the spectrum of cysteine alone is reported in Fig. 11a.

119

As expected, the Raman signal is not strongly influenced by the presence of the alkali metal ions because the cations are placed close to the carboxyl group. Indeed the peaks majorly shifted are related to those whose normal modes involve such moiety. In particular, the peak around 1660 cm^{-1}, that is related to the C=O stretching of the carboxyl group close to the ion and an overall motion of the amide, is enhanced and also red-shifted. The peaks around 1000 cm^{-1} and 1300 cm^{-1}, whose normal modes involve the amide atoms displacement, are slightly shifted. On the other hand, the peak at 1750 cm^{-1}, related to the C=O stretching of the carboxyl group far from the cations, remains in the same position and with the same intensity with and without alkali metal cations. The three lower energy peaks (at 840 cm^{-1},
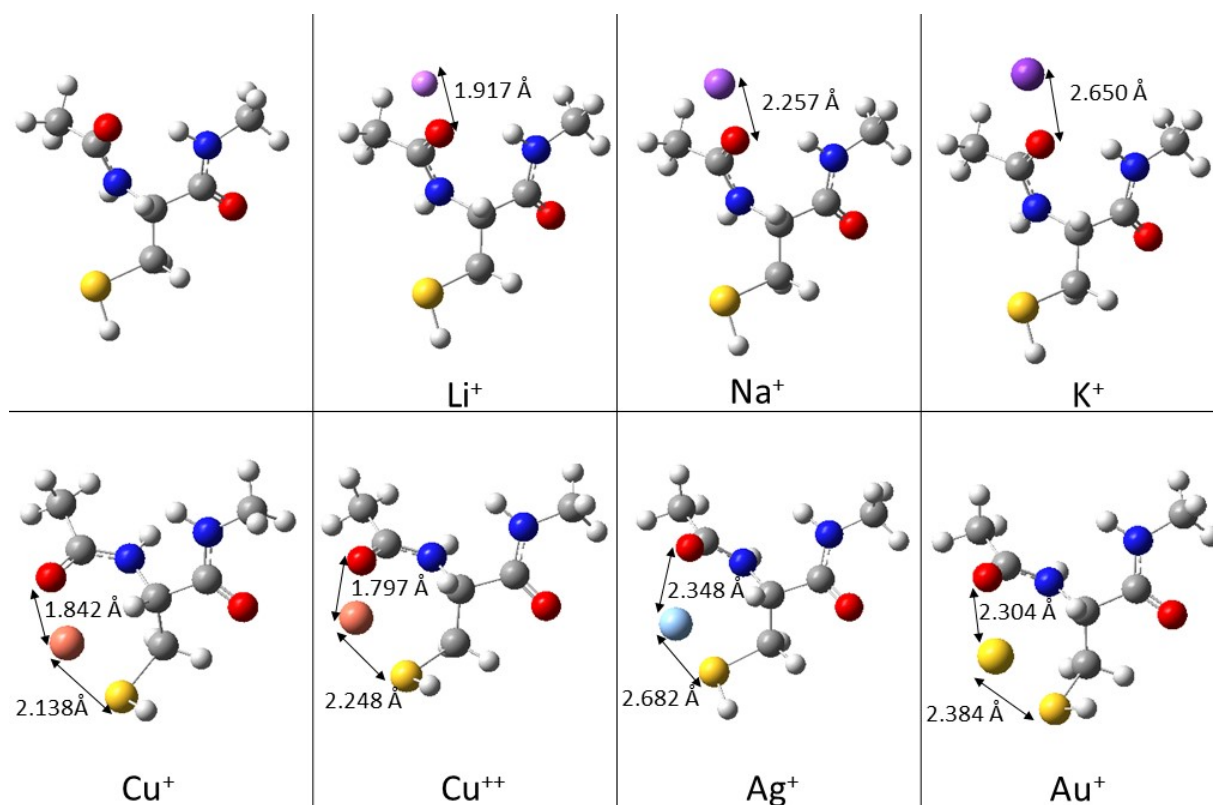
Figure 10: Cysteine optimized structure in presence of different cations, the distance between the oxygen atom and the ion is reported as well as the distance between the sulfur atom and the ion.

895 cm^{-1}, and 943 cm^{-1}) are related to normal modes that pertain to motion of thiol's atoms and they remain definitely superposed when in presence of alkali metal ions. In particular,

the normal mode related to the peak with higher intensity at 945 cm^{-1} is associated to the S−H bending. The most characteristic peak of this amino acid is placed outside the fingerprint region (as shown in Fig. S16 of SI), at 2700 cm^{-1}, and it is related to the S−H stretching.
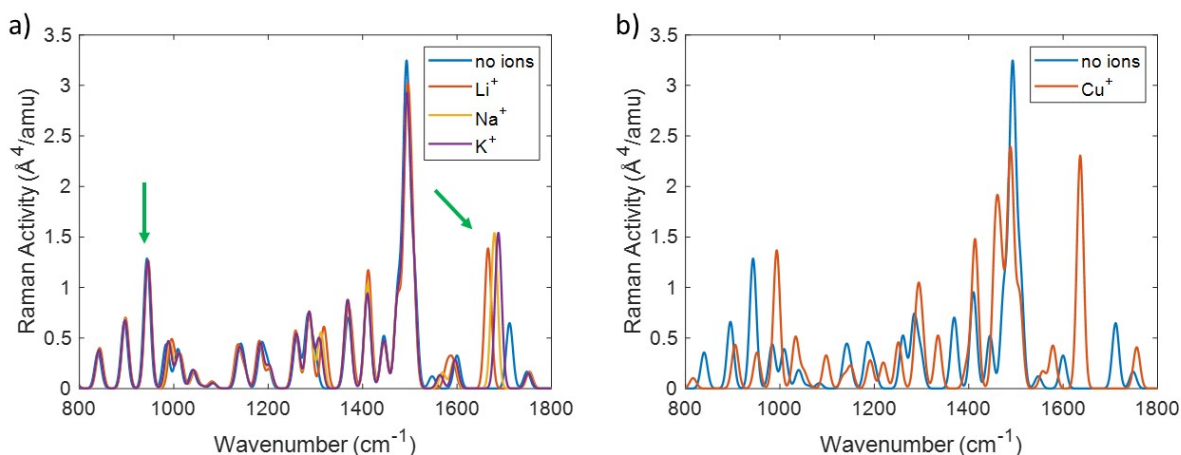

Figure 11: Raman spectra of cysteine in presence of Li$^+$, Na$^+$ or K$^+$ (panel a) and Cu$^+$ (panel b) in the fingerprint region, with incident laser frequency equal to 785 nm.

The Raman spectra of cysteine has been also computed in presence of Ag$^+$, Cu$^+$, Cu^{++}, Au$^+$. As shown above, in these cases the ion is found in between the carboxyl and the thiol groups during the geometry optimization. Three of these spectra seem the result of resonance Raman scattering, looking at the maximum intensity achieved in presence of Ag$^+$, Cu^{++}, Au$^+$ (spectra shown in figure S17 of SI) although only with Cu^{++} TDDFT calculations confirm the presence of an electronic transition very close to the incident laser intensity, at 808 nm. In presence of Ag$^+$ and Au$^+$ the lowest transitions computed are at 272 nm and 361 nm respectively, quite far from the laser energy, and even if they are allowed the magnitude of the transition dipole moment does not explain the high intensity of the Raman spectra. To better investigate these results we computed also the static Raman spectra of cysteine in presence of Ag$^+$ and Au$^+$ (figure S21 in SI) which, surprisingly are still enhanced. In these cases we suggest that a different mechanism than chemical enhancement due to metal-aminoacid interaction, as in typical SERS experiments, takes place, which is

not explainable in terms of electronic transitions close to resonance.

In presence of Cu^+, the Raman spectrum (Fig. 11b) does not show a resonance condition between incident and electronic transitions. However, the Raman spectrum appears quite different from the one computed without the presence of ions. The three low frequency peaks related to normal modes where the thiol bending contribution is relevant (840 cm^{-1}, 895 cm^{-1}, 943 cm^{-1}) move to lower intensities and different frequencies (respectively 815 cm^{-1}, 905 cm^{-1}, 951 cm^{-1}). On the other hand, the peak at 993 cm^{-1} related to a normal mode that involves a stretching of the carboxyl has higher intensity and there is not a clear correspondence on the Raman spectrum of cysteine without ions to the same normal mode. The peaks between 1400 cm^{-1} and 1500 cm^{-1} are approximately due to motions of the methyl termination, which in a real polypeptide would be the C_α of the next amino acids, so differences in this range are meaningless to our aim. Finally, the peak related to the C=O stretching of the carboxyl is red-shifted (from 1711 cm^{-1} to 1636 cm^{-1}) and strongly enhanced.

As a conclusion to this part, the relevant peak to distinguish cysteine from other amino acids is outside the fingerprint region (at 2700 cm^{-1}) due to the peculiar thiol group in its lateral chain. However, also the three low energy peaks below 1000 cm^{-1} are quite distinctive except in presence of Cu^+. Finally, these considerations are not valid in the presence of Ag^+, Cu^{++} and Au^+ because of the resonance expected or estimated between electronic transitions and the incident laser frequency.

Serine

The structure of Serine has been optimized in presence of different metal ions assuming the ions close to the hydroxyl group of the lateral chain as initial guess. The optimized geometries, reported on Fig. 12, show that the cations tend to be in the middle between the oxygen of the carboxyl and the oxygen of the hydroxyl even if they are in any case closer to the carboxyl. The difference in terms of distance from the two functional groups goes from

0.02 Å in case of Na$^+$ to 0.15 Å in case of Au$^+$, so the leanings of closing to form a cycle is even more evident than in the case of cysteine. In particular, the distance from the hydroxy in serine is smaller with all cations than the distance from the thiol of cysteine but for gold, which seems to prefer sulfur atom. Au$^+$ complexes has been already studied theoretically and experimentally in terms of binding energies, confirming the preference of staying closer to thiol groups than to hydroxyl group.[35] Moreover, with serine also the alkali metal ions are in the same position (e.g. in between the hydroxyl and carboxyl oxygen atoms).
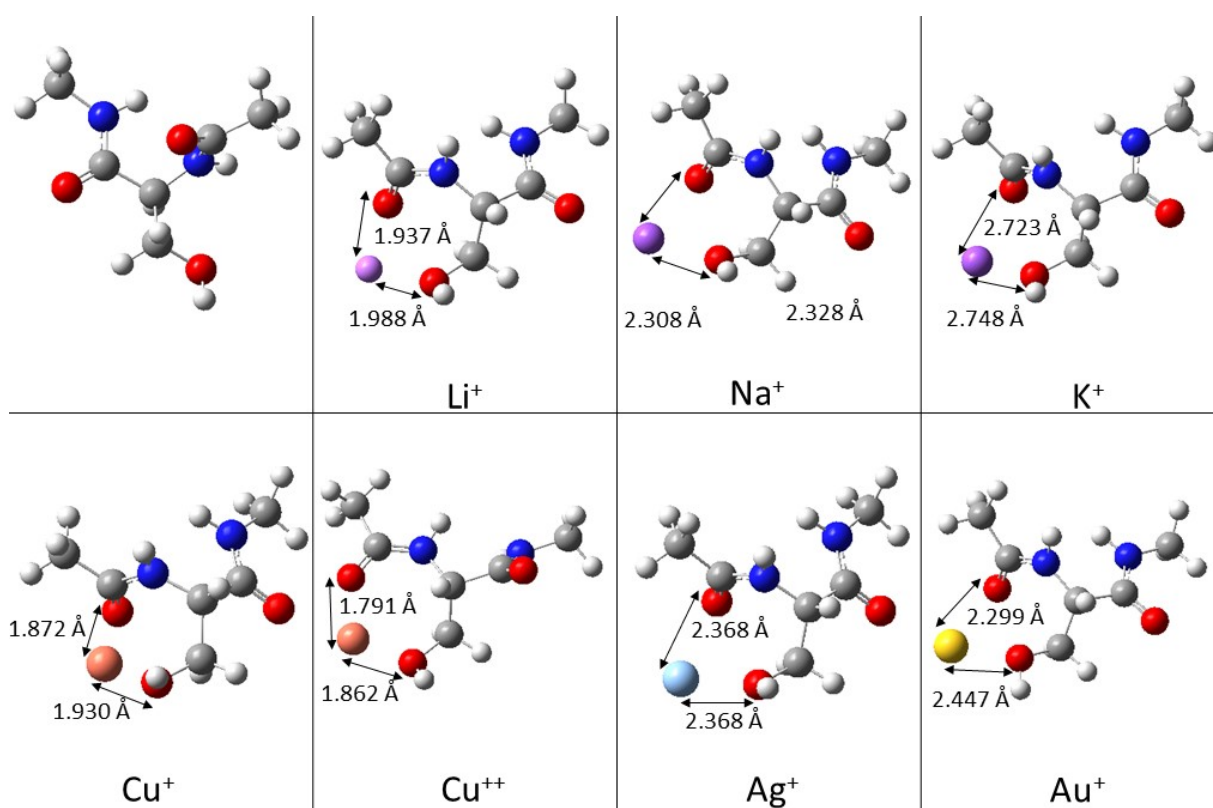
Figure 12: Serine optimized structure in presence of different cations, the distance between the oxygen atom of the carboxyl group and the ion is reported as well as the distance between the oxygen atom of the hydroxyl group atom and the ion.

The Raman spectra of serine in presence of the three alkali cations have been reported in Fig. 13a in comparison to the Raman spectrum of serine computed without ions, when the incident laser frequency is 785 nm. The three lower intensity peaks (around 860 cm^{-1}, 900 cm^{-1}, 940 cm^{-1}) are similar to those of cysteine since they are related to normal modes

that involve lateral chain atoms, although in this case they are slightly shifted and have different intensities compared to the Raman spectrum of serine without ions, due to the influence of the ion on the serine lateral chain. Moreover, the central peak, at 900 cm^{-1}, is not present without the ions. Two peaks, at 1270 cm^{-1} and 1300 cm^{-1} are enhanced in presence of the cations and are also slightly red-shifted: both of these peaks are related to normal modes that involve displacement of atoms inside the cycle generate between the carboxyl and hydroxy because of the ion placed in the middle. Finally, the two peaks due to the C=O stretching of the carboxyl groups, that are quite superposed in absence of ions at 1740 cm^{-1}, split in presence of alkali metal ions to a red-shifted and more intense peak mainly related to the motion of atoms inside the cycle, and a lower intensity peak due to C=O stretching of the carboxyl farther from the ion. In particular the splitting is higher for Li$^+$ and it decreases increasing the size of the ion.

The Raman spectra of serine in presence of Ag$^+$, Cu$^+$, Cu^{++}, Au$^+$ have been computed and the results are reported in Fig. 13, but for Cu^{++}. In presence of Cu^{++}, the spectrum is enhanced due to an electronic transition at 823 nm, close to the incident laser frequency, as a consequence the spectrum is in resonance regime (it has been reported in figure S23 of SI).

The Raman spectrum computed in presence of Ag$^+$, reported in Fig. 13b, shows a peak at 909 cm^{-1} related to a normal mode that involves lateral chain atoms which, in absence of ions, is convoluted with another peak at 950 cm^{-1}. Moreover, the peak at 1740 cm^{-1}, related to C=O stretching of the carboxyl groups, that is a convolution of two equal contributions without ions, splits in two peaks in presence of Ag$^+$: one is quite superposed with the correspondent peak in the spectrum of serine without ions and it is related to the C=O stretching of the carboxyl farther from the ion, while the other peak, related to the C=O stretching of the carboxyl closer to the ion, moved at 1687 cm^{-1} and it is also enhanced. These two features are in common to those observed with different alkali metal ions as described above. Moreover, a peak at 1319 cm^{-1}, related to the C−N stretching, a C−H bending and a C=O bending of the amide close to the ion, is enhanced.

In the Raman spectrum of serine in presence of Cu^+ (Fig. 13c), many peaks are shifted: for example the lower energy peaks, distinctive of normal modes that involve serine lateral chain atoms, are red-shifted as well as the peak related to the $C-O$ stretching of the carboxyl close to the ion that moved at $1590 \, cm^{-1}$. Also in this case the peak at $1310 \, cm^{-1}$ is enhanced.
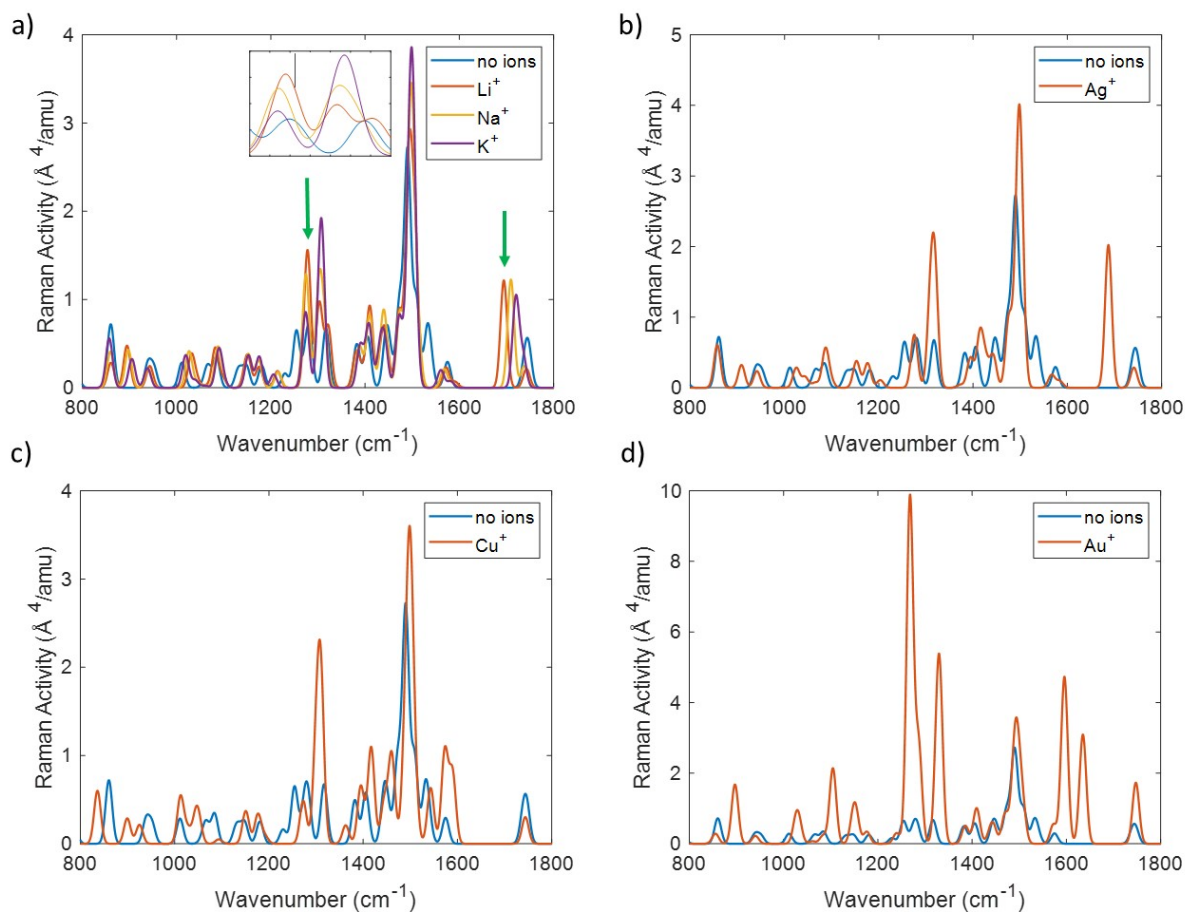

Figure 13: Raman spectra of serine close to Li^+, Na^+ or K^+ (panel a), Ag^+ (panel b), Cu^+ (panel c), Au^+ (panel d) in the fingerprint region, with incident laser frequency equal to 785 nm.

In presence of Au^+ (Fig. 13d), the spectrum appears quite enhanced, although it is not due to a resonance transition but rather to the influence of several low energy electronic states which make the terms in the polarizability larger. As in the previous cases, three peaks below $1000 \, cm^{-1}$ are distinguishable, even though the one in the middle, at $897 \, cm^{-1}$ is the most

visible. Two peaks, respectively at 1268 cm^{-1} and 1331 cm-1, are really enhanced and both of them are related to normal modes which involve movements of the lateral chain atoms. Another peak, at 1595 cm^{-1}, mainly related to N$-$H bending and to C$-$N stretching of the amide close to the ion is really enhanced. Finally, as in previous cases, the two peaks associated to the C=O stretching of the carboxyl groups are wide apart and the one at lower energy, related to the carboxyl closer to the ion, is enhanced.
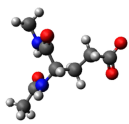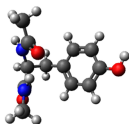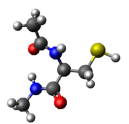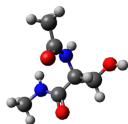
Summarizing, in presence of different ions, three peaks are expected rather than two in the lower energy range, below 1000 cm^{-1}, that make the spectrum closer to that of cysteine, as well as a splitting of the two peaks related to the carboxyl C=O stretching. Moreover, with transition metal ions, such as Ag$^+$, Cu$^+$, Au$^+$, also one or two peaks around 1300 cm^{-1} can be enhanced, particularly in presence of gold ions.

Conclusion

We have explored the effect of different cations on the Raman spectra of selected amino acids. In all the cases the ions stay close to oxygen atoms of the amino acids with one exception: Cu$^+$ in presence of tyrosine tends to form a complex with the aromatic ring instead to stay close to the hydroxyl group. With glutamate the ions prefer to stay close to both the oxygen atoms of the carboxyl group in the side chain but for the gold ion which leans toward the single coordination. Ions are attracted by the oxygen atom in the hydroxyl group of tyrosine side chain, but for Cu$^+$ as mentioned. In presence of amino acids with very flexible side chain and the suitable length such as cysteine and serine, the cations tend to bridged between the oxygen atom of the carboxyl and either the oxygen or sulfur atom of the side chain, but for alkali metal ions in presence of cysteine which show a strong preference towards the oxygen atom.

On the spectra side, we have noticed that in presence of transition metal ions (especially with Cu^{++}) the Raman spectra obtained is in resonance regime while it never happens in

Table 1: Summary of main evidences in N-methylacetamide and four amino acids Raman spectra in presence of different ions. For compactness, all the optimized amino acid-ion pairs structures are not reported here. In case of resonance, the electronic transition energy has been reported in the table instead of the frequency peaks. Abbreviations employed: bending (bend), stretching (str), symmetric (sym), asymmetric (as), wagging (wag), breathing (br).

Amino acid ↓	Normal mode ↓	no ions	Li$^+$	Na$^+$	K$^+$	Ag$^+$	Au$^+$	Cu$^+$	Cu^{++}
N-methyl acetamide	C–O bend	875 cm^{-1}	909 cm^{-1}	889 cm^{-1}	885 cm^{-1}	896 cm^{-1}	894 cm^{-1}	902 cm^{-1}	935 cm^{-1}
	C–O bend	1289 cm^{-1}	1325 cm^{-1}	1313 cm^{-1}	1306 cm^{-1}	1323 cm^{-1}	1342 cm^{-1}	1324 cm^{-1}	1348 cm^{-1}
	C–O str	1737 cm^{-1}	1692 cm^{-1}	1700 cm^{-1}	1711 cm^{-1}	1686 cm^{-1}	1640 cm^{-1}	1625 cm^{-1}	1694 cm^{-1}
Glutamate	COO^- sym str	900 cm^{-1}	947 cm^{-1}	931 cm^{-1}	926 cm^{-1}	938 cm^{-1}	935 cm^{-1}	Resonance: Electronic transition 771nm	Resonance: Electronic transition 775nm
	$C - COO^-$ str					1432 cm^{-1}	see text		
	CH_2 bend/wag								
	COO^- as str	1693 cm^{-1}	1605 cm^{-1}	1621 cm^{-1}	1643 cm^{-1}	1608 cm^{-1}	1702 cm^{-1}		
Tyrosine	ring br	842 cm^{-1}	840 cm^{-1}	840 cm^{-1}	840 cm^{-1}	841 cm^{-1}	Resonance: Electronic transition 659nm	841 cm^{-1}	Resonance: Electronic transition 756nm
	$-CH_2$ wag	1310 cm^{-1}	1315 cm^{-1}	1315 cm^{-1}	1315 cm^{-1}	1316 cm^{-1}		1311 cm^{-1}	
	$-CH_2$ wag	1384 cm^{-1}	1396 cm^{-1}	1396 cm^{-1}	1396 cm^{-1}	1396 cm^{-1}		1393 cm^{-1}	
	ring str	1669 cm^{-1}	1664 cm^{-1}	1665 cm^{-1}	1665 cm^{-1}	1664 cm^{-1}		1603 cm^{-1}	
Cysteine	$S - H$ bend	839 cm^{-1}	843 cm^{-1}	842 cm^{-1}	841 cm^{-1}	Resonance: Electronic transition 272nm	Resonance: Electronic transition 361nm	815 cm^{-1}	Resonance: Electronic transition 808nm
	$S - H$ bend	895 cm^{-1}	898 cm^{-1}	897 cm^{-1}	840 cm^{-1}			905 cm^{-1}	
	$S - H$ bend	943 cm^{-1}	946 cm^{-1}	840 cm^{-1}	840 cm^{-1}			951 cm^{-1}	
	C–O str							993 cm^{-1}	
	C–O str	1711 cm^{-1}	1666 cm^{-1}	1679 cm^{-1}	1687 cm^{-1}			1636 cm^{-1}	
Serine	$O - H$ bend	860 cm^{-1}	861 cm^{-1}	860 cm^{-1}	857 cm^{-1}	857 cm^{-1}	855 cm^{-1}	836 cm^{-1}	Resonance: Electronic transition 823nm
	$O - H$ bend	939 cm^{-1}	895 cm^{-1}	898 cm^{-1}	905 cm^{-1}	909 cm^{-1}	897 cm^{-1}	899 cm^{-1}	
	$O - H$ bend	952 cm^{-1}	943 cm^{-1}	940 cm^{-1}	938 cm^{-1}	941 cm^{-1}	940 cm^{-1}	925 cm^{-1}	
	C–O bend	1738 cm^{-1}	1694 cm^{-1}	1709 cm^{-1}	1720 cm^{-1}	1687 cm^{-1}	1635 cm^{-1}	1590 cm^{-1}	
	C–O str								

presence of alkali metal ions. In many cases, the spectra in presence of Ag^+ are close to the spectra in presence of alkali metal ions. Au^+ ion usually enhances the Raman spectra, even though the incident laser frequency is far from electronic transitions, because of the low energy electronic transitions (present with gold ion) that give high contribution to the polarizability tensor.

Apart from the resonance Raman spectra, we have explained in details the Raman signals mainly related to normal modes localized on the side chain of the amino acids, which are the most significant for amino acids recognition. Summing up the results, glutamate is well identified by the peaks related to carboxyl symmetric and asymmetric stretching whose position changes with the ionic species present in solution. Tyrosine can be distinguished by two peaks related to aromatic ring breathing and stretching that do not shift in presence of ions but for Cu^+ that tends to assume a different position with respect to other cations. The cysteine most relevant peak is outside the fingerprint region and correspond to the thiol stretching at 2700 cm^{-1}. Moreover, three low frequency peak (between 800 and 1000 cm^{-1}) can be detected even in presence of alkali metal ions. Also the Raman spectrum of serine shows three typical peaks between 800 and 1000 cm^{-1} (but of course serine can be distinguished from cysteine by the different position of the OH and SH stretching peaks) which are present with all the ions considered although they are slightly shifted and their intensity varies. It has to be noticed that without ions only two peaks are visible in this region since two of them are convoluted in a single peak. In all the spectra some peaks merely due to normal modes localized on the backbone are present, such as those reported for N-methylacetamide, which can be shifted as well in presence of ions so it is important to take care of them to not mix up these peaks with those relevant for the amino acids identification.

This work is the base of amino acids recognition in ionic solution and has the aim to facilitate the interpretation of phenomenological evidences in future experiments.

Acknowledgement

Supporting Information Available

The data that supports the findings of this study are available as supplementary material:

References

(1) Ferraro, J. R. *Introductory Raman spectroscopy*; Elsevier, 2003.

(2) Graves, P.; Gardiner, D. *Practical Raman spectroscopy*; Springer, 1989; Vol. 10.

(3) Jones, R. R.; Hooper, D. C.; Zhang, L.; Wolverson, D.; Valev, V. K. Raman techniques: fundamentals and frontiers. *Nanoscale Res. Lett.* **2019**, *14*, 1–34.

(4) Rostron, P.; Gaber, S.; Gaber, D. Raman spectroscopy, review. *IJETR* **2016**, *21*, 24.

(5) Kuhar, N.; Sil, S.; Verma, T.; Umapathy, S. Challenges in application of Raman spectroscopy to biology and materials. *RSC adv.* **2018**, *8*, 25888–25908.

(6) Hess, C. New advances in using Raman spectroscopy for the characterization of catalysts and catalytic reactions. *Chem. Soc. Rev.* **2021**, *50*, 3519–3564.

(7) Candeloro, P.; Grande, E.; Raimondo, R.; Di Mascolo, D.; Gentile, F.; Coluccio, M. L.; Perozziello, G.; Malara, N.; Francardi, M.; Di Fabrizio, E. Raman database of amino

acids solutions: A critical study of Extended Multiplicative Signal Correction. *Analyst* **2013**, *138*, 7331–7340.

(8) Zhu, G.; Zhu, X.; Fan, Q.; Wan, X. Raman spectra of amino acids and their aqueous solutions. *Spectrochimica Acta Part A: Molecular and Biomolecular Spectroscopy* **2011**, *78*, 1187–1195.

(9) Jenkins, A. L.; Larsen, R. A.; Williams, T. B. Characterization of amino acids using Raman spectroscopy. *Spectrochimica Acta Part A: Molecular and Biomolecular Spectroscopy* **2005**, *61*, 1585–1594.

(10) Moerner, W. A dozen years of single-molecule spectroscopy in physics, chemistry, and biophysics. 2002.

(11) Moerner, W.; Fromm, D. P. Methods of single-molecule fluorescence spectroscopy and microscopy. *Review of Scientific instruments* **2003**, *74*, 3597–3619.

(12) Jiang, J.; Bosnick, K.; Maillard, M.; Brus, L. Single molecule Raman spectroscopy at the junctions of large Ag nanocrystals. 2003.

(13) Le Ru, E. C.; Etchegoin, P. G. Single-molecule surface-enhanced Raman spectroscopy. *Annu. Rev. Phys. Chem* **2012**, *63*, 65–87.

(14) Chikkaraddy, R.; De Nijs, B.; Benz, F.; Barrow, S. J.; Scherman, O. A.; Rosta, E.; Demetriadou, A.; Fox, P.; Hess, O.; Baumberg, J. J. Single-molecule strong coupling at room temperature in plasmonic nanocavities. *Nature* **2016**, *535*, 127–130.

(15) Sonntag, M. D.; Pozzi, E. A.; Jiang, N.; Hersam, M. C.; Van Duyne, R. P. Recent advances in tip-enhanced Raman spectroscopy. *The journal of physical chemistry letters* **2014**, *5*, 3125–3130.

(16) Deckert, V.; Deckert-Gaudig, T.; Diegel, M.; Götz, I.; Langelüddecke, L.; Schneidewind, H.; Sharma, G.; Singh, P.; Singh, P.; Trautmann, S., et al. Spatial resolution in Raman spectroscopy. *Faraday Discussions* **2015**, *177*, 9–20.

(17) Meng, L.; Yang, Z.; Chen, J.; Sun, M. Effect of electric field gradient on sub-nanometer spatial resolution of tip-enhanced Raman spectroscopy. *Scientific reports* **2015**, *5*, 1–5.

(18) Perney, N.; De Abajo, F. G.; Baumberg, J.; Tang, A.; Netti, M.; Charlton, M.; Zoorob, M. Tuning localized plasmon cavities for optimized surface-enhanced Raman scattering. *Physical Review B* **2007**, *76*, 035426.

(19) Chen, C.; Li, Y.; Kerman, S.; Neutens, P.; Willems, K.; Cornelissen, S.; Lagae, L.; Stakenborg, T.; Van Dorpe, P. High spatial resolution nanoslit SERS for single-molecule nucleobase sensing. *Nature communications* **2018**, *9*, 1–9.

(20) Langer, J.; Jimenez de Aberasturi, D.; Aizpurua, J.; Alvarez-Puebla, R. A.; Auguié, B.; Baumberg, J. J.; Bazan, G. C.; Bell, S. E. J.; Boisen, A.; Brolo, A. G.; et al, Present and Future of Surface-Enhanced Raman Scattering. *ACS Nano* **2020**, *14*, 28–117.

(21) Maccaferri, N.; Barbillon, G.; Koya, A. N.; Lu, G.; Acuna, G. P.; Garoli, D. Recent advances in plasmonic nanocavities for single-molecule spectroscopy. *Nanoscale Advances* **2021**, *3*, 633–642.

(22) Huang, J.-A.; Mousavi, M. Z.; Giovannini, G.; Zhao, Y.; Hubarevich, A.; Soler, M. A.; Rocchia, W.; Garoli, D.; De Angelis, F. Multiplexed discrimination of single amino acid residues in polypeptides in a single SERS hot spot. *Angewandte Chemie International Edition* **2020**, *59*, 11423–11431.

(23) Garoli, D.; Mosconi, D.; Miele, E.; Maccaferri, N.; Ardini, M.; Giovannini, G.; Dipalo, M.; Agnoli, S.; De Angelis, F. Hybrid plasmonic nanostructures based on controlled integration of MoS 2 flakes on metallic nanoholes. *Nanoscale* **2018**, *10*, 17105–17111.

(24) Garoli, D.; Yamazaki, H.; Maccaferri, N.; Wanunu, M. Plasmonic nanopores for single-molecule detection and manipulation: toward sequencing applications. *Nano letters* **2019**, *19*, 7553–7562.

(25) Huang, J.-A.; Mousavi, M. Z.; Zhao, Y.; Hubarevich, A.; Omeis, F.; Giovannini, G.; Schütte, M.; Garoli, D.; De Angelis, F. SERS discrimination of single DNA bases in single oligonucleotides by electro-plasmonic trapping. *Nature communications* **2019**, *10*, 1–10.

(26) Yang, J.-M.; Pan, Z.-Q.; Qin, F.-F.; Chen, M.; Wang, K.; Xia, X.-H. An in situ SERS study of ionic transport and the Joule heating effect in plasmonic nanopores. *Chemical Communications* **2018**, *54*, 13236–13239.

(27) Ru, E.; Etchegoin, P. *Principles of Surface-Enhanced Raman Spectroscopy: and Related Plasmonic Effects*; Elsevier Science, 2008.

(28) Sharma, B.; Frontiera, R. R.; Henry, A.-I.; Ringe, E.; Van Duyne, R. P. SERS: Materials, applications, and the future. *Materials Today* **2012**, *15*, 16–25.

(29) Jensen, L.; Aikens, C. M.; Schatz, G. C. Electronic structure methods for studying surface-enhanced Raman scattering. *Chem. Soc. Rev.* **2008**, *37*, 1061–1073.

(30) Frisch, M. J.; Trucks, G. W.; Schlegel, H. B.; Scuseria, G. E.; Robb, M. A.; Cheeseman, J. R.; Scalmani, G.; Barone, V.; Petersson, G. A.; Nakatsuji, H.; et al, Gaussian~16 Revision B.01. 2016; Gaussian Inc. Wallingford CT.

(31) Tomasi, J.; Mennucci, B.; Cammi, R. Quantum mechanical continuum solvation models. *Chemical reviews* **2005**, *105*, 2999–3094.

(32) Peach, M. J.; Benfield, P.; Helgaker, T.; Tozer, D. J. Excitation energies in density functional theory: An evaluation and a diagnostic test. *The Journal of chemical physics* **2008**, *128*, 044118.

(33) Cotton, F. A.; Wilkinson, G.; Murillo, C. A.; Bochmann, M. *Advanced inorganic chemistry*; John Wiley and Sons, Inc., 1999; pp 1052–1053.

(34) Grodzicki, A.; Łakomska, I.; Piszczek, P.; Szymańska, I.; Szłyk, E. Copper (I), silver (I) and gold (I) carboxylate complexes as precursors in chemical vapour deposition of thin metallic films. *Coordination chemistry reviews* **2005**, *249*, 2232–2258.

(35) Schröder, D.; Schwarz, H.; Hrušák, J.; Pyykkö, P. Cationic gold (I) complexes of xenon and of ligands containing the donor atoms oxygen, nitrogen, phosphorus, and sulfur. *Inorganic Chemistry* **1998**, *37*, 624–632.

Role of ions in solvated Amino acids Raman spectra Supporting Information

Giulia Dall'Osto,[†] Ornella Vaccarelli,[‡] Ciro A. Guido,[¶] and Stefano Corni[*,†,§]

[†]*Department of Chemical Sciences, University of Padova, via Marzolo 1, 35100, Padova, Italy*

[‡]*Department of Physics and Materials Science, Université du Luxembourg 162 A, avenue de la Faïencerie L-1511 Luxembourg*

[¶]*Department of Science and Technological Innovation, Università del Piemonte Orientale, Viale T. Michel 11, 15121 Alessandria, Italy*

[§]*CNR Institute of Nanoscience, via Campi 213/A, 41100, Modena, Italy*

E-mail: stefano.corni@unipd.it

The results of all our calculations that are not already present in the main text, are resumed here. In particular the spectra of all the amino acid-ion pairs is reported in the range $0 - 4000$ cm^{-1} with incident laser frequency equal to 785 nm. All the results of calculations performed when the incident laser has frequency 530 nm are reported in the fingerprint region $(800 - 1800$ cm$^{-1})$ and also in the full range $(0 - 4000$ cm$^{-1})$.
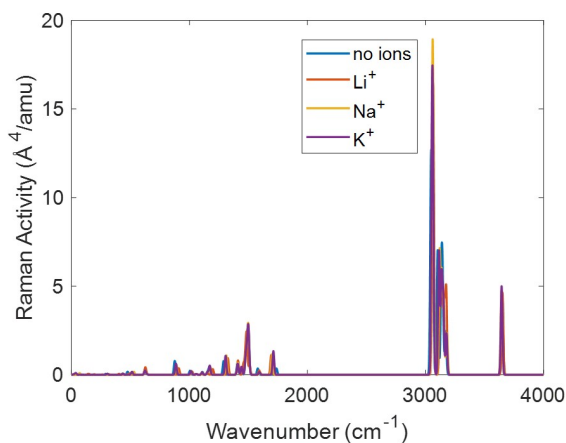
N-methylacetamide

Figure S1: Raman spectra of N-methylacetamide in water without ions and in presence of Li$^+$, Na$^+$, K$^+$, with incident laser frequency equal to 785 nm, in the full range (0-4000 cm^{-1}).

In presence of Cu$^+$ (figure S2b) there is a new peak at 2782 cm^{-1} which corresponds to a C$-$H stretching of the bond closer to the position of Cu$^+$ and for this reason it is red-shifted with respect to the same peak without ions or even in presence of other ions (which occupy a position farther from the methyl group).

The spectrum of N-methylacetamide in presence of Cu$^+$ is enhanced when the incident laser frequency is 530 nm, as shown by figure S4b and S5b, due to two electronic transitions at 466 and 618nm.

The spectrum of N-methylacetamide in presence of Cu^{++} in the fingerprint region (figure S4c) is different moving from incident field frequency 785 nm to 530 nm. In particular, the

peaks at 1037 cm^{-1}, 1100 cm^{-1}, 1348 cm^{-1} are enhanced, while the peak at 1694 cm^{-1} decreases in intensity. All these peaks are related to normal modes which involves the movement of the C$-$O: the region of the molecule closer to the metal.

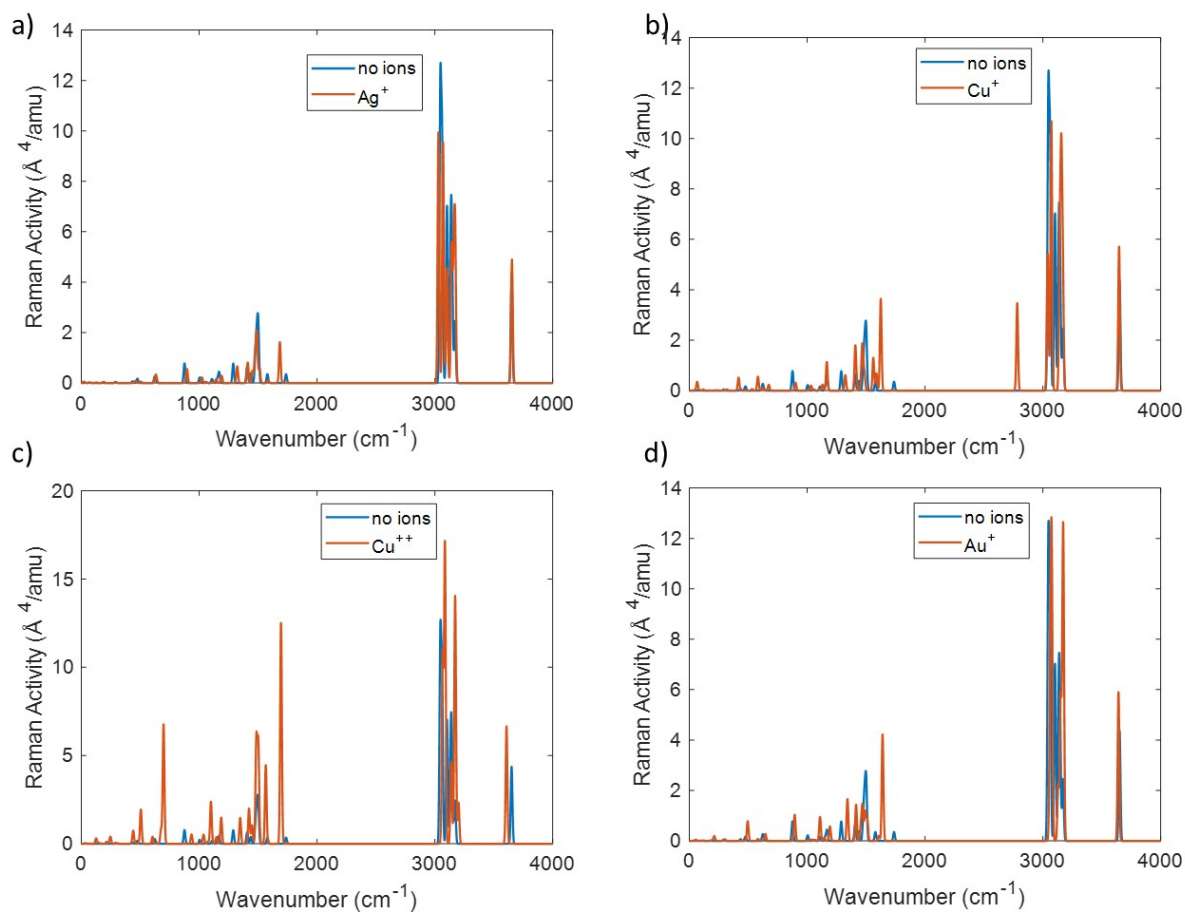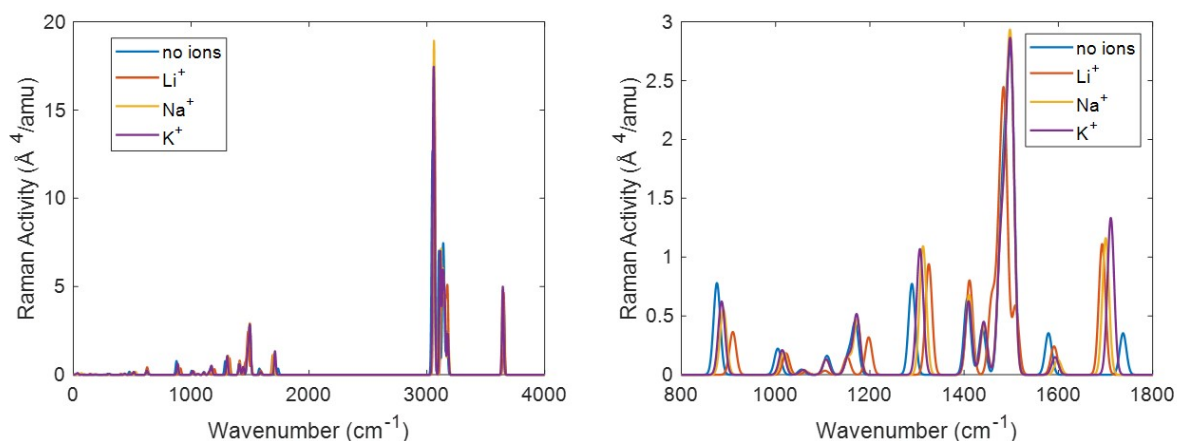All the other spectra computed at 530 nm are quite superimposed with the same spectra at 785 nm.
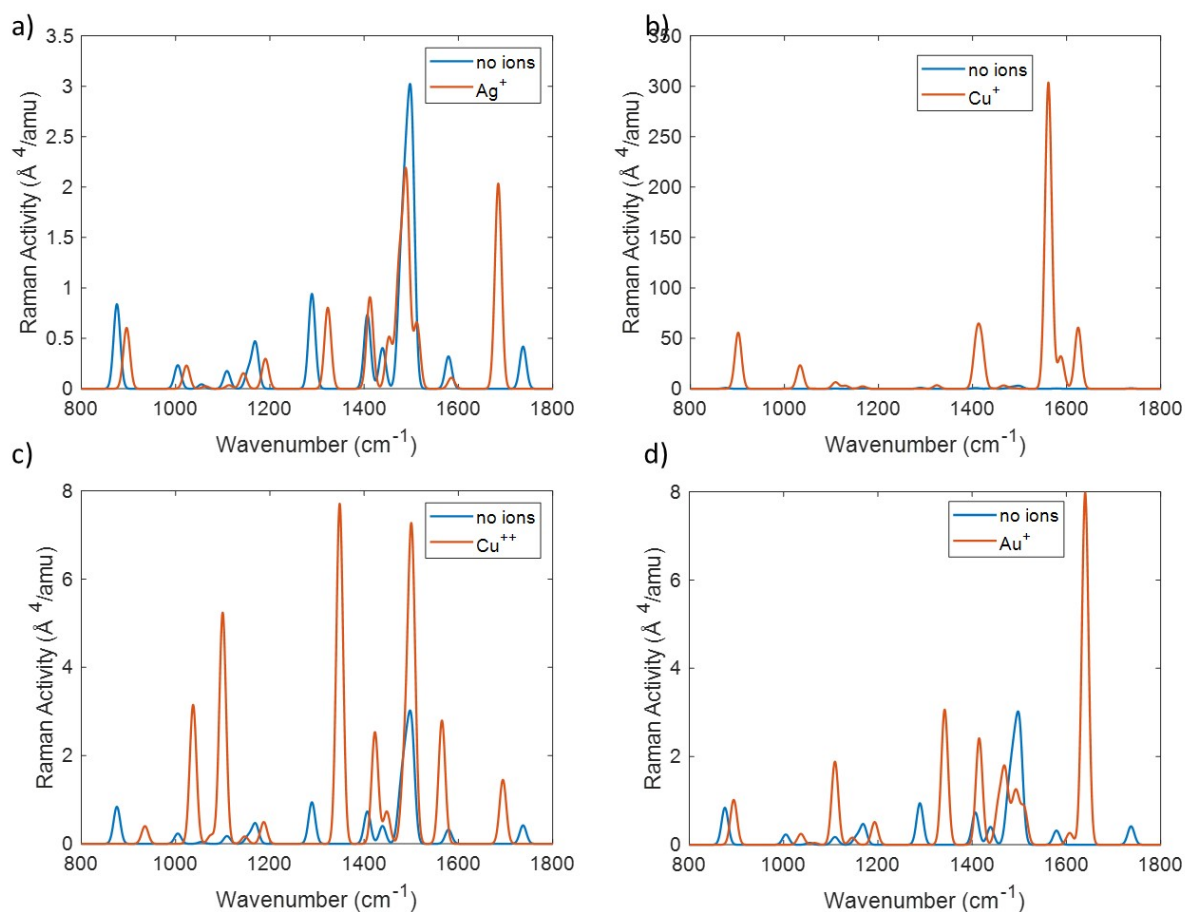

Figure S2: Raman spectra of N-methylacetamide in presence of Ag$^+$ (panel a), Cu$^+$ (panel b), Cu^{++} (panel c), Au$^+$ (panel d), with incident laser frequency equal to 785 nm, in the full range (0-4000 cm^{-1}).

Figure S3: Raman spectra of N-methylacetamide in water without ions and in presence of Li^+, Na^+, K^+, with incident laser frequency equal to 530 nm, in the full range (0-400 cm^{-1}, panel a) and fingerprint region (panel b).

Figure S4: Raman spectra of N-methylacetamide in presence of Ag^+ (panel a), Cu^+ (panel b), Cu^{++} (panel c), Au^+ (panel d), with incident laser frequency equal to 530 nm, in the fingerprint region.
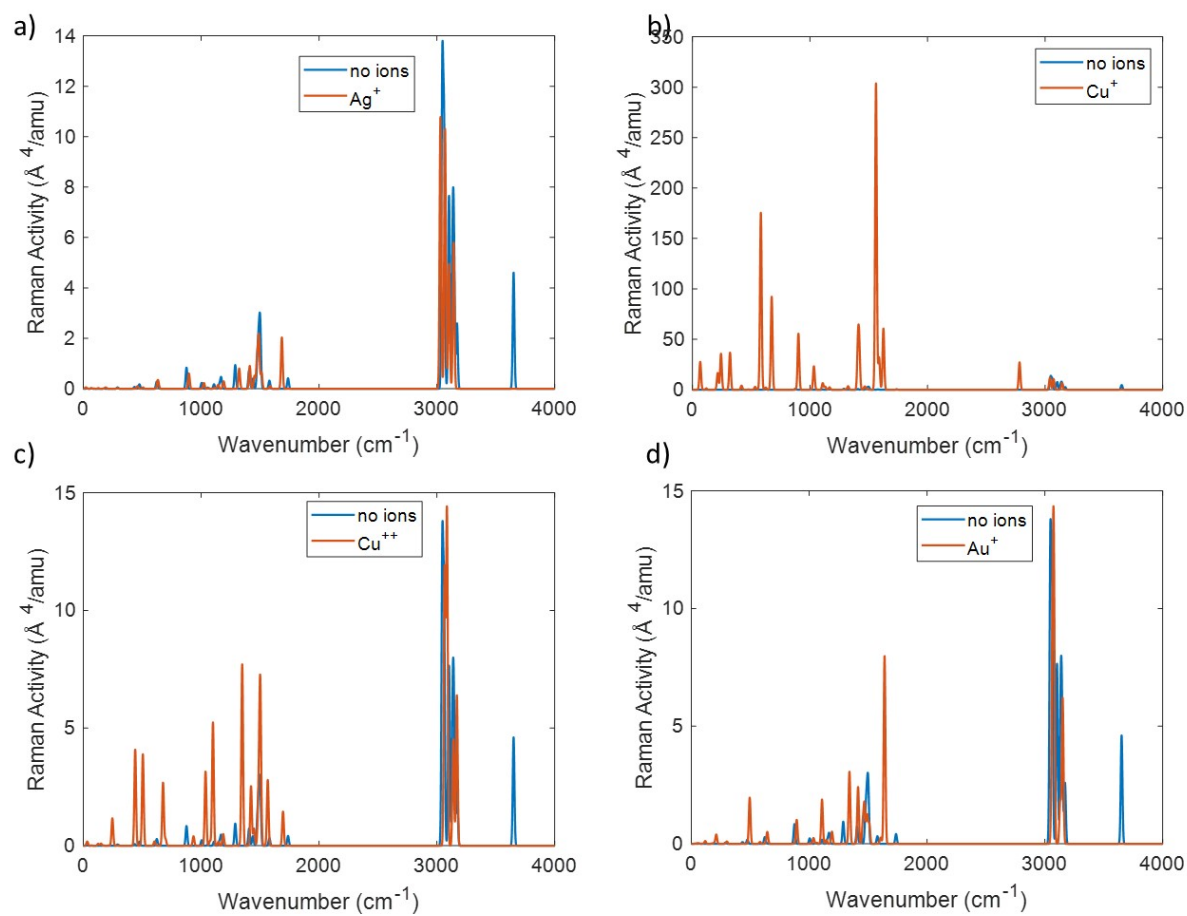
Figure S5: Raman spectra of N-methylacetamide in presence of Ag$^+$ (panel a), Cu$^+$ (panel b), Cu^{++} (panel c), Au$^+$ (panel d), with incident laser frequency equal to 530 nm, in the full range (0-4000 cm^{-1}).

Glutamate

Using a laser frequency of 530 nm produce an enhancement of the spectra of glutamate in presence of Ag^+ (figure S9a) and of Au^+ (figure S9d) even though the main peaks remain in the same position as with 785 nm laser frequency.

On the other hand, in presence of Cu^+ the incident field frequency equal to 530 nm is farther from resonant than with 785 nm laser frequency and only lower frequency signals feel the effect of closer electronic transition (as shown by figure S10b) and thus are enhanced. However, in the fingerprint region the spectrum is quite superposed as that without ions but for two very intense peaks at 944 cm^{-1} and 1587 cm^{-1} (respectively associated to symmetric and asymmetric stretching of the carboxyl in the side chain).

The Raman spectrum of glutamate in presence of Cu^{++} at 530 nm is less enhanced than at 785 nm, such that two main peaks are distinguishable in the fingerprint region, at 965 cm^{-1} and 1515 cm^{-1}, which correspond respectively to the symmetric stretching of the carboxyl in the side chain and to the C$-$C stretching that involves the carbon atom of the carboxyl.
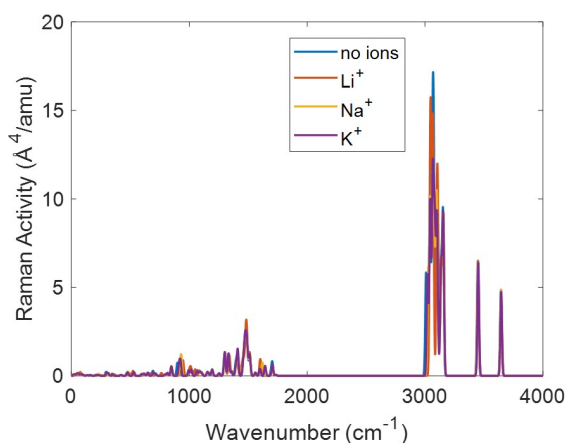

Figure S6: Raman spectra of glutamate in water without ions and in presence of Li$^+$, Na$^+$, K$^+$, with incident laser frequency equal to 785 nm, in the full range (0-4000 cm^{-1}).
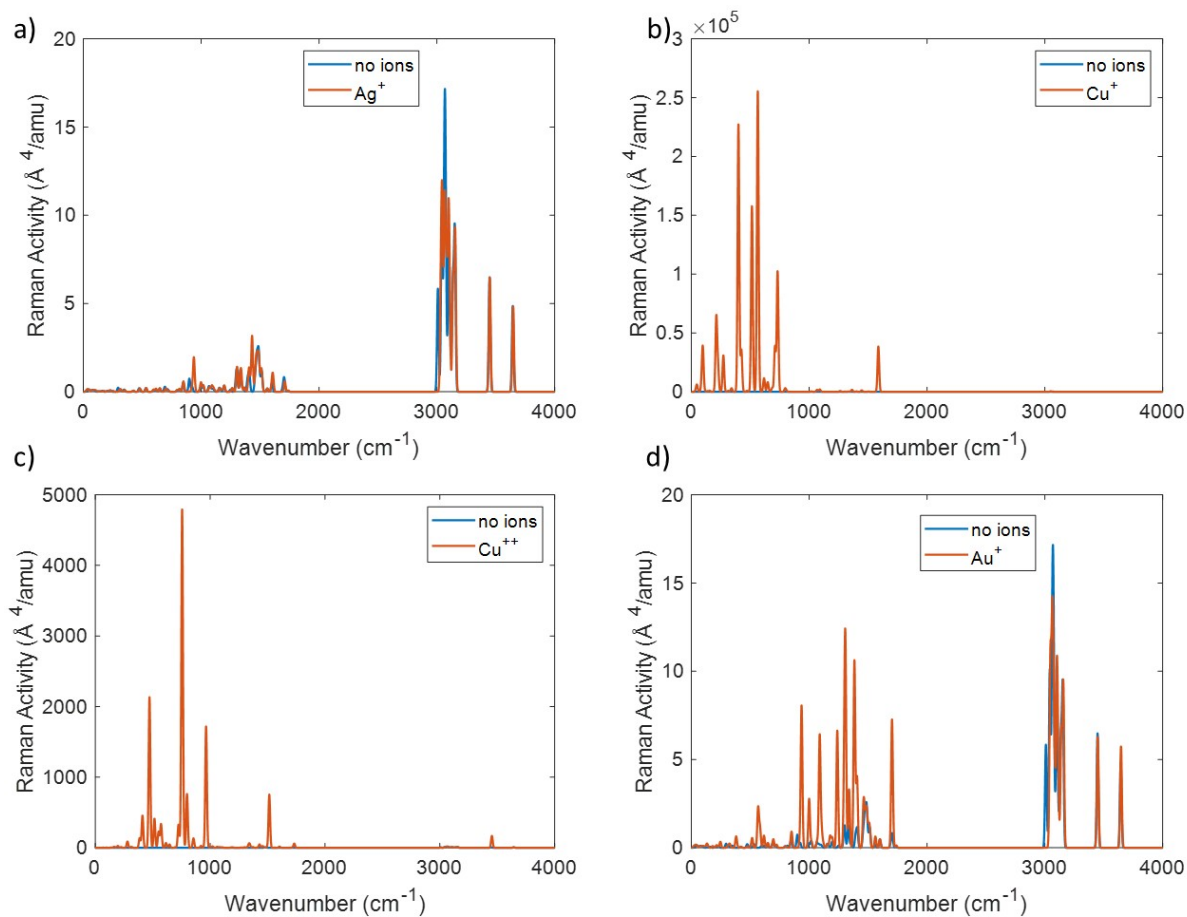
Figure S7: Raman spectra of glutamate in presence of Ag$^+$ (panel a), Cu$^+$ (panel b), Cu^{++} (panel c), Au$^+$ (panel d), with incident laser frequency equal to 785 nm, in the full range (0-4000 cm^{-1}).
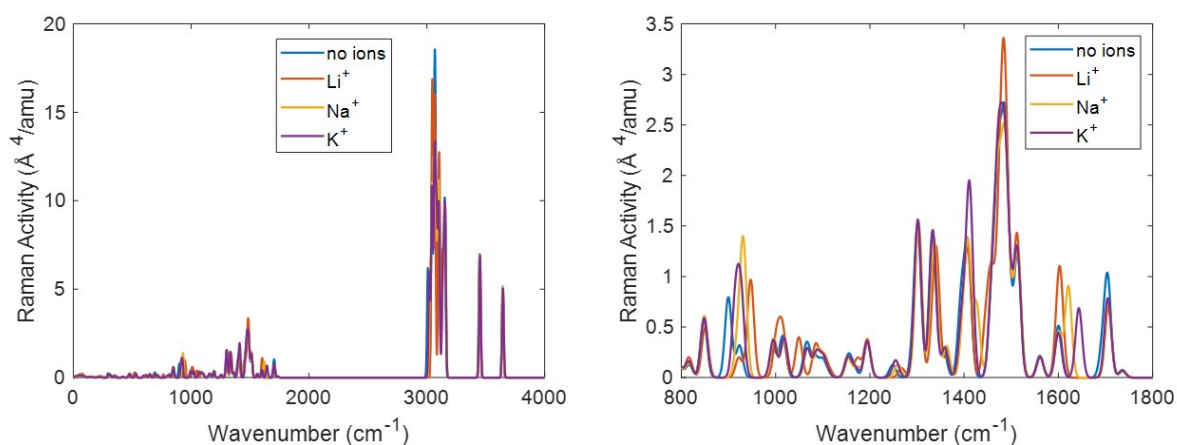

Figure S8: Raman spectra of glutamate in water without ions and in presence of Li$^+$, Na$^+$, K$^+$, with incident laser frequency equal to 530 nm, in the full range (0-400 cm^{-1}, panel a) and fingerprint region (panel b).

Figure S9: Raman spectra of glutamate in presence of Ag$^+$ (panel a), Cu$^+$ (panel b), Cu^{++} (panel c), Au$^+$ (panel d), with incident laser frequency equal to 530 nm, in the fingerprint region.
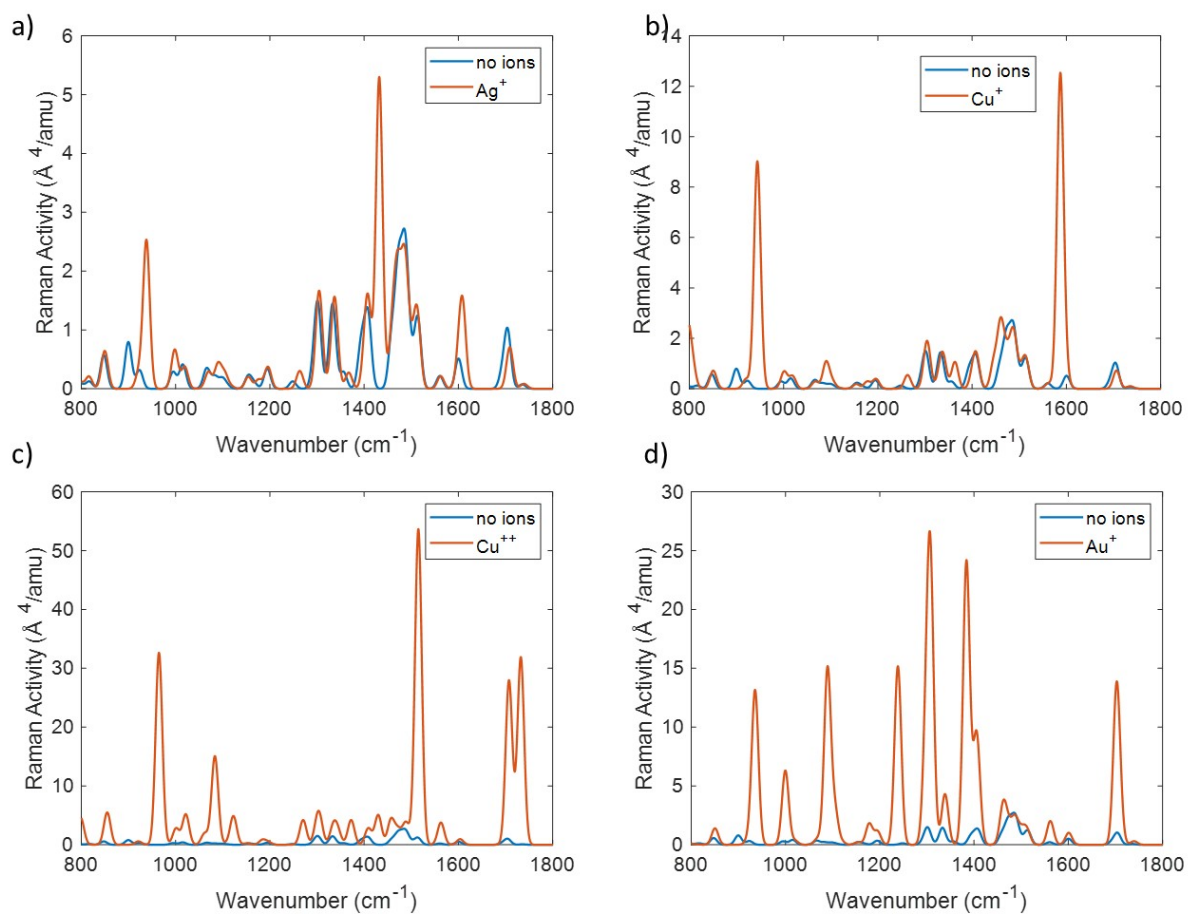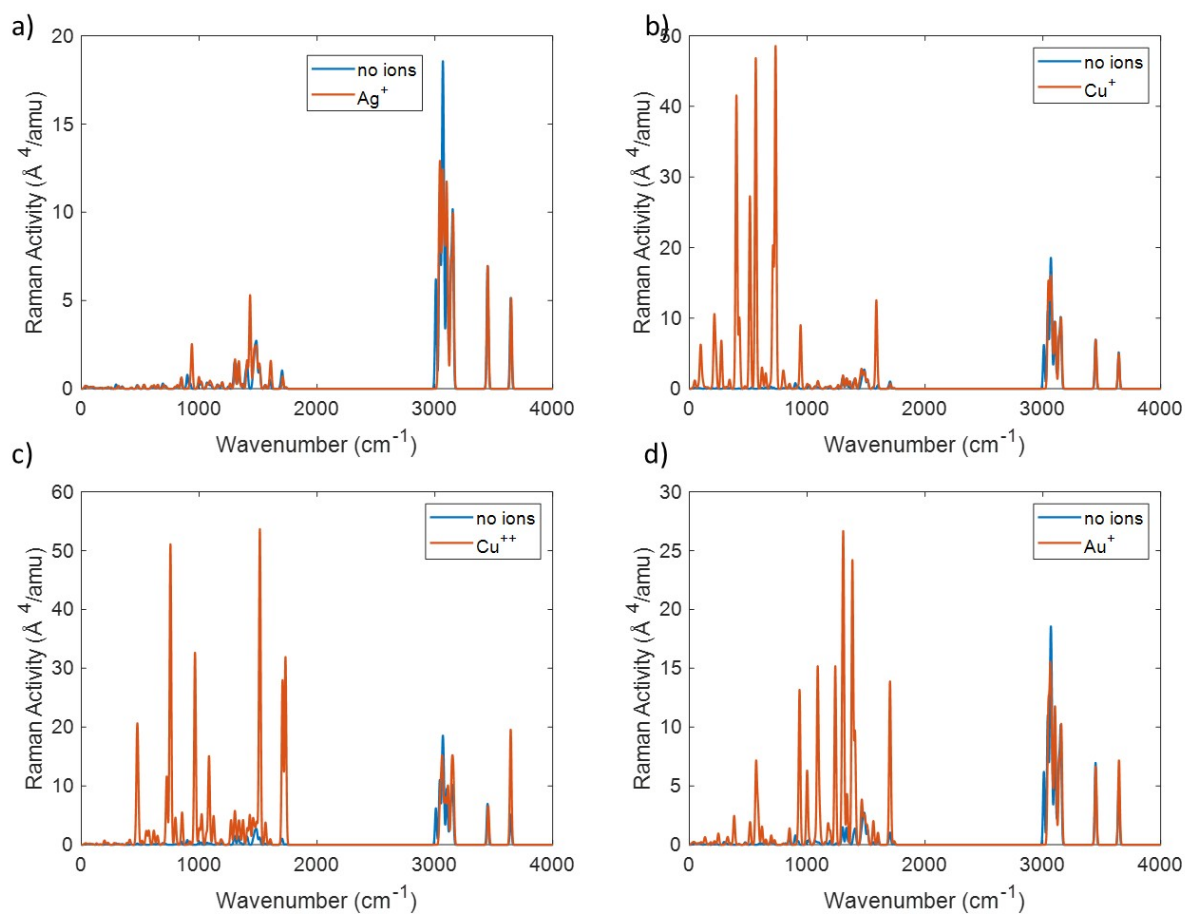
Figure S10: Raman spectra of glutamate in presence of Ag^+ (panel a), Cu^+ (panel b), Cu^{++} (panel c), Au^+ (panel d), with incident laser frequency equal to 530 nm, in the full range (0-4000 cm^{-1}).

Tyrosine

Looking at the full range spectra (in the region 0-4000 cm^{-1}), a peak appears at 3362 cm^{-1} in the spectrum without ions that is an effect of the conformation assumed by the molecule in this case. Indeed the two amide groups in the backbone are facing inducing a hydrogen interaction between the C$-$O of one group and the N$-$H of the other group, therefore it causes a red-shifted of the peak related to N$-$H stretching, usually around 3600 cm^{-1}. Unexpectedly, this peaks is not visible with any of the ions considered.

The spectra computed with incident laser frequency equal to 530 nm are really close to those obtained at 785 nm. In presence of Cu^{++} (figure S15c) and of Au$^+$ (figure S15d) the spectra is enhanced also in this case, but it achieves lower intensities because the incident laser frequency here ($530nm$) is farther from the electronic transitions than the one reported in the main text (785 nm).
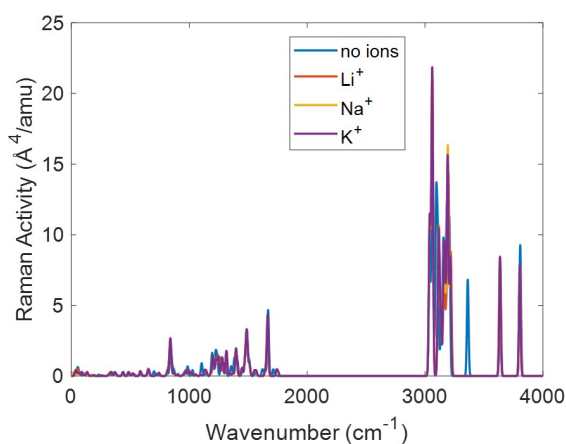

Figure S11: Raman spectra of tyrosine in water without ions and in presence of Li$^+$, Na$^+$, K$^+$, with incident laser frequency equal to 785 nm, in the full range (0-4000 cm^{-1}).

Figure S12: Raman spectra of tyrosine in presence of Ag$^+$ (panel a), Cu$^+$ (panel b), Cu^{++} (panel c), Au$^+$ (panel d), with incident laser frequency equal to 785 nm, in the full range (0-4000 cm^{-1}).

Figure S13: Raman spectra of tyrosine in water without ions and in presence of Li$^+$, Na$^+$, K$^+$, with incident laser frequency equal to 530 nm, in the full range (0-400 cm^{-1}, panel a) and fingerprint region (panel b).
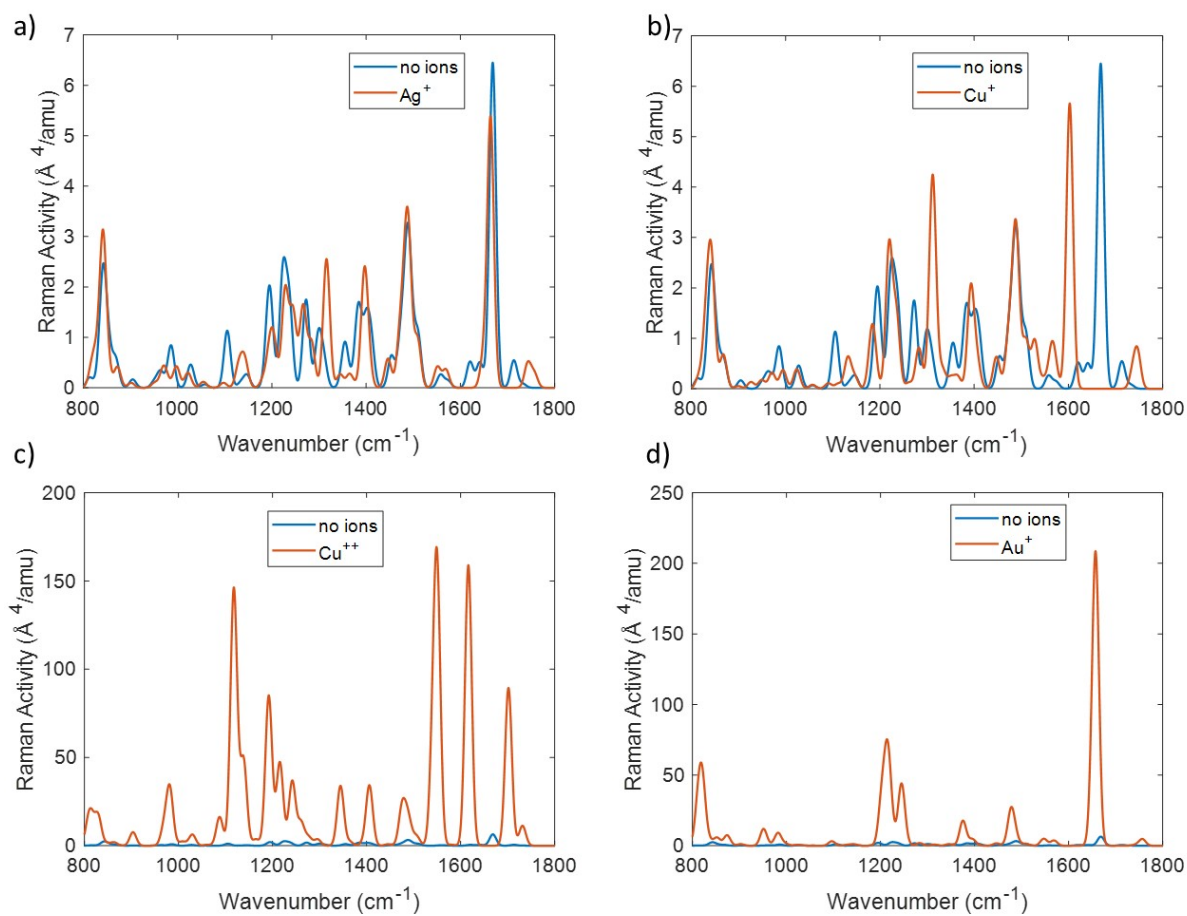
Figure S14: Raman spectra of tyrosine in presence of Ag^+ (panel a), Cu^+ (panel b), Cu^{++} (panel c), Au^+ (panel d), with incident laser frequency equal to 530 nm, in the fingerprint region.
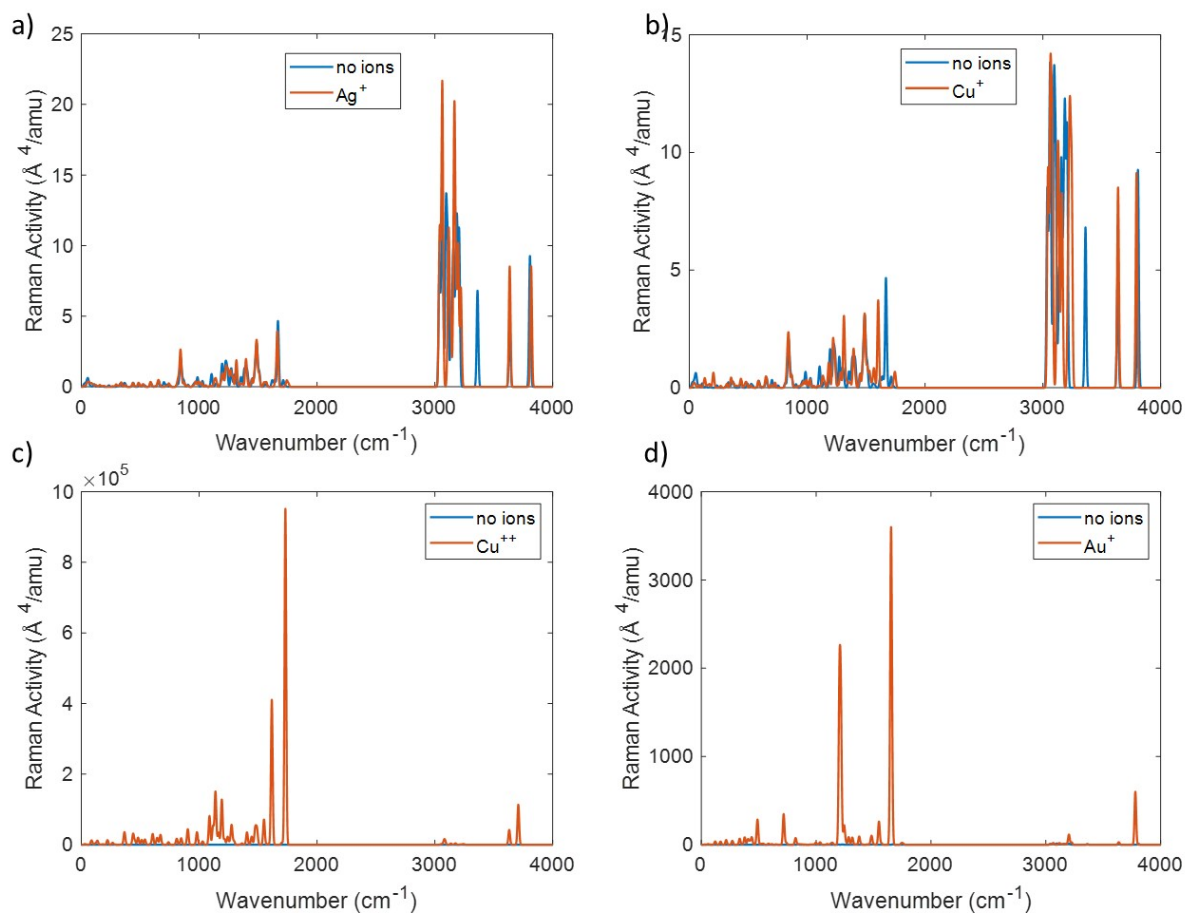
Figure S15: Raman spectra of tyrosine in presence of Ag^+ (panel a), Cu^+ (panel b), Cu^{++} (panel c), Au^+ (panel d), with incident laser frequency equal to 530 nm, in the full range (0-4000 cm^{-1}).

Cysteine

As mentioned in the main text, the most peculiar peak in cysteine Raman spectrum is related to the thiol stretching, at 2700 cm^{-1}. This peak is not subjected to a shift neither varying the ion or the incident laser frequency between 785 nm and 530 nm.

The Raman spectra in the finger print region with incident laser frequency 530 nm show the same features as at 785 nm in terms of peaks position and relative intensity. However the intensity of the spectra of cysteine in presence of Ag$^+$ is overall enhanced while the spectra in presence of Cu^{++} and Au$^+$ show low intensities (figure S19).

The Raman spectrum of Cysteine without ions shows two peaks at 3508 cm^{-1} and at 3631 cm^{-1} related to N$-$H stretching. The peak at lower energy is blue-shifted (in both cases at 530 nm or 785 nm) in presence of ions due to the influence of the cycle formed between the amide, the ion and the cysteine side chain on this peak, when the cation bridged between the sulfur atom of the thiol and the oxygen atom of the carboxyl. The effect is higher with smaller cations with same charge.
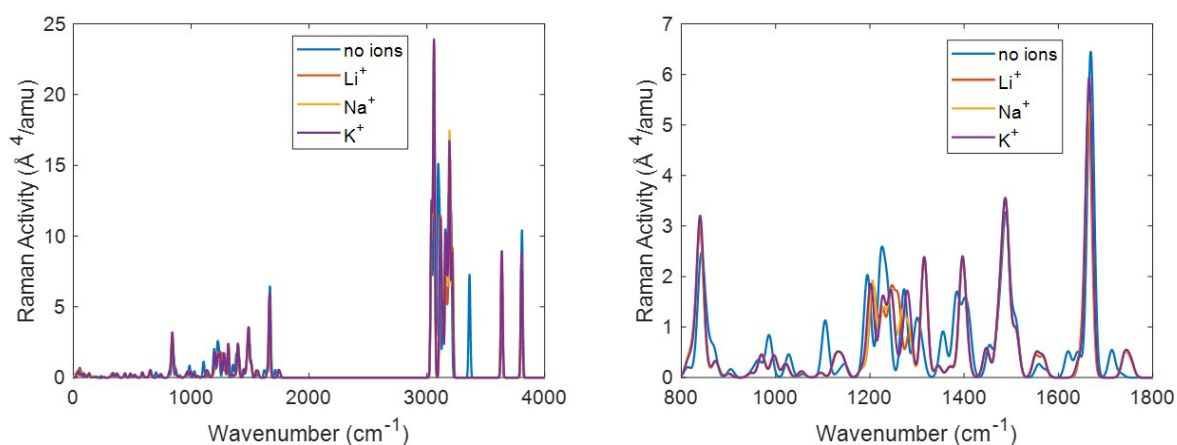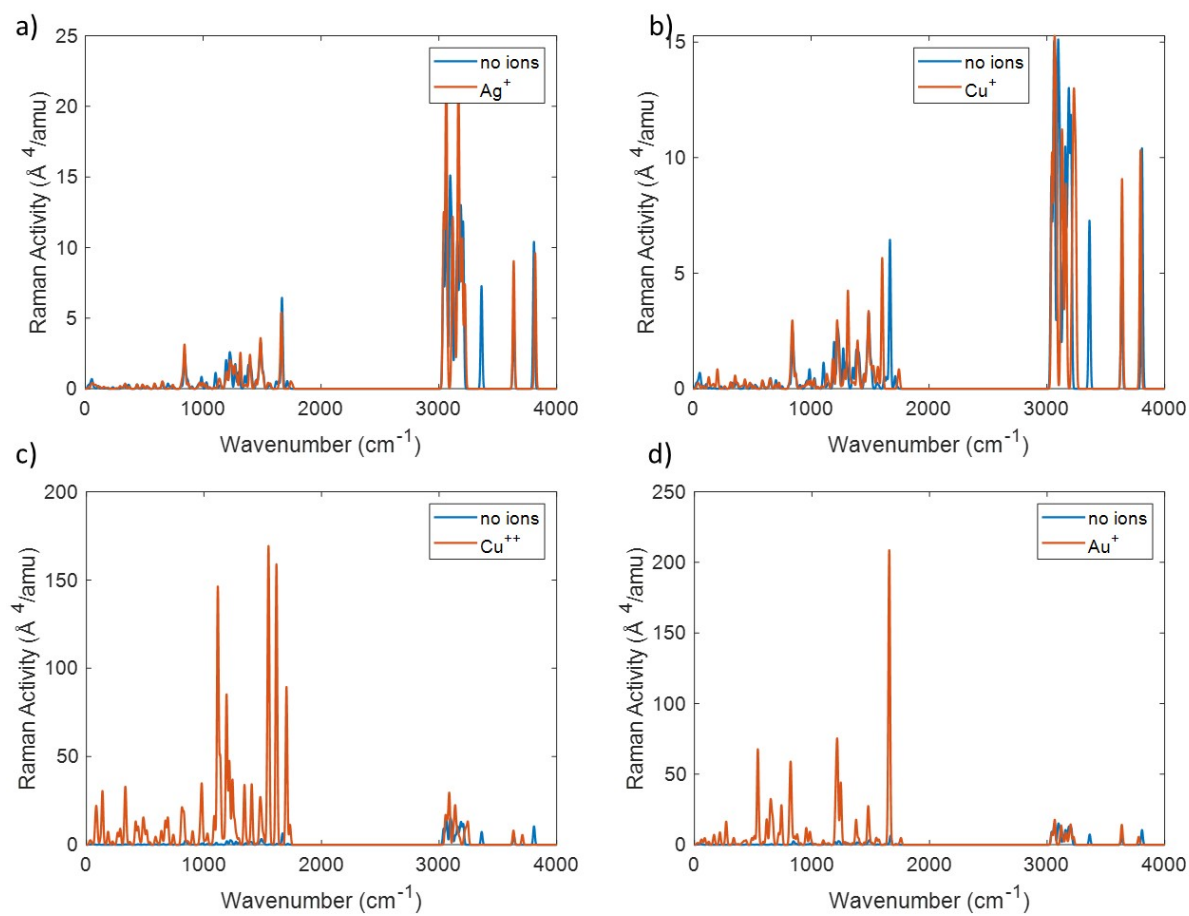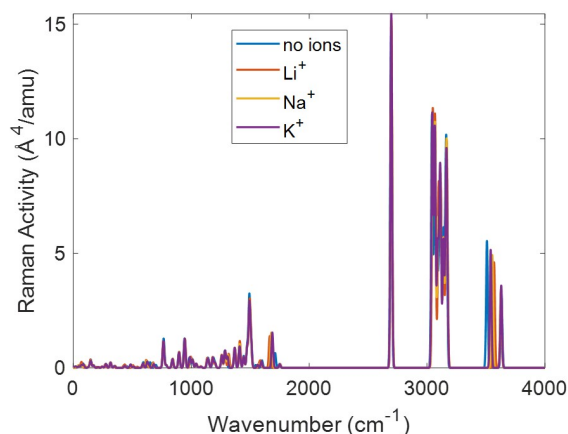

Figure S16: Raman spectra of cysteine in water without ions and in presence of Li$^+$, Na$^+$, K$^+$, with incident laser frequency equal to 785 nm, in the full range (0-4000 cm^{-1}).

Figure S17: Raman spectra of cysteine in presence of Ag$^+$ (panel a), Cu$^+$ (panel b), Cu^{++} (panel c), Au$^+$ (panel d), with incident laser frequency equal to 785 nm, in the full range (0-4000 cm^{-1}).

Figure S18: Raman spectra of cysteine in water without ions and in presence of Li$^+$, Na$^+$, K$^+$, with incident laser frequency equal to 530 nm, in the full range (0-400 cm^{-1}, panel a) and fingerprint region (panel b).

148

Figure S19: Raman spectra of cysteine in presence of Ag$^+$ (panel a), Cu$^+$ (panel b), Cu^{++} (panel c), Au$^+$ (panel d), with incident laser frequency equal to 530 nm, in the fingerprint region.

Figure S20: Raman spectra of cysteine in presence of Ag^+ (panel a), Cu^+ (panel b), Cu^{++} (panel c), Au^+ (panel d), with incident laser frequency equal to 530 nm, in the full range (0-400 cm^{-1}).
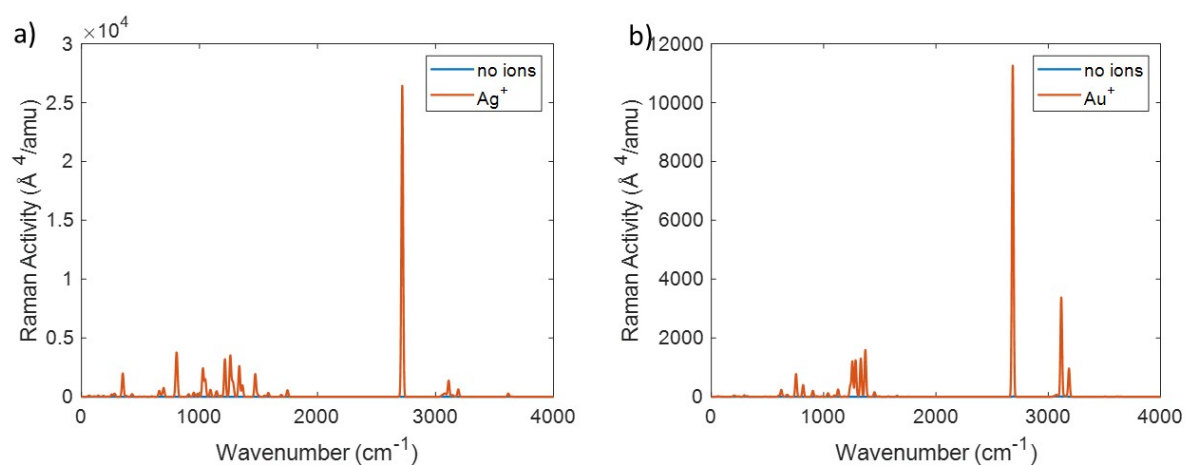
Figure S21: Static Raman spectra of cysteine in presence of Ag^+ (panel a) and Au^+ (panel d), in the full range (0-400 cm^{-1}).

Serine

All the Serine Raman spectra at 530 nm are very close to those computed at 785 nm but for the case of Cu^{++} (in figure S25c and S26c) because in this case the incident laser frequency does not match any electronic transition. However, this spectrum is quite different from the spectrum without ions, in particular some peaks are enhanced: at 1054 cm^{-1}, 1249 cm^{-1}, 1352 cm^{-1}, 1411 cm^{-1}, 1598 cm^{-1}, 1618 cm^{-1}. All this peaks are related to normal modes localized on the ring formed by the amide, the serine side chain and the cation, when the cation bridged between the oxygen atom of the hydroxy and the oxygen atom of the carboxyl.
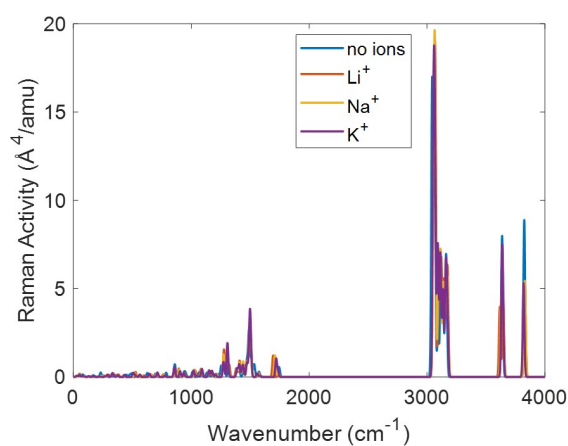
Figure S22: Raman spectra of serine in water without ions and in presence of Li^+, Na^+, K^+, with incident laser frequency equal to 785 nm, in the full range (0-4000 cm^{-1}).
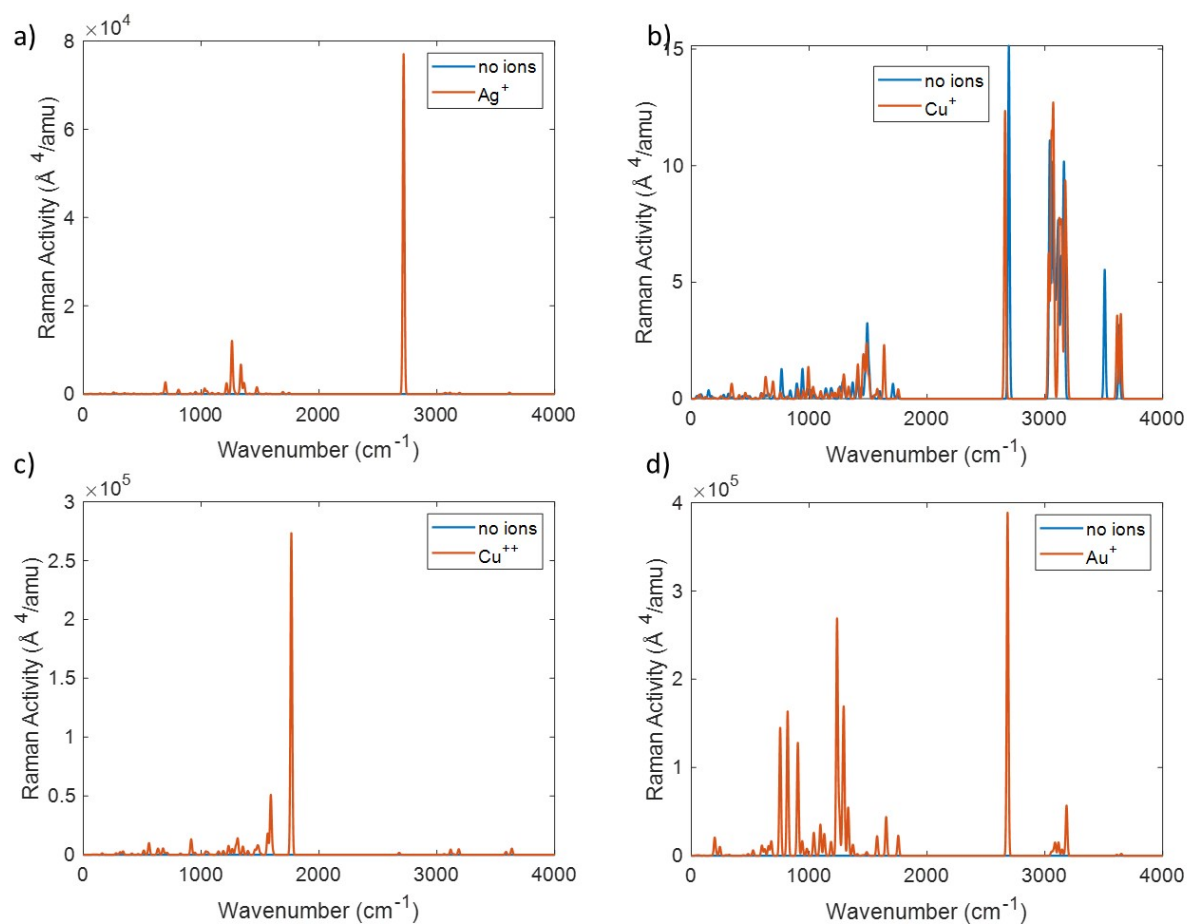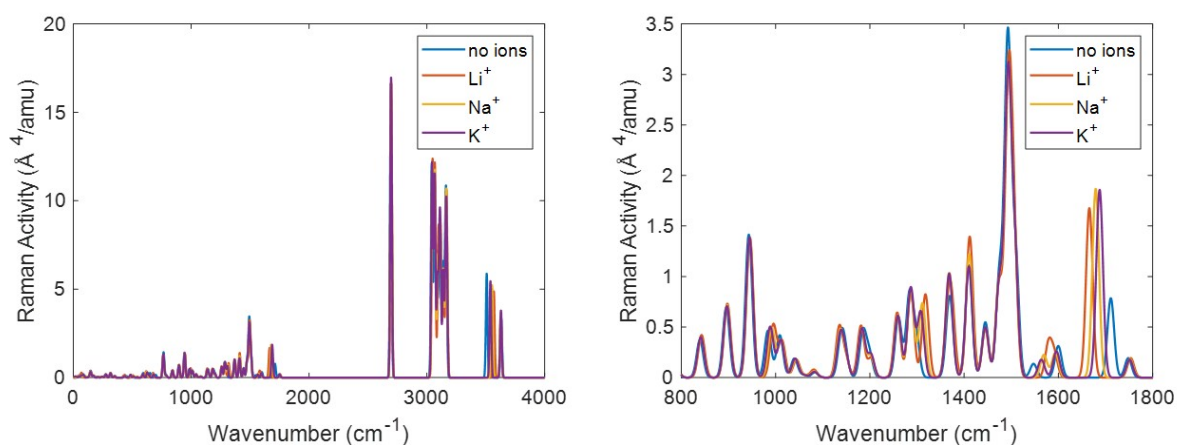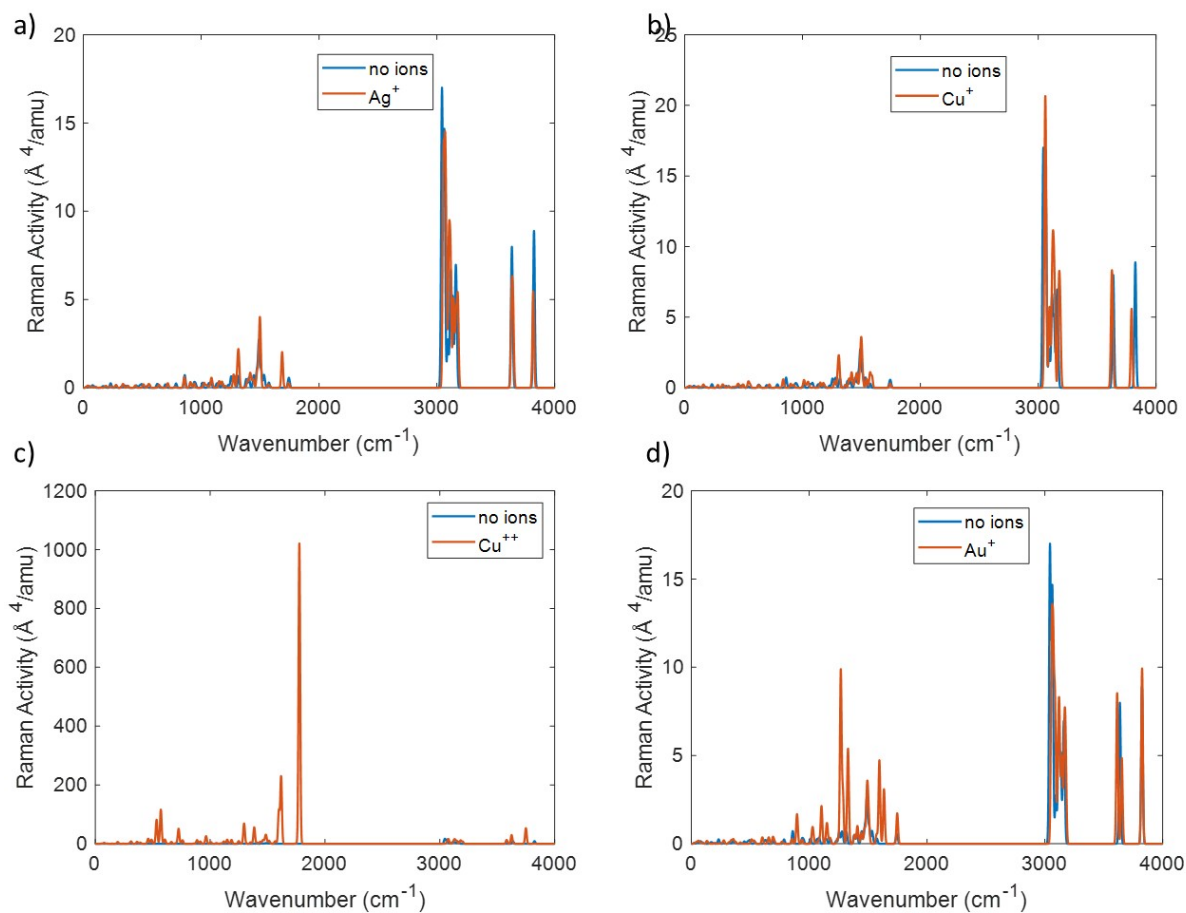
Figure S23: Raman spectra of serine in presence of Ag$^+$ (panel a), Cu$^+$ (panel b), Cu^{++} (panel c), Au$^+$ (panel d), with incident laser frequency equal to 785 nm, in the full range (0-4000 cm^{-1}).
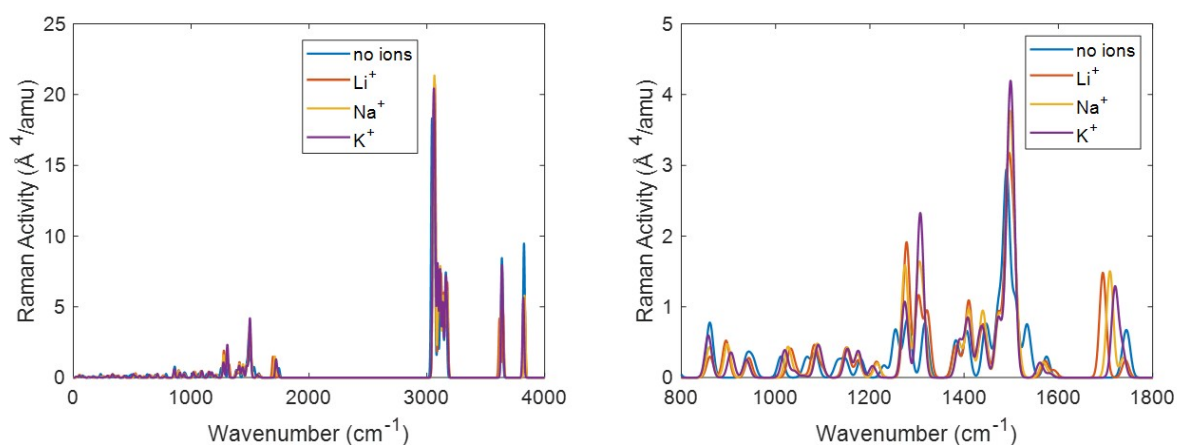
Figure S24: Raman spectra of serine in water without ions and in presence of Li$^+$, Na$^+$, K$^+$, with incident laser frequency equal to 530 nm, in the full range (0-400 cm^{-1}, panel a) and fingerprint region (panel b).
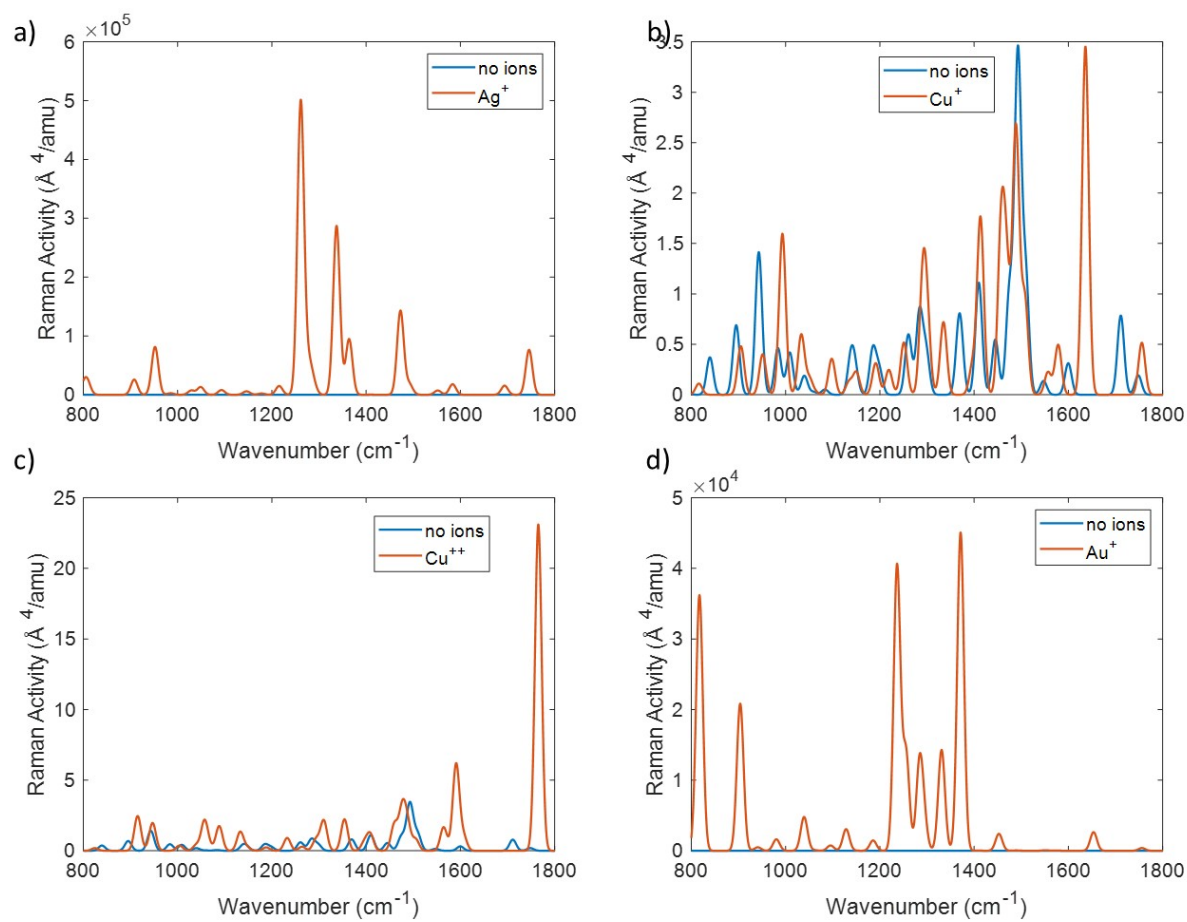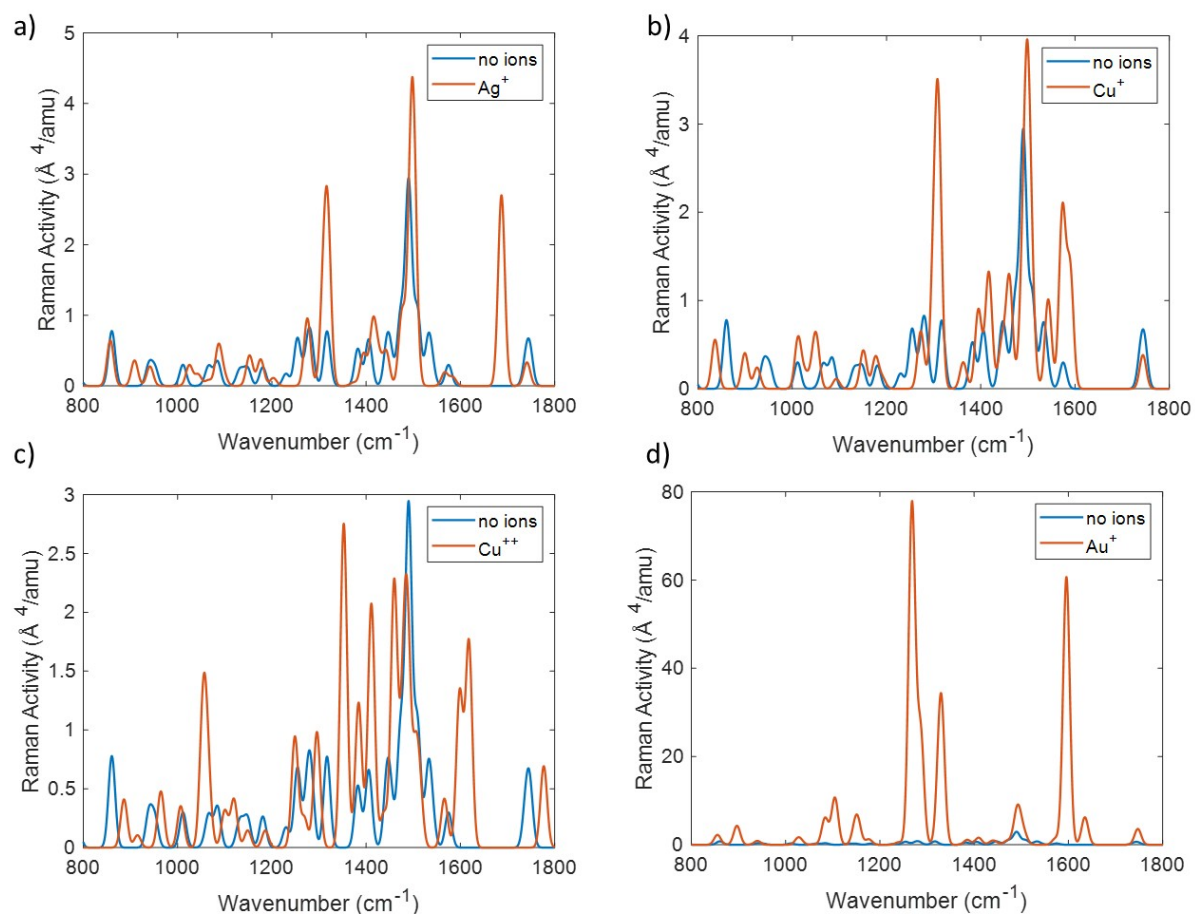
Figure S25: Raman spectra of serine in presence of Ag$^+$ (panel a), Cu$^+$ (panel b), Cu^{++} (panel c), Au$^+$ (panel d), with incident laser frequency equal to 530 nm, in the fingerprint region.
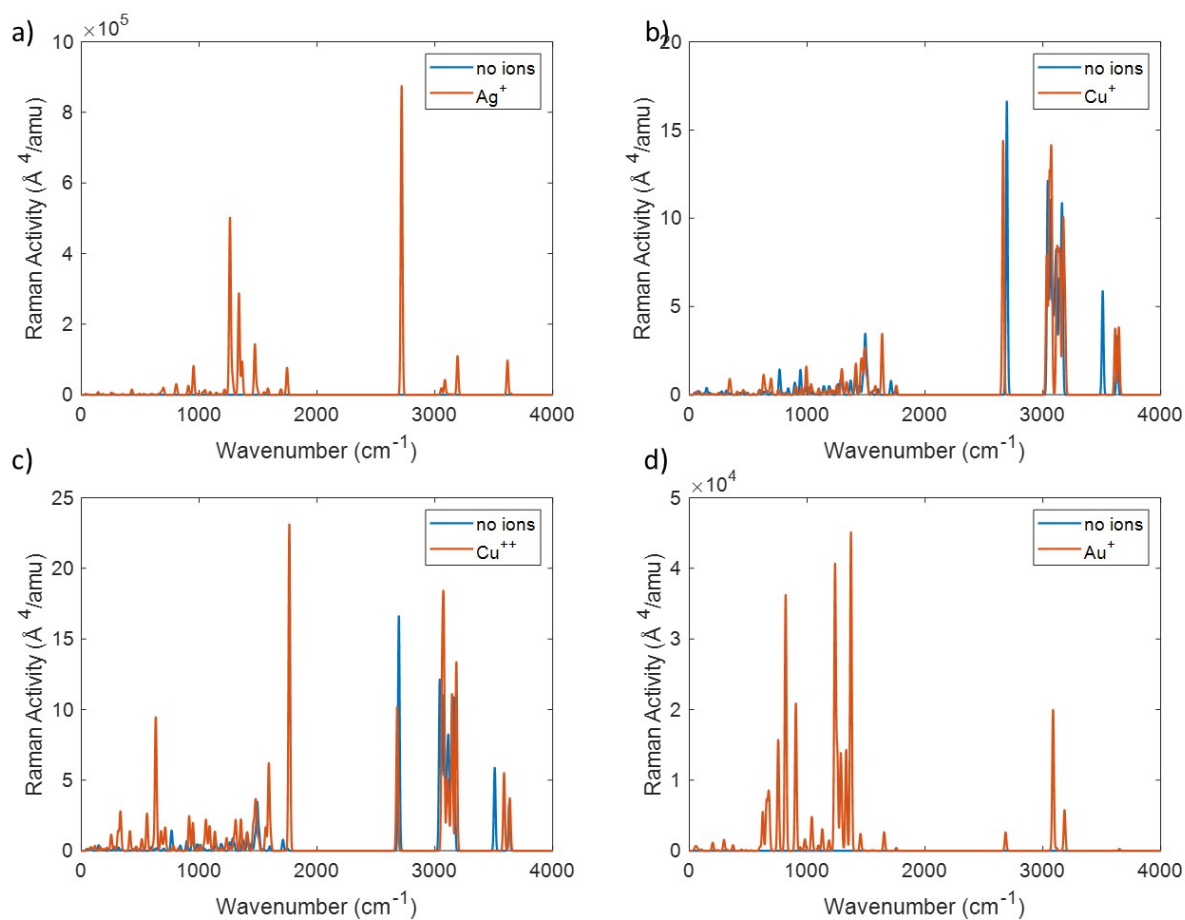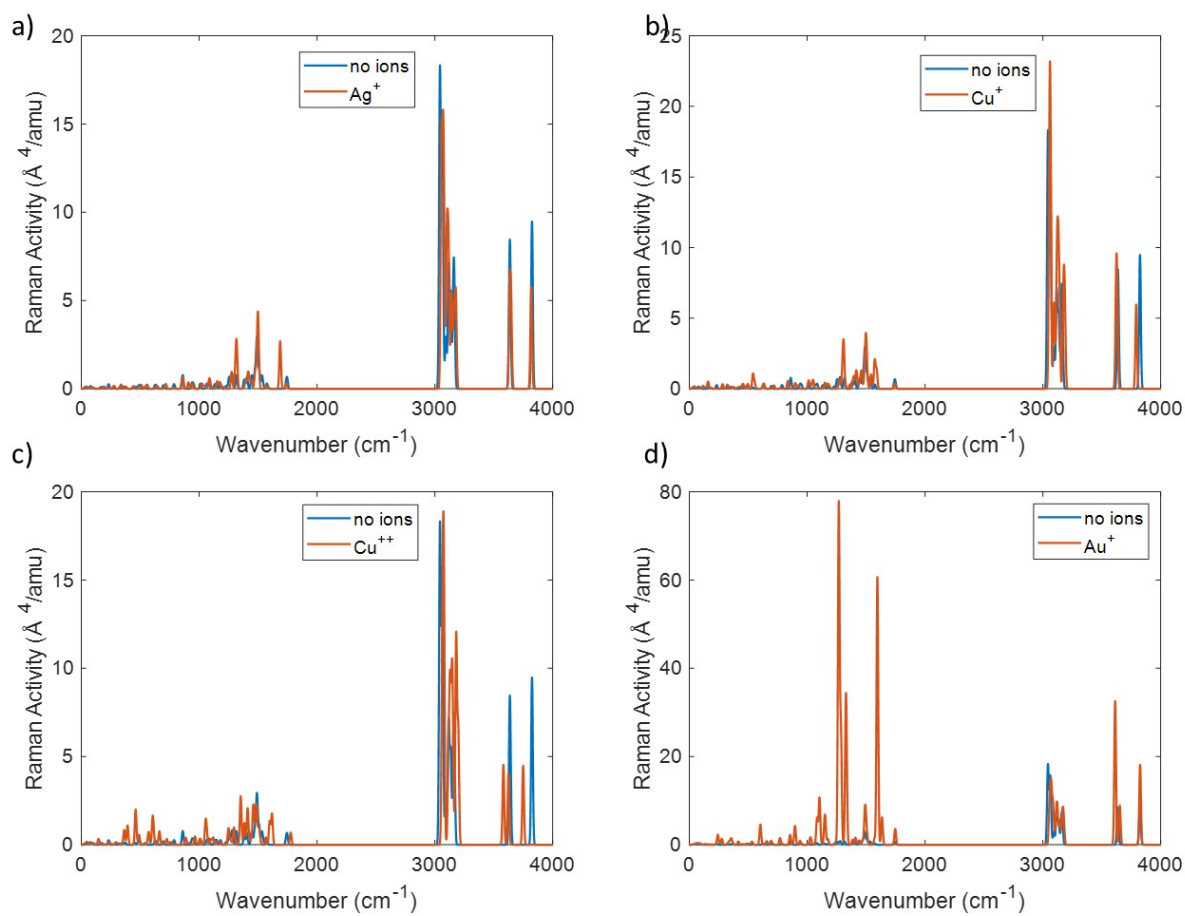
Figure S26: Raman spectra of serine in presence of Ag^+ (panel a), Cu^+ (panel b), Cu^{++} (panel c), Au^+ (panel d), with incident laser frequency equal to 530 nm, in the full range (0-400 cm^{-1}).

Chapter 5

Remaining within the Raman spectroscopy, I moved toward simulation of Raman spectra of single molecules from a time-dependent perspective. My goal was not only to use a time-dependent method to simulate the Raman spectra, but also to obtain information about the process that takes place during the dynamics. The method I developed is based on the pioneering work of Lee and Heller[31] theory, which sets the basis for time-dependent Raman scattering. Within the framework of this theory, the Raman process can be viewed as the result of the propagation of the second-order wave function in terms of the number of pulses involved. The molecular response is obtained through a half Fourier-Transform of the overlap between the initial and final states.[75]

The method I have developed allows the use of different shapes of the incident pulse to bridge the gap between a simulated and an experimental setup. It also offers the possibility of using a known-by-points incident electromagnetic pulse. Furthermore, the description of the molecule is at quantum chemical level, including the Franck-Condon and Herzberg-Teller[76, 77] expansion of the vibrational transition dipole moment.

The method is reported as a paper published in *The Journal of Physical Chemistry A*. It is divided into a methodological part in which the developed theory based on the Lee and Heller's theory as well as all the innovations introduced during my PhD activity are explained in detail. Moreover, the time-dependent Raman scattering was calculated for the test case of a porphyrin molecule using non-resonance and resonance conditions, including the effect of vibrational relaxation, and studying the

role of the incident field duration. To include vibrational relaxation in the model, I took advantage of the existing quantum jump algorithm by means of the Stochastic Schrödinger equation.[78, 79]

The Python code employed to compute the Raman signal from the coefficients dynamics was implemented by me. I also dealt with the pre-processing code to prepare all the preliminary data about the molecule (energies and transition dipole moments) needed for the dynamics based on DFT calculations performed with Gaussian[74] and FCclasses code.[43, 41] The coefficient dynamics has been performed with the existing code WaveT[60] developed in Prof. Corni's group.

This work has been a precursor of the final part of my Ph.D. project, which has the aim to simulate time dependent Raman scattering of molecules close to plasmonic nanoparticles in a time dependent framework. The manuscript was drafted by me, following the useful suggestions of Prof. Corni.

Article

Time Resolved Raman Scattering of Molecules: A Quantum Mechanics Approach with Stochastic Schroedinger Equation

Published as part of The Journal of Physical Chemistry virtual special issue "Vincenzo Barone Festschrift".

Giulia Dall'Osto and Stefano Corni*
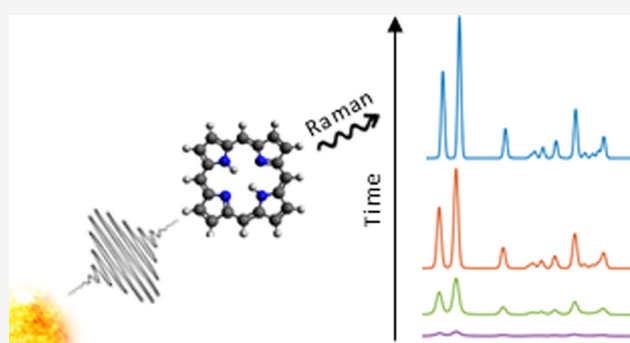
Read Online

ACCESS | Metrics & More | Article Recommendations | Supporting Information

ABSTRACT: Raman scattering is a very powerful tool employed to characterize molecular systems. Here we propose a novel theoretical strategy to calculate the Raman cross-section in time domain, by computing the cumulative Raman signal emitted during the molecular evolution in time. Our model is based on a numerical propagation of the vibronic wave function under the effect of a light pulse of arbitrary shape. This approach can therefore tackle a variety of experimental setups. Both resonance and nonresonance Raman scattering can be retrieved, and also the time-dependent fluorescence emission is computed. The model has been applied to porphyrin considering both resonance and nonresonance conditions and varying the incident field duration. Moreover the effect of the vibrational relaxation, which should be taken into account when its time scale is similar to that of the Raman emission, has been included through the stochastic Schroedinger equation approach.

1. INTRODUCTION

One of the techniques mainly employed to investigate the vibronic structure of molecules is Raman spectroscopy,[1−5] which has become a very powerful tool useful for the characterization of molecular systems.[6] Due to the very short time scale of the process, the Raman signals are very sharp, and thanks also to the richness of information enclosed on the vibronic structure, they can constitute a fingerprint for molecules.[7,8]

What occurs in Raman scattering is a two-photon process[9,10] that involves a first interaction with an incident radiation which makes the molecule explore a virtual state, namely a superposition of excited states, and the emission of a photon with energy that differs from the incident one by a molecular vibrational frequency.[11,12] Considering an incident radiation in resonant conditions, the distinction is made between resonance Raman scattering and fluorescence emission that differ in time scale and spectral shape: Raman scattering is the early time emission (which generates spike lines in the spectrum) and the fluorescence is the late time emission (responsible for broad bands).[13] In nonresonant conditions the Raman scattering and the fluorescence lay on a different range of the scattered energies and thus the distinction is unequivocal.

Raman scattering is distinguished from Rayleigh scattering, the elastic process, in which the scattered photon has the same energy of the incident one, or in other words the scattered

photon brings the molecule back to the initial state. Raman process is related to the inelastic scattering of photons namely the scattered light has a different frequency with respect to the incident light. The bands generated by the Raman scattering are named Stokes when the scattered light has a frequency smaller than the incident light, otherwise they are called anti-Stokes. Differently from other spectroscopic techniques, the quantum mechanical description of the process is not trivial, and a great effort has been employed so far to give insight on the process and to theoretically reproduce the experimental results.

The theoretical methods employed to simulate Raman scattering start from the Kramers, Heisenberg, and Dirac (KHD)[14−16] polarizability tensor and can be categorized in time-independent and time-dependent strategies. To the former belong the so-called sum-overstate methods based on an explicit expansion[17−20] of the transition dipole moments ideally on all the molecular vibronic states.[21−24] On the time-dependent side, the Lee and Heller[12,13] theory gave a new
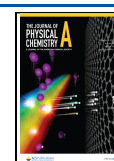
picture of the Raman process as result of the propagation of a wavepacket on the excited-state potential energy surface. In this framework, the Raman intensity is determined by the half Fourier Transform of the overlap of initial and final states.[25] Time-dependent strategies have been developed coupling Raman theory to DFT methods[26−29] or employing Green's function method to calculate the vibronic states overlap.[30] On the other hand a real-time propagation can provide for the molecular response in the perturbation theory framework to retrieve the KHD polarizability.[31,32] Other approaches developed in the time domain, based on the Fourier transform of the polarizability, have also increased the accuracy of results including the Herzberg−Teller vibronic coupling[33−35] and the Duschinsky effect.[36,37]

In this work we propose a time-dependent procedure able to give a view of the process that goes on in Raman scattering, based on a semiclassical approach, that is, an approach which combines the classical treatment of the electric field with a quantum description of the system through its vibronic wave function.[38−42] On the basis of the time-dependent Raman scattering theory proposed by Lee and Heller,[12] a real-time propagation of the system wave function has been coupled with an integration in time[11] that results in the computation of the time-dependent Raman cross-section through the calculation of the second order wave function. Compared with the original treatment of Lee and Heller,[12] and subsequent TD approaches building on that, the main novelties are (i) we are using a numerically defined excitation pulse shape, without assuming a monochromatic continuous wave excitation; (ii) we are not only calculating the total Raman scattered intensity, but we provide the time-dependent cumulative signal; (iii) we include relaxation effects (and potentially also decoherence ones) via the Stochastic Schroedinger equation technique. The latter point allows treating Raman and fluorescence on the same footing, both resulting (on different time scales) from the same simulation.

Employing a generic electric field shape, which could be even defined by points, makes the simulation closer to pulsed experimental setups.

The present approach, which is not only time-dependent but also time-resolved, allows having information on the time scale of the process and also on the way Raman spectra are built in time in comparison with the time scale of the incident radiation.

Within this procedure, phenomena of decoherence and relaxation can be included in the dynamics through stochastic methodologies to consider the interaction with a surrounding environment in an effective way.[43−45] In this work, the stochastic Schroedinger equation has been employed in order to investigate the role of the vibronic relaxation on the Raman process. Vibronic relaxation becomes relevant in the process since it occurs within a picosecond time scale that is also the time scale of the dynamics here reported.

The method here proposed can be applied without further approximations both in resonance and nonresonance conditions between the pulse frequency and the electronic transition. It is worth mentioning that with this strategy both the Raman signal and the fluorescence emission are computed since both contributions, in the present semiclassical formulation, come from the wave function at the second order with respect to the electric field even if the process is different. The scattered photon emitted in the Raman process causes the decay from a virtual state with energy determined by the pulse frequency to a vibronic state of the ground state, while the fluorescence emission needs, at first, to create a population on the excited state and so the emitted photon has energy close to the electronic transition. On this basis, the two phenomena can be distinguished when the two scattering signals are wide apart as in nonresonant conditions. Strategies to computationally tackle time-dependent frequency resolved spontaneous emission have been discussed in the past,[46−48] as well as for time-dependent stimulated Raman;[49,50] computational investigations of the time-development of spontaneous Raman spectra and its interplay with fluorescence received less attention.

This work is a prelude of the more challenging goal of computing the time-dependent spontaneous Raman scattering of molecules close to plasmonic nanoparticles, in order to simulate and predict surface-enhanced Raman scattering (SERS)[51−53] experiments in a time-dependent perspective, combining the real-time dynamics of a molecule vibronic wave function with the propagation of the plasmonic nanostructures dielectric polarization.[44,54−56]

The paper is organized as follows: In section 2 we summarized the theoretical methods divided into the formulation of the time-dependent Raman scattering cross-section, the model for the system vibronic wave function employed, the numerical propagation procedure, and the computational details of the calculations performed; the results obtained with our model and the related discussion are presented in section 3 and final remarks are reported in section 4.

2. METHODS

2.1. Time-Dependent Raman Scattering Formulation.
In this section the main aspects of the theory we employed to describe Raman scattering are highlighted. The time-dependent picture of Raman scattering can be retrieved in the framework of perturbation theory through the two-photon formula. The first order correction to the system wave function allows a description of a one-photon process, such as absorption or emission. It is the result of the interaction between the time evolution of the unperturbed (initial) wave function and the electric field that induces a dynamics on an excited potential energy surface, which in atomic units reads as

$$|\Psi^{(1)}(t)\rangle = i \int_{-\infty}^{t} dt' \, e^{-i\hat{H}(t-t')} \hat{\vec{\mu}} \cdot \vec{\epsilon}_I(t') \, e^{-iE_0 t'} |\Psi_0(-\infty)\rangle \tag{1}$$

$|\Psi_0(-\infty)\rangle$ is the initial unperturbed wave function, considered here to be the ground state, with energy E_0, $\hat{\vec{\mu}}$ is the transition dipole moment operator, $\vec{\epsilon}_I(t')$ is the incident electric field interacting with the system at time t', and $\hat{H}$ is nuclear plus electronic Hamiltonian in the Born−Oppenheimer (BO) approximation. Note that we are also departing from the original Lee and Heller treatment (see also ref 11) since there the propagation is done on electronic wave functions and $\hat{H}$ refers to the electronic Hamiltonian of the proper potential energy surface. Instead, here the vibronic Hamiltonian (i.e., the total Hamiltonian written on the basis of the vibronic wave functions in the BO approximation) enters in the propagation of the wave function. The BO approximation limits our approach to molecules where the vertical excitation region of the lowest excited state is sufficiently far from avoided crossings, where it would break

down.[57−59] To account for spontaneous emission from the virtual state that strictly speaking would require a quantum electrodynamics (QED) treatment, we shall use the same technique proposed by Lee and Heller.[12] In practice, a second classical field $\vec{\epsilon}_S$ is considered, that is monochromatic at the frequency ω_S, whose properties are then chosen to reproduce QED results. At the second order in the mixed $\vec{\epsilon}_S$ and $\vec{\epsilon}_I$ perturbation, neglecting the antiresonant term, one gets

$$|\Psi^{(2)}(t, \omega_S)\rangle = -\frac{1}{2} \int_{-\infty}^{t} dt' \int_{-\infty}^{t'} dt'' \, e^{-i\hat{H}(t-t')} \hat{\vec{\mu}} \cdot \vec{\epsilon}_S \, e^{i\omega_S t'}$$
$$e^{-i\hat{H}(t'-t'')} \hat{\vec{\mu}} \cdot \vec{\epsilon}_I(t'') e^{-iE_0 t''} |\Psi_0(-\infty)\rangle \quad (2)$$

which differs from the original Lee and Heller theory for the missing antiresonant term. In eq 2 the system wave function, after a dynamics guided by the Hamiltonian $\hat{H}$, interacts with $\vec{\epsilon}_S(t') = \vec{\epsilon}_S \, e^{i\omega_S t'}$ that brings the system at a low energy level, which then evolves under the vibronic Hamiltonian. The second electric field is not included explicitly in the dynamics since it is convenient to calculate its effect a posteriori. Neglecting the antiresonant term (that in which the field $\vec{\epsilon}_S$ interacts with the molecule before $\vec{\epsilon}_I$) is an approximation that limits the validity of the present treatment to resonant and preresonant conditions, while it would be unsuitable (in terms of quantitative accuracy for the Raman intensities) for long wavelength excitations. Nothing fundamental prevents the inclusion of this term in our approach, but to be calculated for a generic $\vec{\epsilon}_I(t)$ it would require several numerical propagations, starting from all the possible excited vibronic states, representing an increase of the computational burden not needed in the present work.

Equation 2 can be expressed as a function of the first order wave function as

$$|\Psi^{(2)}(t, \omega_S)\rangle = \frac{i}{2} \int_{-\infty}^{t} dt' \, e^{-i\hat{H}(t-t')} \hat{\vec{\mu}} \cdot \vec{\epsilon}_S \, e^{i\omega_S t'} |\Psi^{(1)}(t')\rangle \quad (3)$$

where the dynamics of $|\Psi^{(1)}(t')\rangle$, expressed by eq 1, can be obtained numerically through a real-time propagation of the initial wave function interacting with any shape of the incident electric field.

Practically, the wave function is expressed as a linear combination of vibronic eigenstates $|J\rangle$

$$|\Psi^{(2)}(t, \omega_S)\rangle = \sum_J C_J^{(2)}(t, \omega_S)|J\rangle \quad (4)$$

weighted by the time-dependent coefficients at the second perturbative order. Multiplying left and right of eq 4 by the eigenstate $\langle N|$ and substituting the definition of $|\Psi^{(2)}(t, \omega_S)\rangle$ given in eq 3, we obtain the time-dependent coefficients of the state N

$$\langle N|\Psi^{(2)}(t, \omega_S)\rangle = \frac{i}{2} \int_{-\infty}^{t} dt' \langle N| \, e^{-i\hat{H}(t-t')} \hat{\vec{\mu}} \cdot \vec{\epsilon}_S \, e^{i\omega_S t'}|$$
$$\Psi^{(1)}(t')\rangle \quad (5)$$

The first order wave function can be expressed as well as an expansion on vibronic states $|J\rangle$ weighted by the first order time-dependent coefficients, $|\Psi^{(1)}(t')\rangle = \sum_J C_J^{(1)}(t')|J\rangle$, which can be computed through the dynamics of the system wave function, initially in the GS, interacting with an incident

radiation (practical details later). Equation 5 can be rewritten as

$$C_N^{(2)}(t, \omega_S) = \frac{i\epsilon_S e^{-i\omega_N t}}{2} \int_{-\infty}^{t} dt' \, e^{i\omega_S t'} \, e^{i\omega_N t'}$$
$$\sum_J C_J^{(1)}(t')\langle N|\hat{\mu}_S|J\rangle \quad (6)$$

where $\epsilon_S = |\vec{\epsilon}_S|$ is the monochromatic scattering field amplitude and $\hat{\mu}_S = (\hat{\vec{\mu}} \cdot \vec{\epsilon}_S)/\epsilon_S$ is the transition dipole moment operator along the direction of $\vec{\epsilon}_S$.

The second order wave function coefficients of a state N at the limit for t that tends to infinity is exactly the Inverse Fourier Transform (IFT) with respect to the scattered frequency of the first order coefficients, that is directly related to the Raman scattering intensity.[12] From another perspective, the IFT of the first order coefficients as in eq 6 considering a finite time t collects the Raman scattering signal emitted until that moment, giving information on the ongoing Raman process. When the time dependence on the coefficients (i.e., without setting the limit to infinite) is kept, the Raman cross-section can be calculated as a function of time.

To get to this point the square modulus of the coefficients are computed as

$$|C_N^{(2)}(t, \omega_S)|^2$$
$$= \frac{\epsilon_S^2}{4} |\int_{-\infty}^{t} dt' \, e^{i\omega_S t'} \, e^{i\omega_N t'} \sum_J C_J^{(1)}(t')\langle N|\hat{\mu}_S|J\rangle|^2$$
$$= \frac{\epsilon_S^2}{4} |z_S^N(t, \omega_S)|^2 \quad (7)$$

enclosing in the term $|z_S^N(t, \omega_S)|^2$ the integral over t'. Numerically, the integral is calculated by a fast Fourier transform including in the integrand a $\Theta(t - t')$ Heaviside function. The square modulus of the coefficients is the population of the molecular state N created by the scattered radiation with frequency ω_S from upper vibronic states. The time dependence of the population gives information on the total photons emitted until the observation time t. When a specific polarization direction for the incident field (η) is chosen and the scattered signal produced by the scattered field oriented along λ is selected, all the components $z_{\lambda\eta}^N(t, \omega_S)$ are calculated with indices λ, η that run over the Cartesian directions. When the $z_{\lambda\eta}^N(t, \omega_S)$ terms for all the combinations of λ and η are collected, they can be combined in the same way as the polarizability tensor to compute the Raman intensity with a precise polarization of the incident and scattered radiation, and an isotropic average of the molecular orientation is assumed. In this situation, eq 7 can be rewritten as

$$\langle|C_N^{(2)}(t, \omega_S)|^2\rangle_{\text{setup}} = \frac{\epsilon_S^2}{4} z_{N,\text{setup}}^2(t, \omega_S) \quad (8)$$

indicating with $\langle|C_N^{(2)}(t, \omega_S)|^2\rangle_{\text{setup}}$ the population in the state N after isotropic orientational average for a specific illumination-detection setup, and with $z_{N,\text{setup}}^2(t, \omega_S)$ the combination of $z_{\lambda\eta}^N(t, \omega_S)$ terms proper for that setup. For example, for incident radiation with linear polarization

159

perpendicular to the detected scattered radiation and any polarization for the scattered radiation, the terms combine as

$$z_{N,\text{setup}}^2(t, \omega_S) = \frac{45\alpha_N^2 + 7\gamma_N^2 + 5\delta_N^2}{45} \tag{9}$$

with

$$\alpha_N = \frac{z_{xx}^N + z_{yy}^N + z_{zz}^N}{3}$$

$$\gamma_N^2 = \frac{1}{2}\Big[|z_{xx}^N - z_{yy}^N|^2 + |z_{xx}^N - z_{zz}^N|^2 + |z_{yy}^N - z_{zz}^N|^2$$
$$+ \frac{3}{2}(|z_{xy}^N + z_{yx}^N|^2 + |z_{xz}^N + z_{zx}^N|^2 + |z_{yz}^N + z_{zy}^N|^2)\Big]$$

$$\delta_N^2 = \frac{3}{4}(|z_{xy}^N - z_{yx}^N|^2 + |z_{xz}^N - z_{zx}^N|^2 + |z_{yz}^N - z_{zy}^N|^2) \tag{10}$$

In order to compute the Raman cross-section as the ratio between the scattered energy and the incident radiation fluence we have to define these two quantities based on the theory developed so far. The whole population of the states involved in the scattering process is the sum of the square modulus of the second order coefficients over all the N vibronic states. The scattered energy is equal to the number of photons emitted at frequency ω_S multiplied by the emitted energy ω_S (in atomic units), where the number of scattered photons is equal to the product between the second order coefficients, representative of the states population achieved by a specific scattered field, and the number of scattered fields with frequency ω_S and amplitude ϵ_S. It follows that the scattered energy over a small $d\omega_S$ frequency interval for a given illumination detection setup $dE_{S,\text{setup}}$, can be written as a function of the second order coefficients as

$$dE_{S,\text{setup}}(t, \omega_S) = \sum_N \langle |C_N^{(2)}(t, \omega_S)|^2 \rangle_{\text{setup}} \rho(\omega_S)\omega_S \, d\omega_S \tag{11}$$

where $\rho(\omega_S)$ is the density of states of the scattered field with frequency ω_S and amplitude ϵ_S. As mentioned, the number of emitted photons can be easily computed from eq 11 by dividing for the photon energy ω_S. Substituting the square of the field amplitude with $\epsilon_S^2 = \frac{8\pi\omega_S}{V}$, the density of states of the scattered field with $\rho(\omega_S) = \frac{V\omega_S^2}{(2\pi c)^3}d\Omega$,[11] and the second order coefficients as in eq 8, we end up with the scattered energy per unit of frequency and per unit of solid angle

$$\frac{dE_{S,\text{setup}}(t, \omega_S)}{d\omega_S d\Omega} = \frac{\omega_S^4}{4\pi^2 c^3} \sum_N z_{N,\text{setup}}^2(t, \omega_S) \tag{12}$$

On the other hand, the fluence of the incident field depends on its integral over time as

$$\mathfrak{I}_I = \frac{c}{4\pi} \int_{-\infty}^{+\infty} dt \, |\vec{\epsilon}_I(t)|^2 \tag{13}$$

Any field shape can be used in principle, even a known-by-points electric field. In this case we considered a Gaussian enveloped sinusoidal field with equation

$$\vec{\epsilon}_I(t) = \vec{\epsilon}_{I,0} \sin(\omega_I t) \, e^{-(t-t_0)^2/(2\sigma^2)} \tag{14}$$

centered in t_0, with amplitude $\vec{\epsilon}_{I,0}$, width σ and frequency ω_I. Integrating the incident electric field over time leads to the fluence of the incident field

$$\mathfrak{I}_I = \frac{c\sigma}{8\sqrt{\pi}} |\vec{\epsilon}_{I,0}|^2 \tag{15}$$

Dividing the scattered energy of eq 12 by the incident field fluence in eq 15, the cumulative time-dependent cross-section per unit of solid angle and per unit of scattered frequency is computed as a sum over the contribution given by each vibronic state N:

$$\sigma_{\text{setup}}^{f \leftarrow i}(t, \omega_S) = \frac{2\omega_S^4}{\pi^{3/2} c^4 \sigma |\vec{\epsilon}_{I,0}|^2} \sum_N z_{N,\text{setup}}^2(t, \omega_S) \tag{16}$$

With eq 16 we can not only recollect the overall Raman cross-section for a given illumination-detection setup, that can be also computed through strategies based on the transition polarizability tensor, but also the Raman signal as a function of time. In other words, this approach lets one know how progressively the Raman signal is accumulated and which is the time scale of the process.

2.2. Vibronic Wave Function. To obtain the Raman signal it is worthwhile to consider a proper wave function in the dynamics, dressing the electronic states with vibrational levels. The wave function, expanded on vibronic states, is considered within the BO approximation to separate electronic and nuclear motions. In this framework each vibronic eigenstate $|J\rangle$ used in the previous section can be expressed as a product between an electronic ($|\phi_{el}\rangle$) and a vibrational ($|\chi_v^{el}\rangle$) wave function $|J\rangle = |\phi_{el}\rangle|\chi_v^{el}\rangle$. Based on this approximation, the transition dipole moment between two vibronic states is expressed as

$$\vec{\mu}_{if} = \langle \chi_i^g | \langle \phi_g | \hat{\vec{\mu}} | \phi_e \rangle | \chi_f^e \rangle = \langle \chi_i^g | \vec{\mu}_{ge} | \chi_f^e \rangle \tag{17}$$

with $|\chi_i^g\rangle$ and $|\chi_f^e\rangle$ being the initial and final vibrational levels which belong respectively to the ground ($|\phi_g\rangle$) and the excited ($|\phi_e\rangle$) electronic states. The vibrational levels are expanded within the normal mode approximation; e.g., anharmonic terms are neglected.[60,61] Transition dipole moments between vibronic states that belong to the same electronic state are also neglected.

At this level the electronic and vibrational parts are decoupled so the Herzberg−Teller (HT) coupling has been included to recover for the transition dipole moment dependence on the normal mode coordinates, even if in an approximated way. Introducing the HT coupling allows inclusion of the dependence on nuclear coordinates in terms of a perturbative expansion of the electronic transition dipole due to the presence of a vibrational manifold. Therefore, the electronic transition dipole can be written as a Taylor expansion in the nuclear displacements around the nuclear equilibrium configuration Q_0[9]

$$\vec{\mu}_{ge} = (\vec{\mu}_{ge})_0 + \sum_k \left(\frac{\partial \vec{\mu}_{ge}}{\partial Q_k}\right)_0 Q_k + o(Q^2) \tag{18}$$

where k runs over the normal mode coordinates. The first term of eq 18 is the electronic transition dipole moment calculated at the nuclear equilibrium position, while in the second term appears the transition dipole moment derivative with respect to

160

the normal mode coordinates evaluated at the ground state equilibrium geometry. When eq 18 is included in eq 17, the new expression for the transition dipole moment between two generic vibronic states reads as

$$\vec{\mu}_{if} = \langle \chi_i^g | \chi_f^e \rangle (\vec{\mu}_{ge})_0 + \sum_k \langle \chi_i^g | Q_k | \chi_f^e \rangle \left(\frac{\partial \vec{\mu}_{ge}}{\partial Q_k} \right)_0 \tag{19}$$

The first term of eq 19 includes the Franck−Condon integral calculated between the final and initial vibronic states when the electric dipole moment is considered at the equilibrium normal mode coordinates. The second term accounts for the Herzberg−Teller contribution including a first order correction of the electric dipole moment with respect to the normal mode coordinates.[62]

2.3. Numerical Propagation. As mentioned above, within our approach the dynamics of the first order wave function is computed numerically. Practically the coefficients of the vibronic expansion are propagated through a second-order Euler algorithm as[55,63]

$$C_N(t + dt) = C_N(t - dt) - 2i \, dt (H_0 - \vec{\mu} \cdot \vec{\epsilon}_I(t)) C_N(t) \tag{20}$$

in which dt is the time step chosen for the propagation, H_0 is the time independent Hamiltonian that returns the energy of the state N while $\vec{\mu} \cdot \vec{\epsilon}_I(t)$ accounts for the interaction with the incident electric field. The incident radiation can have in principle any profile since it is numerically defined. In this work we consider a Gaussian enveloped sinusoidal equation for the incident field as said before.

The greater part of the calculations has been performed considering the molecule as a closed quantum system. However, some others have been performed including the vibrational relaxation from the upper vibronic states to the lower level of the same electronic state. To this purpose the system wave function has been propagated through the Stochastic Schroedinger Equation (SSE)[43,45] including non-radiative decay rate from the upper vibronic states toward the lower level of the electronic excited state. The SSE in a Markovian regime reads

$$\frac{d}{dt} |\Psi^{(1)}(t)\rangle = -i\hat{H}(t)|\Psi^{(1)}(t)\rangle - \frac{1}{2} \sum_q^M \hat{S}_q^\dagger \hat{S}_q |\Psi^{(1)}(t)\rangle$$
$$- i \sum_q^M l_q(t) \hat{S}_q |\Psi^{(1)}(t)\rangle \tag{21}$$

where q runs over the number M of decay channels of the system and $l_q(t)$ is a white noise function associated with the Markov approximation needed to include the fluctuation induced by the environment. The first term in the r.h.s. of eq 21 represents the deterministic term related to the energy of the system and the interaction with the incident field, while the second and third terms are responsible for the decay processes guided by operators $\hat{S}_q$. According to previous works,[43,44,64,65] relaxation has been included by the operator

$$\hat{S}_q^{rel} = \sqrt{\Gamma_q} |\phi_e\rangle |\chi_0^e\rangle \langle \chi_q^e| \langle \phi_e| \tag{22}$$

which is responsible for the decay of the vibronic state $|\phi_e\rangle|\chi_q^e\rangle$ population on the state $|\phi_e\rangle|\chi_0^e\rangle$ where q is the vibrational level and e the electronic state. The decay rate Γ_q can be taken either

as phenomenological parameters (as in the present case, see Computational Details) or estimated by ab initio simulations. Practically the coefficients dynamics are computed through the second-order Euler algorithm as in eq 20 while the stochastic terms of SSE are included by means of a quantum jumps algorithm.[43] This algorithm is based on discontinuous trajectories. At each time step during the dynamics, the probability of the jump to occur associated with the decay operator $\hat{S}_q$ and given by $\langle \Psi^{(1)}(t)|\hat{S}_q^\dagger \hat{S}_q|\Psi^{(1)}(t)\rangle \, dt$ is estimated. Whether the jump actually occurs or not is decided by a Monte Carlo algorithm. When the jump happens, the wave function $|\Psi^{(1)}(t)\rangle$ is replaced by $\hat{S}_q|\Psi^{(1)}(t)\rangle$ and normalized; on the contrary it is only normalized. The density matrix evolution is obtained by averaging over several of these trajectories. For further details see ref 43.

The coefficients dynamics of each trajectory has been employed to compute the second order coefficients. Varying the polarization of the incident field and the scattered radiation, we computed all the terms $z_{\lambda\eta}^N(t, \omega_S)$ needed to calculate, for a given illumination-detection setup and for each trajectory, the time-dependent Raman cross-section $\sigma_{setup,traj}^{f \leftarrow i}(t, \omega_S)$ and finally the average on all the realizations has been taken as

$$\sigma_{setup}^{f \leftarrow i}(t, \omega_S) = \frac{1}{N_{traj}} \sum_{traj} \sigma_{setup,traj}^{f \leftarrow i}(t, \omega_S) \tag{23}$$

The Raman cross-section is a measurement of the amount of population generated in each final vibronic state by scattered fields with different frequencies ω_S. The population computed from a single trajectory is meaningless in itself but when the average over a number of realizations is taken, the SSE converges to the Lindbland master equation results.[43,66]

2.4. Computational Details. The approach presented in the previous sections has been applied to porphyrin, as a test case. The quantum chemical calculations have been performed through DFT methods at the B3LYP/6-31G level of theory using Gaussian 16.[67] The ground state and first excited state were optimized, and then the vibrational calculation was performed on both potential energy surfaces. To obtain a proper wave function for the system, the two electronic states have been dressed with 109 vibrational states each (the ground vibronic state and the first vibronic level for each normal mode). We computed the FC and HT integrals of the molecule between all the vibronic states belonging to different electronic states through FCclasses code.[62,68] The vibronic analysis has been carried out within the adiabatic Hessian model which takes into account the Duschinsky mixing and the frequency changes between ground and excited state. The FC and HT integrals have been employed to compute the transition dipole moments as in eq 19. The system wave function is approximated by including only one excited electronic state, thus when in nonresonance conditions there could be significant differences on the spectra shape and intensity compared with the experimental results. However, the focus of this work is on the time scale of the process and on the interplay with fluorescence.

The dynamics of the first order system wave function has been computed through the WaveT code.[43,69] During the propagation the system interacts with an incident electric field shaped as a Gaussian enveloped sinusoidal signal, as

mentioned above. Three different simulations for each field setup have been computed varying the incident field direction along x, y, and z axes in order to have all the information needed for the calculation of the term $z_{N,\text{setup}}^2(t, \omega_S)$ as in eq 9.

The dynamics length is 24 ps in almost all the calculations and the time step considered is 0.024 fs. When it is not differently specified, the field has a Gaussian enveloped sinusoidal shape (see sec. 2.3) with $\sigma = 256$ fs, $\epsilon_{I,0} = 5.14 \times 10^5$ V/m, centered at $t_0 = 968$ fs. In nonresonant conditions, the excitation energy is $\omega_I = 2.04$ eV, which is 0.24 eV less than the vertical transition frequency $S_1 \leftarrow S_0$. After the calculation of the coefficients dynamics, the cumulative Raman cross-section was computed at different times, through eq 16. The convergence of the spectrum can be checked as explained in ref 21.

In the simulation with the vibrational relaxation, 50 repetitions of the dynamics were computed with vibrational relaxation equal to 1.8 ps.[70] Convergence with respect to the number of employed trajectories when including vibrational relaxation in resonance conditions has been confirmed comparing the Raman spectra at 2.4 ps computed with either 50 or 100 trajectories. The result is reported in Figure S1 of the Supporting Information.

3. RESULTS AND DISCUSSION

The procedure developed to compute Raman scattering cross-section has been applied to porphyrin, laying in the xy plane as Figure 1 shows. The calculation of the cumulative time-
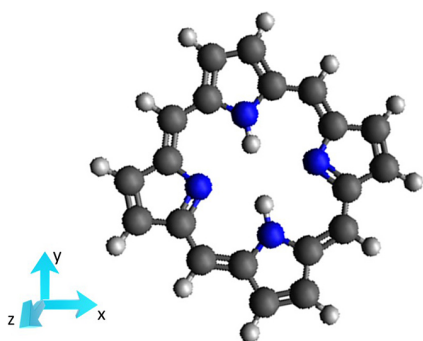

Figure 1. Structure of porphyrin molecule and orientation employed for the calculations.

dependent Raman cross-section has been performed by employing two different field frequencies to study the nonresonance and resonance conditions with respect to the electronic excitation energy. Moreover also the field duration and the presence of the vibrational relaxation have been exploited.

To validate the numerical strategy, we compared porphyrin Raman spectrum computed through our TD method in nonresonant conditions with the spectrum computed with a time independent strategy, by employing the FCclasses code.[21,68] The results, reported in Figure S2, show a good agreement, therefore confirming the correctness of our strategy.

Moreover a comparison with the experimental Raman spectrum of porphyrin[71] is reported in Figure S3. Apart from an overall rescaling of the frequencies, which is expected for harmonic spectra,[72,73] the agreement is good. The remaining discrepancies (beside the frequency rescaling), may be due to

the different environments (the experiment is conducted in CH_2Cl_2, while the calculation is performed in vacuum), to anharmonic effects beside the rescaling and to inherent limitation of the DFT xc functional employed.

3.1. Nonresonance Conditions. In all the calculations reported in this section, the first order coefficients of the system wave function have been computed when the system is initially in the ground electronic state and then interacts with an incident electric field nonresonant with the electronic transition as explained before. After the computation of the coefficients dynamics varying the incident field direction along x, y, and z axes, three different scattering directions (along x, y, and z) have been considered for each incident field direction to compute the time-dependent Raman cross-section in atomic units as in eq 16. Since the electronic transition dipole moment $S_1 \leftarrow S_0$ has the major contribution along the x and y axes, the terms with incident and/or scattered field along the x and y axes give the largest contribution to the Raman cross-section.

Neglecting Vibrational Relaxation. The Raman spectrum as a function of time has been reported in Figure 2a for six different time delays with respect to the beginning of dynamics.

The results show how the Raman intensity is built during and after the interaction with the incident field. Before 484 fs, far from the maximum intensity of the electric field, the Raman intensity is negligible, but before reaching the center of the field at 968 fs, the Raman signal has been already generated due to the short time taken by the process. After 1451 fs from the beginning of the dynamics quite all the Raman intensity is recovered, even if the pulse has not switched off completely. The last spectrum here reported, after 2.4 ps from the beginning of the dynamics, when the pulse is approximately null, is totally equal to the final spectrum computed at 24 ps: all the Raman contribution to emission is achieved in the first hundreds femtoseconds from the interaction with the incident field.

These observations are confirmed by the second column of Table 1 which reports the integral of the peak at 738 cm^{-1} as a function of time, representing the amount of Raman signal collected until the observation time from the beginning of the dynamics without the dependence on the frequency spread signal. The integrals highlight the fast increasing intensity in the first few hundreds of femtoseconds around the maximum field intensity followed by a constant value, a signal that the maximum emitted intensity in this region has been achieved. One possible way to interpret the results is that Raman scattering persists as long as the wave function coefficients have memory of the pulse frequency or, from a more physical viewpoint, until the vibronic excited states are transiently perturbed by the presence of the incident field. After the end of the interaction with the field no more Raman signal is collected since the process, very quickly, is exhausted.

Increasing Field Time Duration. Another calculation has been performed increasing the field time duration by modifying the width of the pulse with $\sigma = 496$ fs and moving the center of the pulse at 2419 fs. In this case the pulse is larger so it is even closer to a monochromatic pulse than the previous one. The Raman spectrum at different time delays from the beginning of the dynamics is reported in Figure 2b. The vibronic states that participate in the Raman spectrum are the same as in the previous case, while the time scale of the signal generation is longer and comparable to the width of the incident pulse employed here. The signal peaks are narrower and well separated due to the incident field shape, closer to a
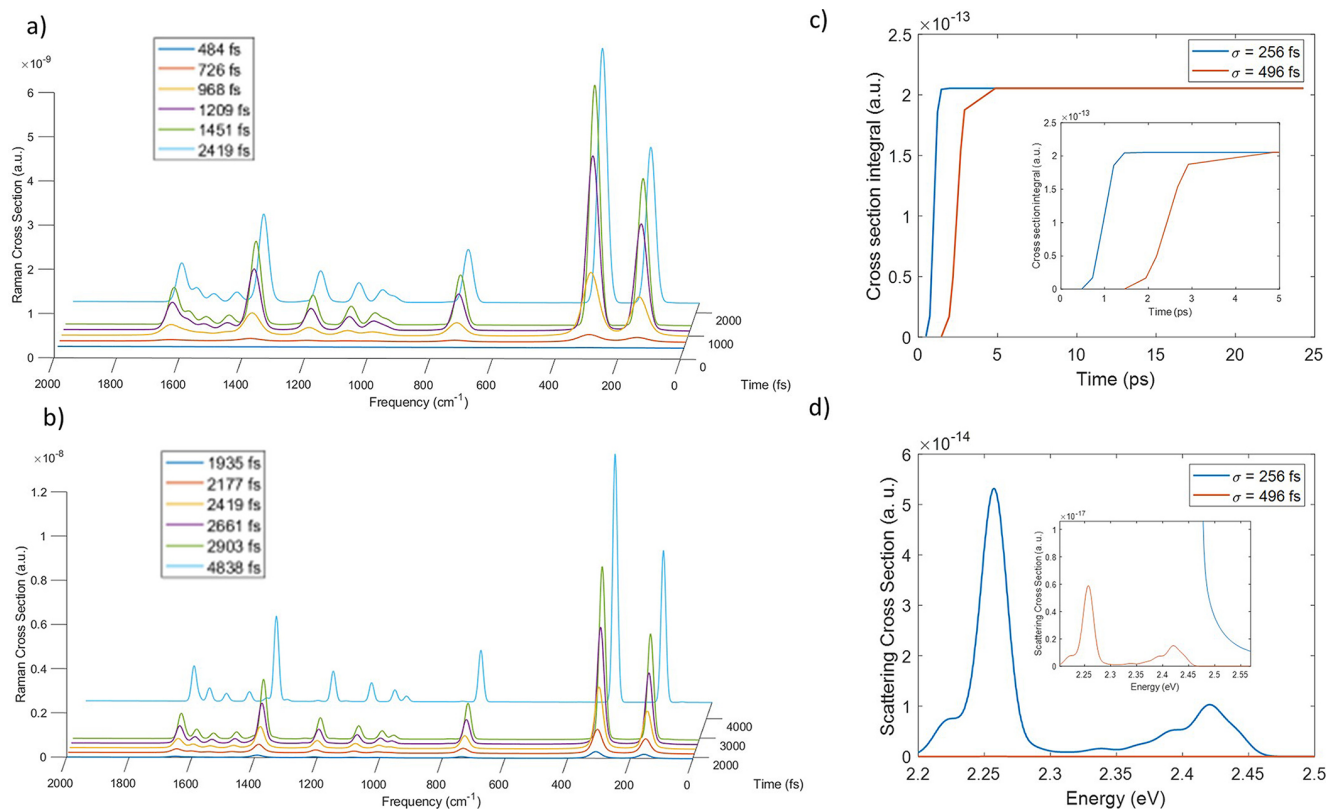
Figure 2. Time dependent Raman cross-section in atomic units at six different time delays with respect to the beginning of dynamics, with incident pulse in nonresonant conditions with $\sigma = 256$ fs (a) and with $\sigma = 496$ fs (b). (c)Time dependent Raman cross-section integral of the peak at 738 cm^{-1} in the case of field with $\sigma = 256$ fs and with $\sigma = 496$ fs. (d) Scattering signal at the end of dynamics in the resonance region when the system interacts with a nonresonant field in which σ is 256 fs or 496 fs. The inset is a magnification of the emitted signal generated with an incident field that has $\sigma = 496$ fs.

Table 1. Cross-Section Integrals of the Peak at 738 cm^{-1} as a Function of Time in Three Cases: with $\sigma = 256$ fs (from Figure 2a), with $\sigma = 496$ fs (from Figure 2b), and with $\sigma = 256$ fs Including also Vibrational Relaxation (from Figure 3)

Time	Cross-section integral ($\sigma = 255$ fs)	Time	Cross-section integral ($\sigma = 496$ fs)	Time	Cross-section integral (vib. relaxation)
fs	a.u.	fs	a.u.	fs	a.u.
484	6.7250×10^{-16}	1457	4.3633×10^{-16}	484	6.7236×10^{-16}
726	1.7272×10^{-14}	1943	1.6738×10^{-14}	726	1.7277×10^{-14}
968	9.9813×10^{-14}	2186	4.9304×10^{-14}	968	9.9807×10^{-14}
1209	1.8585×10^{-13}	2429	1.0129×10^{-13}	1209	1.8582×10^{-13}
1451	2.0457×10^{-13}	2671	1.5386×10^{-13}	1451	2.0456×10^{-13}
1936	2.0538×10^{-13}	2915	1.8756×10^{-13}	1936	2.0536×10^{-13}
2428	2.0538×10^{-13}	4857	2.0538×10^{-13}	2428	2.0536×10^{-13}
24289	2.0538×10^{-13}	24289	2.0538×10^{-13}	4856	2.0536×10^{-13}

monochromatic radiation than in the previous one. As a consequence, these results highlight the dependence of the spectrum line shape on the electric field shape and, in particular in this case, on the duration of the pulse. At last the intensity of the Raman signal in time can be compared with the

previous one by removing the frequency dependence through the integration of the peak at 738 cm^{-1} as reported in Figure 2c and in the fourth column of Table 1. These results show that the amount of scattered radiation is quite the same at the end of the dynamics although the time of the process is longer in the case of a longer incident pulse. On the other hand in the fluorescence emission region (around the transition $S_1 \leftarrow S_0$ energy) the emitted signal has a lower intensity when a longer lasting field is employed, as represented in Figure 2d, because the smaller frequency amplitude of the electric field can excite (nontransiently, as needed for fluorescence emission) less amount of the excited states population.

Including Vibrational Relaxation. Another calculation of porphyrin Raman cross-section has been carried out including vibrational relaxation. To this point, field features have been kept as in the first calculation reported in this section (nonresonant electric field with $\sigma = 256$ fs), and the vibrational relaxation has been included from upper vibronic states to the lowest level of the correspondent electronic state with the phenomenological lifetime of 1.8 ps.[70] 50 trajectories have been computed through SSE equation using in each case three incident field directions (along x, y, z axes) and the dynamics of each simulation is 4.8 ps long. For each trajectory the time-dependent Raman cross-section has been computed, and then they have been averaged to get the mean Raman cross-section. The time evolution of the Raman cross-section including vibrational relaxation, reported in Figure 3, looks very close to the results in which it is neglected (Figure 2a) as expected since the time scale of the process seems faster than the
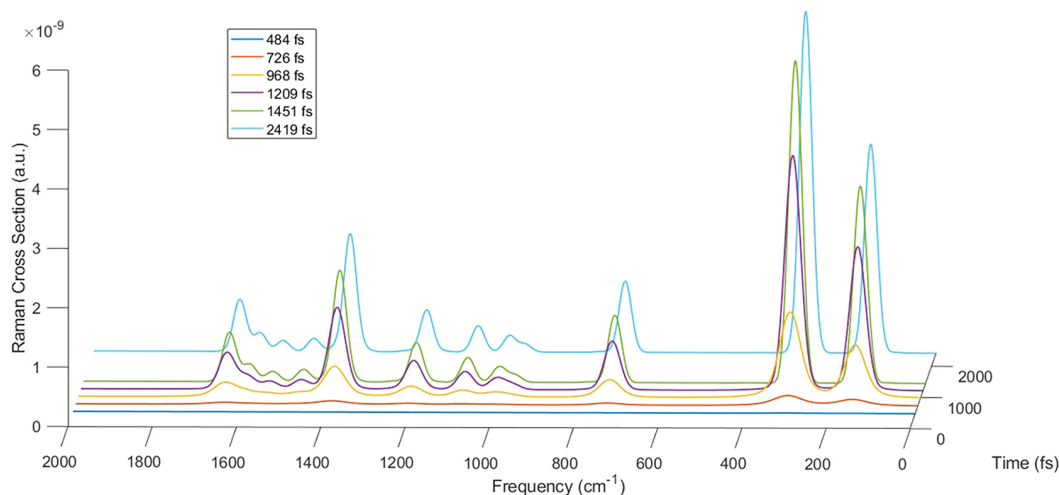
Figure 3. Time-dependent Raman cross-section in atomic units at six different time delays with respect to the beginning of dynamics, with incident pulse in nonresonant conditions, $\sigma = 256$ fs and including vibrational relaxation.
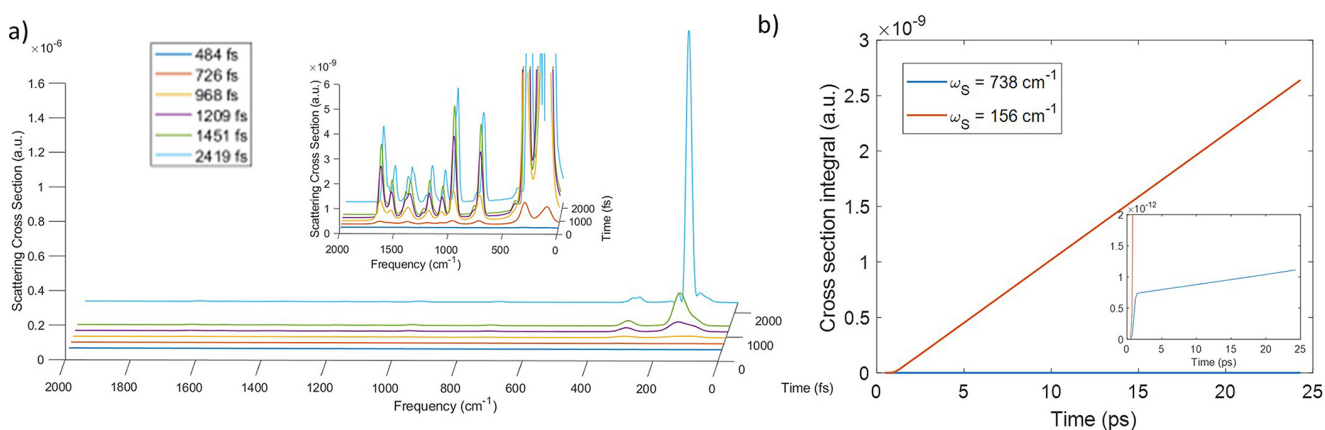

Figure 4. (a) Time-dependent scattering cross-section in atomic units at six different time delays with respect to the beginning of dynamics, with incident pulse in resonance conditions and $\sigma = 256$ fs. The inset shows a magnification of the part of the spectrum with lower intensity. (b) Time-dependent scattering cross-section integral of the peaks at 738 cm^{-1} and the peak at 156 cm^{-1} of the spectra in panel a.

vibrational decay. This result is confirmed by the time-dependent integral of the peak at 738 cm^{-1}, the values of which, reported in column six of Table 1, totally resemble those of the deterministic dynamics (without vibrational relaxation) reported in the second column of the same table. As a conclusion, the introduction of vibrational relaxation is not needed, at least in nonresonant conditions, due to the different time scale of the processes.

3.2. Resonance Conditions. The results reported in this section are related to calculations carried out with the incident field frequency that matches the porphyrin vertical excitation energy ($\omega_I = 2.28$ eV), while the maximum amplitude is equal to 5.14×10^5 V/m, the pulse width has been varied as in the calculations of section 3.1. The time-dependent scattering cross-section has been computed on the basis of the system dynamics when the incident field is polarized alternately along x, y, and z axes. For these calculations in resonant conditions, we refer to the results as to *scattering* cross-sections, rather than to Raman cross-sections given that the Raman scattering and the fluorescence emission lay in the same spectral range. Thus, in principle the two contributions may be mixed and the scattering cross-section is no more the result of the pure Raman contribution.

Neglecting vibrational relaxation. In the first calculation the width of the pulse is $\sigma = 256$ fs and it is centered at $t_0 = 968$ fs, as in the first calculation in nonresonance conditions. In Figure 4a the time-dependent scattering cross-section accumulated at six different times from the beginning of dynamics has been reported. Differently than in nonresonance conditions, in this case the scattering cross-section does not achieve its maximum after 1451 fs but at 2419 fs the intensity is further increasing, as an effect of the fluorescence emission. Moreover the vertical transition matches a few vibronic states in the excited state that give the largest contribution to the scattering spectrum. Also the speed at which the peaks' intensity increases is different, and it is larger for the peak at 156 cm^{-1}, in which the fluorescence emission prevails over the Raman scattering signal, as also Figure 4b shows in terms of the integral of the scattered signals at 156 cm^{-1} and 738 cm^{-1}. This figure highlights both the rate of signal emission and the order of magnitude of the intensity achieved within this time scale, which are very different.

Increasing Field Time Duration. As it has been done in nonresonant conditions, we tested the influence of a longer pulse on the time-dependent scattering cross-section in resonance conditions, by using a larger width of the pulse (σ
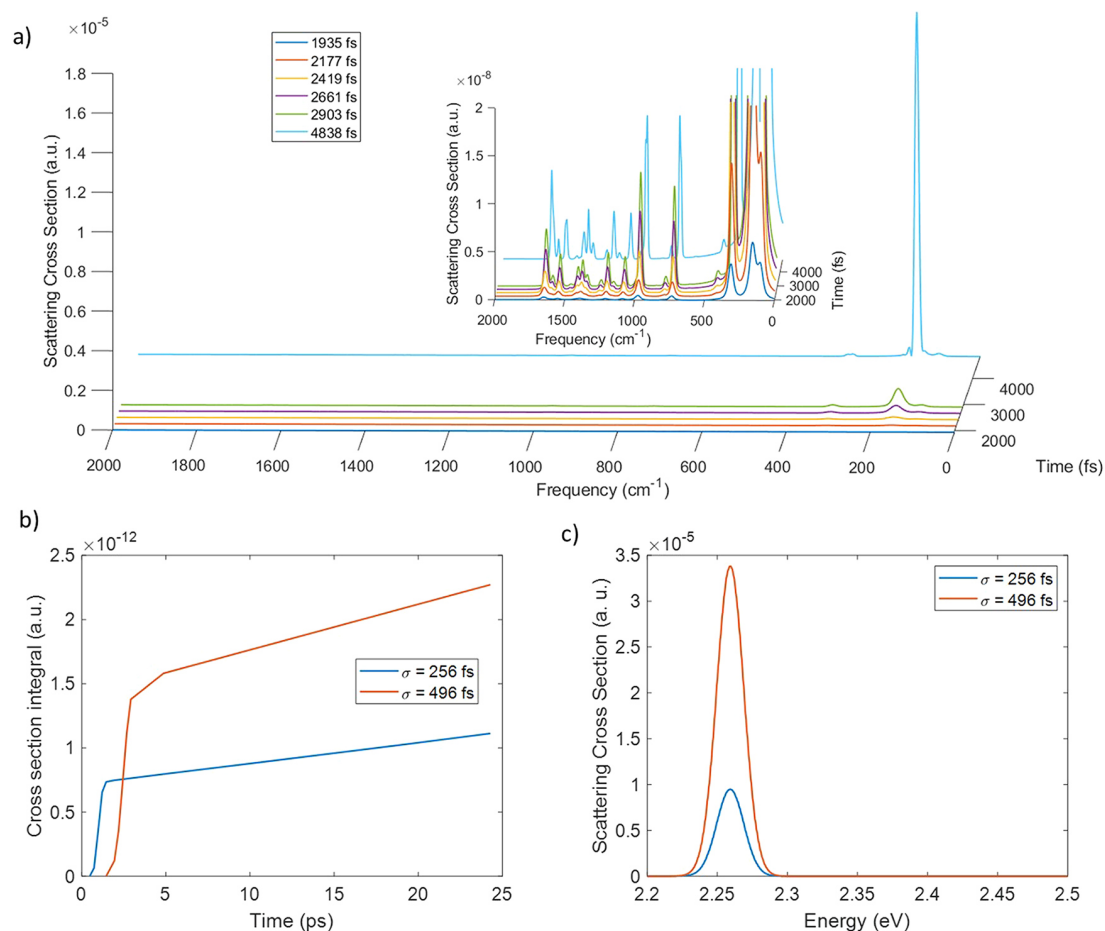
164

Figure 5. (a) Time-dependent scattering cross-section in atomic units at six different time delays with respect to the beginning of dynamics, with incident pulse in resonance conditions and σ = 496 fs. The inset shows a magnification of the part of the spectrum with lower intensity. (b) Time-dependent scattering cross-section integral of the peak at 738 cm^{-1} in the case of field with σ = 256 fs and with σ = 496 fs. (c) Scattering signal at the end of dynamics in the resonance region when the system interacts with a resonant field which σ is 256 fs or 496 fs.
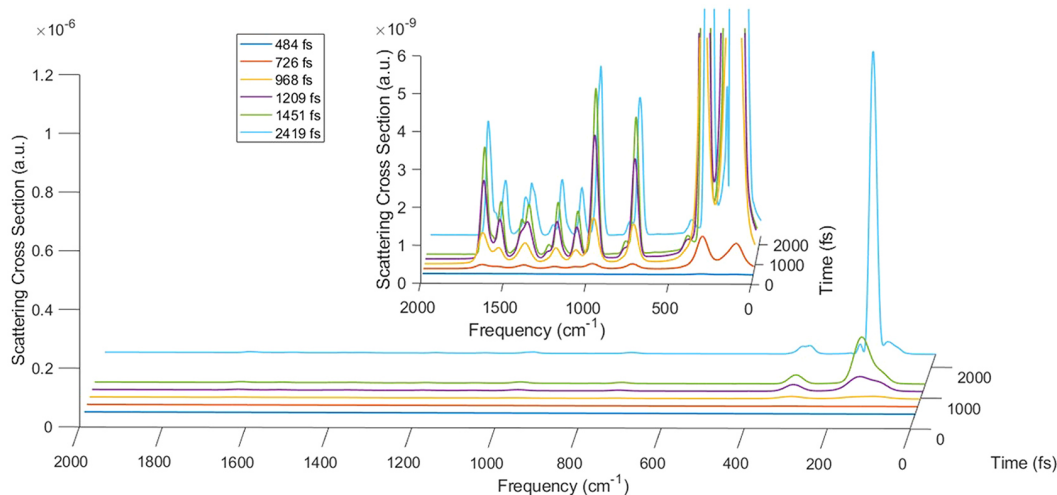
Figure 6. Time-dependent scattering cross-section in atomic units at six different time delays with respect to the beginning of dynamics, with incident pulse in resonant conditions, σ = 256 fs and including vibrational relaxation.

= 496 fs). The cumulative scattering cross-section for six different times, reported in Figure 5a, shows thinner peaks than the previous simulation and a longer time scale as expected. Moreover the peak at 156 cm^{-1} is enhanced also in this case.

The comparison of these results with those obtained with a shorter pulse in terms of the integral of the peak at 738 cm^{-1} are shown in Figure 5b. In this case, differently than in the nonresonant case, the duration of the pulse has an effect on the
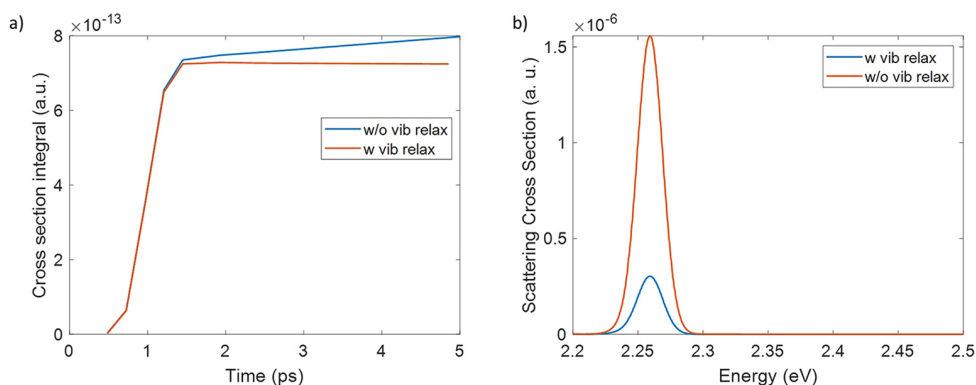
Figure 7. (a) Time-dependent cross-section integral of the peak at 738 cm^{-1}, with incident pulse in resonant conditions, $\sigma = 256$ fs, including or without including vibrational relaxation. (b) Scattering signal at 4.8 ps when the system interacts with a resonant field including or without including vibrational relaxation.

total scattered signal since the cross-section increases with the longer pulse. This is due to the sum of the two processes that are going on: on one hand the pure Raman scattering, that should remain constant with the pulse duration as in nonresonant conditions, and the fluorescence intensity that strongly depends on the amount of population created on the excited state.

In Figure 5c the convoluted scattering cross-section at 24 ps has been reported for the two simulations with different field widths. In this case the trend as a function of the field duration is opposite with respect to the one in nonresonance conditions since, as mentioned before, the longer is the resonant field the more intense is the scattered signal in the emission region in which both the Raman and fluorescence contributions are mixed. Moreover, on the basis of the results, here the fluorescence contribution prevails.

Practically, in resonant conditions, a relevant population on vibronic states that belong to the excited electronic state, is generated, and it persists even after the incident field is switched off giving a non-negligible contribution to the fluorescence emission. Due to the longer time scale of the process, the fluorescence emission at 24 ps is not exhausted as the Raman scattering which is a faster process as it does not need to create a population on the excited state to occur, but it is the result of the quantum superposition of vibronic states that belong to two different electronic states. By computing a longer dynamics for the first order coefficients, all the emission intensity can be retrieved, but that is beyond the aim of this work.

Including vibrational relaxation. Finally, in resonant conditions, a simulation has been carried out including the vibrational relaxation from upper vibronic states to the lower level of the corresponding electronic state. To this point 50 trajectories have been computed for a dynamics 4.8 ps long, considering three directions of the electric field along x, y, and z axes. After computing the time-dependent cross-section for each trajectory, the average of them has been taken. The resulted scattering cross-section, reported in Figure 6, shows a profile close to the one in absence of vibrational relaxation. However, the maximum intensity is lower. This can be better appreciated by the integral of the peak at 738 cm^{-1} (Figure 7a) which shows a flat trend after the maximum emission has been achieved while without including relaxation the emission is still increasing. Moreover the convoluted emission spectrum at 4.8 ps shows a lower intensity when the vibrational relaxation is

included, as Figure 7b shows, since the population of the vibronic state with frequency equal to 156 cm^{-1} (which gives the largest contribution to the scattering spectrum) has decayed.

4. CONCLUSION

A computational procedure to calculate Raman scattering cross-section as a function of time has been presented, based on the first order coefficients of the wave function computed after the interaction with an incident electric field that can have any possible shape. The main advantage of this approach is to give a time-dependent picture of the Raman process, not only because it is based on the time-dependent strategies developed so far, but especially for the possibility to compute the cumulative Raman signal at different times of the process. Giving a time-dependent picture of the process allows explicit inclusion of phenomena that have the same time scale of the Raman scattering, such as the interaction with an incident pulse with femtoseconds to picoseconds duration and any possible profile, and the vibrational relaxation, which is particularly relevant in resonant conditions to simultaneously simulate Raman and fluorescence emission. Moreover, in a future perspective, this method allows inclusion of the mutual interaction with a nearby plasmonic nanoparticle[54] that not only affects the intensity of the Raman signal but may change also the shape and the time scale of the process due to the local field felt by the molecule. Based on this premise, our approach will be useful also to simulate results of SERS experiments in a time-dependent fashion.

This procedure has been applied to porphyrin to calculate the time-dependent Raman cross-section in resonant and nonresonant conditions exploiting also the effect of the electric field duration and the presence of vibrational relaxation. In nonresonant conditions the Raman scattering is perfectly distinguishable from the fluorescence emission as they appear in different spectral regions, and so as well the vibrational relaxation does not affect the Raman signal since it occurs on a longer time scale. On the side of the pulse shape, the field duration does not alter the total Raman signal gathered at the end of the process, while the fluorescence region is strongly affected by it.

On the other hand, when in resonant conditions the Raman scattering is rapidly followed by the fluorescence emission which is a more intense phenomenon that occupies the same spectral region, so the distinction between the two

contributions is not trivial. Also the spectrum shape is very different than the one in nonresonant conditions due to the great enhancement of the peaks generated from the excited vibronic states around the vertical excitation energy. In these conditions, the presence of the vibrational relaxation is needed since it occurs in the time scale of the fluorescence emission, and indeed the spectrum is strongly influenced by the decay process. Our approach gives information on the interplay between Raman scattering and fluorescence emission in terms of relative weight of the two processes on the generation of the spectrum line shape even if the two contributions are not quantitatively distinguishable.

■ ASSOCIATED CONTENT

ⓈⒾ Supporting Information

The Supporting Information is available free of charge at https://pubs.acs.org/doi/10.1021/acs.jpca.2c05245.

> Convergence of Raman spectrum with 50 trajectories, comparison between porphyrin Raman spectrum computed with the present TD method and with a time-independent strategy, comparison between porphyrin Raman spectrum computed with the present TD approach and the experimental one (PDF)

■ AUTHOR INFORMATION

Corresponding Author

Stefano Corni − *Department of Chemical Sciences, University of Padova, Padova 35131, Italy; CNR Institute of Nanoscience, Modena 41125, Italy;* ⓞ orcid.org/0000-0001-6707-108X; Email: stefano.corni@unipd.it

Author

Giulia Dall'Osto − *Department of Chemical Sciences, University of Padova, Padova 35131, Italy*

Complete contact information is available at:
https://pubs.acs.org/10.1021/acs.jpca.2c05245

Notes

The authors declare no competing financial interest.

■ ACKNOWLEDGMENTS

■ REFERENCES

(1) Rostron, P.; Gaber, S.; Gaber, D. Raman spectroscopy, review. *Int. J. Tech. Res.* **2016**, *21*, 24.
(2) Graves, P.; Gardiner, D.*Practical Raman spectroscopy*; Springer, 1989; Vol. 10.
(3) Ferraro, J. R.*Introductory Raman spectroscopy*; Elsevier, 2003.
(4) Kuhar, N.; Sil, S.; Verma, T.; Umapathy, S. Challenges in application of Raman spectroscopy to biology and materials. *RSC adv* **2018**, *8*, 25888−25908.
(5) Jones, R. R.; Hooper, D. C.; Zhang, L.; Wolverson, D.; Valev, V. K. Raman techniques: fundamentals and frontiers. *Nanoscale Res. Lett.* **2019**, *14*, 1−34.

(6) Hess, C. New advances in using Raman spectroscopy for the characterization of catalysts and catalytic reactions. *Chem. Soc. Rev.* **2021**, *50*, 3519−3564.
(7) Das, R. S.; Agrawal, Y. Raman spectroscopy: Recent advancements, techniques and applications. *Vib. Spectrosc.* **2011**, *57*, 163−176.
(8) Balan, V.; Mihai, C.-T.; Cojocaru, F.-D.; Uritu, C.-M.; Dodi, G.; Botezat, D.; Gardikiotis, I. Vibrational spectroscopy fingerprinting in medicine: from molecular to clinical practice. *Materials* **2019**, *12*, 2884.
(9) Long, D. A.; Long, D.*The Raman effect: a unified treatment of the theory of Raman scattering by molecules*; Wiley Chichester, 2002; Vol. 8.
(10) Schatz, G. C.; Ratner, M. A.*Quantum mechanics in chemistry*; Courier Corporation, 2002.
(11) Tannor, D. J.*Introduction to quantum mechanics: A time-dependent perspective*; University Science Books, 2007.
(12) Lee, S.-Y.; Heller, E. J. Time-dependent theory of Raman scattering. *J. Chem. Phys.* **1979**, *71*, 4777−4788.
(13) Williams, S. O.; Imre, D. G. Raman spectroscopy: time-dependent pictures. *J. Phys. Chem.* **1988**, *92*, 3363−3374.
(14) Kramers, H.; Heisenberg, W. Über die Streuung von Strahlung durch Atome. *Z. Phys.* **1925**, *31*, 681−709.
(15) Dirac, P. A. M.; Fowler, R. H. The quantum theory of dispersion. *Proc. R. Soc. London, Ser. A* **1927**, *114*, 710−728.
(16) Tannor, D. J.; Heller, E. J. Polyatomic Raman scattering for general harmonic potentials. *J. Chem. Phys.* **1982**, *77*, 202−218.
(17) Albrecht, A. C. On the theory of Raman intensities. *J. Chem. Phys.* **1961**, *34*, 1476−1484.
(18) Herzberg, G.; Teller, E. Schwingungsstruktur der Elektronenübergänge bei mehratomigen Molekülen. *Z. Phys. Chem.* **1933**, *21*, 410−446.
(19) Small, G. J. Herzberg−Teller vibronic coupling and the Duschinsky effect. *J. Chem. Phys.* **1971**, *54*, 3300−3306.
(20) Kupka, H.; Cribb, P. Multidimensional Franck−Condon integrals and Duschinsky mixing effects. *J. Chem. Phys.* **1986**, *85*, 1303−1315.
(21) Santoro, F.; Cappelli, C.; Barone, V. Effective Time-Independent Calculations of Vibrational Resonance Raman Spectra of Isolated and Solvated Molecules Including Duschinsky and Herzberg−Teller Effects. *J. Chem. Theory Comput.* **2011**, *7*, 1824−1839.
(22) Egidi, F.; Bloino, J.; Cappelli, C.; Barone, V. A robust and effective time-independent route to the calculation of resonance raman spectra of large molecules in condensed phases with the inclusion of Duschinsky, Herzberg−Teller, anharmonic, and environmental effects. *J. Chem. Theory Comput.* **2014**, *10*, 346−363.
(23) Neugebauer, J.; Reiher, M.; Kind, C.; Hess, B. A. Quantum chemical calculation of vibrational spectra of large molecules—Raman and IR spectra for buckminsterfullerene. *J. Comput. Chem.* **2002**, *23*, 895−910.
(24) Kane, K. A.; Jensen, L. Calculation of absolute resonance Raman intensities: Vibronic theory vs short-time approximation. *J. Phys. Chem. C* **2010**, *114*, 5540−5546.
(25) Heller, E. J.; Sundberg, R.; Tannor, D. Simple aspects of Raman scattering. *J. Phys. Chem.* **1982**, *86*, 1822−1833.
(26) Jensen, L.; Zhao, L.; Autschbach, J.; Schatz, G. Theory and method for calculating resonance Raman scattering from resonance polarizability derivatives. *J. Chem. Phys.* **2005**, *123*, 174110.
(27) Jensen, L.; Schatz, G. C. Resonance Raman scattering of rhodamine 6G as calculated using time-dependent density functional theory. *J. Phys. Chem. A* **2006**, *110*, 5973−5977.
(28) Guthmuller, J.; Champagne, B. Time dependent density functional theory investigation of the resonance Raman properties of the julolidinemalononitrile push-pull chromophore in various solvents. *J. Chem. Phys.* **2007**, *127*, 164507.
(29) Guthmuller, J.; Champagne, B. Resonance Raman scattering of rhodamine 6G as calculated by time-dependent density functional theory: vibronic and solvent effects. *J. Phys. Chem. A* **2008**, *112*, 3215−3223.

(30) Ma, H.; Liu, J.; Liang, W. Time-dependent approach to resonance Raman spectra including Duschinsky rotation and Herzberg−Teller effects: Formalism and its realistic applications. *J. Chem. Theory Comput.* **2012**, *8*, 4474−4482.

(31) Thomas, M.; Latorre, F.; Marquetand, P. Resonance Raman spectra of ortho-nitrophenol calculated by real-time time-dependent density functional theory. *J. Chem. Phys.* **2013**, *138*, 044101.

(32) Mattiat, J.; Luber, S. Efficient calculation of (resonance) Raman spectra and excitation profiles with real-time propagation. *J. Chem. Phys.* **2018**, *149*, 174108.

(33) Guthmuller, J. Comparison of simplified sum-over-state expressions to calculate resonance Raman intensities including Franck-Condon and Herzberg-Teller effects. *J. Chem. Phys.* **2016**, *144*, 064106.

(34) Guthmuller, J. Calculation of Vibrational Resonance Raman Spectra of Molecules Using Quantum Chemistry Methods. *Molecular Spectroscopy: A Quantum Chemistry Approach* **2019**, *2*, 497−536.

(35) Guthmuller, J. Sum-over-state expressions including second-order Herzberg−Teller effects for the calculation of absorption and resonance Raman intensities. *J. Chem. Phys.* **2021**, *155*, 084107.

(36) Baiardi, A.; Bloino, J.; Barone, V. A general time-dependent route to Resonance-Raman spectroscopy including Franck-Condon, Herzberg-Teller and Duschinsky effects. *J. Chem. Phys.* **2014**, *141*, 114108.

(37) Baiardi, A.; Bloino, J.; Barone, V. Time-dependent formulation of resonance Raman optical activity spectroscopy. *J. Chem. Theory Comput.* **2018**, *14*, 6370−6390.

(38) Barone, V.; Biczysko, M.; Bloino, J. Fully anharmonic IR and Raman spectra of medium-size molecular systems: accuracy and interpretation. *Phys. Chem. Chem. Phys.* **2014**, *16*, 1759−1787.

(39) Bloino, J.; Biczysko, M.; Barone, V. Anharmonic effects on vibrational spectra intensities: infrared, Raman, vibrational circular dichroism, and Raman optical activity. *J. Phys. Chem. A* **2015**, *119*, 11862−11874.

(40) Baiardi, A.; Bloino, J.; Barone, V. Accurate simulation of resonance-Raman spectra of flexible molecules: An internal coordinates approach. *J. Chem. Theory Comput.* **2015**, *11*, 3267−3280.

(41) Holtum, T.; Bloino, J.; Pappas, C.; Kumar, V.; Barone, V.; Schlücker, S. Ultraviolet resonance Raman spectroscopy of anthracene: Experiment and theory. *J. Raman Spectrosc.* **2021**, *52*, 2292−2300.

(42) Avila Ferrer, F. J.; Barone, V.; Cappelli, C.; Santoro, F. Duschinsky, Herzberg-Teller, and Multiple Electronic Resonance Interferential Effects in Resonance Raman Spectra and Excitation Profiles. The Case of Pyrene. *J. Chem. Theory Comput.* **2013**, *9*, 3597−3611.

(43) Coccia, E.; Troiani, F.; Corni, S. Probing quantum coherence in ultrafast molecular processes: An ab initio approach to open quantum systems. *J. Chem. Phys.* **2018**, *148*, 204112.

(44) Coccia, E.; Corni, S. Role of coherence in the plasmonic control of molecular absorption. *J. Chem. Phys.* **2019**, *151*, 044703.

(45) Dall'Osto, G.; Coccia, E.; Guido, C. A.; Corni, S. Investigating ultrafast two-pulse experiments on single DNQDI fluorophores: a stochastic quantum approach. *Phys. Chem. Chem. Phys.* **2020**, *22*, 16734−16746.

(46) Domcke, W.; Stock, G. Theory of ultrafast nonadiabatic excited-state processes and their spectroscopic detection in real time. *Adv. Chem. Phys.* **1997**, *100*, 15.

(47) Santoro, F.; Petrongolo, C.; Lami, A. Time- and frequency-resolved spontaneous emission: Theory and application to the $NO_2 X2A'/A2A'$ conical intersection. *J. Chem. Phys.* **2000**, *113*, 4073−4082.

(48) Gelin, M. F.; Pisliakov, A. V.; Domcke, W. Time- and frequency-gated spontaneous emission as a tool for studying vibrational dynamics in the excited state. *Phys. Rev. A* **2002**, *65*, 062507.

(49) Sun, Z.; Lu, J.; Zhang, D. H.; Lee, S. Y. Quantum theory of (femtosecond) time-resolved stimulated Raman scattering. *J. Chem. Phys.* **2008**, *128*, 144114.

(50) Gelin, M. F.; Domcke, W.; Rao, B. J. Femtosecond stimulated Raman spectroscopy as a tool to detect molecular vibrations in ground and excited electronic states. *J. Chem. Phys.* **2016**, *144*, 184307.

(51) Langer, J.; Jimenez de Aberasturi, D.; Aizpurua, J.; Alvarez-Puebla, R. A.; Auguié, B.; Baumberg, J. J.; Bazan, G. C.; Bell, S. E. J.; Boisen, A.; Brolo, A. G.; et al. Present and Future of Surface-Enhanced Raman Scattering. *ACS Nano* **2020**, *14*, 28−117.

(52) Le, F.; Brandl, D.; Urzhumov, Y.; Wang, H.; Kundu, J.; Halas, N.; Aizpurua, J.; Nordlander, P. Metallic Nanoparticle Arrays: A Common Substrate for Both Surface-Enhanced Raman Scattering and Surface-Enhanced Infrared Absorption. *ACS Nano* **2008**, *2*, 707−718.

(53) Ding, S.-Y.; Yi, J.; Li, J.-F.; Ren, B.; Wu, D.-Y.; Panneerselvam, R.; Tian, Z.-Q. Nanostructure-based plasmon-enhanced Raman spectroscopy for surface analysis of materials. *Nat. Rev. Mater.* **2016**, *1*, 1−16.

(54) Corni, S.; Tomasi, J. Surface enhanced Raman scattering from a single molecule adsorbed on a metal particle aggregate: A theoretical study. *J. Chem. Phys.* **2002**, *116*, 1156−1164.

(55) Pipolo, S.; Corni, S. Real-Time Description of the Electronic Dynamics for a Molecule Close to a Plasmonic Nanoparticle. *J. Phys. Chem. C* **2016**, *120*, 28774−28781.

(56) Dall'Osto, G.; Gil, G.; Pipolo, S.; Corni, S. Real-time dynamics of plasmonic resonances in nanoparticles described by a boundary element method with generic dielectric function. *J. Chem. Phys.* **2020**, *153*, 184114.

(57) Baer, M. *Beyond Born-Oppenheimer: electronic nonadiabatic coupling terms and conical intersections*; John Wiley & Sons, 2006.

(58) Worth, G. A.; Cederbaum, L. S. Beyond Born-Oppenheimer: molecular dynamics through a conical intersection. *Annu. Rev. Phys. Chem.* **2004**, *55*, 127−58.

(59) Yonehara, T.; Hanasaki, K.; Takatsuka, K. Fundamental approaches to nonadiabaticity: Toward a chemical theory beyond the Born−Oppenheimer paradigm. *Chem. Rev.* **2012**, *112*, 499−542.

(60) Barone, V. Accurate vibrational spectra of large molecules by density functional computations beyond the harmonic approximation: the case of azabenzenes. *J. Phys. Chem. A* **2004**, *108*, 4146−4150.

(61) Carbonniere, P.; Lucca, T.; Pouchan, C.; Rega, N.; Barone, V. Vibrational computations beyond the harmonic approximation: Performances of the B3LYP density functional for semirigid molecules. *J. Comput. Chem.* **2005**, *26*, 384−388.

(62) Santoro, F.; Lami, A.; Improta, R.; Barone, V. Effective method to compute vibrationally resolved optical spectra of large molecules at finite temperature in the gas phase and in solution. *J. Chem. Phys.* **2007**, *126*, 184102.

(63) Pipolo, S.; Corni, S.; Cammi, R. Equation of motion for the solvent polarization apparent charges in the polarizable continuum model: Application to time-dependent CI. *J. Chem. Phys.* **2017**, *146*, 064116.

(64) Van Kampen, N. G. *Stochastic Processes in Physics and Chemistry*; North Holland, 2007.

(65) Tremblay, J. C.; Klamroth, T.; Saalfrank, P. Time dependent configuration interaction calculations of laser driven dynamics in presence of dissipation. *J. Chem. Phys.* **2008**, *129*, 84302.

(66) Biele, R.; D'Agosta, R. A stochastic approach to open quantum systems. *J. Condens. Matter Phys.* **2012**, *24*, 273201.

(67) Frisch, M. J.; Trucks, G. W.; Schlegel, H. B.; Scuseria, G. E.; Robb, M. A.; Cheeseman, J. R.; Scalmani, G.; Barone, V.; Petersson, G. A.; Nakatsuji, H.; et al., *Gaussian 16*, rev B.01; Gaussian Inc: Wallingford CT, 2016.

(68) Santoro, F.; Cerezo, J. FCclasses3, a code for vibronic calculations. http://www.iccom.cnr.it/en/fcclasses, 2022 (accessed 27-July-2022).

(69) Coccia, E.; Dall'Osto, G.; Fregoni, J.; Gil, G.; Marsili, M.; Pipolo, S.; Romanelli, M.; Rosa, M.; Corni, S. WaveT-TDPlas. https://github.com/stefano-corni/WaveT_TDPlas, 2021 (accessed 10-January-2022).

(70) Marcelli, A.; Foggi, P.; Moroni, L.; Gellini, C.; Salvi, P. R. Excited-state absorption and ultrafast relaxation dynamics of

porphyrin, diprotonated porphyrin, and tetraoxaporphyrin dication. *J. Phys. Chem. A* **2008**, *112*, 1864−1872.

(71) Taniguchi, M.; Mass, O.; Boyle, P. D.; Tang, Q.; Diers, J. R.; Bocian, D. F.; Holten, D.; Lindsey, J. S. Structural studies of sparsely substituted synthetic chlorins and phorbines establish benchmarks for changes in the ligand core and framework of chlorophyll macrocycles. *J. Mol. Struct.* **2010**, *979*, 27−45.

(72) Halls, M. D.; Velkovski, J.; Schlegel, H. B. Harmonic frequency scaling factors for Hartree-Fock, S-VWN, B-LYP, B3-LYP, B3-PW91 and MP2 with the Sadlej pVTZ electric property basis set. *Theor. Chem. Acc.* **2001**, *105*, 413−421.

(73) Irikura, K. K.; Johnson, R. D.; Kacker, R. N. Uncertainties in scaling factors for ab initio vibrational frequencies. *J. Phys. Chem. A* **2005**, *109*, 8430−8437.

Supporting Information for Time Resolved Raman Scattering of Molecules: a Quantum Mechanics Approach with Stochastic Schroedinger Equation

Giulia Dall'Osto[†] and Stefano Corni*[,†,‡]

†*Department of Chemical Sciences, University of Padova, via Marzolo 1, Padova, Italy, 35100*

‡*CNR Institute of Nanoscience, via Campi 213/A, Modena, Italy, 41100*

E-mail: stefano.corni@unipd.it
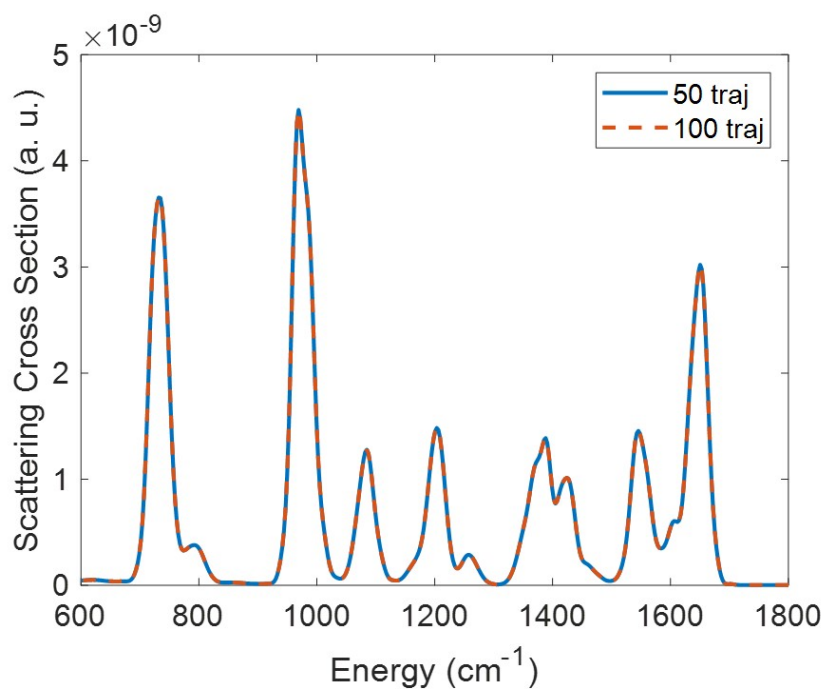
Figure S1: Comparison between Porphyrin Raman spectrum computed through our TD approach at 2.4 ps using 50 trajectories (blu, straight line) and using 100 trajectories (orange, dashed line). The calculations have been carried out in resonance conditions,with the incident field matching the vertical transition and including vibrational relaxation through SSE.

S2
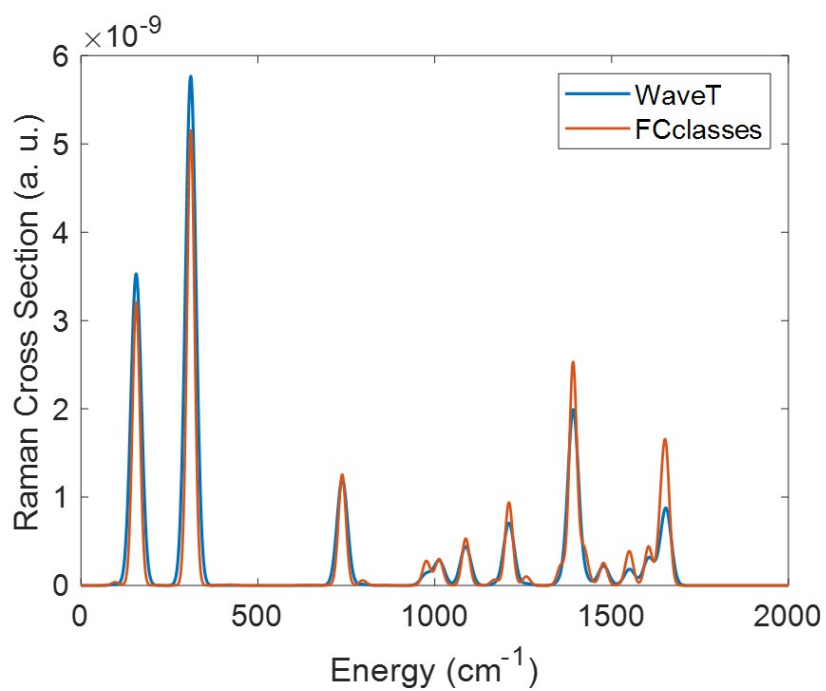
Figure S2: Comparison between Porphyrin Raman spectrum computed through our TD approach (at 24 ps) and with a time independent strategy (through FCclasses code).[1,2] Both spectra are reported with the incident radiation in non-resonance conditions, with energy 0.24 eV lower than the vertical transition.
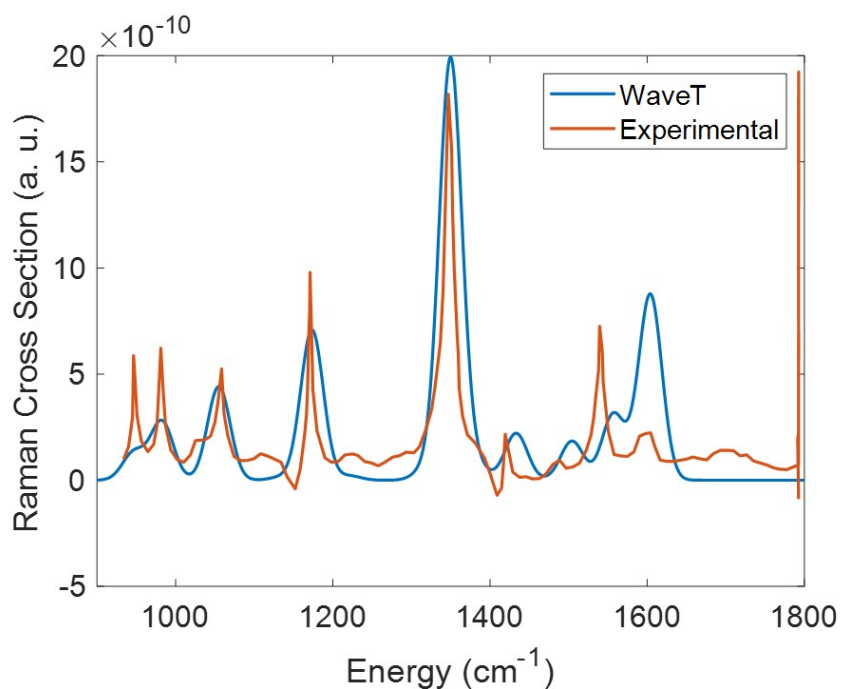
Figure S3: Comparison between Porphyrin Raman spectrum computed through our TD approach (at 24 ps) and the experimental Resonance Raman spectrum obtained in CH_2Cl_2 solution.[3] The theoretical spectrum has been re-scaled by a factor 0.97[4] (scaling factor for B3LYP exchange-correlation functional) to correct the vibrational frequencies computed at DFT level. The theoretical calculation has been performed in non-resonance conditions with the incident radiation energy 0.24 eV lower than the vertical transition.

References

(1) Santoro, F.; Cerezo, J. FCclasses3, a code for vibronic calculations. `http://www.iccom.cnr.it/en/fcclasses`, 2022; [Online; accessed 27-July-2022].

(2) Santoro, F.; Cappelli, C.; Barone, V. Effective Time-Independent Calculations of Vibrational Resonance Raman Spectra of Isolated and Solvated Molecules Including Duschinsky and Herzberg–Teller Effects. *J. Chem. Theory Comput.* **2011**, *7*, 1824–1839.

(3) Taniguchi, M.; Mass, O.; Boyle, P. D.; Tang, Q.; Diers, J. R.; Bocian, D. F.; Holten, D.; Lindsey, J. S. Structural studies of sparsely substituted synthetic chlorins and phorbines establish benchmarks for changes in the ligand core and framework of chlorophyll macrocycles. *J. Mol. Struct.* **2010**, *979*, 27–45.

(4) Irikura, K. K.; Johnson, R. D.; Kacker, R. N. Uncertainties in scaling factors for ab initio vibrational frequencies. *J. Phys. Chem. A* **2005**, *109*, 8430–8437.

Chapter 6

This chapter concludes the path travelled during my Ph.D. activity, including time-dependent Raman scattering simulations on single molecules close to plasmonic nanoparticles. Plasmon- or surface-enhanced Raman scattering (SERS)[17] is a very hot topic born about 50 years ago[80, 81, 82] that has interested many researchers because of the advantages brought in terms of response intensity with respect to experiments in solution.[83, 84] The presence of plasmonic nanoparticles greatly enhances the molecular response, and combined with the richness of information provided by Raman signals, it represents a very powerful tool for molecular detection.[85, 86]

The mechanisms involved in this process are not easy to explain, and theoretical calculations have given a strong help to this aim[87, 88] unraveling the processes that contribute most. In most cases, Raman signal enhancement is related to electromagnetic enhancement generated between a molecule and a nanostructure induced by the plasmon oscillations on the NP surface.[89, 90] However, the chemical mechanism based on charge transfer between the molecule and NP also appears to be relevant in some cases.[91, 92] Some methods to simulate SERS experiments are based on DDA[25], where the NP is treated as a continuum of small polarizable particles, or on FDTD methods[30], which are based on the solution of the full Maxwell equations.

The goal of this chapter is to provide for a different strategy based on the approach developed in chapter 5 for calculating Raman scattering of molecules. The theory explained there has been extended to include the effect of the nanoparticle

on the interaction between the molecule and the incident laser pulse, as well as the enhancement of the scattered field. The former is implicitly taken into account by evolving the electronic wave function in presence of an incident pulse coupled to the NP using the TD-BEM explained in chapter 1. On the other hand, the effect of the NP on the scattered field is calculated a posteriori, as explained in this chapter.

The chapter is reported as a draft paper in preparation, and it consists of an introduction summarizing the main available information on SERS and the reasons that motivated this work, a theoretical section describing the developed methodology to calculate the time-dependent Raman scattering of molecules in the presence of a nearby NP. The strategy was applied to a porphyrin molecule placed close to a gold nanoellipsoid as a test case. All computational features are reported in the Computational Details section, and the results are discussed in the following section.

The manuscript was drafted by me and I took care of including the suggestions received by Prof. Corni.

Time-dependent Surface enhanced Raman scattering: a theoretical approach

Giulia Dall'Osto[†] and Stefano Corni[*,†,‡]

†*Department of Chemical Sciences, University of Padova, via Marzolo 1, Padova, Italy, 35100*

‡*CNR Institute of Nanoscience, via Campi 213/A, Modena, Italy, 41100*

E-mail: stefano.corni@unipd.it

Abstract

A new procedure to compute the time-dependent Raman scattering of molecules close to plasmonic nanoparticles (NP) has been proposed, based on the pioneering Lee and Heller's theory. This strategy is based on the preliminary calculation of the molecular dynamics in presence of a NP and an incident electric field coupled with a posteriori evaluation of the Raman signal through inverse Fourier Transform of the coefficients dynamics applying a fictitious scattered electric field. The system is treated through a multiscale approach coupling the quantum mechanical description of the molecule with the polarizable continuum model (PCM) for the NP. This method allows to know the time evolution of the plasmon-enhanced Raman signal, following the incident electric field dynamics and not only the total Raman signal accumulated at the end of the process. Therefore, also any possible shape for the incident electric field can be employed to be closer to experimental setups.

177

1   Introduction

Raman scattering is a powerful technique that has been known for nearly a century and can provide insights into the vibrational structure of molecules.[1–5] With the advent of modern technologies, instrumentation has improved, allowing higher resolution to be achieved[6,7] making Raman spectroscopy useful for various applications such as single molecule detection and imaging.[8,9] Among all the innovations, the capability achieved by manipulating plasmonic nanoparticles (NP) has allowed to use their properties to enhance molecular response,[10,11] enriching the amount of information that can be achieved by Raman spectroscopy.[12,13] The advantages brought by the presence of nanoparticles are of such importance that surface-enhanced Raman scattering (SERS) has itself become a new field of research, even though it is a fairly new technique.[14,15] By confining light to very small regions such as picocavities, sub-molecular resolution could be achieved, allowing even single normal modes to be visualized.[16–18]

Vibrational Raman scattering is a two-photon process that results from the interaction with a material system of an incident radiation and the subsequent inelastic scattering of a photon whose energy differs by a multiple of a quantum of vibration from that of the incident photon. A scattering energy lower than that of the incident photon leads to a Stokes process, otherwise it is called anti-Stokes. Raman scattering in solution usually gets very low intensity signals, particularly in non-resonant conditions, due to the low probability of a Raman process to take place, which makes this technique not efficient enough for many applications. On the other hand, when the molecule is placed in a nanogap generated by the presence of two nanoparticles in its proximity, the signal amplification can reach factors of 10^5 or 10^6.[19,20]

Theoretical modeling of SERS have given a great impact in understanding the mechanism involved in the process, so a great effort has been made in developing new efficient strategies able to unravel the most crucial aspects of the phenomena.[21–23] Numerical methods commonly employed to study plasmonic nanoparticles, such as discrete dipole approximation[24]

or finite difference time-domain methods,[25] have provided a variety of information on the electromagnetic field enhancement in proximity of a NP surface. Scientific community agrees with correlating the nature of the molecular response enhancement to two different mechanisms, usually named as electromagnetic and chemical interactions.[26,27] The electromagnetic interaction generated when the incident radiation is resonant with the plasmon excitations in the metal nanoparticle is usually very intense. On the other hand, the chemical enhancement mechanism usually includes interactions between the molecule and the nanoparticle when they are in their ground state and when either the nanoparticle or the molecule is excited by a resonant incident pulse.[22] It is generally assumed that the electromagnetic contribution alone provides for the enhancement of SERS signal with the fourth power of the electric field enhancement.[28,29]

Accounting for the enhancement due to chemical interactions between the molecule and the NP would require a quantum description of both of them which is feasible only for small NPs with usual computational resources.[30–34] In order to provide a method able to tackle different NPs size one has to move toward calculations of electromagnetic enhancement and neglect the molecule-NP chemical interaction, which is usually an acceptable approximation. The enhancement can be computed by solving the classical electrodynamics problem, which derives from Maxwell's equations when the NP description is kept at classical level of theory.[35,36]

On the other hand, treating the molecule classically as a point dipole causes a great loss of information, which would lead to an oversimplification of the Raman response. An effective way to treat the model is provided by multiscale approaches where the classical description of the NP is coupled with a quantum description of the molecule.[37–39] This choice prevents to increase excessively the complexity of the problem but at the same time allows including all the necessary information related to the electronic structure of the molecule.[40,41]

Our aim is to compute the plasmon enhanced Raman scattering of single molecules due to the electromagnetic interaction with a nearby NP, by using a time-dependent approach.

The system is treated with a multiscale model that combines a classical treatment of the NP through the polarizable continuum model -NanoParticle (PCM-NP)[42–44] with a quantum mechanical description of the molecule at DFT (density functional theory) level. The PCM problem is solved by boundary elements method (BEM)[45,46] which consists of discretizing the NP surface in small tesserae, each of one is characterized by a polarization charge which represents the NP response to the interaction with external electromagnetic sources (as the incident radiation and the molecular electronic potential).[38,47,48]

The present approach is an evolution of the method we developed to compute the time-dependent Raman scattering of molecules,[49] which has been extended to include the effect of the enhancement induced by a nearby NP. Our approach allows including the mutual interaction between molecule and NP in terms of the potential generated on the NP surface that influences the molecular response which in turn polarizes the NP, during the dynamics.

From the real-time dynamics of the coupled molecule-NP system, the time-dependent Raman scattering can be computed. Starting from the Lee and Heller[50] theory for time-dependent Raman scattering, we extended the procedure to include the enhancement induced by the NP on the Raman response of the molecule. This strategy is not only based on a time-dependent procedure but allows tracking the dynamics of the Raman scattering itself, giving as result the time-resolved plasmon-enhanced Raman scattering of a single molecule. Another advantage of this procedure is the opportunity of employing any possible shape of the incident electric field, which makes the simulation closer to real experimental set-up.

The paper is organized as follows: in the next section the theoretical strategy employed to simulate time-dependent Raman scattering of molecules is reported starting from the theory developed for single-molecule calculations integrated by the new features needed to include the presence of a NP, then in section 3 the computational details of the calculations performed are reported, all the results and the discussion are included in section 4 and final remarks are reported in section 5.

2 Theory

In this section, we briefly resume the theory developed for calculation of single-molecule Raman spectra in time domain,[49] explaining in details the changes needed to include the presence of the NP on the Raman signal. The Raman signal is represented by the second order wave function with respect to the number of electric fields involved in the dynamics as

$$|\Psi^{(2)}(t,\omega_S)\rangle = -\frac{1}{2}\int_{-\infty}^{t}dt'\int_{-\infty}^{t'}dt''e^{-i\hat{H}(t-t')}\hat{\vec{\mu}}\cdot\vec{\epsilon_S}e^{i\omega_S t'}e^{-i\hat{H}(t'-t'')}\hat{\vec{\mu}}\cdot\vec{\epsilon_I}(t'')e^{-iE_0 t''}|\Psi_0(-\infty)\rangle.$$

(1)

The initial wave function of the molecule interacts with an incident electric field $(\vec{\epsilon_I}(t''))$ and then evolves on the vibronic Hamiltonian $\hat{H}$ until the interaction with the scattered field $\vec{\epsilon_S}e^{i\omega_S t'}$ which is monochromatic and centred at frequency ω_S. Afterward, the system wave function evolves on the vibronic Hamiltonian until time t. This equation is derived from the Lee and Heller[50] treatment of the molecular wave function at the second order with respect to the mixed perturbation induced by the incident and scattered electric field. As in the original theory, the scattered field is monochromatic, and its features are chosen to reproduce quantum electrodynamics results even if it is treated classically. The main differences from the original theory are related to the propagation that is made on the vibronic Hamiltonian instead of on the electronic Hamiltonian of the proper potential energy surface and to the neglection of anti-resonant term in our treatment (the term which comes out when the wave function interacts with the scattered field before than with the incident one). The Hamiltonian is written on the basis of the vibronic states in the Born-Oppenheimer (BO) approximation, which is valid as long as the geometry of the ground state is sufficiently far from avoided crossings in the excited states.[51–53]

The first order coefficients obtained by the interaction of the initial wave function with the incident electric field are expanded on the basis of vibronic states $|J\rangle$ as $|\Psi^{(1)}(t')\rangle = \sum_J C_J^{(1)}(t')|J\rangle$ and the second order coefficients are expanded as $|\Psi^{(2)}(t,\omega_S)\rangle = \sum_J C_J^{(2)}(t,\omega_S)|J\rangle$. Thus, an equation for the time-dependent second order coefficients is obtained directly from

equation 1 as a function of the first order coefficients $C_J^{(1)}(t')$

$$C_N^{(2)}(t, \omega_S) = \frac{i\epsilon_S e^{-i\omega_N t}}{2} \int_{-\infty}^{t} dt' e^{i\omega_S t'} e^{i\omega_N t'} \sum_J C_J^{(1)}(t') \langle N|\hat{\mu}_S|J \rangle \tag{2}$$

where N indexes the vibrational level with frequency ω_N and $\langle N|\hat{\mu}_S|J \rangle$ is the projection of the transition dipole moment between two vibronic states along the direction of the scattered field.

Equation 2 should be revised in order to include the interaction between the molecule and the NP, bringing up three main variations: i) the electronic energies and transition dipole moments are computed when the molecular ground state is equilibrated with the charge distribution on the NP surface, ii) the propagation of the first order coefficients is performed including the interaction between molecule and NP, iii) the effect of the NP on the scattering process is included by adding the transition dipole moment induced on the NP by the presence of the molecule transition electron density, to the transition dipole moment of the molecule.

Focusing on the propagation, the first order coefficients are computed as the real-time dynamics of the vibronic wave function under the effect of the Hamiltonian

$$\hat{H}(t) = \hat{H}_0 - \hat{\vec{\mu}} \cdot \vec{E}_{inc}(t) + (\mathbf{q}_{ref}(t) + \mathbf{q}_{pol}(t)) \cdot \hat{V} \tag{3}$$

that includes the time-independent Hamiltonian, the interaction with the incident electric field and the interaction between the reflected ($\mathbf{q}_{ref}(t)$) and polarization ($\mathbf{q}_{pol}(t)$) charges with the molecular potential generated on the NP surface. The reflected charges are due to the response of the NP to the presence of an incident field while the polarization charges are due to the NP response to the oscillating electron density of the molecule. Both reflected and polarization charges are located in the central points of the tesserae on the NP surface. Computing the first order coefficients under the Hamiltonian in eq. 3 allows including the presence of the NP during the interaction with the incident electric field.

The interaction between the NP and the scattered radiation that brings all the Raman frequencies is included directly in equation 2. Indeed, as mentioned, the scattered field has not been included explicitly in the dynamics, but it is added a posteriori as a monochromatic field. Therefore, also the interaction between the NP and the scattered radiation cannot be added through the dynamics but needs to be included a posteriori. The enhancement generated by the NP on a molecular emission process is added in terms of the dipole moment generated on the NP surface due to the potential induced by the molecular electron density.[54] According to this assumption, the transition dipole moment operator along the direction of the scattered field $\vec{\mu}_S$ is the sum of the molecular and the NP transition dipole moments evaluated at frequency ω_S:

$$\hat{\mu}_S = \hat{\mu}_{S,mol} + \hat{\mu}_{S,NP}. \tag{4}$$

The molecular transition dipole moment is computed expanding in Taylor series the electronic transition dipole moments in order to include both the Franck-Condon and the Herzberg-Teller contribution, respectively the first and the second terms in the r.h.s of

$$\vec{\mu}_{S,mol}^{NJ} = \langle \chi_N^g | \chi_J^e \rangle (\vec{\mu}_{ge})_0 + \sum_k \langle \chi_N^g | Q_k | \chi_J^e \rangle \left(\frac{\partial \vec{\mu}_{ge}}{\partial Q_k} \right)_0 \tag{5}$$

where $|\chi_N^g\rangle$ and $|\chi_J^e\rangle$ represent respectively the N vibrational level of the ground state and the J vibrational level of the excited state. The HT term runs over the Q_k normal mode coordinates, and the derivative of the electronic transition dipole moment with respect to the normal mode coordinates is evaluated at the equilibrium geometry. Differently than in the calculations for isolated molecules, here the transition dipole moment derivative is obtained numerically by computing the electronic transition dipole moment in presence of the NP at different molecular geometries obtained by translating the molecule along the normal modes.

On the other hand, the transition dipole moment of the NP is computed from the frequency dependent charges generated on the NP surface when interacting with the molecular

potential generated by a particular molecular vibronic transition using the PCM equation:

$$\mathbf{q}_{NJ}(\omega) = -\mathbf{S}^{-1} \left(2\pi \frac{\epsilon(\omega) + 1}{\epsilon(\omega) - 1} \mathbf{I} + \mathbf{DA} \right)^{-1} (2\pi \mathbf{I} + \mathbf{DA}) \mathbf{V}_{NJ} \tag{6}$$

where $\mathbf{A}$ is a diagonal matrix whose elements are the tesserae areas, the matrices $\mathbf{S}$ and $\mathbf{D}$ are representative of Calderons' projectors, $\epsilon(\omega)$ is the metal dielectric function and $\mathbf{V}_{NJ}$ is the potential generated on the NP surface tesserae by the molecular vibronic transition density associated to the $N \leftarrow J$ transition. The vibronic transition potential on the NP surface is computed as a Taylor expansion of the electronic transition potential on the vibrational normal modes coordinate of the molecule in the excited state considered. Truncating the expansion at the first order we get

$$V_{NJ} = \langle \chi_N^g | \chi_J^e \rangle (V_{ge})_0 + \sum_k \langle \chi_N^g | Q_k | \chi_J^e \rangle \left(\frac{\partial V_{ge}}{\partial Q_k} \right)_0 \tag{7}$$

which includes the electronic potential at equilibrium position weighted by the Franck-Condon integral (first term in the r. h. s.) and the Herzberg-Teller term that is a function of the electronic transition potential derivative with respect to the normal mode coordinates evaluated at the equilibrium position.

With the charges computed at the scattered frequency ω_S as in eq. 6 the metal transition dipole moment is obtained as

$$\vec{\mu}_{S,NP}^{NJ} = \sum_i \mathbf{q}_{NJ}(\omega_S) \cdot \vec{r}_i \tag{8}$$

with $\vec{r}_i$ being the position vector of the tesserae on the NP surface. The electronic potential derivative is computed numerically, via differentiation of the electronic potential when the geometry of the molecule is distorted along a specific normal mode.

As shown for calculation of time-dependent Raman scattering of a single molecule in vacuum, the Raman cross section is directly achievable from the square modulus of the

second order coefficients of the vibronic wave function evolution as

$$\sigma_{setup}(t, \omega_S) = \frac{8\omega_S^4}{\epsilon_S^2 \pi^{3/2} c^4 \sigma |\vec{\epsilon}_{I,0}|^2} \sum_N \langle |C_N^{(2)}(t, \omega_S)|^2 \rangle_{setup}. \tag{9}$$

where c is the light speed, $|\vec{\epsilon}_{I,0}|^2$ is the square modulus of the incident electric field amplitude and σ is the electric field width considering a field shaped as $\vec{\epsilon}_I(t) = \vec{\epsilon}_{I,0} sin(\omega_I t)e^{-\frac{(t-t_0)^2}{2\sigma^2}}$. The label *setup* keeps a general definition of the Raman cross section in terms of polarization of the incident and scattered electric fields, which can be chosen ad-hoc to simulate specific experimental setups. Moreover, using a finite limit to the integral of the first order coefficients when solving equation 2, the second order coefficients and thus the Raman scattering cross section keep a time dependence related to the finite integration boundary.

3 Computational details

The model explained above has been applied to compute the Raman spectrum of porphyrin in presence of a NP. The NP is modeled as a gold nanoellipsoid using gmsh code with semi-axes equal to $5nm$ and $3nm$, the larger dimension is aligned along the x-axis. The surface has been discretized with 760 tesserae, refining the region closer to the molecule position. The dielectric function of the NP is obtained by fitting Johnson and Christy data.[55] The absorption energy of the NP is reported in panel (a) of figure 1 and the NP tessellation is showed in panel (b). The molecular geometry has been optimized through DFT methods at B3LYP/6-31G** level of theory using Gaussian16,[56] when the molecule is either in the ground or in the first excited state. The vibrational frequencies and normal modes have been computed with the molecule in the ground and first excited state in order to prepare the molecular wave function with 109 vibronic states (the ground vibronic state and the first vibronic level for each normal mode) in both the electronic states included in our approximation (with only ground and first excited state). The electronic energies and transition dipole moments have been computed at TDDFT level of theory with B3LYP

exchange-correlation functional and 6-31G** basis set, considering the equilibration of the molecule GS with the NP charge distribution. The molecule lies on the xy plane, with its centre 10 Å far from the NP surface, its orientation with respect to the NP position is reported in panel (b) of figure 1. We have chosen a configuration where the electronic transition dipole moment is aligned with the direction of the major dipole moment generated in the NP.

The vibrational analysis needed to compute the Franck-Condon and Herzberg-Teller integrals has been carried out with FCclasses3 assuming the adiabatic hessian model.[57,58] These integrals have been employed to compute the molecular transition dipole moments as in eq. 5 and the transition potentials on the NP surface as in eq. 7. The potential induced on the NP by the electronic transition has been computed using a locally modified version of Gamess code[59,60] as well as the potential derivatives, which have been computed numerically by differentiating the electronic potential computed at different normal modes' displacement. In the same way, the derivative of the electronic transition dipole moment has been computed numerically through a series of Gamess calculation by differentiating the electronic transition dipole moment computed in presence of the NP shifting the molecular geometry along the normal modes coordinates.
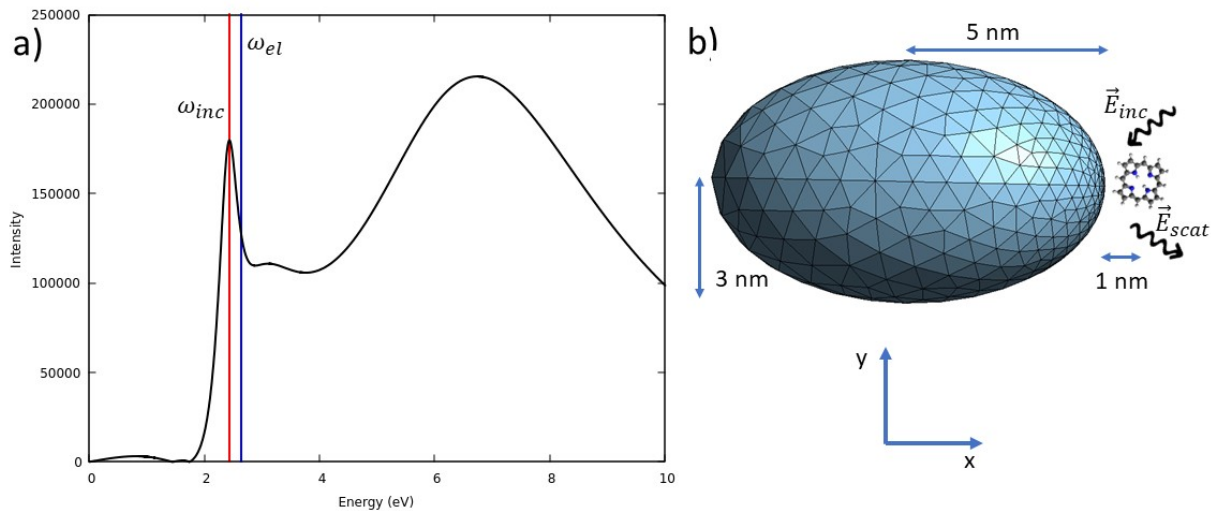

Figure 1: a) Gold nanoellipsoid absorption spectrum, the red line represents the frequency of the incident pulse that matches the plasmonic frequency and the blue line is placed at the molecular electronic energy. b) Scheme of the NP-molecule setup.

The dynamics performed to compute the first order coefficients is $2.4ps$ long and the time step considered is $0.024fs$. In all the simulations, the external field has a Gaussian enveloped sinusoidal shape with $\sigma = 256fs$, $\epsilon_{I,0} = 5.14 \cdot 10^5 V/m$, centred at $t_0 = 968fs$, oscillating with the plasmonic frequency $\omega_{plas} = 2.44eV$. The excitation energy of the molecule has been shifted by 0.39 eV (moving from 2.25 eV to 2.64 eV) to match pre-resonant conditions with respect to the incident pulse frequency employed in the calculations. The excitation energy (ω_{inc}) and the electronic transition energy (ω_{el}) employed in the calculations are highlighted respectively by a red and blue line in panel (a) of figure 1. The propagation of the charges on the NP surface has been performed as explained in ref. 61 through the equation of motion obtained by Fourier Transform of the PCM equation when an experimental dielectric function is used to describe the metal.

The Raman cross section has been computed assuming different orientations of the incident and scattered electric fields. The averaged Raman cross section has been also computed assuming the incident radiation with linear polarization perpendicular to the detected scattered radiation and any polarization for the scattered radiation. Calculations have been performed both in the FC regime (neglecting the HT contribution in eqs. 5 and 7) and in FC-HT regime (using the full equations 5 and 7).

4   Results and discussion

The time dependent averaged Raman cross section of porphyrin in presence of a gold nanoellipsoid is reported in figure 2, when the calculation is performed in the FC regime (panel a) or in the FC-HT regime (panel b). Within the timescale of the incident field, all the Raman intensity is accumulated during the dynamics and the Raman spectra at 2177 fs is superimposed to those at the end of the dynamics (2.4 ps, not reported here) in both regimes. The profile of the final spectra in the two calculations are quite similar, but for the different relative intensity between the regions upper and lower $900cm^{-1}$. The peaks at lower frequencies
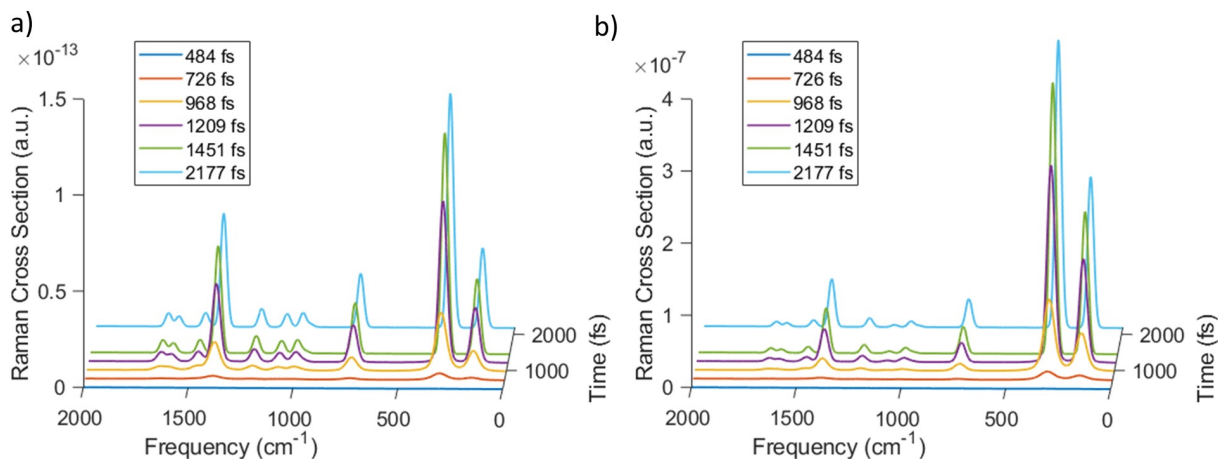
Figure 2: Time dependent Surface enhanced Raman cross section computed averaging over molecular orientation to mimic a setup with incident radiation polarized perpendicular to the detected scattered radiation when the system is described within the FC approximation (a) and when the FC-HT approximation is employed (b).

(which comes from transitions closer to the incident radiation) are more intense than higher energy peaks, and the difference is emphasized moving from FC to FC-HT regime. Surprisingly, including the HT terms in the transition dipole moments and transition potentials causes an increasing by almost six order of magnitude of the maximum intensity achieved, meaning that the HT contribution plays a crucial role in the calculation. Indeed, the first excitation is an electronic dark transition computed at the ground state equilibrium geometry, but moving the position of the atoms toward different, out of equilibrium, geometries "activates" the transition. Therefore, the FC contributions to the transition dipole moments and to the transition potentials, which are computed with the molecule in the ground state equilibrium geometry, do not yield a high intensity Raman signal. On the contrary, the HT contributions are computed bringing the molecule out of equilibrium position and for this reason some transition dipole moments and transition potentials are strongly enhanced so that also the Raman scattering intensity is visibly higher.

In order to compare the results obtained in presence of the NP with those in vacuum, we have reported in figure 3 the averaged Raman cross section computed at the end of the dynamics (at 2.4 ps) in vacuum and with the NP, distinguishing between FC and FC-
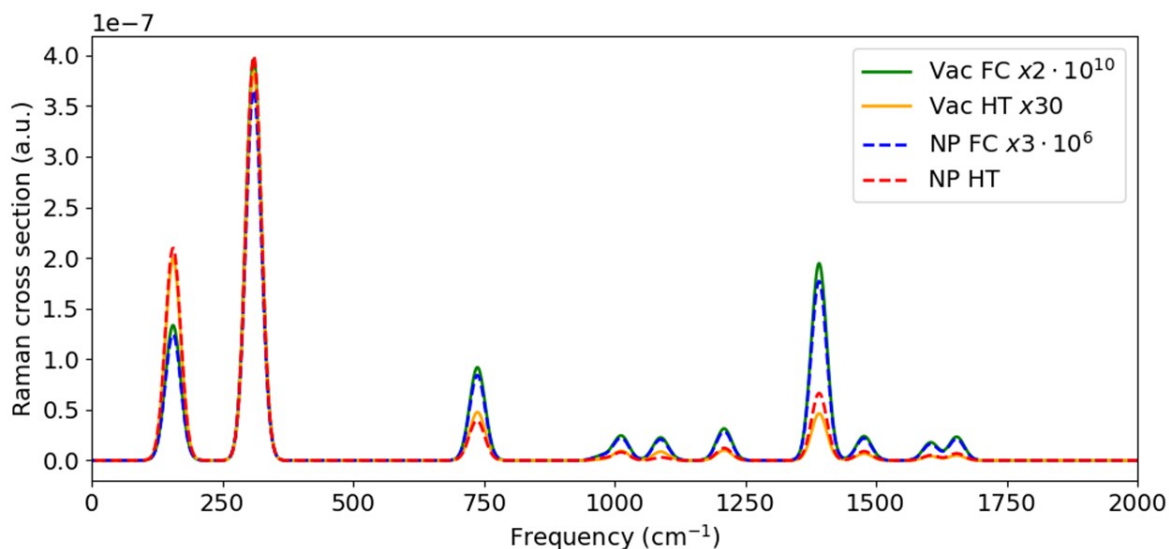
Figure 3: Averaged Raman scattering cross section at the end of the dynamics (2.4 ps) when the molecule is in vacuum using FC approximation (*Vac FC*), in vacuum under the FC-HT approximation (*Vac HT*), in presence of the NP using the FC approximation (*NP FC*) and in presence of the NP using the FC-HT approximation (*NP HT*). The legend reports the multiplication factors used to put all the spectra on the same scale.

HT regime. All the spectra are multiplied by a factor (reported in the legend) chosen to put them in the same scale of the spectrum calculated with the NP including HT terms. In both regimes, a similar profile can be noticed between the results of the calculations performed in vacuum or with the molecule close to the NP. On the other hand, from the results, the enhancement of the Raman signals induced by the nanoparticle appears clear in both regimes. The relative effect is larger in the FC approximation, where the maximum intensity achieved is almost four order of magnitude higher than in vacuum. Introducing the HT approximation, the enhancement induced by the NP is quite smaller, about a factor 30. The low enhancement achieved, with respect to the expectation, can be related to the features of the electronic excitation we are including in the model which is a dark transition as mentioned above, so that also the electronic transition potential induced on the NP surface is quite low. In addition, the HT contributions computed with the molecule in vacuum or in presence of the NP are quite similar. Further explanations are given by investigating the

189

mutual orientation between the molecule and the NP with respect to the orientation of the applied incident field and the scattered direction.

To this aim we have computed the Raman cross section at the end of the dynamics for specific polarization of the incident and scattered fields, in presence of the NP and in vacuum, exploiting both FC and FC-HT regimes. Figure 4 shows the Raman spectra, selecting the
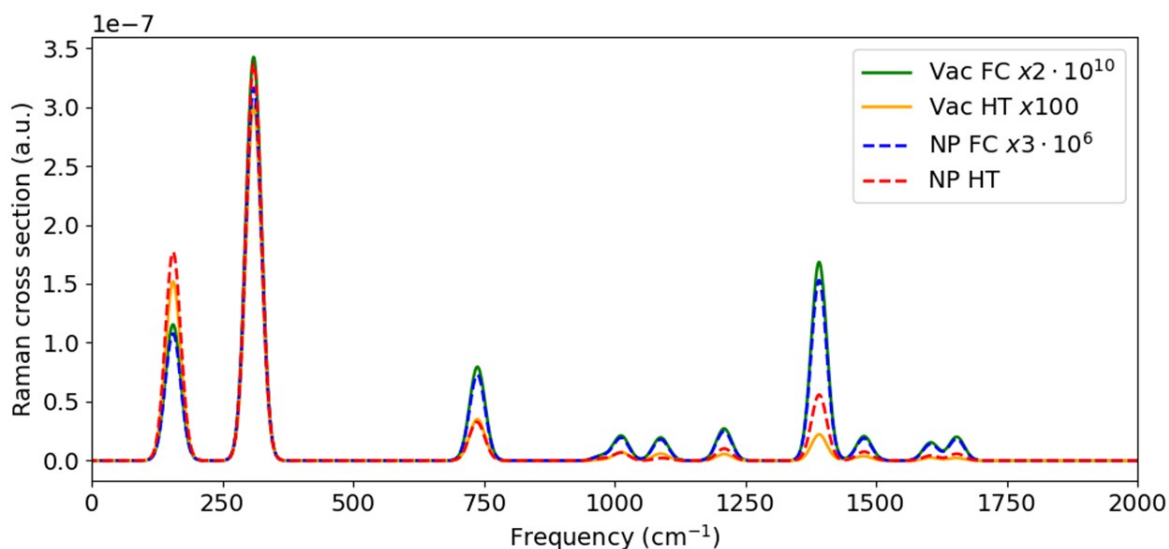

Figure 4: Raman scattering cross section at the end of the dynamics (2.4 ps) for a setup with incident and scattered fields along x-axis, when the molecule is in vacuum and using FC approximation (*Vac FC*), in vacuum under the FC-HT approximation (*Vac HT*), in presence of the NP using the FC approximation (*NP FC*) and in presence of the NP using the FCHT approximation (*NP HT*). The legend reports the multiplication factors used to put all the spectra on the same scale.

incident radiation along X and the scattered radiation along X (which is the direction of the NP major dimension), resulting from the calculations with the NP or in vacuum within the FC-HT regime and in FC approximation. All the spectra are multiplied by a factor (reported in the legend) chosen to put them in the same scale of the spectrum calculated with the NP including HT terms. Since the molecule-NP setup has been tuned to maximize the Raman intensity along the direction of the NP major dipole moment (which is along x-axis) these results appears very similar to those in figure 3, meaning that the major component of the

averaged Raman cross section comes from the XX term (both incident and scattered field along X-axis). Indeed, also the multiplication factors reported in the legend are equal to those employed in figure 3 but for the spectrum computed in vacuum within the FC-HT approximation. The enhancement induced by the presence of the NP within the FC-HT regime is even more evident with respect to figure 3 because the contribution XX (both incident and scattered field along X-axis) to the averaged Raman cross section in figure 3 prevails on the others since the presence of the NP enhances more the electromagnetic field along X direction, where the NP dipole moment is orientated. On the same foot, also the electronic transition dipole moment has a larger component along x-axis in all the calculations.
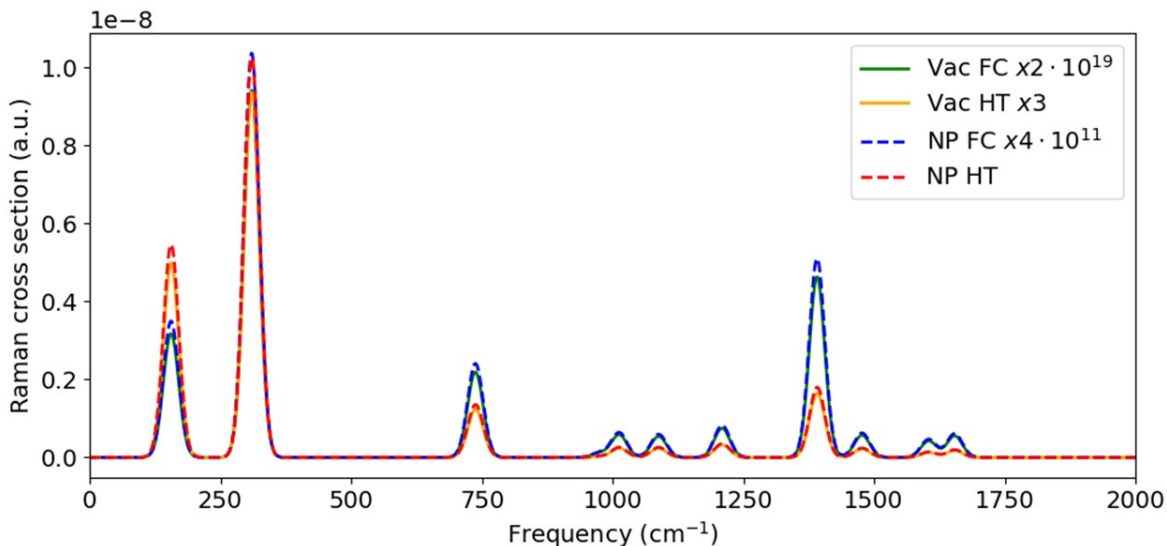
Figure 5: Raman scattering cross section at the end of the dynamics (2.4 ps) for a setup with incident and scattered fields along y axis, when the molecule is in vacuum and using FC approximation (*Vac FC*), in vacuum under the FC-HT approximation (*Vac HT*), in presence of the NP using the FC approximation (*NP FC*) and in presence of the NP using the FC-HT approximation (*NP HT*). The legend reports the multiplication factors used to put all the spectra on the same scale.

In addition, the HT terms added to the vibrational transition dipole moments are in most cases higher along the Y direction than along X, giving transition dipole moments

larger along Y than along X for some vibronic transitions. To better appreciate this point, figure 5 reports the Raman spectra with incident radiation along Y and scattered radiation along Y. All the spectra are multiplied by a factor (reported in the legend) chosen to put them in the same scale of the spectrum calculated with the NP including HT terms. Since the electronic transition dipole moment of the molecule along Y is *400* times lower than the one along X, the intensity of the Raman spectra are expected to be less intense than those in figure 4. This is rapidly appreciated within the FC approximation, where the Raman spectra intensity is very low both in vacuum and in presence of the NP. On the other hand, the HT terms added to the Y direction of the transition dipole moments depend on the derivatives of the electronic transition dipole moment along the molecular normal mode coordinates, which have higher contributions along Y as mentioned. Moreover, in this case the presence of the NP does not strongly affect the enhancement of the porphyrin Raman response because their two dipole moments along Y direction are not aligned but rather parallel. On the contrary, in vacuum, within FC-HT regime, the XX and YY contributions are almost identical as the HT terms along Y compensate for the unbalanced electronic transition dipole moment which is higher along X.

5 Conclusion

We have proposed a method able to compute the time-dependent surface-enhanced Raman scattering of molecules, which gives information on the Raman signal accumulated during the molecule-NP dynamics. This method combines multiple strategies previously developed to treat separate problems as: the TD-BEM[61] used to couple the molecular dynamics with the surface charge dynamics on a NP described through its experimental dielectric function and the time dependent Raman scattering model[49] to calculate how the Raman signal is accumulated in time. This work paves the way for application of TD-BEM also to other kind of spectroscopies and processes which can be investigated in time domain, such as

energy transfer or non-linear spectroscopies.

The procedure has been applied to a porphyrin molecule whose centre is 10 Å far from the surface of a gold nanoellipsoid. We computed the time-dependent Raman cross section exploring the FC regime as well as including the HT terms in the expansion of the transition dipole moments and transition potentials. The two different conditions gave results very different in terms of signal intensity, pointing out the necessity of a fine description of the molecular vibronic structure by including the HT terms in the expansion of dipoles and potentials. In addition, to have a clear view of the different contributions to the Raman cross section is useful to look at results given by selected orientation of the incident and scattered fields. Manipulating the lasers' polarization from a theoretical viewpoint is a great advantage for adjusting the experimental setup to improve the performance for a specific molecule-NP configuration.

Acknowledgement

References

(1) Rostron, P.; Gaber, S.; Gaber, D. Raman spectroscopy, review. *IJETR* **2016**, *21*, 24.

(2) Graves, P.; Gardiner, D. *Practical Raman spectroscopy*; Springer, 1989; Vol. 10.

(3) Ferraro, J. R. *Introductory Raman spectroscopy*; Elsevier, 2003.

(4) Kuhar, N.; Sil, S.; Verma, T.; Umapathy, S. Challenges in application of Raman spectroscopy to biology and materials. *RSC adv.* **2018**, *8*, 25888–25908.

(5) Jones, R. R.; Hooper, D. C.; Zhang, L.; Wolverson, D.; Valev, V. K. Raman techniques: fundamentals and frontiers. *Nanoscale Res. Lett.* **2019**, *14*, 1–34.

(6) Hess, C. New advances in using Raman spectroscopy for the characterization of catalysts and catalytic reactions. *Chem. Soc. Rev.* **2021**, *50*, 3519–3564.

(7) Pérez-Jiménez, A. I.; Lyu, D.; Lu, Z.; Liu, G.; Ren, B. Surface-enhanced Raman spectroscopy: benefits, trade-offs and future developments. *Chem. Sci.* **2020**, *11*, 4563–4577.

(8) Zong, C.; Premasiri, R.; Lin, H.; Huang, Y.; Zhang, C.; Yang, C.; Ren, B.; Ziegler, L. D.; Cheng, J.-X. Plasmon-enhanced stimulated Raman scattering microscopy with single-molecule detection sensitivity. *Nat. Comm.* **2019**, *10*, 5318.

(9) Zhang, Y.; Yang, B.; Ghafoor, A.; Zhang, Y.; Zhang, Y.-F.; Wang, R.-P.; Yang, J.-L.; Luo, Y.; Dong, Z.-C.; Hou, J. G. Visually constructing the chemical structure of a single molecule by scanning Raman picoscopy. *Natl. Sci.* **2019**, *6*, 1169–1175.

(10) Yu, Y.; Xiao, T.-H.; Wu, Y.; Li, W.; Zeng, Q.-G.; Long, L.; Li, Z.-Y. Roadmap for single-molecule surface-enhanced Raman spectroscopy. *Adv. photonics* **2020**, *2*, 014002–014002.

(11) Wang, X.; Huang, S.-C.; Hu, S.; Yan, S.; Ren, B. Fundamental understanding and applications of plasmon-enhanced Raman spectroscopy. *Nat. Rev. Phys.* **2020**, *2*, 253–271.

(12) Maccaferri, N.; Barbillon, G.; Koya, A. N.; Lu, G.; Acuna, G. P.; Garoli, D. Recent advances in plasmonic nanocavities for single-molecule spectroscopy. *Nanoscale Adv.* **2021**, *3*, 633–642.

(13) Almehmadi, L. M.; Curley, S. M.; Tokranova, N. A.; Tenenbaum, S. A.; Lednev, I. K. Surface enhanced Raman spectroscopy for single molecule protein detection. *Sci. Rep.* **2019**, *9*, 12356.

(14) Langer, J.; Jimenez de Aberasturi, D.; Aizpurua, J.; Alvarez-Puebla, R. A.; Auguié, B.; Baumberg, J. J.; Bazan, G. C.; Bell, S. E. J.; Boisen, A.; Brolo, A. G.; et al, Present and Future of Surface-Enhanced Raman Scattering. *ACS Nano* **2020**, *14*, 28–117.

(15) Bell, S. E.; Charron, G.; Cortés, E.; Kneipp, J.; de la Chapelle, M. L.; Langer, J.; Procházka, M.; Tran, V.; Schlücker, S. Towards reliable and quantitative surface-enhanced Raman scattering (SERS): From key parameters to good analytical practice. *Angew. Chem., Int. Ed.* **2020**, *59*, 5454–5462.

(16) Chen, X.; Liu, P.; Hu, Z.; Jensen, L. High-resolution tip-enhanced Raman scattering probes sub-molecular density changes. *Nat. Comm.* **2019**, *10*, 2567.

(17) Lee, J.; Crampton, K. T.; Tallarida, N.; Apkarian, V. A. Visualizing vibrational normal modes of a single molecule with atomically confined light. *Nature* **2019**, *568*, 78–82.

(18) Jiang, N.; Kurouski, D.; Pozzi, E. A.; Chiang, N.; Hersam, M. C.; Van Duyne, R. P. Tip-enhanced Raman spectroscopy: From concepts to practical applications. *Chem. Phys. Lett.* **2016**, *659*, 16–24.

(19) Xu, H.; Bjerneld, E. J.; Käll, M.; Börjesson, L. Spectroscopy of single hemoglobin molecules by surface enhanced Raman scattering. *Phys. Rev. Lett.* **1999**, *83*, 4357.

(20) Alvarez-Puebla, R.; Liz-Marzán, L. M.; García de Abajo, F. J. Light concentration at the nanometer scale. *J. Phys. Chem. Lett.* **2010**, *1*, 2428–2434.

(21) Lombardi, J. R.; Birke, R. L. The theory of surface-enhanced Raman scattering. *J. Chem. Phys.* **2012**, *136*, 144704.

(22) Jensen, L.; Aikens, C. M.; Schatz, G. C. Electronic structure methods for studying surface-enhanced Raman scattering. *Chem. Soc. Rev.* **2008**, *37*, 1061–1073.

(23) Schatz, G. C. Theoretical studies of surface enhanced Raman scattering. *Acc. Chem. Res.* **1984**, *17*, 370–376.

(24) Yang, W.-H.; Schatz, G. C.; Van Duyne, R. P. Discrete dipole approximation for calculating extinction and Raman intensities for small particles with arbitrary shapes. *J. Chem. Phys.* **1995**, *103*, 869–875.

(25) Taflove, A.; Hagness, S. C.; Piket-May, M. Computational electromagnetics: the finite-difference time-domain method. *The Electrical Engineering Handbook* **2005**, *3*, 629–670.

(26) Campion, A.; Kambhampati, P. Surface-enhanced Raman scattering. *Chem. Soc. Rev.* **1998**, *27*, 241–250.

(27) Schatz, G. C.; Van Duyne, R. P. Handbook of vibrational spectroscopy. *New York: Wiley* **2002**, *1*, 759.

(28) Gersten, J.; Nitzan, A. Electromagnetic theory of enhanced Raman scattering by molecules adsorbed on rough surfaces. *J. Chem. Phys.* **1980**, *73*, 3023–3037.

(29) Le Ru, E.; Etchegoin, P. Rigorous justification of the| E| 4 enhancement factor in surface enhanced Raman spectroscopy. *Chem. Phys. Lett.* **2006**, *423*, 63–66.

(30) Wu, D.-Y.; Liu, X.-M.; Duan, S.; Xu, X.; Ren, B.; Lin, S.-H.; Tian, Z.-Q. Chemical enhancement effects in SERS spectra: A quantum chemical study of pyridine interacting with copper, silver, gold and platinum metals. *J. Phys. Chem. C* **2008**, *112*, 4195–4204.

(31) Morton, S. M.; Jensen, L. Understanding the molecule- surface chemical coupling in SERS. *J. Am. Chem. Soc.* **2009**, *131*, 4090–4098.

(32) Payton, J. L.; Morton, S. M.; Moore, J. E.; Jensen, L. A hybrid atomistic electrodynamics–quantum mechanical approach for simulating surface-enhanced Raman scattering. *Acc. Chem. Res.* **2014**, *47*, 88–99.

(33) Link, S.; El-Sayed, M. A. Optical properties and ultrafast dynamics of metallic nanocrystals. *Annu. Rev. Phys. Chem.* **2003**, *54*, 331–366.

(34) De Heer, W. A. The physics of simple metal clusters: experimental aspects and simple models. *Reviews of Modern Physics* **1993**, *65*, 611.

(35) Hao, E.; Schatz, G. C. Electromagnetic fields around silver nanoparticles and dimers. *J. Chem. Phys.* **2004**, *120*, 357–366.

(36) Trautmann, S.; Aizpurua, J.; Götz, I.; Undisz, A.; Dellith, J.; Schneidewind, H.; Rettenmayr, M.; Deckert, V. A classical description of subnanometer resolution by atomic features in metallic structures. *Nanoscale* **2017**, *9*, 391–401.

(37) Esteban, R.; Borisov, A. G.; Nordlander, P.; Aizpurua, J. Bridging quantum and classical plasmonics with a quantum-corrected model. *Nat. Commun.* **2012**, *3*, 825.

(38) Pipolo, S.; Corni, S. Real-Time Description of the Electronic Dynamics for a Molecule Close to a Plasmonic Nanoparticle. *J. Phys. Chem. C* **2016**, *120*, 28774–28781.

(39) Mullin, J.; Valley, N.; Blaber, M. G.; Schatz, G. C. Combined quantum mechanics (TDDFT) and classical electrodynamics (Mie theory) methods for calculating surface enhanced Raman and hyper-Raman spectra. *J. Phys. Chem. A* **2012**, *116*, 9574–9581.

(40) Anger, P.; Bharadwaj, P.; Novotny, L. Enhancement and quenching of single-molecule fluorescence. *Phys. Rev. Lett.* **2006**, *96*, 113002.

(41) Della Sala, F.; D'Agostino, S. *Handbook of molecular plasmonics*; CRC Press, 2013.

(42) Tomasi, J.; Persico, M. Molecular interactions in solution: an overview of methods based on continuous distributions of the solvent. *Chem. Rev.* **1994**, *94*, 2027–2094.

(43) Cances, E.; Mennucci, B.; Tomasi, J. A new integral equation formalism for the polarizable continuum model: Theoretical background and applications to isotropic and anisotropic dielectrics. *J. Chem. Phys.* **1997**, *107*, 3032–3041.

(44) Tomasi, J.; Mennucci, B.; Cammi, R. Quantum mechanical continuum solvation models. *Chem. Rev.* **2005**, *105*, 2999–3094.

(45) Volakis, J. L.; Sertel, K. *Integral Equation Methods for Electromagnetics*; 2012; pp 1–392.

(46) Corni, S.; Tomasi, J. Surface enhanced Raman scattering from a single molecule adsorbed on a metal particle aggregate: A theoretical study. *J. Chem. Phys* **2002**, *116*, 1156–1164.

(47) Corni, S.; Pipolo, S.; Cammi, R. Equation of motion for the solvent polarization apparent charges in the polarizable continuum model: Application to real-time TDDFT. *J. Phys. Chem. A* **2015**, *119*, 5405–5416.

(48) Coccia, E.; Fregoni, J.; Guido, C.; Marsili, M.; Pipolo, S.; Corni, S. Hybrid theoretical models for molecular nanoplasmonics. *J. Chem. Phys.* **2020**, *153*, 200901.

(49) Dall'Osto, G.; Corni, S. Time Resolved Raman Scattering of Molecules: A Quantum Mechanics Approach with Stochastic Schroedinger Equation. *J. Phys. Chem. A* **2022**, *126*, 8088–8100.

(50) Lee, S.-Y.; Heller, E. J. Time-dependent theory of Raman scattering. *J. Chem. Phys* **1979**, *71*, 4777–4788.

(51) Baer, M. *Beyond Born-Oppenheimer: electronic nonadiabatic coupling terms and conical intersections*; John Wiley & Sons, 2006.

(52) Worth, G. A.; Cederbaum, L. S. Beyond Born-Oppenheimer: molecular dynamics through a conical intersection. *Annu. Rev. Phys. Chem* **2004**, *55*, 127–58.

(53) Yonehara, T.; Hanasaki, K.; Takatsuka, K. Fundamental approaches to nonadiabaticity: Toward a chemical theory beyond the Born–Oppenheimer paradigm. *Chem. Rev.* **2012**, *112*, 499–542.

(54) Li, J.-F.; Li, C.-Y.; Aroca, R. F. Plasmon-enhanced fluorescence spectroscopy. *Chem. Soc. Rev.* **2017**, *46*, 3962–3979.

(55) Johnson, P. B.; Christy, R. W. Optical Constants of the Noble Metals. *Phys. Rev. B* **1972**, *6*, 4370–4379.

(56) Frisch, M. J.; Trucks, G. W.; Schlegel, H. B.; Scuseria, G. E.; Robb, M. A.; Cheeseman, J. R.; Scalmani, G.; Barone, V.; Petersson, G. A.; Nakatsuji, H.; et al, Gaussian 16 Revision B.01. 2016; Gaussian Inc. Wallingford CT.

(57) Santoro, F.; Lami, A.; Improta, R.; Barone, V. Effective method to compute vibrationally resolved optical spectra of large molecules at finite temperature in the gas phase and in solution. *J. Chem. Phys* **2007**, *126*, 184102.

(58) Santoro, F.; Cerezo, J. FCclasses3, a code for vibronic calculations. `http://www.iccom.cnr.it/en/fcclasses`, 2022; [Online; accessed 27-July-2022].

(59) Dykstra, C.; Frenking, G.; Kim, K.; Scuseria, G. *Theory and applications of computational chemistry: the first forty years*; Elsevier, 2011.

(60) Schmidt, M. W.; Baldridge, K. K.; Boatz, J. A.; Elbert, S. T.; Gordon, M. S.; Jensen, J. H.; Koseki, S.; Matsunaga, N.; Nguyen, K. A.; Su, S., et al. General atomic and molecular electronic structure system. *Journal of computational chemistry* **1993**, *14*, 1347–1363.

(61) Dall'Osto, G.; Gil, G.; Pipolo, S.; Corni, S. Real-time dynamics of plasmonic resonances in nanoparticles described by a boundary element method with generic dielectric function. *J. Chem. Phys* **2020**, *153*, 184114.

Conclusion

This Ph.D. thesis is situated in the field of Molecular Plasmonics, and has the aim of developing new methods able to investigate different processes from a fresh perspective, as well as applying them to situations of relevant scientific interest. In some cases, new implementations have grown from the necessity to improve existing procedures to tackle systems whose complexity was larger than that of systems investigated in the past, whereas in other cases new implementations have been inspired by a lack in the literature of possible simulation strategies that can be more informative of existing ones.

Therefore, this thesis has not been organized following strictly the chronological order of the topics I focused on, but on the basis of the two macro areas encompassing my Ph.D. activity. All the material reported is devoted to apply new or existing strategies on calculation of interaction between molecule and plasmonic nanosystems, preferably in time domain, which in some cases has needed preliminary calculations to assess or to develop a theoretical procedure. Different chapters, even if belonging to two different blocks of the thesis, are strongly connected and in some cases the theory employed and the kind of calculations performed found their basis on previous chapters.

In the first part of the thesis, I focused on code developments and applications which aim to investigate electronic excited states of molecules in presence of metal nanoparticles. The first chapter reports a methodological development of existing tools in order to improve the way to calculate the interaction between a molecule and a nanoparticle in time domain. This was needed as the first step of my activity

to overcome the limitations imposed by previous methods on the description of the metallic nature of a nanoparticle when computing the real-time dynamics of polarization charges on a NP surface through TD-BEM. The improvements I brought to TD-BEM by adding the possibility to evolve the polarization charges employing the experimental frequency-dependent dielectric function to describe the metal, have allowed later to consider metals with complicate behaviour in presence of light, such as gold or rhodium.

In particular, the method developed in chapter 1 has been employed to investigate hole and electron injection involved in the CO_2 hydrogenation, catalysed by a rhodium nanoparticle in presence of light. The novelty brought by this application is mainly on the topic discussed, which is of great interest in the scientific community and at the same time this kind of process has not been investigated with such sophisticated tools as TD-BEM before. The strategy employed has proven to be suitable to treat a quantum mechanics—molecular mechanics interface in order to consider two portion of the NP described at different level of theory. More importantly, the method results effective to explain the driving force of the process in terms of hole injection rather than electron injection as previously proposed in literature.

On the other hand, PCM-NP in frequency domain has been employed for simulating Tip-enhanced photoluminescence experiments and a time-dependent procedure was not required. Nevertheless, some improvements of the existing method were needed in order to deal with more than one nanostructure and eventually with complicated shapes than those investigated in the past. To this point, I developed a new computational way based on a different diagonalization procedure of the BEM equation for the polarization charges, which will be useful also in other applications. Moreover, these improvements combined with additional equations implemented in the TDPlas code[60] make possible the simulation of TEPL intensity of zinc phthalocyanine in agreement with experimental results.

The second part of the thesis focused on calculation of Raman scattering moving among different target molecules, as well as using different methodologies. Never-

theless, all the calculations support the aim to set up a strategy to compute time-dependent Raman scattering of single amino acids in proximity of metal nanoparticles, which would be useful to support new experiments in the field of protein detection. I have used different approaches and also different target molecules in order to explore the object of study and at the same time to develop a strategy which can align the theory with the experiment in the best way possible. The application of well known computational strategies allowed me to focus on the target molecules, some selected amino acids, and to explore the features of their Raman spectra in presence of some cations usually employed in the experiments. This information was not already available in the literature and can be really useful for experimentalists to define the goodness of new results as well as to guide the choice of cations to use in the experiments.

Although these simulations are useful to give an idea of the experimental outcomes, the methods employed are lacking in some features in order to draw nearer to the experimental set-up. In particular, the method employed does not allow including a metal nanoparticle in the calculation as well as to properly describe an incident laser pulse. For this reason, I developed a time-dependent strategy to compute the Raman spectra of single molecules, which I recently improve to account also for the presence of a metal nanoparticle. A time-dependent method is the natural choice when one wants to investigate the dynamics of a molecule, since one or more incident pulses can be included properly by mimicking the experimental lasers. Moreover, a time-dependent approach gives additional information, as the timescale of the process, not easily accessible through different methodologies. The method developed has been efficaciously applied to a porphyrin molecule whose vibrational structure is not trivial to be described, obtaining its time-dependent Raman scattering in different conditions.

The final achievement of this thesis regards the developments of a time-dependent procedure able to simulate the Raman scattering of molecules in proximity of plasmonic nanoparticle. The procedure is based on TD-BEM, reported in chapter 1, and

on the time-dependent Raman protocol for molecules in vacuum, reported in chapter 5, both developed during my Ph.D. activity. Within this strategy, the mutual interaction between the molecule and the NP is accounted in a real-time picture in order to include the electric field enhancement induced by the plasmonic nanoparticle at each instant and to reproduce the accumulation of the Raman signal in time.

As future perspective, the TD-BEM procedure can be coupled with new post-processing tools able to investigate different processes not reported in this thesis as non-linear spectroscopies in presence of a metal NP.[93] Indeed, optical non-linearities are very weak, but they can be enhanced by strong local electromagnetic fields such those generated in proximity of plasmonic surfaces following the same mechanism as in SERS. This is equal to an increasing of the non-linearity of the material.[94, 95] Moreover, manipulating metal nanoparticle features results in modification of plasmonic resonances, inducing a change in the refractive index which is relevant to tune the non-linear response of the material. A time dependent picture of non-linear spectroscopy in presence of plasmonic materials can be really informative and can help in designing new experimental setups. Moreover, the method developed in this thesis can be employed to simulate ultrafast experiments in non-linear regime. The PCM-NP model in time domain can also be applied to study plasmon-mediated energy transfer, which has given promising experimental results in the past twenty years[96] even though the comprehension of the mechanism involved is still not complete.

On the other hand, the already developed methods can be applied to more challenging goals. In particular, the time-dependent Raman scattering tool has been applied so far on a test-case molecule, and it could be interesting moving towards more relevant and complicated molecule-NP setup. In this perspective, it would be useful to apply the procedure to simulation of Raman scattering of single amino acids inside a peptide chain when floating along a plasmonic gold nanopore, in support of the newest and challenging experiments on protein detection.[71] To do so preliminary molecular dynamics calculations are needed in order to understand

the mutual position of amino acids in a peptide chain, in particular in presence of some ions employed in the experiments. Afterwards, Raman calculations can be performed on single amino acids in the chain by exploiting a QM/MM approach in which only the target portion of the peptide is treated at quantum level of theory. Finally, the effect of the surrounding NP can be included either in a mediated way through an effective static field or explicitly through the TD-SERS procedure developed during my Ph.D. activity.

Bibliography

[1] Novotny, L. & Hecht, B. *Principles of nano-optics* (Cambridge university press, 2012).

[2] Hohenester, U. U. *Nano and quantum optics : an introduction to basic principles and theory* (Springer, 2020).

[3] Kelly, K. L., Coronado, E., Zhao, L. L. & Schatz, G. C. The optical properties of metal nanoparticles: the influence of size, shape, and dielectric environment (2003).

[4] Maccaferri, N. *et al.* Recent advances in plasmonic nanocavities for single-molecule spectroscopy. *Nanoscale Adv.* **3**, 633–642 (2021).

[5] Van Duyne, R. P. Molecular Plasmonics. *Science* **306**, 985 – 986 (2004).

[6] Sonntag, M. D. *et al.* Molecular plasmonics for nanoscale spectroscopy. *Chem. Soc. Rev.* **43**, 1230–1247 (2014).

[7] Mejía-Salazar, J. & Oliveira Jr, O. N. Plasmonic biosensing: Focus review. *Chem. Rev.* **118**, 10617–10625 (2018).

[8] Minopoli, A., Acunzo, A., Della Ventura, B. & Velotta, R. Nanostructured surfaces as plasmonic biosensors: A review. *Adv. Mater. Interfaces* **9**, 2101133 (2022).

[9] Padmanabhan, P., Kumar, A., Kumar, S., Chaudhary, R. K. & Gulyás, B. Nanoparticles in practice for molecular-imaging applications: an overview. *Acta Biomater.* **41**, 1–16 (2016).

[10] Bouché, M. *et al.* Recent advances in molecular imaging with gold nanoparticles. *Bioconj. Chem.* **31**, 303–314 (2019).

[11] Della Sala, F. & D'Agostino, S. *Handbook of molecular plasmonics* (CRC Press, 2013).

[12] Nitzan, A. & Brus, L. Can photochemistry be enhanced on rough surfaces? *J. Chem. Phys.* **74**, 5321–5322 (1981).

[13] Linic, S., Aslam, U., Boerigter, C. & Morabito, M. Photochemical transformations on plasmonic metal nanoparticles. *Nat. Mat.* **14**, 567–576 (2015).

[14] Zhang, Y. *et al.* Surface-plasmon-driven hot electron photochemistry. *Chem. Rev.* **118**, 2927–2954 (2017).

[15] Cortés, E. *et al.* Challenges in plasmonic catalysis. *ACS nano* **14**, 16202–16219 (2020).

[16] Cortés, E. & Camargo, P. H. *Plasmonic Catalysis: From Fundamentals to Applications* (John Wiley & Sons, 2021).

[17] Langer, J. *et al.* Present and future of surface-enhanced raman scattering. *ACS Nano* **14**, 28–117 (2020).

[18] Huang, J.-A. *et al.* Sers discrimination of single dna bases in single oligonucleotides by electro-plasmonic trapping. *Nat. Comm.* **10**, 1–10 (2019).

[19] Liu, P., Chulhai, D. V. & Jensen, L. Single-molecule imaging using atomistic near-field tip-enhanced raman spectroscopy. *ACS Nano* **11**, 5094–5102 (2017).

[20] Yu, H., Peng, Y., Yang, Y. & Li, Z.-Y. Plasmon-enhanced light–matter interactions and applications. *Npj Comput. Mater.* **5**, 1–14 (2019).

[21] Maier, S. A. *Plasmonics: fundamentals and applications* (Springer Science & Business Media, 2007).

[22] Yang, B. *et al.* Sub-nanometre resolution in single-molecule photoluminescence imaging. *Nat. Photonics* **14**, 693–699 (2020).

[23] Trivedi, D. J., Barrow, B. & Schatz, G. C. Understanding the chemical contribution to the enhancement mechanism in sers: Connection with hammett parameters. *J. Chem. Phys.* **153**, 124706 (2020).

[24] Wriedt, T. Mie theory: a review. *The Mie theory: Basics and applications* 53–71 (2012).

[25] Yang, W.-H., Schatz, G. C. & Van Duyne, R. P. Discrete dipole approximation for calculating extinction and raman intensities for small particles with arbitrary shapes. *J. Chem. Phys.* **103**, 869–875 (1995).

[26] Ungureanu, C., Rayavarapu, R. G., Manohar, S. & van Leeuwen, T. G. Discrete dipole approximation simulations of gold nanorod optical properties: Choice of input parameters and comparison with experiment. *J. Appl. Phys.* **105**, 102032 (2009).

[27] Myroshnychenko, V. *et al.* Modeling the optical response of highly faceted metal nanoparticles with a fully 3d boundary element method. *Adv. Mat.* **20**, 4288–4293 (2008).

[28] Hohenester, U. Quantum corrected model for plasmonic nanoparticles: A boundary element method implementation. *Phys. Rev. B* **91**, 205436 (2015).

[29] Hao, F., Nehl, C. L., Hafner, J. H. & Nordlander, P. Plasmon resonances of a gold nanostar. *Nano Lett.* **7**, 729–732 (2007).

[30] Taflove, A., Hagness, S. C. & Piket-May, M. Computational electromagnetics: the finite-difference time-domain method. *The Electrical Engineering Handbook* **3**, 629–670 (2005).

[31] Lee, S.-Y. & Heller, E. J. Time-dependent theory of raman scattering. *J. Chem. Phys* **71**, 4777–4788 (1979).

[32] Hohenberg, P. & Kohn, W. Inhomogeneous Electron Gas. *Phys. Rev.* **136**, B864–B871 (1964).

[33] Kohn, W. & Sham, L. J. Self Consistent Equations Including Exchange and Correlation Effects. *Phys. Rev.* **140**, A1133–A1138 (1965).

[34] Lombardi, J. R., Birke, R. L., Lu, T. & Xu, J. Charge-transfer theory of surface enhanced raman spectroscopy: Herzberg–teller contributions. *J. Chem. Phys.* **84**, 4174–4180 (1986).

[35] Lombardi, J. R. & Birke, R. L. A unified view of surface-enhanced raman scattering. *Acc. Chem. Res.* **42**, 734–742 (2009).

[36] Baer, M. *Beyond Born-Oppenheimer: electronic nonadiabatic coupling terms and conical intersections* (John Wiley & Sons, 2006).

[37] Yonehara, T., Hanasaki, K. & Takatsuka, K. Fundamental approaches to nonadiabaticity: Toward a chemical theory beyond the born–oppenheimer paradigm. *Chem. Rev.* **112**, 499–542 (2012).

[38] Small, G. J. Herzberg–teller vibronic coupling and the duschinsky effect. *J. Chem. Phys.* **54**, 3300–3306 (1971).

[39] Baiardi, A., Bloino, J. & Barone, V. General time dependent approach to vibronic spectroscopy including franck–condon, herzberg–teller, and duschinsky effects. *J. Chem. Theory Comput.* **9**, 4097–4115 (2013).

[40] Santoro, F., Improta, R., Lami, A., Bloino, J. & Barone, V. Effective method to compute Franck-Condon integrals for optical spectra of large molecules in solution. *J. Chem. Phys.* **126**, 84509 (2007).

[41] Santoro, F., Cappelli, C. & Barone, V. Effective time-independent calculations of vibrational resonance raman spectra of isolated and solvated molecules including duschinsky and herzberg–teller effects. *J. Chem. Theory Comput.* **7**, 1824–1839 (2011).

[42] Sharp, T. & Rosenstock, H. Franck—condon factors for polyatomic molecules. *The Journal of Chemical Physics* **41**, 3453–3463 (1964).

[43] Santoro, F. & Cerezo, J. Fcclasses3, a code for vibronic calculations. `http://www.iccom.cnr.it/en/fcclasses` (2022). [Online; accessed 27-July-2022].

[44] Tomasi, J. & Persico, M. Molecular interactions in solution: an overview of methods based on continuous distributions of the solvent. *Chem. Rev.* **94**, 2027–2094 (1994).

[45] Corni, S., Pipolo, S. & Cammi, R. Equation of motion for the solvent polarization apparent charges in the polarizable continuum model: Application to real-time tddft. *J. Phys. Chem. A* **119**, 5405–5416 (2015).

[46] Corni, S. & Tomasi, J. Enhanced response properties of a chromophore physisorbed on a metal particle. *J. Chem. Phys.* **114**, 3739–3751 (2001).

[47] Pipolo, S. & Corni, S. Real-Time Description of the Electronic Dynamics for a Molecule Close to a Plasmonic Nanoparticle. *J. Phys. Chem. C* **120**, 28774–28781 (2016).

[48] Cances, E., Mennucci, B. & Tomasi, J. A new integral equation formalism for the polarizable continuum model: Theoretical background and applications to isotropic and anisotropic dielectrics. *J. Chem. Phys.* **107**, 3032–3041 (1997).

[49] Tomasi, J., Mennucci, B. & Cammi, R. Quantum mechanical continuum solvation models. *Chem. Rev.* **105**, 2999–3094 (2005).

[50] Corni, S. & Tomasi, J. Surface enhanced raman scattering from a single molecule adsorbed on a metal particle aggregate: A theoretical study. *J. Chem. Phys.* **116**, 1156–1164 (2002).

[51] Vukovic, S., Corni, S. & Mennucci, B. Fluorescence enhancement of chromophores close to metal nanoparticles. optimal setup revealed by the polarizable continuum model. *J. Phys. Chem. C* **113**, 121–133 (2009).

[52] Angioni, A., Corni, S. & Mennucci, B. Can we control the electronic energy transfer in molecular dyads through metal nanoparticles? a qm/continuum investigation. *Phys. Chem. Chem. Phys.* **15**, 3294–3303 (2013).

[53] Coccia, E. & Corni, S. Role of coherence in the plasmonic control of molecular absorption. *J. Chem. Phys.* **151**, 044703 (2019).

[54] Latorre, F. *et al.* Spatial resolution of tip-enhanced raman spectroscopy – dft assessment of the chemical effect. *Nanoscale* **8**, 10229–10239 (2016).

[55] Zhu, W. *et al.* Quantum mechanical effects in plasmonic structures with sub-nanometre gaps. *Nat. Commun.* **7**, 11495 (2016).

[56] Corni, S. & Tomasi, J. Surface enhanced Raman scattering from a single molecule adsorbed on a metal particle aggregate: A theoretical study. *J. Chem. Phys.* **116**, 1156–1164 (2002).

[57] Marcheselli, J. *et al.* Simulating Plasmon Resonances of Gold Nanoparticles with Bipyramidal Shapes by Boundary Element Methods. *Journal of chemical theory and computation* **16**, 3807–3815 (2020).

[58] Corni, S. & Tomasi, J. Enhanced response properties of a chromophore physisorbed on a metal particle. *J. Chem. Phys.* **114**, 3739 (2001).

[59] Tomasi, J., Mennucci, B. & Cammi, R. Quantum mechanical continuum solvation models. *Chem. Rev.* **105**, 2999–3094 (2005).

[60] Coccia, E. *et al.* Wavet-tdplas. `https://github.com/stefano-corni/WaveT_TDPlas` (2021).

[61] Lakowicz, J. *et al.* Advances in surface-enhanced fluorescence. *J. Fluoresc.* **14**, 425–441 (2004).

[62] Mackowski, S. *et al.* Metal-enhanced fluorescence of chlorophylls in single light-harvesting complexes. *Nano Lett.* **8**, 558–564 (2008).

[63] Zrimsek, A. B. *et al.* Single-molecule chemistry with surface-and tip-enhanced raman spectroscopy. *Chemical reviews* **117**, 7583–7613 (2017).

[64] Liu, Z. *et al.* Revealing the molecular structure of single-molecule junctions in different conductance states by fishing-mode tip-enhanced raman spectroscopy. *Nat. Comm.* **2**, 1–6 (2011).

[65] Cancès, E., Mennucci, B. & Tomasi, J. A new integral equation formalism for the polarizable continuum model: Theoretical background and applications to isotropic and anisotropic dielectrics. *J. Chem. Phys.* **107**, 3032–3041 (1997).

[66] Zhang, X. *et al.* Product selectivity in plasmonic photocatalysis for carbon dioxide hydrogenation. *Nat. Comm.* **8**, 14542 (2017).

[67] Grobas Illobre, P. *et al.* Time-resolved excited-state analysis of molecular electron dynamics by tddft and bethe–salpeter equation formalisms. *J. Chem. Theory Comput.* **17**, 6314–6329 (2021).

[68] Candeloro, P. *et al.* Raman database of amino acids solutions: A critical study of extended multiplicative signal correction. *Analyst* **138**, 7331–7340 (2013).

[69] Zhu, G., Zhu, X., Fan, Q. & Wan, X. Raman spectra of amino acids and their aqueous solutions. *Spectrochimica Acta Part A: Molecular and Biomolecular Spectroscopy* **78**, 1187–1195 (2011).

[70] Huang, J.-A. *et al.* Multiplexed discrimination of single amino acid residues in polypeptides in a single sers hot spot. *Angew. Chem., Int. Ed.* **59**, 11423–11431 (2020).

[71] Garoli, D., Yamazaki, H., Maccaferri, N. & Wanunu, M. Plasmonic nanopores for single-molecule detection and manipulation: toward sequencing applications. *Nano letters* **19**, 7553–7562 (2019).

[72] Yang, J.-M. *et al.* An in situ sers study of ionic transport and the joule heating effect in plasmonic nanopores. *Chemical Communications* **54**, 13236–13239 (2018).

[73] Long, D. A. & Long, D. *The Raman effect: a unified treatment of the theory of Raman scattering by molecules*, vol. 8 (Wiley Chichester, 2002).

[74] Frisch, M. J. *et al.* Gaussian16 {R}evision {B}.01 (2016).

[75] Heller, E. J., Sundberg, R. & Tannor, D. Simple aspects of raman scattering. *J. Phys. Chem.* **86**, 1822–1833 (1982).

[76] Guthmuller, J. Calculation of vibrational resonance raman spectra of molecules using quantum chemistry methods. *Molecular Spectroscopy: A Quantum Chemistry Approach* **2**, 497–536 (2019).

[77] Baiardi, A., Bloino, J. & Barone, V. Accurate simulation of resonance-raman spectra of flexible molecules: An internal coordinates approach. *J. Chem. Theory Comput.* **11**, 3267–3280 (2015).

[78] Coccia, E., Troiani, F. & Corni, S. Probing quantum coherence in ultrafast molecular processes: An ab initio approach to open quantum systems. *J. Chem. Phys* **148**, 204112 (2018).

[79] Dall'Osto, G., Coccia, E., Guido, C. A. & Corni, S. Investigating ultrafast two-pulse experiments on single dnqdi fluorophores: a stochastic quantum approach. *Phys. Chem. Chem. Phys.* **22**, 16734–16746 (2020).

[80] Fleischmann, M., Hendra, P. J. & McQuillan, A. J. Raman spectra of pyridine adsorbed at a silver electrode. *Chem. Phys. Lett.* **26**, 163–166 (1974).

[81] Jeanmaire, D. L. & Van Duyne, R. P. Surface raman spectroelectrochemistry: Part i. heterocyclic, aromatic, and aliphatic amines adsorbed on the anodized silver electrode. *J. electroanal. chem. interfacial electrochem.* **84**, 1–20 (1977).

[82] Albrecht, M. G. & Creighton, J. A. Anomalously intense raman spectra of pyridine at a silver electrode. *J. Am. Chem. Soc.* **99**, 5215–5217 (1977).

[83] Gersten, J. & Nitzan, A. Electromagnetic theory of enhanced raman scattering by molecules adsorbed on rough surfaces. *J. Chem. Phys.* **73**, 3023–3037 (1980).

[84] Le Ru, E. & Etchegoin, P. Rigorous justification of the— e— 4 enhancement factor in surface enhanced raman spectroscopy. *Chem. Phys. Lett.* **423**, 63–66 (2006).

[85] Kneipp, K. *et al.* Single molecule detection using surface-enhanced raman scattering (sers). *Phys. Rev. Lett.* **78**, 1667 (1997).

[86] Sharma, B., Frontiera, R. R., Henry, A.-I., Ringe, E. & Van Duyne, R. P. Sers: Materials, applications, and the future. *Mater. today* **15**, 16–25 (2012).

[87] Jensen, L., Aikens, C. M. & Schatz, G. C. Electronic structure methods for studying surface-enhanced raman scattering. *Chem. Soc. Rev.* **37**, 1061–1073 (2008).

[88] Schatz, G. C. Theoretical studies of surface enhanced raman scattering. *Acc. Chem. Res.* **17**, 370–376 (1984).

[89] Schatz, G. C., Young, M. A. & Van Duyne, R. P. Electromagnetic mechanism of sers. *Surface-enhanced Raman scattering: physics and applications* 19–45 (2006).

[90] Le Ru, E., Meyer, M., Blackie, E. & Etchegoin, P. Advanced aspects of electromagnetic sers enhancement factors at a hot spot. *J. Raman Spectrosc.* **39**, 1127–1134 (2008).

[91] Xia, L. *et al.* Visualized method of chemical enhancement mechanism on sers and ters. *J. Raman Spectrosc.* **45**, 533–540 (2014).

[92] Wu, D.-Y. *et al.* Chemical enhancement effects in sers spectra: A quantum chemical study of pyridine interacting with copper, silver, gold and platinum metals. *J. Phys. Chem. C* **112**, 4195–4204 (2008).

[93] Kauranen, M. & Zayats, A. V. Nonlinear plasmonics. *Nat. Photon.* **6**, 737–748 (2012).

[94] Zayats, A. V., Smolyaninov, I. I. & Maradudin, A. A. Nano-optics of surface plasmon polaritons. *Phys. Rep.* **408**, 131–314 (2005).

[95] Stockman, M. I. Nanoplasmonics: past, present, and glimpse into future. *Opt. Express.* **19**, 22029–22106 (2011).

[96] Andrew, P. & Barnes, W. Energy transfer across a metal film mediated by surface plasmon polaritons. *science* **306**, 1002–1005 (2004).